Quartz as an archive of deformation and metamorphism of the continental crust

A DISSERTATION SUBMITTED TO
THE FACULTY OF THE UNIVERSITY OF MINNESOTA
BY

William O. Nachlas

IN PARTIAL FULFILLMENT OF THE REQUIREMENTS
FOR THE DEGREE OF

DOCTOR OF PHILOSOPHY

Christian Teyssier, co-adviser
Donna Whitney, co-adviser

December 2015

Acknowledgements

Reflecting on five years in Minnesota, I could not have anticipated the intellectual and personal growth that I would experience in my time here. In MN and along my research travels, I have met many great people who have advised, taught, and inspired me in my development as a scientist and person and I have many to thank for that.

First and foremost I want to thank my advisers, Christian Teyssier and Donna Whitney, for your support and constant encouragement over the last five years. You have supported me in the pursuit and development of my individual curiosities and I am forever grateful for this. I would also like to thank thesis committee members of my written, oral, and final exam committees, Peter Hudleston, David Kohlstedt, Marc Hirschmann, Mark Zimmerman, and Bill Seyfried – I appreciate all of your revisions and insight throughout the progress of my dissertation. Thanks a bunch to Greg Hirth for lots of great advice and interesting discussions.

This thesis would not have been possible without support from multiple funding sources. I gratefully acknowledge the National Science Foundation and Grant EAR-0911497 awarded to Donna Whitney, Christian Teyssier, and Greg Hirth for supporting this research. I also acknowledge a University of Minnesota Doctoral Dissertation Fellowship that supported me in the final year of my thesis. Thank you to several funding sources and awards that supported various aspects of this dissertation research – the Geological Society of America; the Mineralogy-Geochemistry-Petrology-Volcanology Division of the Geological Society of America; Sigma Xi; the Department of Earth Sciences at University of Minnesota; the University of Minnesota Doctoral Dissertation Travel Award; the Council of Graduate Students at University of Minnesota, the Graduate and Professional Schools Assembly at University of Minnesota, the University of Minnesota Thesis Research Travel Award, and the University of Minnesota Undergraduate Research Opportunities Program.

I am thankful to have learned analytical skills from many talented and thoughtful analysts. Thank you to lab managers of analytical laboratories who assisted me with data collection and taught me about analytical methods – at UMN: Anette von der Handt, Nick Seaton, Brian Bagley, Rick Knurr; at NENIMF WHOI: Nobu Shimizu, Brian Monteleone;

at USGS-Stanford: Marty Grove; at RPI: Jared Singer, Dan Ruscitto; at USGS-Denver: Heather Lowers; at UW-Madison: John Fournelle.

I am immensely fortunate to have had the opportunity to be a visitor in multiple experimental laboratories over the course of my PhD. Thank you to the research groups who graciously allowed me to work in their labs and whose members taught me how to prepare and run experiments – Hirth Research Group at Brown (Chris and Leo Concalves, Brooks Proctor, Amanda Getsinger, Eric Goergen, Leif Tokle, Keishi Okazaki); Kohlstedt Research Group at UMN (Matej Pec, Miki Tasaka, Mark Zimmerman); Seyfried Research Group at UMN (Adam Schaen, Drew Syverson, Rick Knurr); Watson Research Group at RPI (Jay Thomas, Mike Ackerson). Without the kindness and patience of these folks who volunteered their time to train me in the lab, I would never had the experimental discoveries that were critical to the direction of this research.

I am grateful for the learning experiences provided in attending multiple short courses and workshops over the last five years – Ion Probe Short Course at Arizona State University; MSA Short Course Diffusion in Minerals and Melts; NSF SIMS Workshop at UCLA; AGU Workshop Technology for Research at Elevated Pressure; DMG-MSA Workshop on Diffusion Modeling at Ruhr University; EarthCube Workshop Petrology Geochemistry at the Smithsonian Institution; SIMS workshop at WHOI; EarthCube Earth-Centered Communication for Cyberinfrastructure.

A special thank you to Annia Fayon, Chris Paola, and Peter Hudleston for many incredible memories during five years of field camps. I feel like the luckiest person in the world to have gotten to TA field camp for so many summers. Thank you to all my students in Advanced Field Geology Camps 2011, 2012, 2013, 2014, and 2015 and Mineralogy Labs 2012 and 2013 for your good spirits in the field (and lab), for your hard work, and for being so much fun to work with.

I want to extend my sincerest appreciation to many scientists that I have been fortunate to interact with and learn from during my time as a PhD student: Sumit Chakraborty, Reid Cooper, Larry Edwards, Josh Feinberg, John Fournelle, Scott Johnson, Steve Kidder, Karen Kleinspehn, Yan Liang, Clayton Loehn, Craig Manning, Tony Runkel, Frank Spear, Paul Spry, Jay Thomas, Jan Tullis, John Valley, Jeff Vervoort, Bruce Watson, Mike Williams, and Don Winston.

Thank you to Fred Davis and Ellery Frahm for guidance during my time as interim electron microprobe laboratory manager, and special thanks to Fred for all your patience in helping me figure out how to analyze the many random industrial materials that were brought into the lab. I also want to thank Anette von der Handt for many interesting and helpful discussions on electron probe microanalysis, it's been great having you in the

department. Thank you to Tony Withers for teaching me to mount and polish tiny crystals. A special thanks to Holger Stunitz for all of the great discussions during your sabbatical visit; I had not previously experienced such pleasant and congenial disagreements as Holger and I shared together. I thoroughly enjoyed your time here, although perhaps not *quite* as much as you enjoyed your time here. Thanks to Scott Currie in the UMN School of Music for allowing me to play in your samba classes and inviting me to perform in three Mayday Parades. Thanks to many friends for all of the interesting discussions, scientific and otherwise: Matej Pec, Alejandra Quintanilla, Cameron Meyers, Adam Schaen, Drew Syverson, Sharon Kressler, Johnny Zhang, Ben Tutolo, Chris Crosby, Matt Carter, Antoine Quilichini, Raphael Gottardi, Lars Hansen, Tom Mitchell, Elisa Fitz-Diaz, Come Lefebvre, Maud Meijers, Erkan Toraman, and Paula Ardia.

On many occasions over the last five years I have reflected on my gratitude for the exceptional undergraduate education provided to me by the Geosciences Department at Virginia Tech, in particular the guidance and instruction of Bob Tracy, Rick Law, Nancy Ross, and Don Rimstidt.

Finally, I want to send my love to my family, Mom, Dad, Ben, Caitlin, Adam, Jesse, Dave, Eli, Joel, Beverly, and the Sargents. I am so lucky to have had all of your support over the last five years. Looking forward to spending more time with you all!

Dedication

This dissertation is dedicated to my parents, Paul and Sally, who, as geologists themselves, instilled in me from a young age a great curiosity for the rocks underfoot.

Abstract

Quartz is perhaps the most rheologically-significant mineral in the continental crust. It occurs in many different rock types, it is susceptible to deformation over a range of crustal conditions, and it yields plastically at stresses lower than other rock-forming minerals. Consequently the deformation behavior of quartz – its rheology, microstructures, and recrystallization fabrics – has been well-studied in both natural and laboratory settings and is commonly used by structural geologists to interpret the direction and magnitude of forces in exhumed shear zones.

In the last decade, it was discovered that quartz can be used as a quantitative indicator of metamorphic conditions. The solubility and diffusivity of trace concentrations of Ti in quartz was determined experimentally, establishing a technique that uses quartz geochemistry as a thermometer, barometer, and geospeedometer to estimate temperatures, pressures, and rates of crystallization in natural rocks. However, the experiments that determined these parameters were conducted under hydrostatic stress. Given the propensity for quartz to deform ductiley in the Earth, it is important to investigate the influence of dynamic recrystallization on Ti substitution to determine if quartz geochemistry provides reliable information on the conditions and rates of ductile deformation.

This dissertation combined field and experimental approaches to study the effect of deformation on Ti exchange in quartz. Observations of quartzite mylonites from extensional shear zones in the North American Cordillera inspired the design of rock deformation experiments to simulate natural deformation processes under controlled laboratory conditions. Multiple quantitative (electron-, ion-, and laser-beam techniques) and semi-quantitative (cathodoluminescence) analytical methods were used to measure the Ti content of fine-scale microstructures, which were compared with crystallographic fabric analysis (electron back-scattered diffraction) to correlate the extent of recrystallization with Ti exchange. Results of this research show that dynamic recrystallization is effective at resetting Ti concentrations in quartz, indicating that Ti-in-quartz is capable of recording the conditions of ductile deformation. With the documented importance of quartz for accommodating ductile strain during orogenesis, findings presented in this dissertation demonstrate that quartz is capable of linking metamorphic petrology with deformation microstructures to contribute a new perspective on interpreting deformation in continental shear zones.

Table of Contents

Acknowledgements i

Dedication iv

Abstract v

Table of Contents vii

List of Figures xii

List of Tables xix

CHAPTER 1

Introduction to the thesis

Background and Motivation 2

Outline of the thesis 5

CHAPTER 2

Titanium concentration in quartz as a record of multiple deformation mechanisms in an extensional shear zone

Synthesis 12

2.1 Introduction 13

2.2 Geologic Setting 16

2.2.1 Shuswap Metamorphic Core Complex, British Columbia, Canada 16

2.2.2 Existing P-T-t constraints on deformation in the CRD 17

2.3 Petrology of non-mylonitic and mylonitic quartzite 18

2.3.1 Quartz microstructures 20

2.4 Analysis of Ti concentration in quartz 22

2.4.1 Ion Microprobe Analysis 26

2.4.2 Results - Titanium concentration of deformed quartz 31

2.5 Recrystallization of co-existing muscovite 32
2.5.1 Analysis – Muscovite Composition 35
2.6 Accessory Phase Distribution 38
2.6.1 Analysis – Accessory Phase Distribution 40
2.7 Exhumation of the CRD 45
2.7.1 t_0 – Non-mylonitic quartzite protolith 47
2.7.2 t_1 – Cores of quartz in mylonite 48
2.7.3 t_2 – Recrystallized quartz grain margins 49
2.7.4 t_3 – Neocrystallized quartz 51
2.8 Discussion 52
2.8.1 Titanium concentration of deformed quartz 52
2.8.1.1 Quartz in non-mylonitic quartzite 54
2.8.1.2 Quartz in mylonite 55
2.8.2 Factors controlling the Ti content of deformed quartz 57
2.8.2.1 Ti solubility in crustal fluids 57
2.8.2.2 Diffusion of Ti and ^{18}O in quartz during deformation 61
2.8.2.3 Buffering a_{TiO2} in quartzite mylonites 63
2.8.2.4 Comparison between Ti solubility calibrations 64
2.9 Conclusions 66
Acknowledgments 68

CHAPTER 3

High-precision doping of nanoporous silica gel for the preparation of trace element microanalytical reference materials

Synthesis 70
3.1 Introduction 71
3.2 Nanoporous Silica Gel – Background and Motivation 74
3.3 Experimental Methods 77
3.4 Analytical Methods 80
3.6 Results and Discussion 84
3.7 Conclusions 92
Acknowledgements: 93

CHAPTER 4

Experimental constraints on the role of dynamic recrystallization on resetting the Ti-in-quartz thermobarometer

Synthesis 95

4.1 Introduction 96
4.2 Experimental Methods 99
4.2.1 Starting Material 99
4.2.2 Experimental Procedure 103
4.3 Analytical Methods 106
4.4 Results 108
4.4.1 Quartz in Hydrostatic Experiments 109
4.4.2 Quartz in Deformation Experiments 111
4.4.3 Accessory Phases 116
4.5 Discussion 120
4.5.1 Buffering a_{TiO2} in a deforming aggregate 121
4.5.2 Resetting Ti concentrations during dynamic recrystallization 124
4.5.3 Comparison with previous experimental studies 129
4.6 Conclusions and Implications 133
Acknowledgements 134

CHAPTER 5

Geospeedometry of quartz mylonites: a technique to determine the longevity of ductile shear zones

Synthesis 136
5.1 Introduction 137
5.2 Rutilated quartz in mylonites 140
5.3 Geospeedometry of rutilated quartz – theory 145
5.4 Analytical Methods 153
5.5 Geospeedometry of quartz deformed in nature 155
5.5.1 Geologic Setting – Pioneer Core Complex 156
5.5.2 Existing temperature-time constraints 159
5.5.3 Estimating temperature of deformation 160
5.5.3.1 Zr-in-rutile thermometry 161
5.5.3.2 Ti-in-quartz thermometry 162
5.5.4 Microstructures 164
5.5.4.1 Quartz microstructures 164
5.5.4.2 Feldspar microstructures 167
5.5.4 Results of Ti diffusion modeling during natural deformation 170
5.6 Geospeedometry of quartz deformed in experiments 171
5.6.1 Experiment design 172
5.6.2 Rutile needles in deformation experiments 174

5.6.3 Results of Ti diffusion modeling during experimental deformation at T=900 °C for t=39-87 h 175
5.7 Findings and Implications 178
5.7.1 Timescales and kinematics of shear zone deformation in the PCC 179
5.7.2 Ti diffusion in deforming quartz 185
5.7.3 Two mechanisms to rutilate quartz – exsolution and overgrowth 187
5.8 Conclusions 191
Acknowledgements 192

CHAPTER 6

Conclusions of the thesis

6.1 Summary of Results 193
6.1.1 Chapter 2 193
6.1.2 Chapter 3 194
6.1.3 Chapter 4 195
6.1.4 Chapter 5 196
6.2 Implications of this research 197
6.3 Concluding Remarks 198

References Cited 199

Appendix 1 246

Supplementary Figures for Chapter 2 246

Appendix 2 253

Supplementary Tables for Chapter 2 253

Appendix 3 264

Supplementary Figures for Chapter 3 264

Appendix 4 273

Supplementary Tables for Chapter 3 273

Appendix 5 294
Supplementary Experimental Materials for Chapter 3 294
Appendix A5.1. Silica Gel Activation Procedure 295
Appendix A5.2. Silica Gel Doping Procedure 297
Appendix A5.3. Recipes for doping silica gel batches #1-9 299
Appendix A5.4. Analytical procedure for electron probe analysis at UMN. 308
Appendix 6 310
Supplementary Figures for Chapter 4 310
Appendix 7 316
Supplementary Tables for Chapter 4 316
Appendix 8 318
Supplementary Figures for Chapter 5 318
Appendix 9 336
Supplementary Tables for Chapter 5 336

List of Figures

Figure 2.1. Simplified geologic map of the southern Shuswap MCC showing the Thor-Odin migmatite dome and mantling paragneiss and quartzite units with the approximate location of the Columbia River Detachment (CRD)..... 19

Figure 2.2. Schematic cross section of the Columbia River Detachment system along the eastern margin of the Shuswap MCC, showing the sampling traverse analyzed in this study.. 20

Figure 2.3. Cross-polarized light photomicrographs showing the characteristic microstructures preserved within the 1000 m section of quartzite. 25

Figure 2.4. A correlative analysis transect across a single-crystal quartz ribbon showing measurements from core and rim regions of quartz for comparison between the two different ion probes utilized in this study. 28

Figure 2.5. Histogram showing all Ti in quartz data collected using two different ion probes. 31

Figure 2.7. Textures of neocrystallized quartz in quartzite mylonite as revealed by transmitted light photomicrographs (XPL) of samples TO-181 (above) and TO-065 (below). 33

Figure 2.6. Summary of ion probe data showing Ti in quartz measurements collected from both lab facilities and the calculated *P-T* space for all samples throughout the vertical extent of the shear zone. 34

Figure 2.8. Cross-polarized light photomicrograph of the non-mylonitic quartzite (TO-031) displaying the results of ion probe analysis. 36

Figure 2.10. Muscovite analyses showing Si vs. Al atoms per formula unit (p.f.u.), displaying the progressive obliteration of pre-existing compositional zoning in higher strain samples beneath the detachment. 41

Figure 2.11. The average distance between each ion probe analysis spot and the nearest Ti-buffering phase is measured to better constrain assumptions on a_{TiO2} for the application of TitaniQ thermobarometry. 43

Figure 2.12. Results of XRCT 3-D phase distribution analysis. 46

Figure 2.13. Titanium in quartz thermometry showing the estimated *T* for each of the 6 samples throughout the quartzite shear zone. 50

Figure 2.14. A reconstructed exhumation path for the CRD shear zone showing the calculated *P-T* conditions as predicted by both Ti in quartz solubility calibrations for the quartzite protolith, cores of recrystallized quartz ribbons, recrystallized grain rims of quartz, and neocrystallized quartz 53

Figure 2.15. Conceptual diagram illustrating the characteristic quartz microstructures and observed patterns of Ti distribution from different levels of the detachment shear zone. 60

Figure 3.1. Photograph and secondary electron images (SEI) of silica gel 75

Table 3.1. Trace element contents of silica gel and pure quartz separate from Black Hills Quartzite (BHQ) as measured with ICP-OES. 76

Figure 3.2. Effect of pH on doping recovery evaluated at multiple scales 78

Figure 3.3. CL images of silica gel particles doped with 300 μg g^{-1} Ti. 88

Figure 3.4. Analysis of 3-layered reference material with ICP-OES and EPMA. 90

Figure 3.5. Analysis of 7-layered reference material with ICP-OES, EPMA, and LA-ICP-MS 91

Figure 4.1. Experiments were designed to deform a layered aggregate containing quartz layers doped at different Ti concentrations.. 100

Figure 4.2. Illustration, photographs, and X-ray Computed Tomography (XRCT) images of a deformed solid-salt assembly following a high strain experiment 104

Figure 4.3. Differential stress vs. time/shear strain plot shows the strength of each experimental aggregate from the water-added and no water-added suites of experiments. 110

Figure 4.4. Cross-polarized light (XPL) and cathodoluminescence (CL) images of quartz microstructures in the water-added sample suite – (A) hydrostatic, (B) low strain, (C) intermediate strain, and (D) high strain. 113

Figure 4.5. Equal area, lower hemisphere EBSD pole figure diagrams document progressive strengthening of quartz recrystallization fabrics from the water-added suite of experiments 115

Figure 4.6. Cross-polarized light images showing quartz recrystallization microstructures from the undoped layer of the (A) hydrostatic, (B) low strain, (C) intermediate strain, and (D) high strain experiments. 117

Figure 4.7. Electron probe measurements of Ti concentration in quartz from water-added and no-water-added suites of experiments.....119

Figure 4.8. Plane-polarized (PPL) and cross-polarized light (XPL) images of acicular rutile crystals present in the undoped layer of experiments 123

Figure 5.1. Microstructures of deformed rutile needles from the Pioneer Core Complex, Idaho. 141

Figure 5.2. Photomicrographs of rutilated quartzite mylonite from rock deformation experiments 146

Figure 5.3. Secondary electron images (SEI) and cathodoluminescence images (CL) from natural samples (A-B) and from experimental samples (C-E)..... 148

Figure 5.4. Technique for modeling Ti diffusion profiles surrounding rutile needles for both depletion diffusion profiles (A-F) and enrichment diffusion profiles (G-L) 152

Figure 5.5. Timescales obtained from inverse-modeling of measured diffusion profiles. 154

Figure 5.6. Satellite image and geologic map of the Pioneer Core Complex, Idaho..... 158

Figure 5.7. Quartz microstructures from the Kinnikinic quartzite in the WSZ 165

Figure 5.8. Evidence for subgrain rotation and grain boundary bulging deformation mechanisms in quartz..... 166

Figure 5.9. Comparison of feldspar microstructures from the top (A-B) and base (C-D) of the shear zone..... 168

Figure 5.10. Temperature-time conditions calculated from measured diffusion profiles. 171

Figure 5.11. Cooling rates for different initial temperatures calculated from measured diffusion profiles. 173

Figure 5.12. Secondary electron images of rutile needle microstructures present along grain boundaries of a broken sample surface 176

Figure 5.13. Secondary electron (left) and cathodoluminescence (right) images of polished thin sections demonstrating the correlation between rutile needle inclusions and high-intensity CL halos 177

Figure 5.14. Diffusive mobility coefficients solved for Ti in deforming quartz at the conditions of our experiments. 180

Figure 5.15. Comparison of T-t history from deformation geospeedometry with that of existing geochronological constraints. 182

Figure 5.16. Schematic interpretation of two end-member interpretations of diffusion geospeedometry results 183

Figure 5.17. 3-D tomography analysis reveals curving, arcuate rutile needles in a rutialted quartz gemstone 188

Figure A1.1. SEM-EBSD pole figure diagrams for quartz, showing the fabrics of quartzites from different levels of the shear zone..... 248

Figure A1.2. Analytical transects of Ti concentration collected across an individual quartz ribbon, showing the high-Ti plateau in the cores of quartz 249

Figure A1.3. AFM analysis of the sputtered craters created by analysis with both ion microprobes..... 250

Figure A1.4. EMPA results of Si vs. Al p.f.u. from 5 samples (a) – (e) showing the variation in muscovite composition throughout the vertical extent of the shear zone. 251

Figure A1.5. 3-D measurements on accessory phase distribution from XRCT analysis 252

Figure A3.1. SE images of silica gel surface topology before and after calcination. 265

Figure A3.2. Mass loss on ignition for water in silica gel following various heating treatments. 266

Figure A3.3. XRD Spectra of silica gel following various heating treatments. 267

Figure A3.4. Effect of molecular size of the solvent medium on doping efficiency..... 268

Figure A3.5. SE images of TiO2 precipitates from high concentration doping experiments. 269

Figure A3.6. Experimentally-derived efficiency of doping technique..... 270

Figure A3.7. SIMS analysis of polished grain mounts of doped silica gel particles. 271

Figure A3.8. SEI of vesicles in hot-pressed glass aggregate. 272

Figure A6.1. Analysis of Ti concentration (ppm Ti) from the grain boundary of a single crystal of quartz from the undoped layer of a low strain experiment (W1674), revealing the same concentrations as the population of measurements collected from thin section analysis (see Table 2, Table S1) 311

Figure A6.2. Full CL spectrum collected from doped quartz showing luminosity in the blue region, suggesting that the CL signal is dominated by Ti substitution in quartz. 312

Figure A6.3. Plane-polarized light micrographs of nodular rutile inclusions present in the doped layer of experimental aggregates from hydrostatic (A-B) and high strain deformed samples (C). 313

Figure A6.4. Cathodoluminescence intensity halos surrounding rutile needles from hydrostatic (A), low strain (B), intermediate strain (C), and high strain (D) samples.... 314

Figure A6.5. Plots showing one representative transect (out of three) of EMP measurements collected across the aggregate layering (points were set with equidistant spacing in all samples except hydrostatic samples, where points were set manually to avoid porosity). 315

Figure A8.1. Photomicrographs of SIMS analysis locations of rutilated quartz. 319

Figure A8.2. Grid of EPMA analysis over rutile needle inclusion. 320

Figure A8.3. Histogram of Ti concentrations measured from Pioneer rutilated quartzite mylonite samples. 321

Figure A8.4. Comparison of diffusion modeling approach with the results of Morgan et al. [2013]. 322

Figure A8.5 Histograms of diffusion modeling results for natural samples. 323

Figure A8.6 Histograms of diffusion modeling results for experimental samples. 324

Figure A8.7. Representative diffusion profiles and modeling results for natural samples. 325

Figure A8.8. Representative diffusion profiles and modeling results for experimental samples. 330

Figure A8.9. EDS analysis of acicular phases in rutilated quartz gemstone from Brazil. 334

List of Tables

Table 2.1. Summary of ion probe data of [Ti] in quartz from the six samples selected for this study 30

Table 2.2. Representative microprobe analyses of muscovite, reported in weight percent. 37

Table 2.3. Quantitative measurements from XRCT analysis of accessory phase distribution in quartzite. 44

Table A2.1. Raw data from ion microprobe analysis using the SHRIMP-RG at Stanford/USGS used to calculate ppm Ti for each analysis spot and to monitor counts of ^{30}Si to detect possible contamination by a non-quartz phase. 254

Table A2.2. Raw data from ion microprobe analysis using the Cameca IMS-1280 at WHOI used to calculate ppm Ti for each analysis spot and to monitor counts of ^{30}Si to detect possible contamination by a non-quartz phase. 260

Table A4.1. Geochemistry of silica gel following various activation and doping treatments. 274

Table A4.2. ICP-OES major and minor element analysis of reference materials. 278

Table A4.3. ICP-OES trace element analysis of silica gel. 279

Table A4.4. EPMA of reference materials with the JEOL-8900 at UMN. 282

Table A4.5. EPMA of reference materials with the Cameca SX-100 at RPI. 283

Table A4.6. SIMS analysis of reference materials. 284

Table A4.7. LA-ICP-MS analysis of reference materials. 285

Table A4.8. Results of EPMA of 3-layered reference material – HPS-3. 286

Table A4.9. Results of EPMA of 7-layered reference material – HPS-7. 292

Table A4.10. Results of LA-ICP-MS analysis of 7-layered reference material (HPS-7). 293

Table A7.1. Compiled EMP measurements from the doped and undoped layers of the aggregate showing the data processing steps of removing contaminated measurements and outliers..... 316

Table A9.1. Results of diffusion modeling analysis of natural samples. 337

Table A9.2. Results of diffusion modeling analysis of experimental samples. 341

CHAPTER 1

Introduction to the thesis

Chapter 1

Background and Motivation

A decade ago, the temperature dependence of Ti solubility in quartz was quantified by Wark and Watson [2006]. Five years ago, Thomas et al. [2010] documented a pressure dependence and showed that Ti^{4+} substitutes for Si^{4+} in the quartz tetrahedral site and that this exchange scales with titania activity. The Ti-in-quartz solubility calibration predicts that Ti concentrations in quartz grown in most crustal environments will be very low, on the order of 1-10s of parts per million. Calibration of equilibrium Ti solubilities was combined with determination of the diffusion parameters for Ti in quartz. Cherniak et al. [2007] showed that Ti diffuses very slowly in quartz under most crustal conditions, on the order of microns in millions of years at moderate temperatures. Slow Ti diffusion in quartz makes this technique robust and potentially capable of retaining information from multiple events. However, it also means that to apply it to natural rocks, it is necessary to measure very low Ti concentrations from small regions of crystals; this is not trivial and requires specialized microanalytical methods to ensure accurate results. Nevertheless, the simplicity of using Ti-in-quartz as a single-mineral thermometer, barometer, and geospeedometer has generated interest from a wide range of geoscientists to determine the formation conditions of quartz in many different geologic environments.

For reconstructing quartz crystallization in plutonic, volcanic, and hydrothermal settings, results of Ti-in-quartz are mostly consistent with existing constraints from other techniques. However, given the importance of quartz for accommodating crustal

deformation, there has also been interest in using it to reconstruct the conditions of deformation in shear zones. Results of these studies have been less conclusive. Pressure-temperature (P-T) estimates from Ti-in-quartz do not always agree with results of other thermobarometric techniques from the same or nearby rocks. Some authors have attributed this disagreement to reflect a disruption in the equilibrium partitioning during dynamic recrystallization. Since the Ti-in-quartz thermobarometer was calibrated from crystals that were statically-grown from a fluid, it is plausible that equilibrium partitioning may be disturbed during recrystallization via dislocation-accommodated processes. Regardless, it is difficult to conclude that recrystallization is ineffective at resetting quartz Ti contents solely based on the observations available; if substitution and diffusion of Ti in quartz is influenced by dynamic recrystallization, and quartz deforms at conditions different from those of metamorphic reactions on which conventional thermobarometers rely, then it is conceivable that quartz could reflect a distinct portion of the P-T path that is not retained in other phases. The lack of agreement with other techniques is not conclusive evidence of disequilibrium but instead could be reflecting a sensitivity of Ti-in-quartz to reset during portions of a deformation event that are not recorded in conventional metamorphic minerals.

Quartz is particularly susceptible to deformation and deforms ductiley over a wide range of crustal conditions. Crystal-plastic deformation of quartz in most crustal settings is accommodated primarily by the flow of lattice dislocations. When stress is applied to a

crystal, the lattice responds by accumulating dislocations [Kohlstedt and Weathers 1980; Poirier 1985]. The mechanisms that mobilize and subsequently annihilate dislocations reduce the free energy of the stressed crystal and impart plastic strain. Grain boundary migration, one common mechanism of dynamic recrystallization of quartz, occurs as atoms exchange structural positions across the interface of a moving boundary. In the most basic sense, this interpretation implies that recrystallization is a physical reconstitution of mineral grains by changes in the crystallographic orientation of lattices, and consequently, would not be predicted to modify mineral compositions [Lister and Snoke 1984; Urai et al. 1986]. However, evidence from rock deformation experiments suggests that deformation by dislocation creep enhances major element and isotopic exchange (e.g., Yund and Tullis [1991], and even in the absence of an imposed stress field, it is possible for static recrystallization by grain boundary migration to result in chemical re-equilibration [Hillert and Purdy 1977; Hay and Evans 1987]. These observations suggest that recrystallization via grain boundary migration is capable of altering mineral composition at the level of major element components, but whether this remains valid at the trace element level, and whether it results in complete re-equilibration or some intermediate degree of partial re-equilibration, remains untested. It is thus important to determine if crystal-plastic deformation of quartz by dislocation creep is capable of systematically modifying mineral compositions at the trace level and consequently if Ti-in-quartz thermometry and barometry can provide reliable information on the conditions at which ductile deformation occurs.

Chapter 1

Outline of the thesis

This thesis investigates the behavior of Ti in deforming quartz by combining observations from natural shear zones and rock deformation experiments. Analysis of naturally-deformed quartz collected from exhumed crustal shear zones inspires the design of experiments that provide a better understanding of processes operating in the Earth. The feedback between natural and experimental perspectives enables novel contributions to be made to understanding Ti solubility and diffusion in deforming quartz.

Chapter 2 presents results of quartz thermometry and barometry tested to reconstruct the conditions of deformation during crustal extension in the Columbia River Detachment (CRD) of the Shuswap metamorphic core complex (British Columbia, Canada). Analysis of Ti contents from different quartz microstructures using high-resolution ion microscopy revealed that quartz grains in the undeformed quartzite (interpreted to reflect the protolith) contain an initially high, uniform Ti content, whereas recrystallized quartz in mylonites within the shear zone contain different Ti concentrations depending on textural location. Cores of recrystallized quartz preserve the highest P-T, rims of quartz preserve moderate P-T, and neocrystallized quartz precipitated in fractures preserves the lowest P-T conditions. The range of temperatures estimated from Ti-in-quartz is within error of those from quartz-muscovite oxygen isotope thermometry from the same samples [Mulch 2004; Mulch et al. 2006]. However, isotope thermometry is measured from bulk separates of quartz and muscovite, yet microanalysis shows that both of these phases are

compositionally-zoned in trace and minor element components. Regardless, the general agreement between trace element and isotope thermometry techniques is encouraging for evaluating the reliability of Ti-in-quartz when applied to deformed rocks. The retrograde progression of quartz microstructures suggests that Ti-in-quartz was reset at different periods of the exhumation history, and by measuring Ti content from different microstructural sites, results of this research show that it is possible to link deformation microstructures with a polyphase deformation history. This work is published in *Geochemistry, Geophysics, Geosystems* [Nachlas et al. 2014].

While results of Ti-in-quartz appear to provide a good estimate of the conditions of deformation in the CRD, there are too many unconstrained variables in a dynamic shear zone to fully understand the effect of dynamic recrystallization on the resetting Ti contents in quartz. For this reason, a parallel strand of this dissertation was to conduct laboratory experiments in which many of these variables can be controlled. To provide the best analogue to deformation in nature, it is important to synthesize experimental samples that most-closely replicate characteristics of natural samples. Quartz in the undeformed quartzite protolith displays Ti contents that are uniform within grains and higher than the solubility predicted for the conditions of recrystallization. Synthesizing quartz with a specific, uniformly-distributed Ti content in grains that are sufficiently large to deform plastically is prohibitively time-consuming owing to the sluggish diffusivity of Ti in quartz. To overcome this, an experimental doping approach was developed to synthesize high-

purity silica aggregates that proved useful not only for preparing experimental samples but also for fabricating microanalytical reference materials with precise, trace-level concentrations.

Chapter 3 outlines this technique for synthesizing trace element microanalytical reference materials. Nanoporous silica gel was found to be an effective doping substrate, and optimum synthesis conditions were determined that enable nearly-complete recovery of the dopant. This technique is capable of synthesizing large batches of silica doped at a precise Ti concentration (within 10 ppm of a target concentration less than 1000 ppm) and was used to fabricate multi-layered reference materials with layers doped at specific Ti concentrations. These were tested as reference materials by comparing analytical measurements from multiple techniques (inductively-coupled plasma optical-emission spectroscopy (ICP-OES), laser-ablation inductively-coupled plasma mass spectrometry (LA-ICP-MS), secondary ion mass spectrometry (SIMS), and electron probe microanalysis (EPMA)). Comparison between results of various analytical methods enables evaluation of the accuracy and reproducibility of the doping technique at a variety of spatial scales. This research is currently under review for publication in *Geostandards and Geoanalytical Research* [Nachlas, *in review*].

Chapter 4 presents rock deformation experiments that were conducted using a layered quartz aggregate composed of two layers of Ti-doped silica: one layer doped with a Ti concentration higher than the equilibrium solubility predicted for the experimental

conditions, and a second layer with Ti concentrations below the predicted solubility. This layered aggregate was deformed in a shear assembly at constant temperature, pressure, and strain rate for increasing intervals of time (with and without the addition of water) and compared with samples that were statically-annealed at the same conditions. Analysis of progressively-deformed sample aggregates shows that dynamic recrystallization of quartz via grain boundary migration is effective at resetting Ti-in-quartz to the equilibrium solubility for the P-T conditions at which recrystallization occurs. Additionally, measurements of Ti contents in quartz in the undersaturated layer show that Ti solubilities were maintained in the absence of abundant Ti-bearing buffering phases, suggesting that Ti activity can be upheld by the Ti content of the aqueous solution. Careful inspection of experimental samples also revealed a previously-unrecognized mechanism for forming rutilated quartz in which migrating quartz grain boundaries include acicular rutile crystals. The principal finding of this experimental research that demonstrates progressive re-equilibration with increasing strain provides strong evidence that it is possible for Ti-in-quartz to record the conditions of ductility in crustal shear zones. This research was published in the *Journal of Geophysical Research: Solid Earth* [Nachlas and Hirth 2015].

Chapter 5 combines natural and experimental perspectives to develop a method for using quartz as a geospeedometer to estimate the timescales of shear zone deformation. Modeling Ti diffusion profiles trapped in deformed quartz grains using experimentally-determined Arrhenius parameters yields reasonable estimates for the timescales of ductile shearing.

Chapter 1

Quartz geospeedometry was tested to reconstruct timescales of deformation in the Wildhorse detachment system of the Pioneer core complex (Idaho, USA). The geometry and extent of Ti diffusion profiles is unique for different samples and suggests that under isothermal deformation conditions, shear localization migrated upward such that samples at the base of the section were deforming for longer than samples at the top. Integrating the duration of deformation across the width of the shear zone, these results are consistent with regional geochronology and suggest that quartz was deforming over a prolonged interval between the closure of high- and low-temperature geochronometers. By estimating temperature of deformation from Ti-in-quartz, Zr-in-rutile, quartz fabrics, quartz and feldspar microstructures, and previously-published oxygen isotope thermometry, inverse modeling of diffusion profiles indicates that the shear zone was active for c. 1-3 Myr. Results of geospeedometry combined with estimates of structural offset across the detachment equate to a strain rate of ~1-4x10^{-13} s^{-1} for deformation of the 100 m thick quartzite zone. This technique was also applied to experimental samples, where it yields timescales that appropriately coincide with longer duration experiments, but differ in magnitude; measured timescales are approximately 1-2 orders of magnitude longer than the known experiment durations. A possible explanation for this finding is that Ti diffusion in quartz is faster under the high-P, water-present conditions of our experiments compared to the 1-atm, water-absent calibration experiments of Cherniak et al. [2007]. Introducing a technique to determine timescales of ductility using the deformation-accommodating mineral itself provides a new perspective on interpreting the longevity of crustal shear

zones. This work is currently in preparation for submission to *Contributions to Mineralogy and Petrology*.

Chapter 6 summarizes the overall findings of this dissertation. By integrating high-resolution analytical observations of quartz trace element contents and recrystallization microstructures from naturally-deformed quartzite mylonites with the development of novel approaches for the experimental synthesis and deformation Ti-doped quartz aggregates, this thesis contributes to understanding the temperatures, pressures, and rates of ductile deformation events as recorded by the physical and chemical characteristics of quartz.

CHAPTER 2

Titanium concentration in quartz as a record of multiple deformation mechanisms in an extensional shear zone

This chapter has been published in *Geochemistry, Geophysics, Geosystems* with co-authors Donna Whitney, Christian Teyssier, Brian Bagley, and Andreas Mulch and is included in this thesis with permission from the American Geophysical Union.

Synthesis

Results of high precision analysis of Ti concentration ([Ti]) in quartz representing different recrystallization microstructures in a suite of progressively deformed quartzite mylonites show the effect of recrystallization on distribution of Ti in quartz. Petrographic observations and ion microprobe analysis reveals three texturally and geochemically distinct quartz microstructures in mylonites: (1) cores of recrystallized quartz ribbons preserve the highest [Ti] and are interpreted to have recrystallized via grain boundary migration recrystallization, (2) recrystallized rims and quartz grain margins preserve a lower and more variable [Ti] and are interpreted to reflect the combined influence of subgrain rotation and bulging recrystallization, and (3) neocrystallized quartz precipitated in dilatancy sites has low (~1 ppm) [Ti]. Muscovite in non-mylonitic quartzite (at the base of the sampling traverse) is compositionally zoned, whereas muscovite in mylonitic quartzite shows a progressive decreasing in zoning with higher strain. Three-dimensional phase distribution mapping using X-ray computed tomography analysis of rock hand samples reveals that Ti-bearing accessory phases are less abundant and more dispersed in higher strained mylonites compared to non-mylonitic quartzite. This study demonstrates the influence of deformation and dynamic recrystallization on Ti substitution in quartz and evaluates the Ti buffering capacity of aqueous fluids (meteoric vs. metamorphic/magmatic) as well as the distribution and reactivity of Ti-bearing accessory phases in a deforming quartzite. Results of this study suggest that Ti-in-quartz thermobarometry of deformed

quartz is a sensitive technique for resolving the multi-stage history of quartz deformation and recrystallization in crustal shear zones.

2.1 Introduction

Quartz is the most dynamic mineral in the continental crust – its presence and distribution control crustal rheology and dictate strain partitioning during orogenesis [Brace & Kohlstedt, 1980; Paterson & Luan, 1990; Bürgmann & Dresen, 2008; Lowry & Pérez-Gussinyé, 2011; Chin et al., 2013]. The responsiveness of quartz recrystallization mechanisms to variations in temperature, strain rate, and fluid activity through the operation of different mechanisms of dynamic recrystallization makes it possible for quartz to record intricate variations in these variables during deformation. Geodynamic models of continental deformation rely on experimental and natural studies of the ductile behavior of quartz to simulate feedback mechanisms during changing pressure (P), temperature (T), and stress (σ) conditions. This extensive research on quartz deformation has created a vast array of observational strategies that can record the P-T-σ conditions at which quartz was deformed in natural rocks. Quartz recrystallization microstructures [Hirth & Tullis, 1992; Hirth et al., 2001], including the geometries of recrystallized grains [Stipp & Tullis, 2003; Platt & Behr, 2011] and the patterns of crystallographic fabrics [Law, 1990; Halfpenny et al., 2006], can be used to reconstruct the conditions of quartz deformation. These studies contribute to an understanding of the physical response of the quartz lattice to crystal plasticity – the mechanisms of dislocation generation, mobility, and annihilation that enable

plastic deformation of quartz. However, the chemical response of quartz to crystal plasticity is less clearly understood.

Owing to its compositional simplicity, quartz has long held little interest for geochemical studies until a series of hydrostatic crystallization experiments uncovered a *P*-*T* dependence for the solubility of trace levels of Ti in quartz [Wark & Watson, 2006; Ostapenko et al., 2007; Thomas et al., 2010; Huang & Audétat, 2012]. This solubility relationship establishes the foundation for TitaniQ, the Ti-in-quartz thermometer and barometer [Wark & Watson, 2006; Thomas et al., 2010], which uses a measurement of Ti concentration with an estimation of a_{TiO2} and one intensive variable (*P* or *T*) to calculate the other intensive variable (*T* or *P*). The kinetics of Ti diffusion in quartz have also been investigated experimentally, through quartz-rutile diffusion experiments to extract the *T*-*t* dependent diffusivity of Ti in quartz [Cherniak et al., 2007]. These experimental calibrations set the framework for the interpretive potential of TitaniQ to record the *P*-*T* conditions of quartz crystallization in an array of geologic environments.

The ubiquity of quartz in the continental crust and its propensity to deform ductilely make application of quartz thermobarometry a potentially powerful technique for reconstructing the conditions of deformation during orogenesis. However, the ductility of quartz in crustal shear zones is accommodated through a multitude of different deformation mechanisms, simultaneously operative to varying degrees in response to changing conditions during deformation. These mechanisms include high-*T* grain boundary migration recrystallization

(GBM), lower-*T* grain margin recrystallization including subgrain rotation (SGR) and bulging (BLG) recrystallization, and reaction-enhanced solution transfer. Each of these mechanisms responds uniquely to changes in temperature, stress and strain rate, or chemical environment [Hirth & Tullis, 1992; Hirth et al., 2001; Stipp et al., 2006]. As a consequence, each of these deformation mechanisms has the potential to affect Ti substitution in quartz in different ways.

This paper addresses the applicability of Ti in quartz thermobarometry for reconstructing the conditions of ductile deformation in an extensional shear zone by measuring the Ti concentration ([Ti]) of quartz in different textural settings of progressively deformed quartzite mylonite. High precision analysis of recrystallized quartz microstructures is accompanied by analysis of white mica composition and the 3-dimensional distribution of Ti-bearing accessory phases (e.g., rutile). These new data are considered in the context of previous research on the same samples, including bulk mineral stable isotope variation of quartz and muscovite, and muscovite $^{40}Ar/^{39}Ar$ geochronology that together reveal the *T* and timing of mylonitization [Mulch et al., 2006]. The goal of this study is to resolve the extent to which trace element systematics in quartz are affected by different recrystallization mechanisms during ductile deformation, to evaluate how the buffering capacity of Ti-bearing accessory phases evolves in a deforming matrix, and to determine the influence of dynamic recrystallization on the thermodynamics and kinetics of Ti substitution in quartz.

2.2 Geologic Setting

Crustal-scale shear zones that accommodate extension deform over a range of P-T-t conditions during exhumation [e.g., Baldwin et al., 2004; Gordon et al., 2008; Teyssier, 2011; Behr & Platt, 2012; Kylander-Clark et al., 2012; Whitney et al., 2013]. Because these crustal shear zones accommodate translation of large tectonic units, many rock types are affected, and each possesses the potential to record distinct intervals of their transport through the crust. Consequently, extensional shear zones may retain evidence from multiple portions of the exhumation path, as recorded in the geochemical systematics of several independent mineralogical systems. By selecting the Columbia River Detachment (CRD) of the Shuswap metamorphic core complex (British Columbia), an extensional shear zone that has previously been studied using other thermobarometric techniques (e.g., oxygen isotope thermometry in quartzite; major element thermobarometry in metapelite, amphibolite, and other rocks), a contextual framework can be established within which to compare our observations from quartz thermobarometry.

2.2.1 Shuswap Metamorphic Core Complex, British Columbia, Canada

The Shuswap Metamorphic core complex (MCC) of southeastern British Columbia is the largest of several exhumed migmatite terranes that together comprise the Omineca Crystalline Belt, where the deepest crustal levels are exposed in the Canadian Cordillera [Reesore & Moore, 1971; Brown & Read, 1983]. The Shuswap MCC contains domal

exposures of high-grade metamorphic rocks that are bounded to the east by a thick crustal shear zone, the Columbia River Detachment (CRD) [Read & Brown, 1981]. Metamorphic grade is highest in the core of the domes, where corona reaction textures record ascent of deep crustal material under conditions of near-isothermal decompression [Norlander et al. 2002; Whitney et al. 2004; Goergen & Whitney 2012a, b]. Localized shearing within the CRD mylonite zone accommodated rapid exhumation of the core complex during late-orogenic collapse of the Canadian Cordillera [Parrish et al., 1988; Carr, 1992; Lorencak et al., 2001; Vanderhaeghe et al., 2003; Gordon et al., 2008].

2.2.2 Existing P-T-t constraints on deformation in the CRD

This study focuses on a suite of quartzite mylonites within the CRD exposed along the eastern flank of the Thor-Odin gneiss dome (Figs. 2.1, 2.2). Rocks in and near the core of the Thor-Odin dome record granulite to upper-amphibolite facies conditions, preserving evidence for burial to depths of 25–35 km (P = 8–10 kbar) and temperatures of 700–800 °C [Ghent, 1976; Lane et al., 1989; Nyman et al., 1995; Norlander et al., 2002; Spalla et al., 2011; Goergen & Whitney, 2012b]. Metamorphic assemblages from the overlying CRD record greenschist facies retrogression during intense mylonitization [Vanderhaeghe et al., 2003; Mulch et al., 2004, 2006; Spalla et al., 2011].

A thermo-chronological profile across the CRD has been established by combining results of oxygen isotope thermometry based on fractionation between quartz and muscovite with

$^{40}Ar/^{39}Ar$ geochronology of muscovite [Mulch et al., 2006]. These data record the highest temperatures (~475 °C) of deformation directly beneath the detachment surface and a *T* decrease of 100-150 °C into deeper levels (~ 750 m) of the footwall. This thermal profile developed over a short timescale (ca. 1 Ma), as deformation localization and progressive strain hardening migrated the active zone of shearing to greater depths of the footwall.

2.3 Petrology of non-mylonitic and mylonitic quartzite

The variably deformed quartzite mylonite analyzed here likely originated as a Neoproterozoic sandstone. These quartzites form a markedly thick unit in a sequence of platform sediments that accumulated along the continental shelf of the ancestral North American margin and that today compose the dominant lithologies preserved in the detachment zone of the Shuswap MCC [Brown et al., 1986; Price, 1986]. Metamorphosed sandstone units have been identified in a number of extensional shear zones bounding metamorphic core complexes in the North American Cordillera (Kettle [Mulch et al., 2007]; Pioneer [Vogl et al., 2012]; Raft River [Gottardi et al., 2011; Wells et al., 1998]; northern Snake Range [Gébelin et al., 2011; Miller et al., 1999]). These quartzites may have accommodated decoupling between the underlying crystalline basement and overlying brittle crust and could therefore define a significant rheological interface in the lithosphere [Whitney et al., 2004].

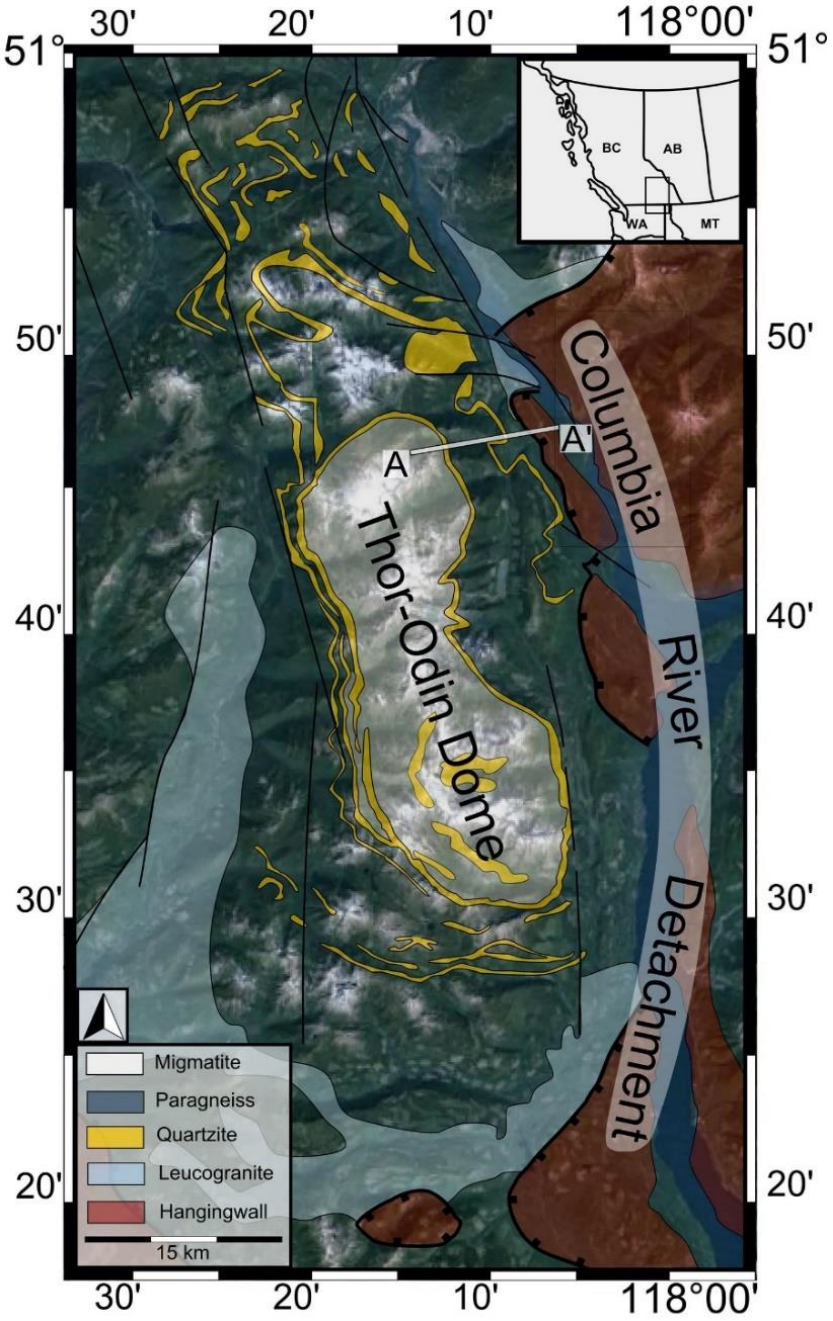

Figure 2.1. Simplified geologic map of the southern Shuswap MCC showing the Thor-Odin migmatite dome and mantling paragneiss and quartzite units with the approximate location of the Columbia River Detachment (CRD). After Vanderhaeghe and Teyssier [1997] and Kruse et al., [2004].

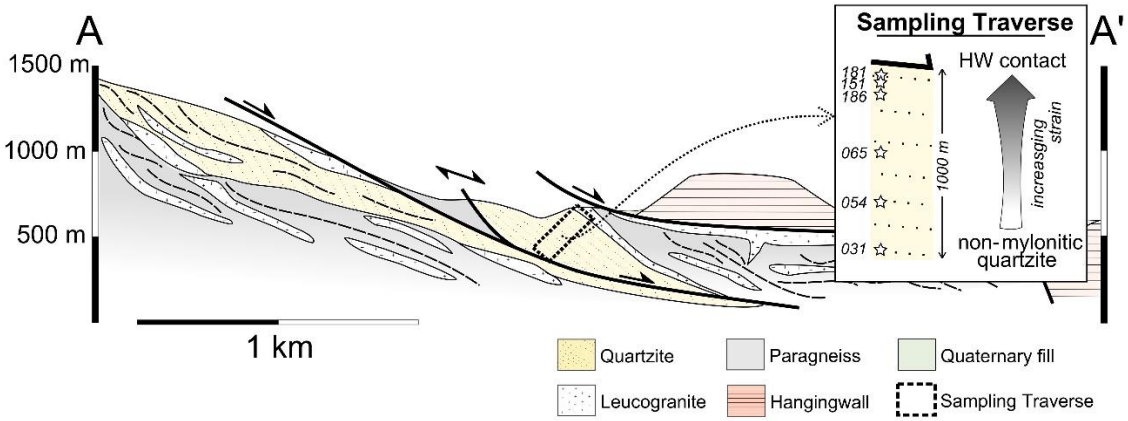

Figure 2.2. Schematic cross section of the Columbia River Detachment system along the eastern margin of the Shuswap MCC, showing the sampling traverse analyzed in this study. Modified from Mulch et al., [2007].

2.3.1 Quartz microstructures

The ~1000 m outcrop section of quartzite mylonite selected for this study preserves a strain gradient, from relatively undeformed, coarse-grained quartzite at the deepest levels to highly strained, finely recrystallized mylonites directly beneath the detachment (Figure 2.3) [Mulch et al., 2006]. Given the variability and distribution of quartz recrystallization microstructures in this quartzite section, we are able to evaluate the relationship between deformation mechanisms and the substitution of Ti in quartz.

Samples of quartzite from the deepest levels of the traverse preserve textures characterized by an annealed fabric. Coarsely crystalline (0.5-2 mm) quartz grains lack evidence for

intracrystalline deformation features such as deformation lamellae or undulose extinction. Quartz grains have straight, interlocking grain boundaries that show pinning by tabular mica crystals, suggestive of highly mobile grain boundary migration at high *T* [Poirier, 1985]. Several lines of evidence indicate that this rock may have been the 'protolith' of the mylonites: its structural position at the base of the mylonite section (Figure 2.2), microstructural observations of shape fabrics of quartz and muscovite (Figure 2.3), an absence of any crystallographic preferred orientation fabric in quartz (Auxiliary Materials – Figure A1.1), preservation of a typical metamorphic stable isotope compositions [Mulch et al., 2007], and the $^{40}Ar/^{39}Ar$ age of co-existing white mica [Mulch et al., 2006]. The quartzite sample (TO-031) that we interpret to be the mylonite 'protolith' was collected 1000 m beneath the contact with the hanging wall, at the base of the nearly continuous section of quartzite (Figure 2.2).

In structurally higher levels of the shear zone, this annealed fabric becomes progressively over-printed with variable degrees of deformation and metamorphism. The microstructural changes can be attributed to a combination of multiple dislocation and dissolution creep processes, all of which occurred progressively during exhumation of the core complex. Microstructures are characterized by elongate quartz ribbons with serrate and irregular grain boundaries with abundant evidence for internal deformation features such as undulose extinction and deformation bands. Sigmoidal white mica fish [ten Grotenhuis et al., 2003] are aligned into the shear plane and display evidence for basal glide and kinking.

Mylonitic fabric intensity increases with proximity to the detachment surface, and samples collected within ~25 m of the detachment surface record a strong crystallographic preferred orientation (CPO) (Auxilliary Materials – Figure A1.1) and preserve high-stress microstructures such as very fine (<10 μm) subgrains and abundant deformation lamellae in quartz.

Quartzite also contains neocrystallized, or precipitated, quartz, which is volumetrically the least abundant but which occurs in numerous textural locations. Neocrystallized quartz occurs within local dilatancy sites, where silica is interpreted to have precipitated from an intergranular fluid [Mulch et al. 2006]. One of the more common sites for the preservation of neocrystallized quartz is within strain shadows adjacent to porphyroclastic feldspar. Additionally, neocrystallized quartz is preserved in high angle cross-cutting veins that are composed of fine grained, equant quartz crystals. Quartz that has precipitated either in strain shadows or within high-angle veins could reflect the composition of the syndeformational fluid phase, and therefore this textural type of quartz has the potential to retain valuable insight into the trace element systematics of dynamically recrystallizing quartz in crustal shear zones.

2.4 Analysis of Ti concentration in quartz

The small grain sizes of the mylonite pose analytical challenges in quantifying the chemical changes imparted during mylonitization and necessitates spatial resolution on the order of

10 μm. Furthermore, application of Ti-in-qz thermobarometry to medium-to-low grade metamorphic quartzite requires detection of very low (~1 ppm) variations in [Ti]. This study has applied two different types of analytical instrumentation – ion microprobe analysis (SIMS) and electron microprobe analysis (EMPA) – to measure [Ti] in fine-grained recrystallized quartz. Using these analytical instruments, comparisons are made between different lab facilities and analytical protocols to evaluate the relative accuracy of each approach and inform the most efficient approach to measuring the Ti content of quartz in mylonites. Ultimately, it is determined that ion microprobe analysis is the only one of these two techniques capable of obtaining the spatial and mass resolution necessary to analyze fine-grained quartz microstructures from greenschist-facies mylonites. Here, we report the results of the ion microprobe analyses collected from two different ion microprobe analytical facilities (USGS/Stanford, WHOI). Details of the

EMPA analysis, including a correlative transect across a single quartz crystal comparing multiple SIMS and EMPA instruments, is in the Auxiliary Materials – Figure 2.

Thirty-five thin sections of quartzite were investigated petrographically before selection of six representative samples that capture the range of deformation fabrics present in the shear zone. Full thin section photomicrographs in transmitted and reflected light were gathered prior to further analysis to preserve all original optical features of the samples prior to the multi-step, non-reversible sample preparation procedure.

Chapter 2: Ti in quartz microstructures

SEM-based cathodoluminescence imaging (CL) is the first technique applied to the samples, as it is the most sensitive and least destructive of the sample surface. CL is used to map the spatial distribution of Ti content through variations in CL intensity. This is followed by electron back-scattered diffraction (EBSD) analysis to characterize the crystallographic fabric of recrystallized quartz. The high beam current of EBSD quenches the CL signal in quartz, thereby necessitating the collection of CL imagery prior to EBSD analysis. Collection of CL imagery and EBSD data was performed using the JEOL-6500F scanning electron microscope (SEM) equipped with Oxford EBSD detector and Gatan Mono-CL housed in the University of Minnesota Characterization Facility.

These semi-quantitative, textural analysis techniques were used in conjunction with transmitted light petrography to select particular regions of interest from each sample for targeted analysis of quartz trace element abundance using ion probe analysis. Preparation of thin sections for SIMS involves extraction of a 1 cm^2 region of interest from each thin section using a diamond blade slow-speed saw, then mounting this sample in a 1 inch epoxy mount before polishing to 0.5 μm roughness and coating with Au immediately prior to loading the sample into the instrument. Meticulous documentation of ion probe target locations with reflected light imagery and diamond microscribe markings is critical to a successful analytical session. Following ion probe analysis, photomicrographs are taken before and after removal of the Au coat to precisely identify the location of each ion probe analysis crater.

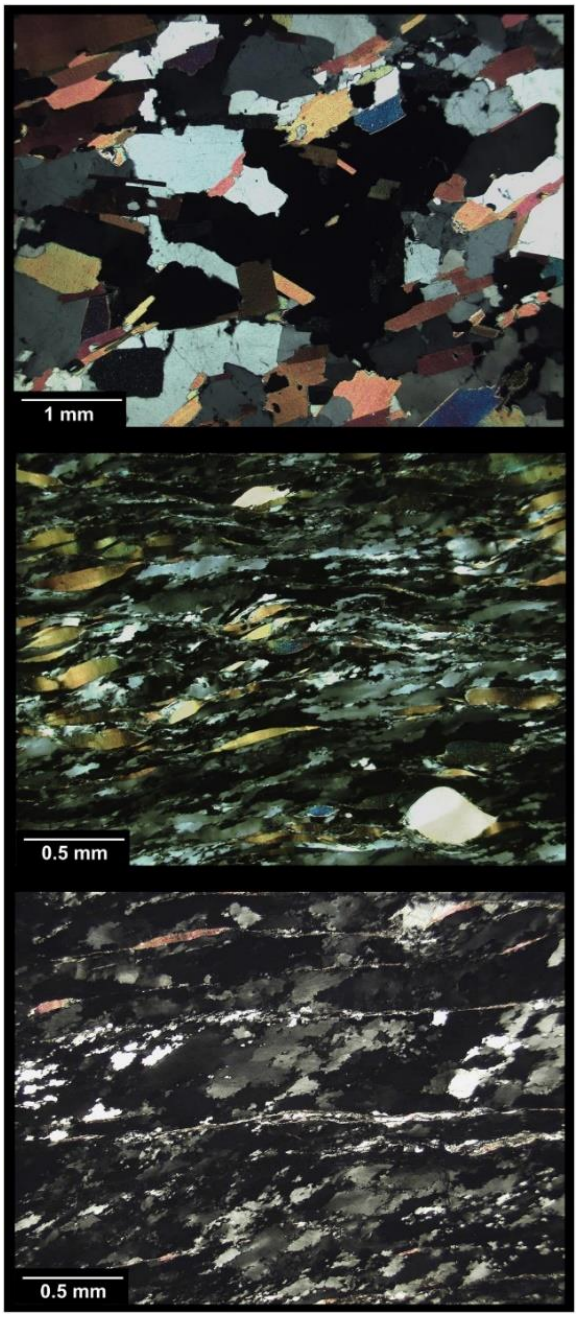

Figure 2.3. Cross-polarized light photomicrographs showing the characteristic microstructures preserved within the 1000 m section of quartzite. The structurally deepest levels of the section contain a coarse grained, non-mylonitic quartzite (top image – TO-031: 1000 m from detachment) which becomes progressively mylonitized with increasing distance to the detachment (center image – TO-065: 290 m; bottom image – TO-181: 10 m).

2.4.1 Ion Microprobe Analysis

Two types of instrumentation for secondary ion mass spectrometry (SIMS) analysis have been applied for this study. Roughly half (n= 106/201) of the data were collected using the Sensitive High Resolution Ion Microprobe – Reverse Geometry (SHRIMP-RG) at the U.S. Geological Survey – Stanford University ion microprobe facility. An analytical protocol analogous to that detailed in Grujic et al. (2011) was followed. A primary ion beam of O^{2-} was used to raster the area of analysis to clean surface contamination prior to collection of the measurement. Standardization was performed with a synthetic quartz crystal (sample QTiP-13 of Thomas et al. [2010]) documented to contain 46 ppm. Analytical reproducibility with this routine is accurate within 2 ppm as calculated from replicate analyses of synthetic quartz crystal QTiP-13 as a secondary reference material. The 106 SHRIMP-RG analyses were collected from 3 samples, displaying a range of concentrations from 3.3 to 25.2 ppm; 2 analyses were based on highly irregular counts of ^{30}Si, which suggests of intersection of the ion beam with a non-quartz, contaminating phase (see Auxiliary Materials – Table 1). The strategy of analysis with the SHRIMP-RG involved the automated collection of long transects of equidistant analytical points set roughly perpendicular to the foliation. The resultant data set reflects a random sampling of all textural sites within the quartzite mylonite.

The remainder (n=95/201) of the Ti in quartz data were collected using a Cameca IMS-1280 ion microprobe located in the Northeast National Ion Microprobe Facility (NENIMF)

at the Woods Hole Oceanographic Institution. A primary ion beam of O^{2-} was used to sputter secondary ions from specific locations on the sample surface. The analytical protocol, following a routine similar to those detailed in Thomas et al. [2010] and Ashley et al. [2013], included a pre-sputter at higher beam current with larger beam diameter to clean the sample of surface contamination before focusing the beam into the rastered crater to perform the measurement (see Auxiliary Materials – Figure 3). A working curve calibration was generated using four synthetic quartz crystals (QTiP series) experimentally synthesized by J. Thomas, as well as Herkimer quartz (estimated to contain <6 ppb Ti [Kohn & Northrup, 2009], measured to be 4-5 ± 2 ppb Ti [Kidder et al., 2013]) to standardize the unknown ion counts to known concentrations. Reproducibility of this analysis is accurate within 1-5% on measurements of the QTiP synthetic quartz crystals as secondary reference materials (ranging from 19-380 ppm). Measurements were made from 6 different samples that show variation from 0.1 to 44 ppm Ti, of which 7 analyses were selected for removal on the basis of irregular ^{30}Si counts and probable contamination (see Auxiliary Materials – Figure 2). The analysis routine of the IMS-1280 requires near-continuous manual operation rather than automated collection of a pre-set transect. As a result, this approach encourages the selection of specific microstructural textures within the sample; this enables collection of a representative population of data from each microstructural site and allows precision sampling of very fine-scale quartz recrystallization textures.

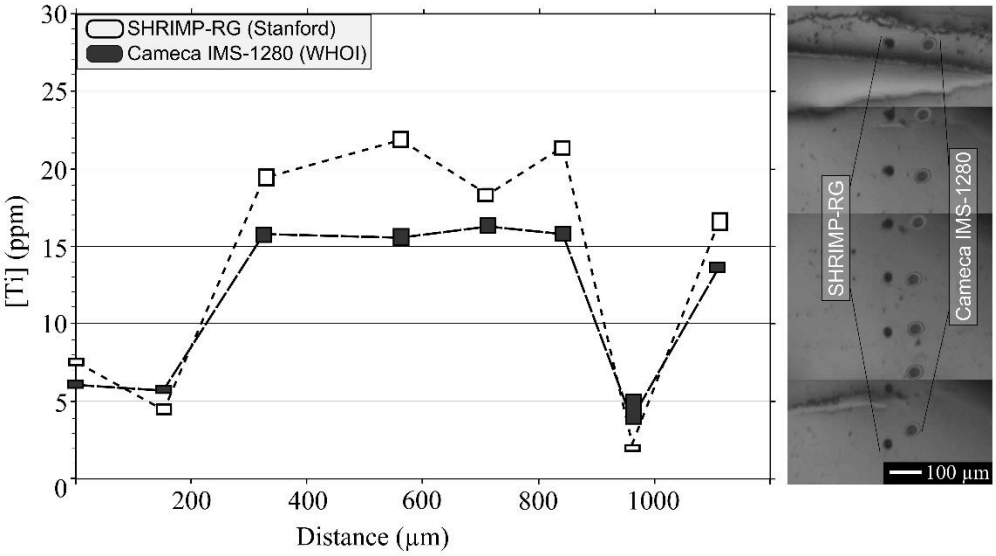

Figure 2.4. A correlative analysis transect across a single-crystal quartz ribbon showing measurements from core and rim regions of quartz for comparison between the two different ion probes utilized in this study. The height of the markers reflects the analytical uncertainty from each measurement. Reflected light photomicrograph captured after the analysis shows the location of the ion probe analysis craters. Results of analysis of this transect collected using EMPA are included in the Auxiliary Materials.

The 1σ standard error in ion counting statistics for measurements from each ion probe is within the range of 0.1-0.5 ppm Ti, which equates to an analytical uncertainty of 1–3 °C in application of the TitaniQ thermometer. The largest source of uncertainty is in the spread of the pooled analyses for a particular microstructure, which ranges from 1-5 ppm Ti – as a consequence, any variance in the calculated temperature that is >10 °C is interpreted to reflect true variation between different quartz measurements within the sample.

Comparison of the reproducibility between the two ion probes is made by analysis of a parallel transect across a single-crystal quartz ribbon with correlative analyses from both methods (Figure 2.4). This analysis reveals that both instruments produce measurements of [Ti] that are less than the variance in measurements for a particular microstructure. Furthermore, samples that were analyzed with both ion probes reveal a population of pooled measurements that are coincident between the two methods (Figure 2.5). Based on these observations, it is determined that Ti in quartz measurements from the two ion probe facilities are in agreement will be aggregated into a single dataset prior to application of quartz thermobarometry.

Analysis of the spatial resolution of the two ion microprobes was made using Atomic Force Microscopy (AFM) to map the 3-dimensional geometry of an analysis crater sputtered by the ion beam. Results of AFM analysis reveal a sputtered analysis crater produced by the SHRIMP-RG that is 13 x15 μm in diameter and 1.2 μm in depth and an analysis crater produced by the IMS-1280 that is 10 x 15 μm in diameter and 0.9 μm in depth. These geometries are important in resolving the ultimate spatial resolution limiting the detection of trace element abundance from fine-grained quartz in mylonites. Detailed results of the AFM analysis procedure are included in the Auxiliary Materials – Figure 3.

Sample	distance to HW (m)	full sample (ppm Ti)	strd dev. (n=)	cores of qz (Ti ppm)	strd dev. (n=)	rims of qz (Ti ppm)	strd dev. (n=)	neocrystallized qz (Ti ppm)	strd dev. (n=)	distance to buffer (µm)	Δδ18O (‰)	Tδ18O (°C)
TO-181	10	13.65	7.31 (42)	18.55	3.14 (21)	11.75	5.97 (15)	1.18	0.59 (6)	675	2.79	435
TO-151	25	23.7	9.47 (13)							6190	2.49	475
TO-186	40	11.96	3.12 (47)	13.39	2.33 (31)	9.2	2.57 (16)			5280	2.89	422
TO-065	290	9.62	5.93 (17)	14.1	2.13 (9)	8.48	2.66 (4)	0.68	0.08 (4)	2150	2.14	533
TO-054	757	7.21	2.16 (39)	8.45	1.48 (33)	5.35	1.61 (22)			6025	3.22	386
TO-031	1000	39.2	2.99 (18)							20	2.92	419

Table 2.1. Summary of ion probe data of [Ti] in quartz from the six samples selected for this study. The distance to nearest Ti buffer is a measurement of the maximum distance from an analysis location to a Ti-buffer in thin section.

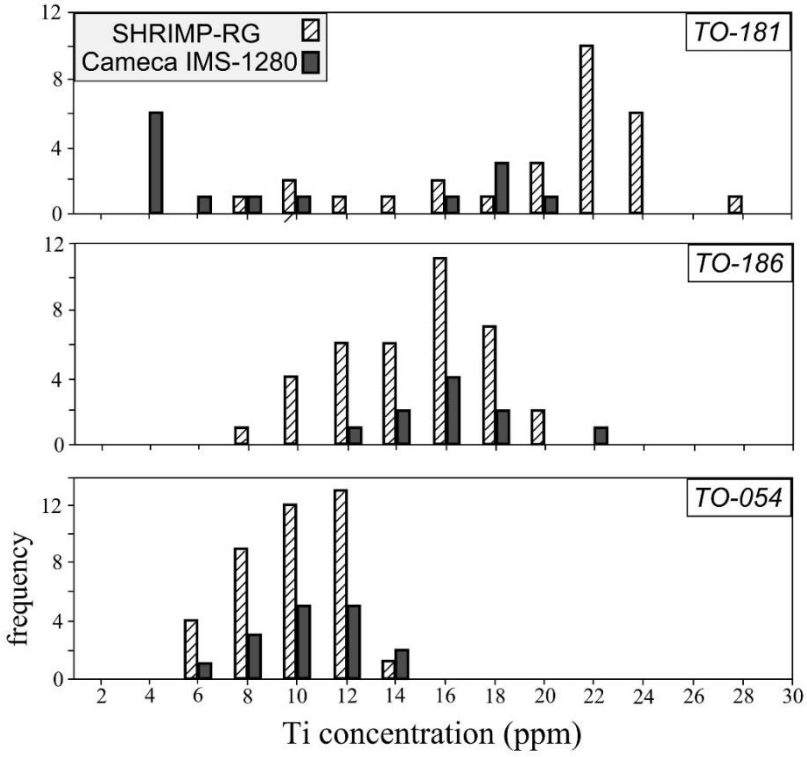

Figure 2.5. Histogram showing all Ti in quartz data collected using two different ion probes. A table of all ion probe measurements from each instrument is contained in the Auxiliary Materials.

2.4.2 Results - Titanium concentration of deformed quartz

Results from quantitative analysis reveal three distinct populations of [Ti] in quartz, each of which correlates with a particular microstructural domain in recrystallized quartz (Table 2.1, Figure 2.6). The cores of elongate quartz ribbons preserve the highest Ti concentrations in all quartzite mylonite samples. The recrystallized rims of quartz (within 50 μm from the

grain boundary) in addition to recrystallized subgrains and grain boundary bulges, have a lower (~40-60%) and more variable [Ti] than adjacent core regions. All measurements of [Ti] clearly show a shift towards lower values at deeper levels of the mylonite section (Figure 2.6). The textural discrimination between core and rim locations is also apparent upon correlation of CL imagery with petrographic observation of ion probe measurements from different quartz microstructures. Separate evaluations of CL intensity and proximity to grain boundary or mechanism of recrystallization both allude to a depletion of [Ti] in the margins of deformed quartz grains. The third population of [Ti] data is observed in neocrystallized quartz that has precipitated within local dilatancy sites such as pressure shadows and high-angle cross cutting veins (Figure 2.7). Analysis of neocrystallized quartz reveals a population of Ti measurements that exhibit a very low spread of concentrations that are consistently lower (ca. 1 ppm Ti) than all other locations in the sample. In contrast to the mylonite, non-mylonitic ('protolith') quartzite located in the deepest levels of the footwall does not preserve zoning in [Ti]. Quartz typically preserves a uniform Ti content, regardless of textural location or proximity to rutile (Figure 2.8).

2.5 Recrystallization of co-existing muscovite

Muscovite occurs in all analyzed samples of quartzite, and comprises 2-15% of the modal mineralogy as estimated from EDS phase mapping of representative 1 cm^2 regions of each thin section. Textures indicate that muscovite deformation was coeval with quartz

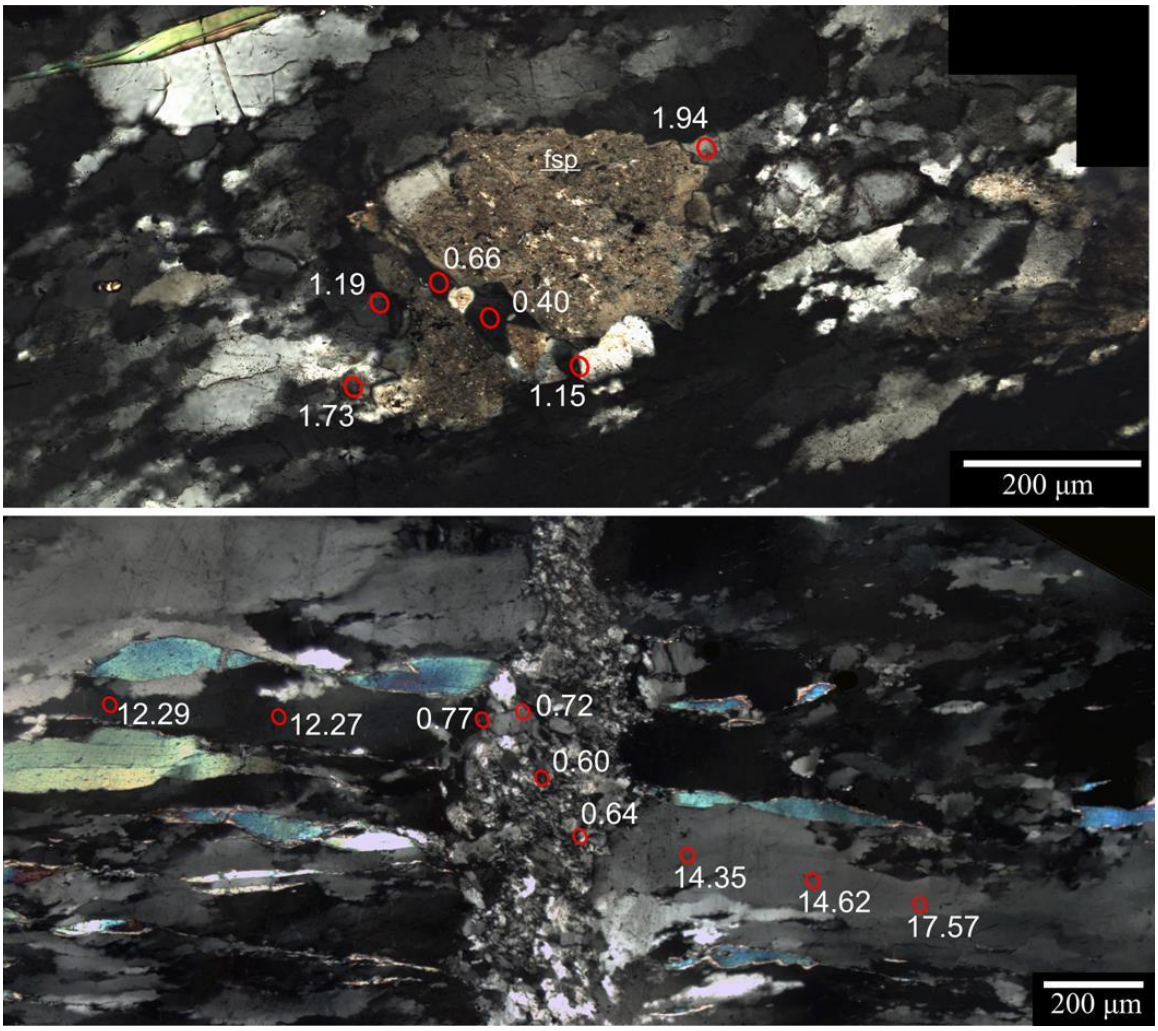

Figure 2.7. Textures of neocrystallized quartz in quartzite mylonite as revealed by transmitted light photomicrographs (XPL) of samples TO-181 (above) and TO-065 (below). Ion microprobe analysis demonstrates a consistently low (ca. 1 ppm) [Ti] in all neocrystallized quartz analyzed. Values are in ppm Ti and were measured using the Cameca IMS-1280 at WHOI.

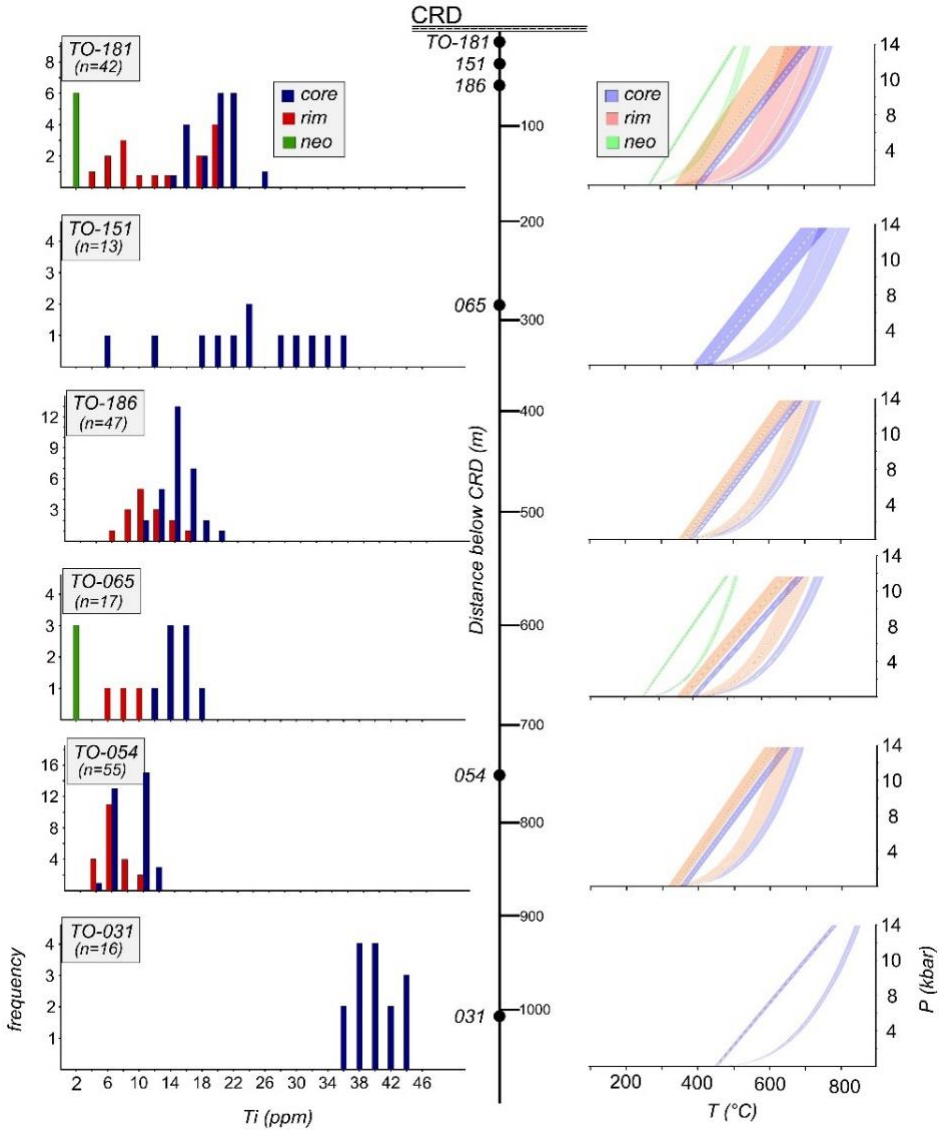

Figure 2.6. Summary of ion probe data showing Ti in quartz measurements collected from both lab facilities and the calculated *P-T* space for all samples throughout the vertical extent of the shear zone. Histograms show the magnitude and spread of Ti in quartz measurements, with frequency distributions plotted in bins of 2 ppm. The center column shows a line transect with the targeted sampling locations throughout the shear zone. The predicted *P-T* regions of Ti in quartz equilibration are derived from pooled measurements of the core, rim, and neocrystallized quartz ('neo'). *P-T* calculations from both calibrations are shown, with the Thomas et al. [2010] calibration (assuming $a_{TiO2} = 1$) designated by the linear arrays and the Huang & Audétat [2012] calibration designated by the curving arrays.

recrystallization. Based on this assumption, Mulch et al. [2004, 2006, 2007] determined oxygen isotope fractionation from quartz-muscovite mineral separates to evaluate the thermal conditions of recrystallization and to track the source region of syndeformational fluids (i.e., meteoric vs. metamorphic/magmatic fluid).

Muscovite in the quartzites of the CRD preserves a progression in grain size through the shear zone, from coarsely crystalline (1000 x 800 μm), tabular clasts in the deepest levels of the footwall to finer-grained (250 x 50 μm) sigmoidal mica fish in quartzite at higher levels of the section, closer to the detachment. Evidence for mechanical grain size reduction exists in the form of slip on the basal (001) plane and necking and boudinage of elongate mica clasts. Evidence for chemical grain size reduction include fine grained mica trails that parallel the foliation and textures indicative of dissolution including diffuse grain boundaries.

2.5.1 Analysis – Muscovite Composition

Electron probe microanalysis (EMPA) was applied to evaluate compositions and zoning in muscovite. The JEOL JXA-8900 electron microprobe in the Department of Earth Sciences at the University of Minnesota was used to collect semi-quantitative WDS maps of major elements (Si, Al, Mg, Fe, Ti) to resolve the spatial extent of compositional zoning. The zoning patterns were then targeted with in-situ quantitative analysis of all common

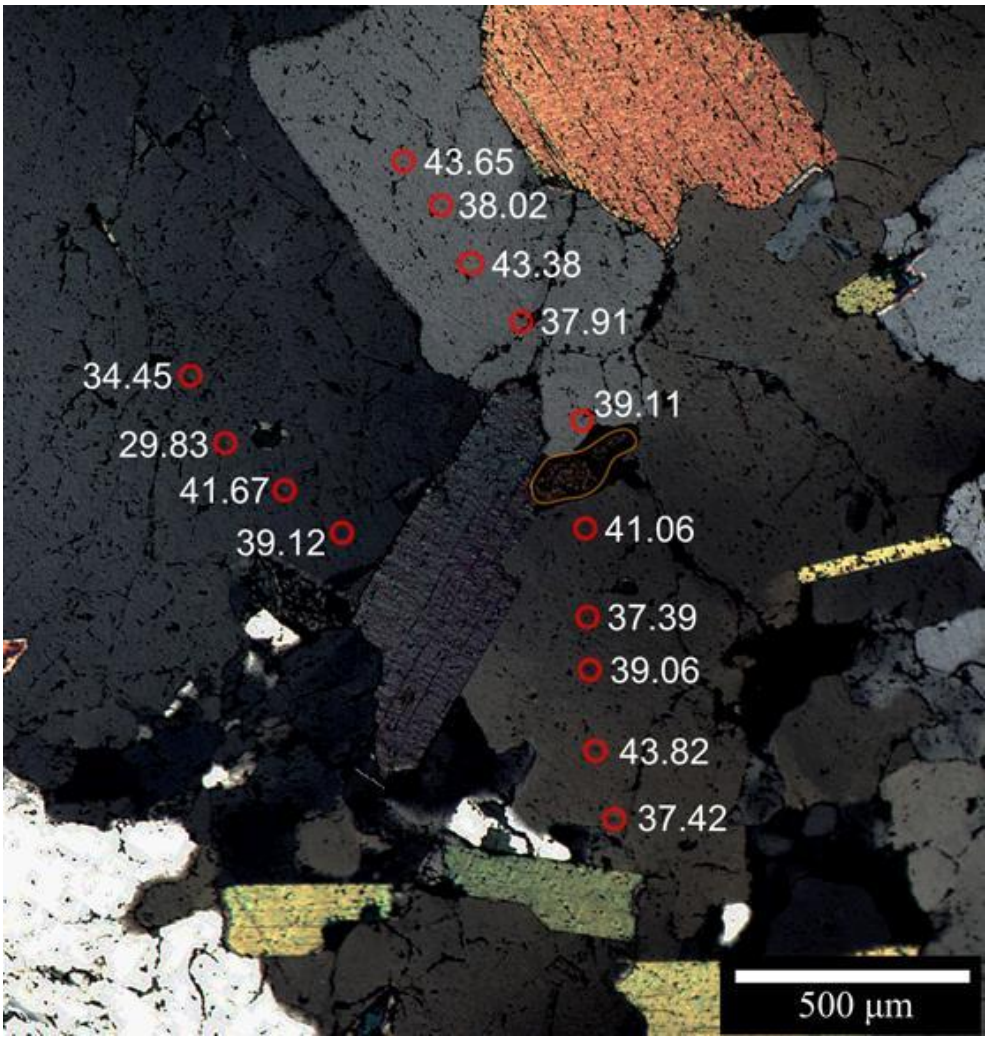

Figure 2.8. Cross-polarized light photomicrograph of the non-mylonitic quartzite (TO-031) displaying the results of ion probe analysis. These data demonstrate that the undeformed precursor has a uniformly high, homogenous [Ti]. Analytical transects collected in the vicinity of a rutile grain (circled) suggest that the quartz in this rock equilibrated the [Ti] prior to exhumation and deformation. Values are in ppm Ti and were collected using the Cameca IMS-1280 at WHOI.

	Non-mylonitic quartzite TO-031		Quartzite mylonite TO-181	
	core	rim	core	rim
SiO2	46.84	44.58	45.43	45.04
TiO2	1.88	1.77	2.1	1.77
Al2O3	29.53	32	31.37	31.47
FeO	2.79	3.19	3.25	3.39
MgO	1.66	1.08	0.94	0.95
MnO	0.02	0.01	0.01	0.02
Cr2O3	<d.l.	0.04	<d.l.	0.01
K2O	11.16	11.21	10.83	10.88
Na2O	0.26	0.31	0.48	0.36
CaO	0.01	0.05	0.01	0.01
F	0.02	<d.l.	0.01	<d.l.
Cl	0.01	0.03	0.01	<d.l.
Total	94.105	94.246	94.032	94.281

Table 2.2. Representative microprobe analyses of muscovite, reported in weight percent.

components of muscovite (Si, Al, Mg, Fe, Ti, Mn, Cr, K, Na, Ca, Cl, F). Quantitative analysis reveals that mica in the CRD is nearly pure muscovite in composition (Table 2) and preserves compositional zoning that is unique for different structural positions in the shear zone. Mapping and quantitative analysis of muscovite was performed for all samples that were analyzed for Ti in quartz.

EMPA analysis of single crystals of muscovite reveals a core and rim pattern of zoning in major and minor element abundance. The magnitude and geometry of this compositional zoning is variable between samples, but the presence of some chemical variation between the core and rim is detectable in major element maps of all samples analyzed (Figure 2.9,

Auxiliary Materials – Figure 4). The core domain of porphyroblastic muscovite is slightly enriched in the phengite component relative to the adjacent rims and tips of recrystallized mica fish, as documented by higher concentration of Mg and Si relative to Al in the core compared to the rim of the same grain (Table 2.2, Figure 2.10).

In the structurally lowest sample, the muscovite grains preserve intricate boundaries between compositional domains and record the largest magnitude of chemical variation between core and rim. In samples closer to the detachment surface, the magnitude of zoning diminishes and is locally offset owing to shearing and slip on the basal cleavage plane of sigmoidal mica fish. In samples located directly beneath the hangingwall contact, the zoning that remains is very faint, with indistinct boundaries between compositional domains. Comparison between samples throughout the section documents a progressive obliteration of muscovite zoning toward the detachment surface (Figs. 2.9, 2.10).

2.6 Accessory Phase Distribution

Critical to accurate application of Ti in quartz thermobarometry is confident assumption of a_{TiO2} in the system at the time of recrystallization. Presently, the identification of a Ti-buffer, contained within the region of the thin section or identified in nearby rocks, has been used to estimate an a_{TiO2} for TitaniQ thermobarometry. Different Ti-bearing accessory phases have been used to assume different values for Ti activity in metamorphic rocks

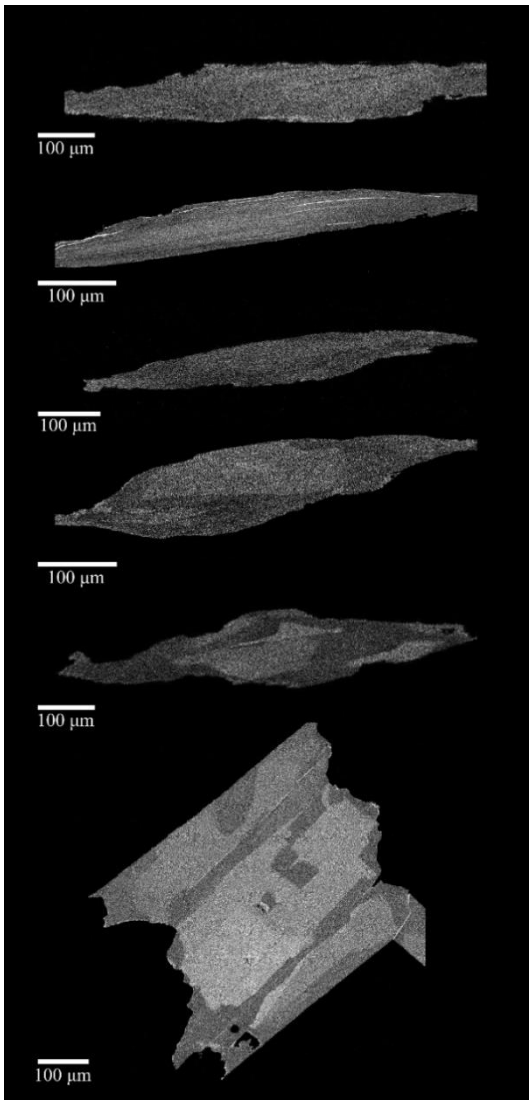

Figure 2.9. Electron microprobe maps of Al concentration in muscovite documenting a progression in the strength of chemical zoning through the shear zone. Variation in Al content was accompanied by inverse variation in Mg and Si. Samples are displayed in order of increasing depth, from top to bottom: TO-181, -151, -186, -065, -054. and -031.

[Ghent and Stout, 1984], including an $a_{TiO2} = 1$ in the presence of rutile [Kawasaki and Osanai, 2008; Storm and Spear, 2009; Ashley et al., 2013; Kidder et al., 2013], $a_{TiO2} = 1$ in

the presence of anatase [Haertel et al., 2013], a_{TiO2} = 0.7 – 1 in the presence of ilmenite [Peterman and Grove, 2010; Menegon et al., 2011; Spear et al., 2012], and a_{TiO2} = 0.6 in the presence of titanite [Behr and Platt, 2011]. However, it remains unclear how the reactivity of these phases affects buffering efficiency, how the oxidation state of the chemical environment affects a_{TiO2} [Ghiorso and Gualda, 2013], what is the effective buffering distance required between the nearest Ti-buffer and the site of quartz recrystallization, and how the fabric anisotropy of ductile rocks affects Ti buffering in quartz. This study will address the confidence of activity assumptions for buffering of quartz in mylonite by combining analysis of 3-dimensional particle distribution from rock hand samples with large region phase mapping in thin section to determine both the distribution and character of accessory phases in the progressively deformed mylonite samples.

2.6.1 Analysis – Accessory Phase Distribution

This study utilizes multiple strategies to confidently estimate a_{TiO2} for recrystallization of quartz in each of the mylonite samples. A first approximation is performed petrographically, by measuring the distance in thin section from the location of an ion probe quartz analysis to the nearest Ti-buffering phase (Figure 2.11). Rutile is present in all thin sections of quartzite studied, and measurements of the maximum distance to the nearest rutile crystal in thin section range from 100 to 6200 μm (Table 1).

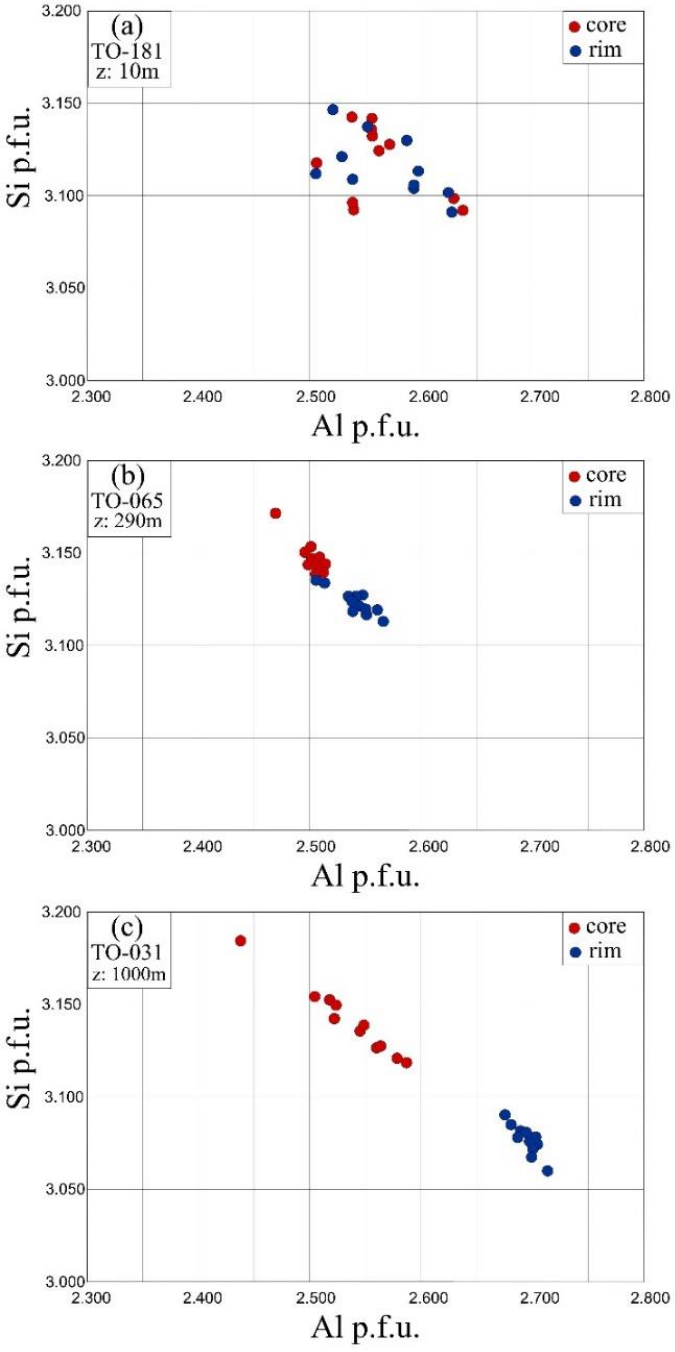

Figure 2.10. Muscovite analyses showing Si vs. Al atoms per formula unit (p.f.u.), displaying the progressive obliteration of pre-existing compositional zoning in higher strain samples beneath the detachment.

It is possible that Ti-bearing accessory phases possess a heterogeneous distribution in mylonites, thereby creating an anisotropic distribution of buffering potential. To study the 3-D distribution of accessory phases in quartzite mylonite, we employed X-Ray Computed Tomography (XRCT) using the X5000 high resolution micro-CT in the Department of Earth Sciences at the University of Minnesota. Five thin section billets (~1 x 2 x 4 cm each) of quartzite mylonite prepared from samples also analyzed for quartz and white mica composition were scanned and reconstructed to produce a 3-D volume of each sample. The voxel (3-D pixel) size in each volume is approximately 11 x 11 x 11 μm, and the grayscale value of each voxel reflects its relative density. Raw data are collected using a high resolution (3889 x 3073 pixels) Dexela detector running in 16 bit mode, and the size of the resulting 3-D reconstruction ranges from ~ 30 to 60 GB. We are able to render volumes of that size for visual inspection but they are far too large for quantitative analysis. To reduce data size, and therefore processing time, these data were downsampled to a voxel size of 35 x 35 x 35 μm.

Avizo Fire © was used for basic image processing that included filtering, interactive thresholding, object separation, and removal of small objects. We used a windowed non-local means filter which removes noise while preserving image detail. Thresholding the accessory phases was easily accomplished since they have a much higher density relative to the surrounding matrix. Once thresholded we separated the individual objects using the separate objects module in Avizo Fire ©, which uses a combination of watershed and

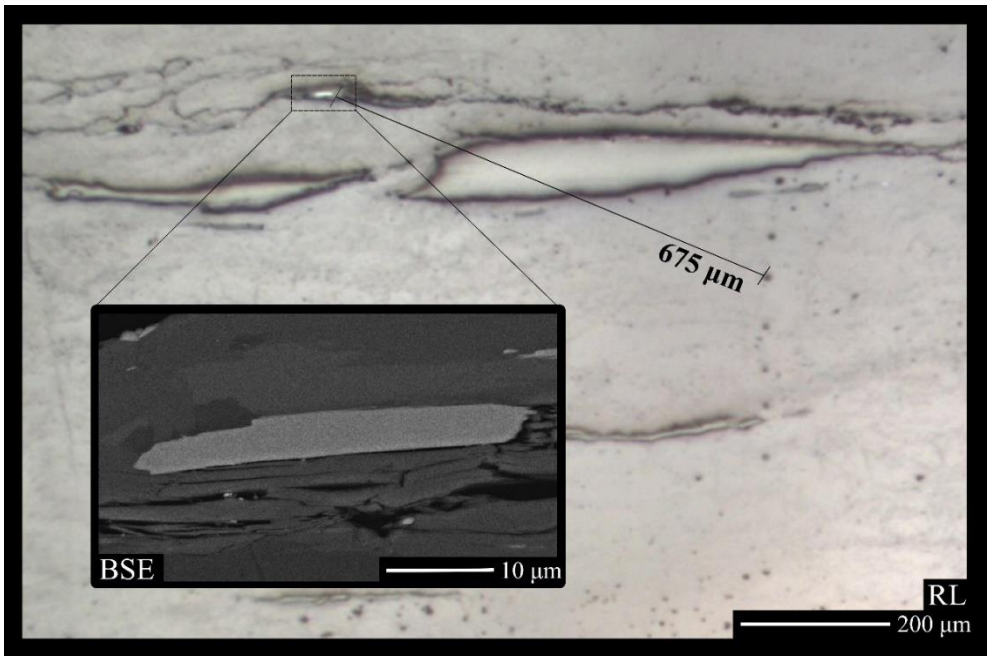

Figure 2.11. The average distance between each ion probe analysis spot and the nearest Ti-buffering phase is measured to better constrain assumptions on a_{TiO2} for the application of TitaniQ thermobarometry. This figure shows a Reflected Light (RL) photomicrograph of a transect of ion probe analysis craters, with a Back-Scattered Electron (BSE) image revealing compositional uniformity in the nearest rutile grain.

distance transforms for separation. Finally we used the remove small spots module to remove objects whose longest axis is less than 65 µm. This number was chosen for two reasons: 1) The thresholding step left some small artifacts, and 2) objects that are near the lower resolution limit are not well resolved. The processed volumes were exported as a series of 2-D tiffs and analyzed using *Blob3D* [Ketcham, 2005] to extract 3-D quantitative measurements (Table 3).

Results of 3-D phase distribution analysis reveal that accessory phases in quartzite mylonite range from 280 to 1670 grains per cm^3 of rock, with a clear trend towards

depletion of accessory phases in higher strain samples (Figure 2.12, Table 2.3). Additionally, accessory phases become volumetrically smaller in higher strain mylonites, recording an average volume of 3.3 nl in the non-mylonitic quartzite decreasing to 0.9 nl in mylonites directly beneath the detachment. Despite the reduction in volume of accessory phases in higher strained samples, the 3-D aspect ratio of particles remains indistinguishable for all samples analyzed (Auxiliary Materials – Figure 5). The depletion of accessory phases in higher strain samples equates to a reduction in the reactive surface area of accessory phases in the aggregate, measured using XRCT to decrease from 170 mm^2/cm^3 in the protolith to 10 mm^2/cm^3 in high strained mylonites.

Sample	sample volume (mm^3)	total number of accessory phases	number of grains per cm^3 of sample	surface area of accessory phases per cm^3 of sample (mm^2/cm^3)	mean grain volume (nL)
TO-031	9801	16339	1667	169	3.2
TO-045	6179	4037	653.4	29.6	1.1
TO-065	8069	5214	646.2	40.2	1.5
TO-186	9044	2540	280.8	10.9	0.87
TO-181	9580	3316	346.1	14.9	1.0

Table 2.3. Quantitative measurements from XRCT analysis of accessory phase distribution in quartzite.

The accessory phase distribution from XRCT is a combined calculation of all high-density accessory phases in the rock – however, only the Ti-bearing accessory phases (rutile, ilmenite, titanite) are of interest for buffering of quartz. For this reason, energy dispersive spectrometry (EMPA-EDS) mapping of 2 cm^2 regions of the thin section was used to measure the relative proportions of accessory phases in each sample. The suite of accessory phases systematically changes from rutile (72%), monazite (20%), and zircon (8%) in the less deformed protolith to rutile (61%), monazite (4%), and zircon (35%) in the highest strain samples located directly beneath the detachment.

2.7 Exhumation of the CRD

Analysis of the [Ti] of quartz microstructures from the CRD reveals a dynamic history of deformation and metamorphism in the mantling rocks of the Thor-Odin dome spanning a change in *P-T* conditions of over 5 kbar and 350 °C (Figs. 2.13, 2.14). This record is preserved within different quartz recrystallization microstructures. Four stages of shear zone deformation can be resolved from analysis of a suite of quartzite mylonites from the CRD shear zone (Figure 2.15) – (1) the [Ti] in the non-mylonitic quartzite protolith equilibrated prior to exhumation, (2) GBM recrystallization preserved in the [Ti] of the cores of recrystallized quartz ribbons occurred early during the exhumation path (higher T, higher P), (3) grain margin recrystallization (SGR and BLG) in the presence of meteoric fluids preserved in the [Ti] of the quartz grain margins and recrystallized subgrains occurred during the later stages of exhumation (lower T, lower P), and (4) cataclastic

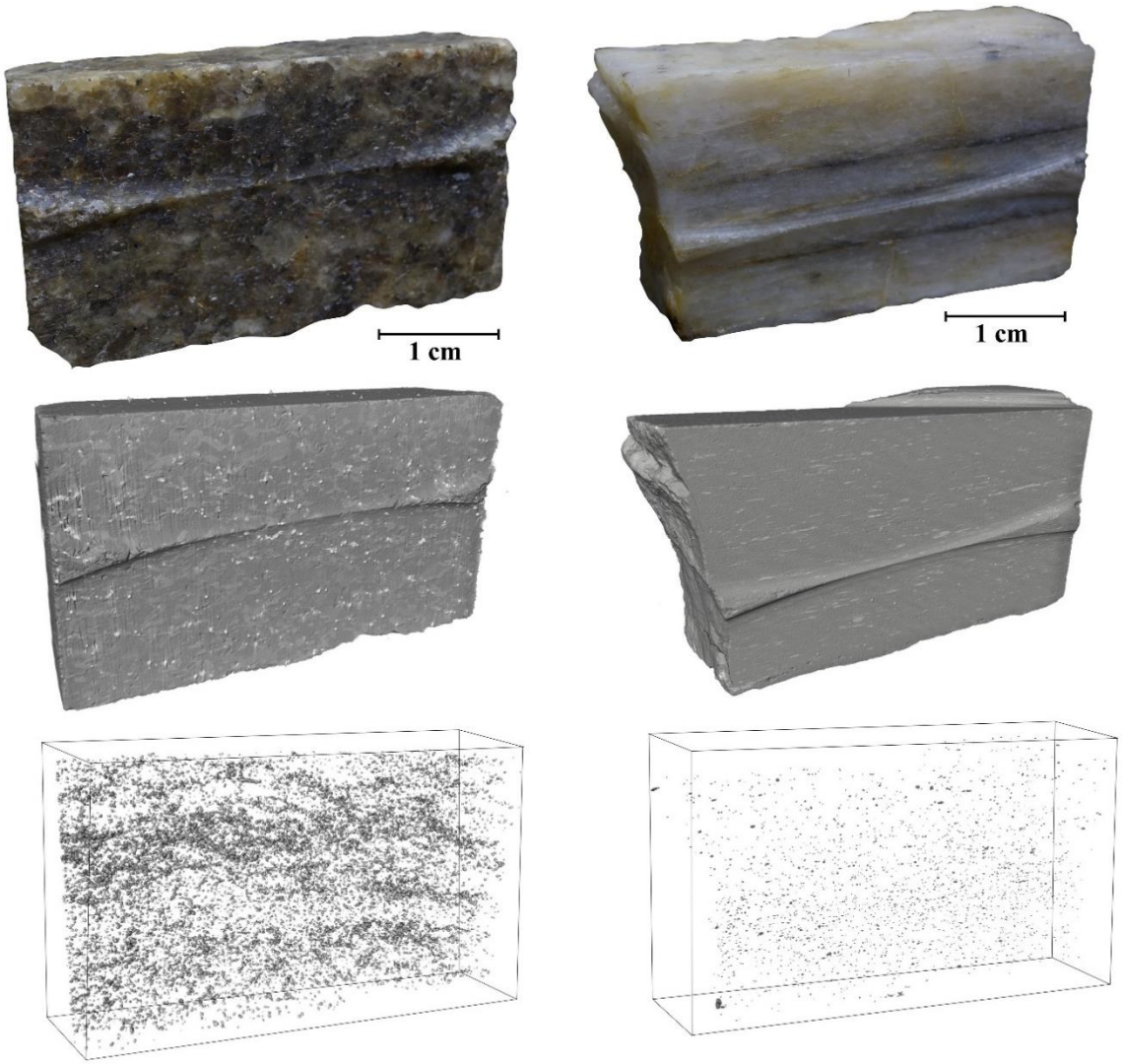

Figure 2.12. Results of XRCT 3-D phase distribution analysis. The top panel shows photographs of thin section billets that were scanned using XRCT, including the non-mylonitic quartzite (sample TO-031, left) and a high strain quartzite mylonite (sample TO-186, right). XRCT reconstructions enable separation, extraction, and quantification of the distribution of accessory phases in the sample aggregate.

deformation of mylonite as recorded in the [Ti] of quartz precipitated in high angle cross-cutting veins and pressure shadows occurred as a result of deformation embrittlement during the last stages of ductility in the shear zone. Evidence from quartz is supported by microchemical observations from coexisting white mica and 3-D distribution analysis of Ti-bearing accessory phases to confidently reconstruct the polyphase deformation and reaction history of the CRD shear zone (Figure 2.15).

2.7.1 t_0 – Non-mylonitic quartzite protolith

Non-mylonitic quartzite preserves a uniform [Ti] in quartz regardless of textural location in quartz or proximity to rutile. Muscovite comprises 15% of the quartzite as randomly oriented, tabular mica clasts that preserve intricate zoning patterns with the largest magnitude of compositional variation between zones. This quartzite retains the highest modal proportion of accessory phases, and these grains are larger and more densely distributed than accessory phases in the shear zone mylonites (Table 2.3, Figure 2.12).

The non-mylonitic quartzite preserves the highest density of accessory phases of all samples analyzed (1700 grains/cm^3), and rutile is proportionately more abundant than in all mylonite samples, confidently constraining $a_{TiO2} = 1$. Application of Ti in quartz thermometry using the bulk Ti concentration from this sample with an estimated pressure of crystallization of 7 kbar (from previous studies of nearby metapelite and garnet amphibolite; e.g., Norlander et al. [2002]) produces a calculated temperature of

equilibration of 600 °C using the TitaniQ calibration of Thomas et al. [2010], and 740 °C using the calibration of Huang & Audétat, [2012] (for discussion of comparison of calibrations, see part *8.2.4*).

2.7.2 t_1 – Cores of quartz in mylonite

The deformation conditions from the early stages of exhumation are preserved in the [Ti] of the cores of elongate quartz ribbons. The onset of ductile shearing initiates GBM of quartz, which facilitates equilibration of the [Ti] during crystal-plastic deformation. Recrystallization via GBM at higher *T* causes more rapid Ti diffusion that is reflected in the lower variance of concentration values from the quartz cores relative to quartz rims. This is in agreement with recent studies that have concluded GBM to be an effective recrystallization mechanism to equilibrate the [Ti] of quartz [Grujic et al., 2011; Haertel et al., 2013; Kidder et al., 2013].

Rutile occurs in quartzite mylonite at lower abundance and is more dispersed than in the non-mylonitic quartzite, but it is still ubiquitous at the thin section scale and therefore can be assumed to buffer Ti activity at unity. The [Ti] from quartz grain cores decreases progressively in samples from deeper levels of the mylonite zone. Application of TitaniQ thermometry (in the range of P = 2 – 5 kbar) predicts the cores of quartz ribbons to have recrystallized at 425 – 475 °C [Thomas et al., 2010] or 550 – 625 °C [Huang & Audétat, 2012], with the highest *T* recorded directly beneath the detachment and gradually

decreasing into deeper levels of the mylonite zone, in agreement with the previously documented "top-down" thermo-mechanical cooling model proposed by [Mulch et al., 2006] (Figure 2.15).

2.7.3 t_2 – Recrystallized quartz grain margins

The [Ti] in the margins of recrystallized quartz grains records the deformation conditions during the later stages of exhumation. Ion probe measurements from recrystallized quartz grain margins reveal a statistically lower and more variable [Ti] than the adjacent cores of elongate quartz ribbons. These measurements were collected from regions of quartz interpreted to have deformed by SGR and BLG recrystallization, potentially suggesting that these lower *T* recrystallization mechanisms are less effective at distributing and equilibrating the Ti signature of quartz. This has been suggested by previous studies that have documented minor to non-detectable re-setting of [Ti] during SGR or BLG [Grujic et al., 2011; Haertel et al., 2013; Kidder et al., 2013].

However, recrystallization of quartz grain margins occurred over an interval of shear zone deformation that has been documented to record a strong influx of meteoric fluids [Holk and Taylor, 1997; Mulch et al., 2004, 2006; Person et al., 2007]. High strain mylonites

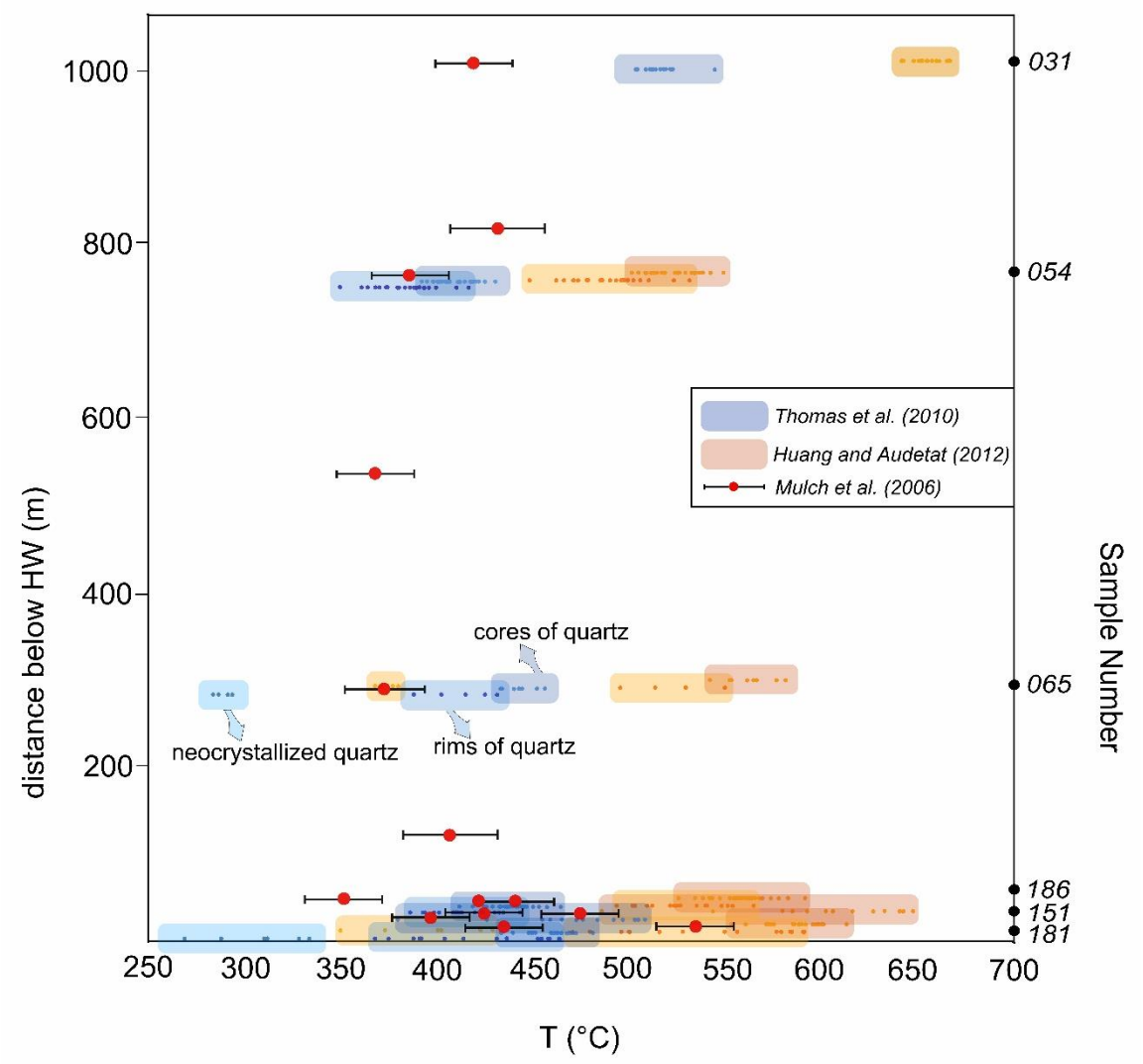

Figure 2.13. Titanium in quartz thermometry showing the estimated *T* for each of the 6 samples throughout the quartzite shear zone. TitaniQ thermometry estimates are calculated assuming isobaric (5 kbar) conditions and assuming $a_{TiO2} = 1$. Results from Ti in quartz thermometry using the two Ti in quartz solubility calibrations [Thomas et al., 2010; Huang & Audétat, 2012] are compared with *T* estimates from oxygen isotope equilibrium thermometry between quartz and muscovite [Mulch et al., 2006].

beneath the detachment preserve evidence for extensive solution transfer, recorded in the chemical homogenization of muscovite and the systematic depletion of accessory phases from rock aggregates closer to the detachment (Figure 2.12). A meteoric fluid would have a substantially diminished capacity to dissolve and mobilize HFSE, and therefore would be less likely to buffer the Ti activity of quartz – this could result in precipitation of Ti-undersaturated silica, another possible contribution to the diminished [Ti] of quartz rims. This would suggest that it is not necessarily the kinetic inefficiency of any particular recrystallization mechanism (SGR or BLG) to equilibrate the [Ti] that controls the ultimate Ti signature of recrystallized quartz, but instead it is the ubiquity of low-carry-capacity meteoric fluids at the crustal conditions where quartz is deforming via those mechanisms.

The observation of a rim depletion in [Ti] relative to cores of quartz ribbons in mylonite occurs in all samples that contain rutile within the region of the thin section, therefore justifying the assumption of $a_{TiO2} = 1$. Application of TitaniQ (in the range of P = 2 – 5 kbar) reveals that recrystallization of quartz grain margins occurred at a *T* of 375 – 450 °C [Thomas et al., 2010] or 475 – 625 °C [Huang & Audétat, 2012].

2.7.4 t_3 – Neocrystallized quartz

Deformation embrittlement through strain hardening of quartz and hydrothermal convection of meteoric fluids initiated the formation of neocrystallized quartz that was precipitated into local dilatancy sites in the mylonite. Neocrystallized quartz is not

deformed, and therefore its [Ti] has not been modified following precipitation. High precision SIMS analysis allows sampling of fine-scale neocrystallized quartz precipitated within cracks or pressure shadows around porphyroclastic feldspar or in high angle cross-cutting veins. Results from these analyses document a very low [Ti] of neocrystallized quartz. This measurement provides insight into the carrying capacity of the intergranular fluid at the time of deformation.

Rutile is present in all samples in which neocrystallized quartz was analyzed. This is interpreted to be an adequate argument to assume $a_{TiO2} = 1$ for buffering the neocrystallized quartz. Application of TitaniQ thermometry (in the range of P = 2 – 5 kbar) to neocrystallized quartz reveals a *T* of 275 – 340 °C [Thomas et al., 2010] or 355 – 435 °C [Huang & Audétat, 2012]. The frictional-viscous transition for quartz, depending on strain rate, is constrained to be within the range of 275 – 325 °C [Hirth & Tullis, 1994]. This would support the interpretation that neocrystallized quartz is capturing the final stages of ductility during the transition to brittle failure.

2.8 Discussion

2.8.1 Titanium concentration of deformed quartz

Ion microprobe analysis of [Ti] in deformed quartz from three different microstructural sites in progressively deformed mylonites reveals a correlation between [Ti] and inferred

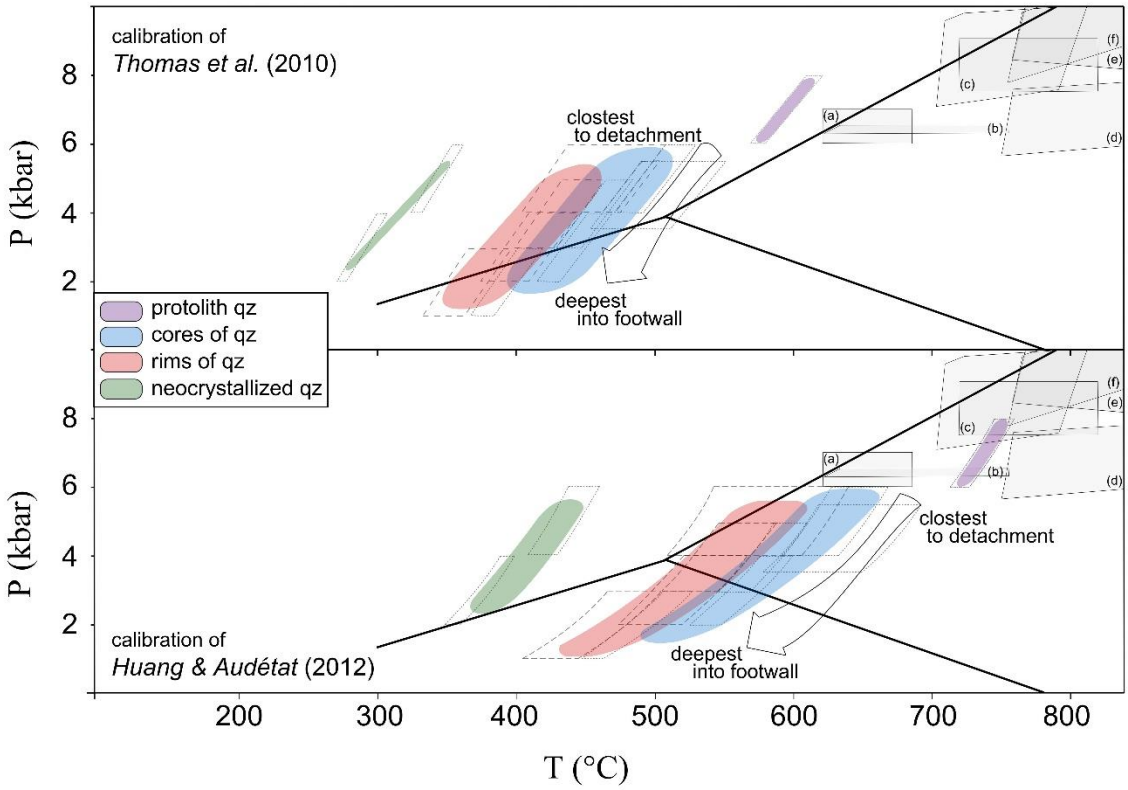

Figure 2.14. A reconstructed exhumation path for the CRD shear zone showing the calculated *P-T* conditions as predicted by both Ti in quartz solubility calibrations for the quartzite protolith, cores of recrystallized quartz ribbons, recrystallized grain rims of quartz, and neocrystallized quartz. Pressure estimates are based on a top-down cooling profile in the shear zone as demonstrated with $^{40}Ar/^{39}Ar$ geochronology of white mica, such that samples at the structurally highest levels recrystallized at higher *P* than samples lower in the section. Shaded boxes show the regions previously defined by different thermobarometric techniques: (a) Ghent et al., [1977]; (b) Lane et al., [2007]; (c) Nyman et al., [1995]; (d) – (f) Norlander et al., [2002].

recrystallization mechanism. A statistically distinct Ti signature is present within relict cores of elongate quartz ribbons, recrystallized subgrains and quartz grain margins, and neocrystallized quartz in dilatancy sites (veins, pressure shadows). Two interpretations for this correlation between microstructure and [Ti] exist: (1) each of these quartz textures

crystallized at a different set of *P-T* conditions and therefore has a distinct Ti content, and/or (2) the deformation mechanisms operative during ductile deformation of quartz mobilize Ti with varying efficiency. In the following sections, we discuss these possibilities using our integrated chemical and textural dataset for quartz, syndeformational muscovite, and Ti-bearing accessory phases.

2.8.1.1 Quartz in non-mylonitic quartzite

Quartz crystals in the non-mylonitic quartzite (sample TO-031) preserve the highest, most uniform [Ti] of all samples analyzed (Table 2.1, Figure 2.8). This would suggest that this rock resided in the middle crust for an extended duration (e.g., during Late Cretaceous metamorphism – Brown & Tippett [1978], Gibson et al. [1999]), sufficiently long to enable diffusive homogenization of the [Ti] of the formerly detrital quartz grains. Moreover, the intense folding and boudinage of the quartzite interlayered with migmatite in deep structural levels of the complex indicates it was deformed at high *T*. The absence of a crystallographic fabric (Auxiliary Materials – Figure A1.1) in the quartzite suggests that quartz deformed dominantly by diffusion creep The observation of intracrystalline uniformity (± 1 ppm or ± 3 °C) in quartz crystals that had a detrital history enables estimation of the timescale required for diffusional homogenization of the [Ti]. Using the experimentally determined Arrhenius relationship for Ti diffusion in quartz [Cherniak et al., 2007] and the approximate mean of quartz grain radii (600 μm), it can be estimated that it would require approximately 3820 Myr (at T = 600 °C) or 20.7 Myr (at T = 740 °C) to

diffusively equilibrate the [Ti], setting a minimum estimate for the duration at which this rock resided in the middle crust.

2.8.1.2 Quartz in mylonite

In contrast to the non-mylonitic quartzite, which records the highest temperature and pressure conditions at which these rocks resided prior to exhumation, the quartzite mylonites were deformed during exhumation and therefore record the conditions at which the shear zone was active. As described in previous sections, there are three texturally and compositionally distinct populations of recrystallized quartz in the quartzite mylonite. The cores of elongate quartz ribbons preserve the highest [Ti] (Figure 2.6). This is interpreted to reflect the conditions of the early stages of ductile deformation, as heat advected by the juxtaposition of migmatitic rocks and associated leucogranitic intrusions in the Thor-Odin dome (Figs. 2.1, 2.2) initiated dynamic recrystallization of quartz. Despite the relatively short (ca. 1 Myr) timescale for which each sample is predicted to have been deforming based on in-situ UV-laser $^{40}Ar/^{39}Ar$ recrystallization ages of synkinematic muscovite [Mulch et al., 2006], the influence of dynamic recrystallization (primarily by GBM recrystallization) enabled the [Ti] to equilibrate on much shorter time scales despite the large grain size of quartz (500 x 2000 μm). This implicates the influence of grain boundary diffusion and fast-path diffusion through dislocation cores as pathways for expedited Ti mobility in quartz during dynamic recrystallization. As a result of these processes, Ti

equilibration in quartz may occur over more rapid time scales than would be afforded by volume diffusion alone [Cherniak et al. 2007; Watson & Baxter 2007; Clay et al. 2011].

With progressive exhumation of the footwall, deformation embrittlement and refrigeration through hydrothermal circulation of fluids (primarily meteoric water, Mulch et al. [2004, 2006]) initiated the development of the recrystallized quartz rims (Figure 2.15). The recrystallized rims record a Ti signature that is 3-7 ppm lower and more variable than the adjacent core region. The lower values and greater variance in [Ti] of quartz grain margins potentially reflects the influence of different deformation mechanisms operative during recrystallization of the rims of quartz. Subgrain rotation recrystallization (SGR), minor bulging recrystallization (BLG) of quartz grain margins, and connectivity with a dynamic fluid source enables mobilization of Ti with varying efficiency and apparently results in more variation in the preserved [Ti] in recrystallized quartz grain rims.

However, in addition to evidence for different deformation mechanisms affecting the core and rim regions of deformed quartz, these two microstructural domains also likely recrystallized at different *P-T-t* conditions. If it is assumed that ductility of quartz occurred continuously over a finite interval of the exhumation path, then it can be surmised that equilibration of Ti in the core of quartz grains occurred first, followed by recrystallization and equilibration of the quartz rims. The switch in dynamic recrystallization mechanisms preserved the core Ti content and relocated the site of active recrystallization to the grain margins. This then promoted equilibration of the quartz grain margins before the cooling

action of hydrothermal convection cells quenched further ductility of quartz and migrated the active deformation front to lower levels of the detachment zone [Holk & Taylor, 1997; Mulch et al., 2006; Gottardi et al., 2011]. Based on the assumption of a core to rim progression of dynamic recrystallization, results of Ti in quartz thermobarometry predict that recrystallization of the cores of quartz grains occurred at 20-35 °C higher than the adjacent rims. In an exhuming system, if the core is assumed to have recrystallized at a *P* that is ~1 kbar higher than the rim, the calculated *T* difference between core and rim increases to 40-55 °C. The magnitude of the compositional variation between core and rim domains reflects the *P-T* path interval in which quartz recrystallization occurred in different levels of the shear zone during exhumation of the complex.

2.8.2 Factors controlling the Ti content of deformed quartz

2.8.2.1 Ti solubility in crustal fluids

In a dynamic, multi-source hydrothermal setting such as an extensional detachment system [Kerrich et al. 1984; McCaig & Knipe 1990; Holk & Taylor 1997; Mulch et al. 2007; Allan & Yardley 2007; Gébelin et al. 2011; Gottardi et al. 2011; Siebenaller et al. 2013], consideration of the role of fluid in Ti redistribution is important for interpreting the observed correlation of [Ti] and textural location in deformed quartz. Fluids are also of critical importance as a buffering medium, as the connectivity and mobility of an

intergranular fluid can substantially enhance the effective distance of chemical buffering by Ti-bearing phases in the rock.

Classically, oxides of high field-strength elements (HFSE) such as Ti are considered refractory phases in the crust and are largely insoluble in supercritical crustal fluids [Baes & Mesmer, 1976; Winchester & Floyd, 1977]. However, evidence from field observations of quartz veins rich in HFSE-bearing phases such as rutile show that crustal fluids can dissolve and transport substantial volumes of HFSE [van Baalen, 1993; Sepahi et al., 2004; Bucholz & Ague, 2010; Jiang et al., 2005; Manning, 2006]. Additionally, Ti solubility in aqueous solution has been investigated experimentally at elevated *P-T* conditions in saline- and silica-rich fluids, simulating the conditions predicted to exist in the mid-lower curst [Tropper & Manning, 2005; Hayden & Watson, 2007; Antignano & Manning, 2008; Hayden & Manning, 2011]. These experimental studies document a Ti solubility that is dependent on the presence of complexing agents available in solution; Ti solubility is observed to be 1-2 orders of magnitude higher in saline- and silica-bearing fluids relative to a pure aqueous solution. These results suggest that magmatic, deep crustal fluids, with a high carrying capacity for HFSE owing to a high concentration of dissolved silica and salts, have the potential to redistribute and effectively buffer quartz with a Ti activity at or approaching unity.

These experimental results also suggest that meteoric, predominantly aqueous solutions would have far lower carrying capacity for HFSE if these fluids lack the complexing agents

of magmatic/metamorphic fluids, and therefore would be less likely to be buffered with respect to Ti. In the case of the Shuswap MCC, there is a well-documented signal of meteoric water infiltration into the actively deforming detachment zone, as recorded in large negative shifts in deuterium ratios in synkinematic muscovite [Kerrich et al., 1984; Fricke et al., 1992; Holk & Taylor, 1997; Mulch et al., 2004, 2007; Person et al., 2007]. This indicates that the dominant fluid phase at the time of deformation was a relatively pure hydrous solution derived from surface waters [Rimstidt, 1997; Yardley, 2009], with little capacity to dissolve and mobilize large quantities of Ti.

Results presented in this study from XRCT analysis of accessory phase distribution document a depletion in the abundance of accessory phases, a reduction in volume, and a reduction in the reactive surface area of accessory phase particles. Despite a reduction in the size and abundance of accessory phases, the 3-D aspect ratio of accessory phase grains remains indistinguishable between deformed and undeformed samples (Figure A1.5). Plotting the long axis of the accessory phases relative to the lineation direction shows a strengthening in shape preferred orientation as elongated particles align to the lineation direction. Assuming that the modal mineralogy of the mylonitized quartzite was similar to that which is observed in the non-mylonitic (pre-deformed) quartzite, these results suggest that accessory phases are acting as rigid, passive markers in the mylonite that are preferentially undoing dissolution and leaching from quartzite in higher strain mylonites closest to the detachment.

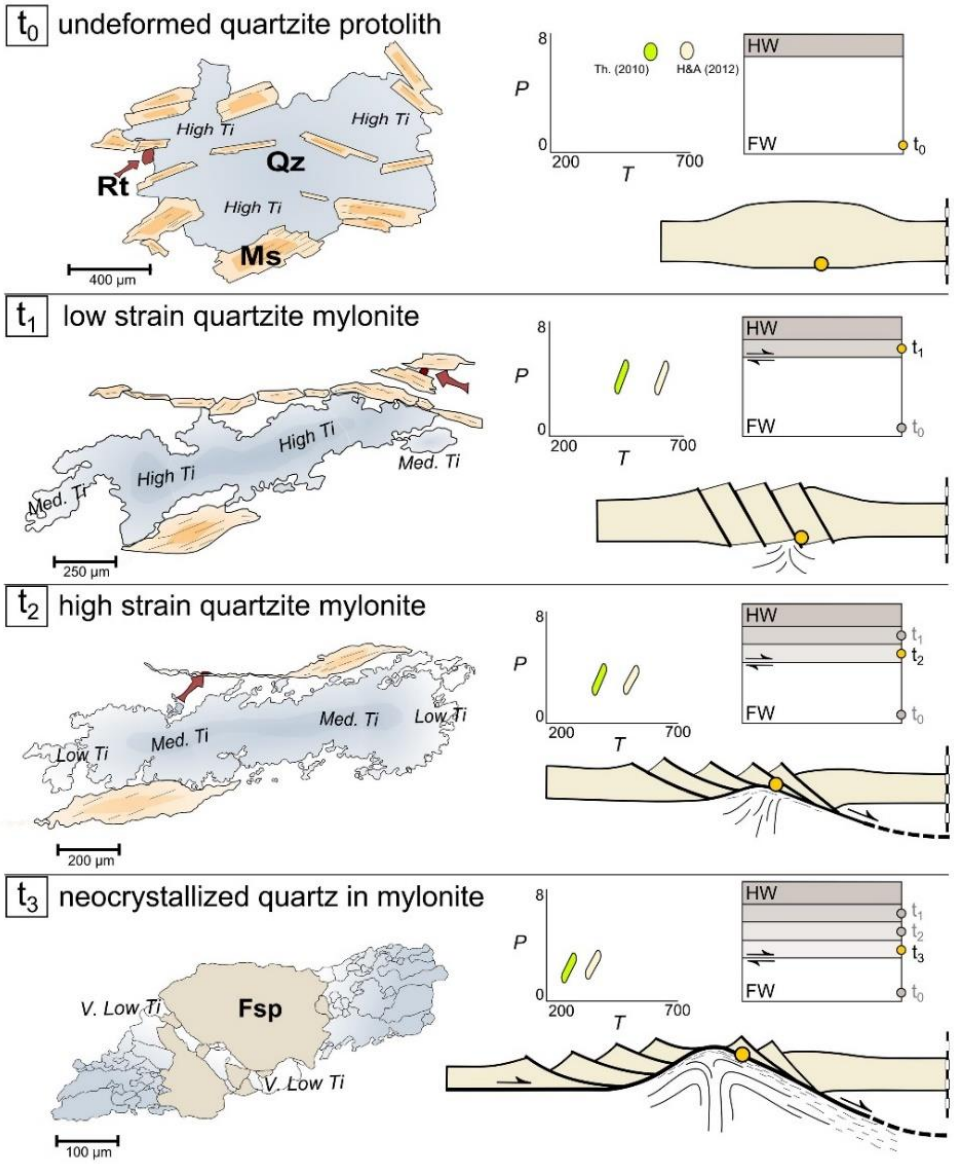

Figure 2.15. Conceptual diagram illustrating the characteristic quartz microstructures and observed patterns of Ti distribution from different levels of the detachment shear zone. Illustrations of different quartz microstructures from 4 consecutive Ti in quartz equilibration events ($t_0 - t_3$) show the changes in microstructure and composition of deforming quartz and muscovite. The values of [Ti] measured from different microstructures are used to reconstruct the *P-T* conditions at which each microstructure formed. Deformation in the CRD migrated downwards during progressive exhumation, sequentially locking-in microstructures at higher levels of the shear zone before moving to lower levels of the footwall. The *P-T* reconstructions from quartz microstructures are framed within the context of an exhuming metamorphic core complex with a rolling-hinge geometry.

2.8.2.2 Diffusion of Ti and ^{18}O in quartz during deformation

Isothermal decompression of deep crustal rocks in the Thor-Odin dome delivered material from pressures of 8–10 kbar to <5 kbar while sustaining a temperature of ≥700 °C [Norlander et al., 2002; Whitney et al., 2004]. This creates a scenario in which advection of material outpaced the kinetics of diffusive equilibration, resulting in the development of reaction textures (e.g., Goergen and Whitney [2012a, b]). In contrast, in shear zones, deformation expedites the kinetics of equilibration and therefore metamorphic rocks in shear zones have the potential to preserve a more detailed record of deformation and metamorphism along the exhumation path. Evaluation of in-situ variation in trace quantities of Ti relative to stable isotope variation collected from bulk mineral separates of the same samples enables comparison of the relative rates of diffusion and equilibration between Ti concentration and O isotopes in quartz.

Oxygen diffusion in quartz has been investigated experimentally [Giletti & Yund, 1984], and the effects of temperature, water fugacity [Dennis, 1984; Farver & Yund, 1991], crystallographic anisotropy [Clay et al., 2010], and deformation [Kirschner et al., 1995; Gleason & DeSisto, 2008] are well established. Multiple lines of evidence confirm that deformation under hydrous conditions results in resetting of O isotopes in quartz [Kirschner et al., 1995], a process that has proven valuable in the assumption of equilibrium stable isotope fractionation between synkinematic phases used to predict thermal conditions of shear zone deformation [Chacko et al., 1996; Valley, 2001].

Titanium diffusion in quartz has been measured through a series of quartz-rutile diffusion experiments conducted at atmospheric pressure over a range of elevated temperatures, from which diffusion profiles were measured and used to extract a diffusivity relationship for Ti in quartz [Cherniak et al., 2007]. These results demonstrate that the diffusive torpidity of Ti in quartz, even under the thermal conditions of the mid-lower crust, would prevent homogenization of Ti compositional domains, and thus quartz could hold promise as a robust recorder of multiple crystallization events in the crust. Following the documented isochemical substitution of tetravalent Ti for Si in the quartz structure (XANES measurements of Thomas et al. [2010]), it can be hypothesized that there would not be a predicted water fugacity dependence on Ti substitution, nor would the presence of mono- or divalent complexing ions such as Li, Na, or Ca affect Ti substitution in quartz. It is well documented that quartz has a substantial capacity to dissolve appreciable (trace) quantities of these species [Dennen, 1964, 1966; Müller et al., 2003; Götze et al., 2004], yet the effect of their presence and concentration on the diffusion of Ti in quartz remains unclear. On the contrary, O diffusion has been shown to be strongly dependent on fluid activity; oxygen self-diffusion under dry conditions has been measured to be slower than Ti diffusion, whereas under hydrous conditions, O diffusivity is up to an order of magnitude faster than that of Ti [Zhang & Cherniak, 2010].

It therefore follows that in a dynamic hydrothermal system such as an extensional shear zone, a high water-rock ratio at the time of dynamic recrystallization would enhance

diffusive equilibration of O, while the immobile Ti would remain relatively stationary over the rapid time scales of mylonitization. Based on this condition, we propose that the O isotope signature, as measured from a bulk analysis of pure quartz separate, equilibrated during the same fluid infiltration event that recrystallized and equilibrated the Ti signature of the rims of quartz grains.

2.8.2.3 Buffering a_{TiO2} in quartzite mylonites

The distribution and abundance of Ti-buffering phases has been evaluated using 3-D reconstructions of accessory phase distribution in rock hand samples and 2-D phase mapping of large regions of thin sections. The density distribution and 3-D volume of all accessory phases in quartzite mylonite decreases with increasing amounts of finite strain. A concentration of accessory phases is also documented within foliation-parallel layering, suggesting that HFSE transport is greatest along foliation planes owing to the strongly anisotropic fabric of sheared rocks. Importantly, no correlation is detected between the bulk [Ti] in quartz from a sample and the density distribution of Ti-buffering phases, suggesting that even the samples with the least abundant rutile are still adequately buffered with respect to a_{TiO2}.

Different interpretations can emerge based upon different assumptions of a_{TiO2} and the observations of quartz chemistry in each textural site of mylonite from the CRD: if it is assumed that (1) the cores of recrystallizing quartz equilibrated at $a_{TiO2} = 1$ since rutile is

abundant in the protolith, (2) the rims of recrystallized quartz equilibrated at $a_{TiO2} = 0.7$ since there would be some contribution of quartz precipitation from meteoric fluid and ilmenite increases in abundance relative to rutile, and (3) the neocrystallized quartz equilibrated at $a_{TiO2} < 0.1$ since a meteoric fluid will have a low carrying capacity for HFSE (see section *8.2.1*), then for a singular *P* estimate, it would be predicted that all of these quartz textures formed at approximately the same *T*. Although this particular scenario can be refuted on the grounds of the well-documented *T*-dependence of recrystallization microstructures for quartz [Law, 1990; Hirth & Tullis, 1992; Hirth et al., 2001], it is nonetheless critical to very carefully consider a Ti activity assumption when reconstructing the *P-T* conditions from quartz deformed by different deformation mechanisms, and it is clear that further experimental and natural observational work is required to constrain the appropriate solubility calibration for quartz in nature.

2.8.2.4 Comparison between Ti solubility calibrations

There are currently two calibrations for the *P-T* dependence of Ti solubility in quartz: Thomas et al. [2010] (which includes the original calibration of Wark & Watson [2006]) and Huang & Audétat [2012]. Both of these solubility calibrations were conducted on quartz precipitated from solution at elevated P-T in a hydrothermal apparatus, but the predicted *P-T* conditions vary substantially from one another. As it remains unclear what fundamental process is responsible for the variance between the calibrations and how this extrapolates to application of Ti-in-qz thermobarometry in the crust, we have carefully

evaluated both calibrations to determine which is more suitable for quartz mylonites of this study.

The non-mylonitic quartzite sample is useful for comparison of the two calibrations because it records the most uniform [Ti], contains the most abundant rutile for confident assumption of Ti buffering, and possesses the most detailed *P-T* estimates from metamorphic reconstructions of neighboring rocks for estimation of *P* for TitaniQ thermometry calculations. Metamorphic conditions of this part of the Thor-Odin dome region have been estimated at 625– 825 °C and 6.0–8.5 kbar from metamorphic reconstructions of co-existing amphibolitic and metapelitic mineral assemblages [Nyman et al., 1995; Norlander et al., 2002]. If an intermediate *P* estimate of 7 kbar is assumed for application of TitaniQ thermometry, the calculated *T* of quartz equilibration is 600 °C [Thomas et al., 2010] and 740 °C [Huang & Audétat, 2012]. If a lower pressure estimate of 5 kbar is assumed, the thermometry results from quartz are 560 °C [Thomas et al., 2010] and 700 °C [Huang & Audétat, 2012]. Based on this set of assumptions, it would appear that the Huang & Audétat [2012] calibration more closely agrees with pre-existing thermobarometric constraints from co-existing metamorphic assemblages.

However, it could be argued that quartz may have continued recrystallizing and thus equilibrating its Ti signature at lower *P-T* conditions than those determined by "classical" thermobarometers (e.g., garnet-kyanite-plagioclase-quartz barometry). If quartzite continues recording deformation at ca. 100 °C and 2–4 kbar below the conditions where

"classical" thermobarometers are thought to equilibrate, then the calibration of Thomas et al. [2010] would be the preferred interpretation for this scenario. Indeed, temperatures predicted by the Thomas et al. [2010] calibration most closely agree with pre-existing oxygen isotope thermometry [Mulch et al., 2006], assuming reasonable *P* estimates for quartz crystallization (Figure 2.13).

2.9 Conclusions

This study shows that the Ti content of different quartz microstructures has the potential to preserve multiple stages of deformation in a crustal shear zone. Titanium in quartz thermobarometry is applied to these microstructures to reconstruct a progression of retrograde exhumation of the shear zone. High resolution analysis enables comparison between in-situ (Ti in quartz, major and minor components of muscovite) and bulk (O in quartz and muscovite) analysis techniques, demonstrating that multiple events can be resolved from the systematics of intragrain zonation that is otherwise obscured in bulk mineral analysis or lower-resolution (>20 μm spot size) in-situ techniques. Future studies could further this effort by performing parallel in-situ observations of Ti-in-quartz and oxygen isotope thermometry to directly compare these two geochemical systems for recording conditions of shear zone deformation, and by combining in-situ microchemical thermometry techniques for quartz recrystallization with other microstructural thermometers such as the c-axis opening angle thermometer for quartz [e.g., Law et al., 2011].

The process of ductile shearing is shown to result in major, minor, and trace element redistribution during mylonitization. This is recorded in the CRD shear zone by the obliteration of compositional zoning in muscovite and the depletion of accessory phases in higher strained mylonites. The presence of a syndeformational fluid phase is critical for this mobilization process, and the chemical character and source region of crustal fluids can impact the efficiency of mass transfer in the crust. Crustal fluids of different compositions likely have varying efficiency for buffering a_{TiO2} for the application of quartz thermobarometry.

There remains uncertainty in the selection of an appropriate Ti in quartz solubility calibration for reconstructing the conditions of quartz recrystallization in the crust. Results from this study are unable to confirm the accuracy of one calibration over another for quartz in the CRD, as uncertainties in pressure, a_{TiO2}, fluid interaction, and crystal growth rate prevent deconvolution between these variables and the variance between the two calibrations. It is clear that further studies on natural and experimental recrystallization of quartz and the resultant [Ti] are needed to better constrain the reliability and applicability of different calibrations.

With the advent of Ti in quartz thermobarometry [Wark & Watson, 2006; Thomas et al., 2010], the documented sluggish diffusion of Ti in quartz [Cherniak et al., 2007], and the modernized analytical capabilities for high resolution quantitative analysis, variation in [Ti] from dynamically recrystallized quartz has the potential to record a poly-phase

metamorphic history of deformation in the crust. If it assumed that deformation facilitates equilibration of Ti in quartz, and that shearing in the crust is localized into quartz-dominated lithologies, it can be hypothesized that quartzite shear zones have the potential to preserve a prolonged record of the physical conditions at which strain localization occurs. In this way, Ti in quartz thermobarometry of quartz microstructures could record a more detailed continuum history of tectonic activity relative to the statically metamorphosed terranes away from the deformation zones.

Acknowledgments

This work was supported by National Science Foundation grant EAR-0911497 awarded to DLW and CT. WON gratefully acknowledges Nobu Shimizu and Brian Monteleone for assistance with ion microprobe analysis at WHOI, and Marty Grove for assistance with ion probe analysis at Stanford. Nick Seaton in the UMN Characterization Facility is thanked for assistance with sample preparation and EBSD analysis. AM acknowledges support through the LOEWE funding program (Landes-Offensive zur Entwicklung wissenschaftlich-ökonomischer Exzellenz) of Hesse's Ministry of Higher Education, Research, and the Arts. We thank Djordje Grujic and an anonymous reviewer for constructive and insightful reviews, and Cin-Ty Lee for editorial handling.

CHAPTER 3

High-precision doping of nanoporous silica gel for the preparation of trace element microanalytical reference materials

This chapter is currently under review for publication in *Geostandards and Geoanalytical Research*.

Synthesis

A novel approach for synthesizing microanalytical reference materials is introduced that is capable of fabricating a high-purity glass containing a selected element at a specified concentration. This technique is used to synthesize silica glasses with specific, trace-level concentrations of Ti, with the aim of improving petrogenetic reconstructions based on trace element geochemistry of quartz. Nanoporous silica gel is cleaned in concentrated HCl then immersed in a nonpolar doping medium at a controlled pH and doped with precise quantities of plasma standard solution. Using liquids composed of longer-chain molecules as the doping medium diminishes recovery, suggesting that large molecules may obstruct silica gel nanopores to inhibit capillary uptake of the dopant. A control experiment using pure quartz reinforces the effectiveness of nanoporous silica gel for doping. Layered aggregates of silica gel doped with different Ti concentrations were hot-pressed to create multi-layered reference materials which were analysed with multiple techniques at a variety of spatial scales; analysis at the intragrain scale (SEM-CL, EPMA), at the single grain scale (SIMS), at the sample layer scale (EPMA, LA-ICP-MS), and at the bulk scale (ICP-OES) demonstrates acceptable homogeneity at the analyte volumes characteristic of most microanalysis techniques.

3.1 Introduction

Advances in understanding the solubility of trace elements in minerals has generated interest in quantifying low elemental concentrations from micrometre-scale regions of crystals. Attempts at in-situ trace element analysis made by pushing the limits of conventional techniques have been met with varied success, in part due to a lack of suitable reference materials available for testing instrumental calibrations. Incorporating reference materials into an analysis routine improves the confidence of measurements that can refine petrological interpretations based on trace element techniques. The experimental doping approach introduced here is tested for fabricating reference materials containing specific, trace-level concentrations of Ti for the purpose of improving thermobarometry applications based on Ti solubility in quartz.

Quartz contains an array of elemental impurities at the trace (<1000 μg g^{-1}) concentration level (e.g., Dennen (1966); Muller et al. (2003), Gotze et al. (2004)). The solubility of one of these elements, Ti, been experimentally quantified over a range in P-T conditions (Wark & Watson 2006; Thomas et al. 2010; 2015). These experiments indicate that quartz growing in most geologic environments will contain Ti contents ranging from ca. 1-100 μg g^{-1}. Owing to the generally-sluggish rates of cation diffusion in quartz relative to the rates of quartz crystal growth (Cherniak et al. 2007), trace element concentrations in natural quartz are commonly inhomogeneous across small spatial scales (e.g., Muller et al. (2003); Rusk et al. (2008); Leeman et al. (2009)). Consequently, using trace element concentrations in

quartz for petrogenetic reconstructions requires techniques capable of detecting low elemental concentrations (~1 μg g^{-1}) from small (<5 μm) regions of samples.

At present, the NIST SRM series of trace element glasses (NIST SRM 610-617) is the most widely-used reference material for trace element microanalysis of quartz. The NIST glasses were synthesized in the early 1970s as large (c. 100 kg) batches of soda-lime glasses spiked with sixty-one trace elements at four different concentration levels (Kane 1998; Jochum et al. 2011). NIST glasses are useful because they contain numerous elements, they are widely-available, and they have been tested with multiple analytical techniques (e.g., Horn et al. (1993); Pearce et al. (1997); Jochum et al. (2011)). However, since these glasses were not originally intended for use as microanalytical reference materials (Kane 1998), using them to calibrate trace element measurements can be problematic. For instance, inhomogeneities in some elements have been detected at the resolution of some in-situ techniques (Eggins & Shelley 2002; Jochum et al. 2011). Also, the great abundance of elements contained in the NIST glasses can generate analytical interferences that require special care to avoid. Finally, and perhaps most importantly, the supply of NIST glasses is finite and the exact recipe used for their production is unknown.

Owing to uncertainties with coupling of the ion-, electron-, or laser-beam with glass matrices, analytical measurements of quartz at very low concentrations can be improved by matrix-matching of reference materials with the analyte matrix (e.g., Behr et al. (2011); Leeman et al. (2012); Cruz-Uribe et al. (2014)). For analyzing trace levels of Ti in quartz,

a commonly-used crystalline reference material is the TitaniQ series of high-Ti quartz grown by J. Thomas (Thomas et al. 2010), distributed as single crystals that contain 18, 100, 380, and 764 μg g^{-1} Ti. These crystals contain a range of Ti concentrations similar to those expected for high-temperature (therefore high Ti) quartz, and thus provide a good test of measurements expected for analysis of many high-grade igneous and metamorphic rocks. However, since they were not produced by artificial doping but instead reflect the equilibrium solubility at the conditions of growth, concentrations are limited to the range of solubilities attainable experimentally (Wark & Watson 2006; Thomas et al. 2010, 2015).

Certain occurrences of natural quartz have been tested for use as trace element in quartz reference materials. Rims of quartz phenocrysts from the lowest member of the Bishop Tuff have been found to contain consistent Ti concentrations (~46 ± 4 μg g^{-1}, Peterman & Grove (2010); ~41 ± 2 μg g^{-1}, Cruz-Uribe et al. (2014)) and have been employed as reference materials for EPMA (Wark & Watson; 2006), SIMS analysis (Peterman & Grove 2010; Nachlas et al. 2014) and LA-ICP-MS analysis (Cruz-Uribe et al. 2014). Herkimer quartz, a variety of doubly-terminated quartz crystals extracted from vugs in dolostone from Herkimer county, NY, have been shown to contain very low Ti concentrations (~ 3 ng/g) (Kidder et al. 2013) and are useful as a Ti-in-quartz "blank" to evaluate instrumental background (Kohn & Northrup 2009, Donovan et al. 2011; Kidder et al. 2013, Nachlas et al. 2014). Audétat et al. (2014) describe a smoky quartz crystal from Shandong province, China, as a reference material for Ti (~57 μg g^{-1}), Al, Li, Fe, Mn, Ge, and Ga owing to its relatively uniform distribution of these elements.

Each of these reference materials is useful, and ideally all should be used in parallel, because each contains a relatively uniform distribution of Ti. However, in some cases it is necessary to use reference materials containing a specific concentration or bracketing a range of concentrations that are close to levels expected in unknown samples. Additionally, interferences can be avoided by using high-purity materials whose trace element concentration can be controlled. In order to contribute to advancing techniques for measuring trace element concentrations in minerals for petrogenetic applications, with particular emphasis on improving the confidence and resolution of Ti-in-quartz thermobarometry, this study presents an approach to synthesize doped silica glasses that are demonstrated to be effective across multiple spatial scales as reference materials for trace element analysis.

3.2 Nanoporous Silica Gel – Background and Motivation

Nanoporous silica gel was selected as a doping substrate for synthesizing trace element reference materials (Figure 3.1). Silica gel is a form of high-purity, amorphous silica characterized by an internal network of interconnected hydrophobic nanopores. It is synthesized through a sol-gel processing technique involving hydrolysis of silicic alkoxide precursors, from which gelaceous silica condenses and is then dried to form a powder (Gonzalez-Oliver et al. 1982; Hench & Vasconcelos 1990). By controlling the pH conditions and the rate of gelation during the sol-gel process, silica gel particles can be synthesized and obtained commercially with specific grain and pore size dimensions.

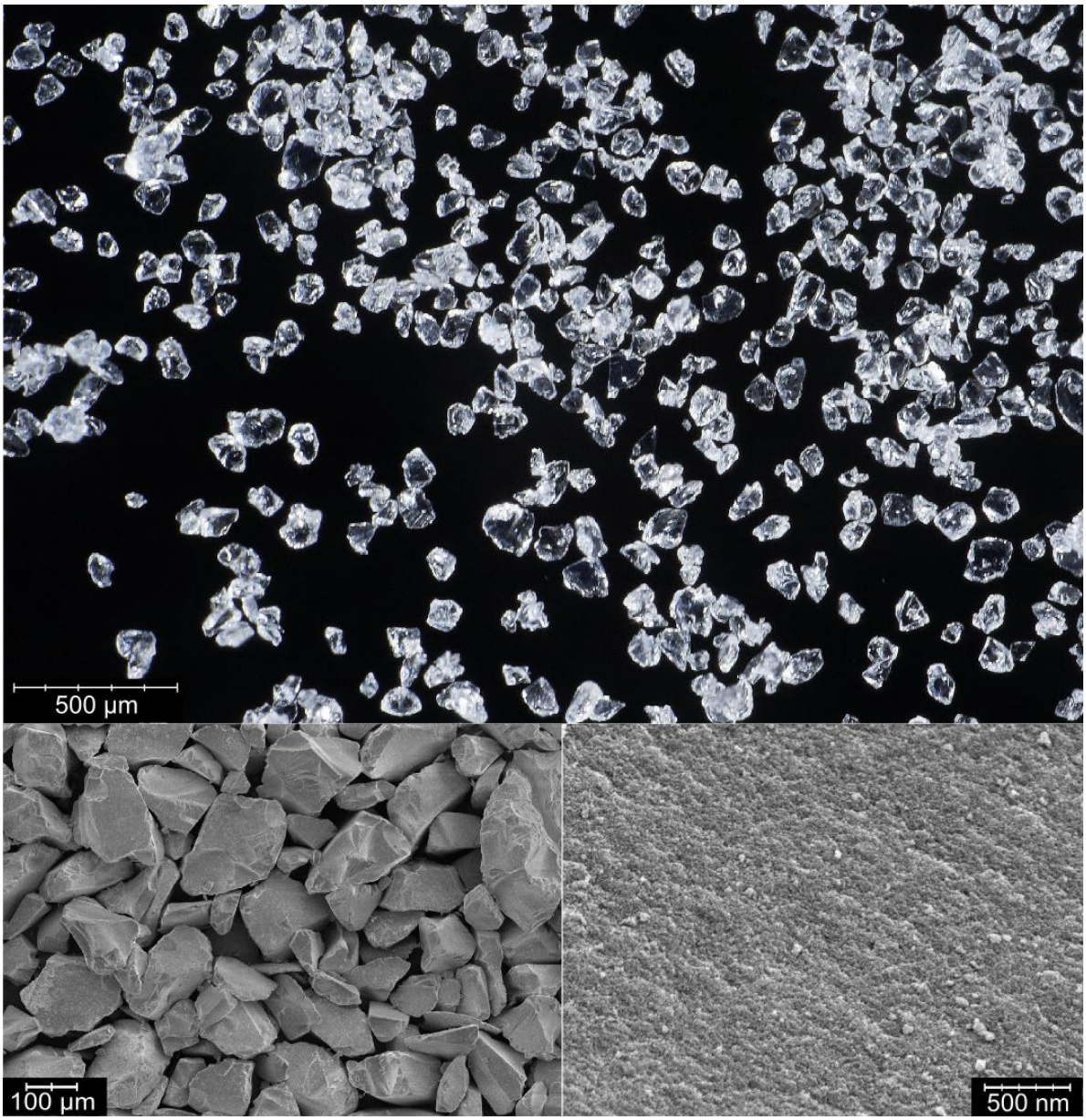

Figure 3.1. Photograph and secondary electron images (SEI) of silica gel. Silica gel grains cleaned in concentrated acid resemble translucent conchoidal shards. SEI show the morphology of silca gel grains and the 60 Å nanopores intersecting the silica surface.

	Al	Ba	Ca	Fe	K	Mg	Mn	Na	P	Sr	Ti	Zr
Silica gel as received	223.2	15.5	532.7	213.8	35.7	167.0	--	786.4	12.1	7.6	142.0	64.7
Silica gel - 9hr activation fluxed with 6M HCl for 9hr	61.0	3.3	193.4	200.7	--	94.7	--	52.4	10.0	3.7	110.3	62.7
Black Hills Quartz (BHQ) as received	728.0	9.3	849.0	912.1	183.7	250.4	15.0	61.9	102.4	7.7	140.7	8.8
BHQ - 9hr activation fluxed with 6M HCl for 9hr	457.4	8.5	619.8	588.0	37.6	219.1	12.6	48.1	15.4	6.5	47.2	3.3

Table 3.1. Trace element contents of silica gel and pure quartz separate from Black Hills Quartzite (BHQ) as measured with ICP-OES. All values in μg g-1.

Owing to its high purity, silica gel has previously been used as a quartz starting material for laboratory experiments (Luth & Ingamells 1965; Luan & Paterson 1992; Nachlas & Hirth, 2015).

Silica gel has potential to be an effective doping substrate in part because of its high absorptive capacity. The nanoporosity of silica gel exerts a strong capillary force that drives imbibition to evenly distribute polar dopant molecules throughout grain interiors (e.g., Huber et al. (2007); Gruener et al. (2009); Gruener & Huber (2011); Wu & Navrotsky (2013)). As a result, silica gel is commercially used (and perhaps most commonly-known) as a low-cost, chemically-inert desiccant. The absorptivity properties of silica gel are also widely used in chromatography (Nawrocki 1991a, 1991b; Barrett et al. 2001; Liang et al. 2008) and as a substrate for preconcentration and recovery of trace metals from natural

waters (Leyden & Luttrell 1976; Mahmoud et al. 2000; Goswami & Singh 2002; Akl et al. 2004; Jal et al. 2004; Venkatesh et al. 2004; Karbasi et al. 2009).

The strongly adsorptive surface of silica gel further qualifies this material as a high precision doping substrate. The silica gel surface is densely-populated with silanol groups that have a strong affinity for metallic ions (Nawrocki et al. 1989; Unger 1994; Chuang & Maciel 1997; Nawrocki 1997). Silanization of the silica gel surface can be optimized by controlling the chemical environment of doping synthesis for the specific species of interest (Unger 1994; Venkatesh et al. 2004; Zougagh et al. 2005).

Silica gel possesses thin silica walls that act to minimize the effective diffusion distance and therefore facilitate homogenisation of the dopant within the silica framework. Previous investigations have calculated the thickness of silica gel walls to be on the order of several to tens of silicon atoms (Nawrocki et al. 1989). Based on the strong absorption of its nanoporous structure, the high chemical affinity of its surface bonding environment, and the thin walls that form the silica framework, silica gel presents an ideal substrate to synthesize high purity reference materials with specified, trace-level concentrations.

3.3 Experimental Methods

A batch of commercial-grade silica gel (VWR International, no. BDH9004) characterized by 60 Å nanopores and 60-200 μm grain size was obtained for this study. The silica gel was first activated by fluxing it in concentrated hydrochloric acid for 3-168 h (for complete

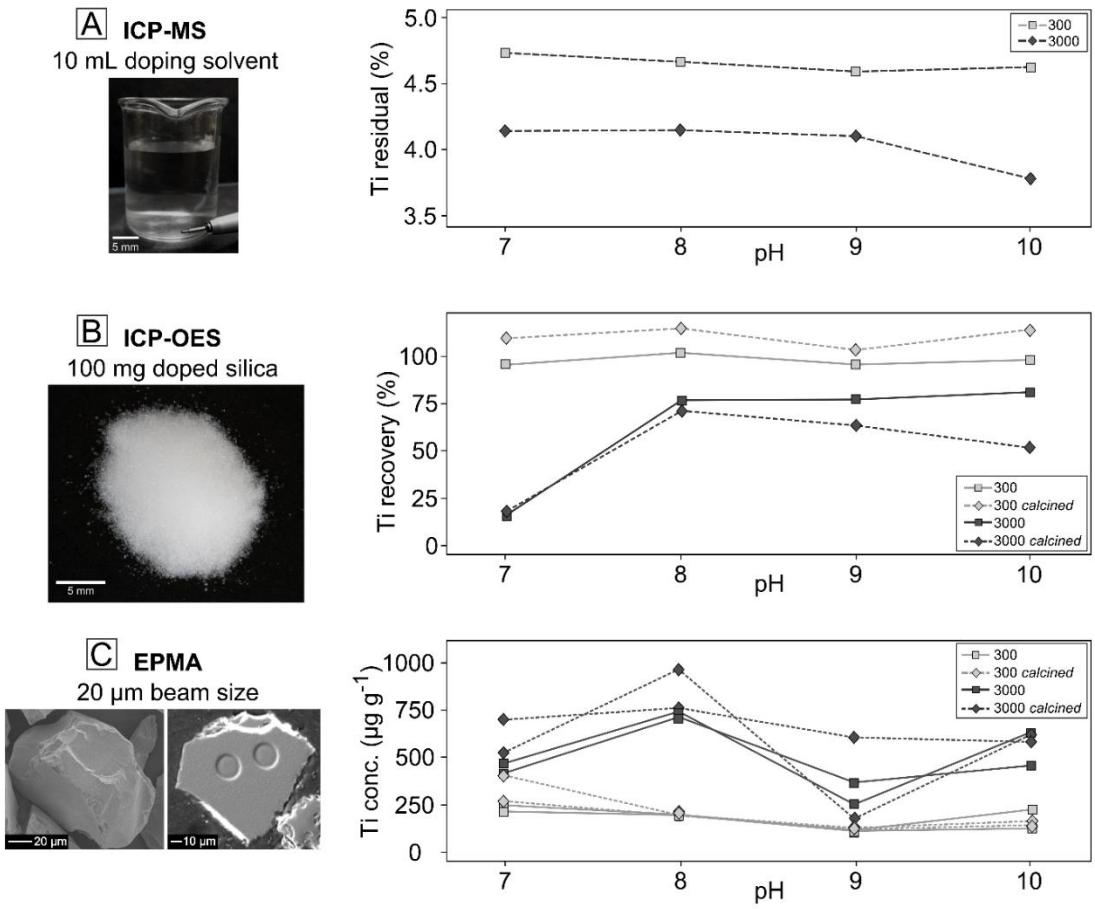

Figure 3.2. Effect of pH on doping recovery evaluated at multiple scales. Doping experiments were conducted across a range in pH (7, 8, 9, 10) to determine conditions for highest doping efficiency. Doping efficiency was evaluated by (A) measuring the residual dopant in the doping solvent solution (ICP-MS), (B) measuring bulk Ti content of silica gel before and after calcination (ICP-OES), and (C) analysing polished grain-mounts of doped silica gel grains with defocused-beam EPMA measurements.

Activation Procedure, see Appendix 5.1). Following acid-rinsing, the cleaned silica gel was thoroughly washed with de-ionized water (DIW) until no acid was detected in the decanted rinsings (>25 rinsings, as tested with 0.1 M $AgNO_3$). After all acid was removed, silica gel was dried in a conventional furnace at 120 °C for >120 h. A long-duration, low-temperature

drying procedure was employed to evacuate volatiles from the pores of silica gel without damaging the fragile silica pore network (Benesi & Jones 1959; Adachi & Sakka 1990).

Prior to addition of the dopant, the activated and dried silica was immersed in a solvent medium composed of nonpolar liquids (for complete Doping Procedure, see Appendix 5.2). To investigate interactions between the solvent medium and the pores of silica gel, tests were performed with alkane molecules characterized by different chain lengths: Ethanol (99.5%, Sigma-Aldrich, no. 459844), reagent-grade alcohol (Fisher Scientific, no. A406P-4), Heptane (Sigma-Aldrich, no. 592579), Hexadecane (Sigma-Aldrich, no. H6703), Squalane (Sigma-Aldrich, no. 234311), and De-ionized water.

A micropipette was used to add precise amounts of a Ti plasma standard solution (Ti in 5% HNO_3^-), commercially-available for most elements and here obtained for Ti in two concentrations: 10 μg ml^{-1} (Alfa Aesar, no. 45267) and 1000 μg ml^{-1} (Alfa Aesar, no. 35768). The reported error (1-3 μl) of the finest micropipette (10-100 μl) translates to a minimum error in doping precision of 3-8 μg g^{-1} using the lower concentration solutions. After adding the dopant to the silica gel immersion, the solution was titrated using 3 M NH_4OH and 0.3 M NH_4OH as base buffers and 0.2 M HNO_3 as an acid buffer (for complete list and quantity of ingredients for each batch, see Appendix 5.3). Once the desired pH stabilized, the vessel containing silica gel, doping solution, and solvent medium was placed into an oscillating apparatus for 3 h. After removal, the contents of the container were filtered using a vacuum filtration assembly (Sigma-Aldrich, no. 290440) with 0.45 μm

nylon filters (Sigma-Aldrich, no. Z269530). The doped gels were then placed in a conventional furnace at 100 °C for 24 h then 120 °C for 120 h before storage in an air-tight container.

Hot-pressing of silica gels has been shown to be an effective approach for synthesizing high-density glasses (e.g., Decottignies et al. (1978); Jabra et al. (1980); Phalippou et al. (1982)). This study utilized the Paterson gas-medium apparatus at the University of Minnesota to hot-press 3- and 7-layer aggregates of doped silica gels at 1100 °C and 300 MPa for 1-3 h, following an experimental procedure similar to Tasaka et al. (2015). Layered samples were prepared by cold-pressing silica gel into a Ni can with Fe spacers (spacers only used in the 7-layer experiment), which was inserted into an outer Fe jacket and sandwiched by alumina pistons. Once loaded into the apparatus, the sample was pressurized to 100 MPa, temperature was ramped to 1100 °C in 1.5 h, and pressure was increased to 300 MPa. Upon reaching the P-T of the experiment, a load of ~10 MPa was applied to collapse sample porosity.

3.4 Analytical Methods

Inductively-coupled plasma optical emission spectrometry (ICP-OES) was used to analyse the trace element chemistry of 100 mg samples of dried silica gel (Table A4.1). Analyses were performed with a Thermo Scientific iCAP 6500 dual view ICP-OES housed in the Department of Earth Sciences at the University of Minnesota. Samples were diluted 40-

fold before analysis with the addition of a Cesium matrix modifier and Yttrium as an internal standard. Each analysis was repeated three times and the concentrations aggregated to improve error. USGS reference materials Icelandic Basalt (BIR-1) and Rhyolite Glass Mountain (RGM-1) were analysed as reference materials for the ICP-OES routine (Table A4.2). ICP-OES was also used to measure the full trace element chemistry of silica gel following acid treatment (Table A4.3).

Electron probe microanalysis (EPMA) was performed with the Cameca SX-100 electron microprobe at Rensselaer Polytechnic Institute, equipped with enlarged diffracting crystals (LPET) and LAB6 electron source. Ti K-α X-rays were collected for 400 s (on peak and on high/low background) from four spectrometers and aggregated. Si K-β was measured on the final spectrometer. Analysis of unknown samples was performed at 15 kV and 200 nA with a focused beam. Standardization for Ti was performed on rutile at low current (15 nA) to prevent peak shifts in the pulse-height analyser (PHA) that are problematic at high count rates. Calculated detection limits for Ti following this routine were ~ 7 μg g^{-1}. Analysis of QTiP high-Ti single crystals (synthesized by J. Thomas) and Herkimer quartz were used as reference materials. Analysis of reference materials demonstrated a relative error of ~20% at low concentrations (<100 μg g^{-1}) and ~10-15% at high concentrations (>100 μg g^{-1}) (Table A4.2).

Attempts to measure trace level Ti contents of samples using the conventional electron microprobe JEOL 8900 at UMN were unsuccessful as determined from analysis of

reference materials (see Appendix 5.4 for analytical procedure). Despite outputted instrumental detection limits of ~20 μg g^{-1}, measurement of reference materials gave an overall reproducibility of ~50-100% at low concentrations (<100 μg g^{-1}) and ~30% reproducibility at high concentrations (>100 μg g^{-1}) (Table A4.4). Concentrations varied by >100 μg g^{-1} between spectrometers and measurements from adjacent analysis locations were not reproduced. For this reason, all EPMA measurements used to characterize silica gel reference materials were collected using the electron probe at RPI.

Secondary Ion Mass Spectrometry (SIMS) was applied using the Cameca IMS-1280 at the Northeast National Ion Microprobe Facility (NENIMF) at Woods Hole Oceanographic Institute (WHOI). SIMS was used to analyse the Ti concentration of polished grain mounts of doped silica gel. The analytical routine outlined in Nachlas et al. (2014) was followed and involved a pre-sputter to clean the surface of contamination before the beam was focused into the inset crater. Analysis of the QTiP high Ti quartz crystals as reference materials reveals concentrations that are ~3-10% lower than expected values at high concentrations (>100 μg g^{-1}) and ~20% higher than expected at low concentration (20 μg g^{-1}) (Table A4.6).

Laser-Ablation Inductively-Coupled Plasma Mass Spectrometry (LA-ICP-MS) was applied using a Bruker 820-MS quadrupole mass spectrometer with a Photon Machines Analyte 193 ultra-short pulse excimer laser housed at Rensselaer Polytechnic Institute. LA-ICP-MS was used to measure Ti contents of hot-pressed aggregates of doped silica. Silica

was ablated using an 80 μm^2 laser spot with a 9 J/cm^2 energy pulsed at 6 Hz for ~30 s. Analyses of NIST 610 and 612 as reference materials resulted in measurements that were ~3-5% lower than reference values at high concentrations (452 $\mu g\ g^{-1}$) and ~12-15% lower than reference values at low concentrations (44 $\mu g\ g^{-1}$) (Table A4.7).

Inductively-coupled plasma mass spectrometry (ICP-MS) was used to analyse 10 mL aliquots of the doping solvent medium to evaluate stability of the Ti standard solution at different pH conditions. Analyses were performed with a Thermo Scientific XSERIES 2 ICP-MS housed in the Department of Earth Sciences at the University of Minnesota equipped with ESI PC3 Peltier cooled spray chamber, SC-FAST injection loop, and SC-4 autosampler. Samples were diluted appropriately and 20 ng g^{-1} of Yttrium internal standard was added. All elements were analysed using He/H2 collision-reaction mode. Each sample was analysed three consecutive times and the concentrations averaged to improve error.

Secondary electron imaging (SEI) and cathodoluminescence analysis (CL) was performed using the JEOL-6700 Scanning Electron Microscope equipped with a Gatan Mono-CL detector at the University of Minnesota College of Science and Engineering Characterization Facility. Instrumental conditions for SEI analysis were 5.0-10.0 kV accelerating voltage and ~30 pA beam current. Effort was made to minimize the working distance to enhance spatial resolution. All samples analysed with SEI were coated with 50 Å Pt prior to analysis. Cathodoluminescence analysis was performed on grain mounts of

doped silica gel that were coated with 50 Å C prior to analysis. CL analysis was conducted at 15 kV accelerating voltage, ~20 nA beam current, and 12.5 mm working distance.

X-ray diffraction spectra were collected with a Rigaku MiniFlex X-ray Diffractometer at the University of Minnesota. Analytical conditions used included a Cu K-α radiation source, scan rate of 0.5 °/min, scan range of 10-70 °, and sampling width of 0.02 °, which resulted in a 2 h analysis. A linear background correction was applied to the data, and the data was smoothed to reduce noise.

3.6 Results and Discussion

The experimental protocols presented here for cleaning, drying, and doping nanoporous silica gel enables fabrication of silica glasses with trace-level precision. This technique was used to fabricate multi-layered reference materials composed of layers doped with specific Ti concentrations. Multiple analytical techniques characterized by different mass- and spatial-resolution scales were applied to evaluate the utility of this material as a reference material for analyzing trace levels of Ti in quartz.

Silica gel was first acid-treated to leach many of the initial impurities and vacate the silanol groups prior to doping. Fluxing silica gel in 6 M HCl for increasing durations of time (3, 6, 9, 72, 168 h) is effective at removing most of the initial impurity content (Table 3.1, Table A4.1). Calcination of silica gel to high temperature disturbs pores on the silica gel surface (Figure A3.1) and contaminates silica gel from alumina and Y-zirconia crucibles

for small sample sizes (0.1 g silica gel) but not large sample sizes (1.0 g silica gel) (see Table A4.1). Long duration acid-treatments can also result in contamination of silica gel from abrasion and subsequent dissolution of the Teflon-coated magnetic stir-bar (Table A4.1). Mass-loss upon calcination measurements on silica gel heated at a range of temperature-time intervals show that hydrated silica gel contains c. 10 wt% evacuatable water (Figure A3.2). XRD analysis of doped silica gel subjected to heat-treatment over a range of temperature and time conditions reveals an absence of crystalline phases following calcination at all conditions (Figure A3.3).

Activated silica gel was suspended in a nonpolar doping solvent prior to addition of the dopant. Four different alkane solutions with increasing molecular chain length – ethanol (C_2H_6O), heptane (C_7H_{16}), hexadecane ($C_{16}H_{34}$), and squalane ($C_{30}H_{62}$) – were tested as doping solvents to investigate interactions between the solvent and the silica gel nanopores. Doping experiments conducted with longer chain alkanes as the doping medium were less effective (i.e., lower recovery of the dopant) than experiments conducted with shorter chain alkanes (Figure A3.4, Table A4.1). The diminished recovery exhibited in experiments conducted using solvents with molecular lengths similar to the diameter of silica gel pores suggests that large molecules can obstruct pores and inhibit recovery of the dopant. This is consistent with studies that measured rheology of liquids in mesoporous silica and found that larger molecules are slower to imbibe (Huber et al. 2007; Gruener et al. 2009). To maximize doping efficiency, all doping experiments were conducted using ethanol, a short-

sample name	Dopant concentration (µg g-1)	recovered Ti concentration (µg g-1)	**% recovery**	ICP-OES sample ID
Target 30	30	40	**133**	SG-25
Target 60	60	72	**120**	SG-26
Target 85	85	99	**116**	SG-20
Target 90	90	106	**118**	SG-27
Target 147	147	145	**99**	SG-42
Target 347	347	327	**94**	SG-43
Target 300	300	294	**98**	SG-0.03
Target 3000	3000	2181	**69**	SG-0.11
Target 3000	3000	2255	**71**	SG-0.12
Target 3000	3000	2305	**72**	SG-5
Target 3000	3000	2288	**74**	SG-6
Target 3000	3000	2337	**73**	SG-10
Over-dope	3746	2288	**61**	SG-13
Double-dope	2254+746	2811	**94**	SG-14
BHQ Target 300	300	76	**25**	SG-24
BHQ Target 3000	3000	1800	**60**	SG-18

Table 3.2. Results of doping silica gel with different Ti concentrations.

chain, nonpolar, inexpensive, and relatively low-hazard material that is shown to result in the highest dopant recovery of the examined solvent solutions (Figure A3.4).

The pH of the doping solvent influences the silanization of the silica surface as well as the stability of the Ti-species in the plasma standard solution. High concentration (3000 µg g^{-1}) doping experiments produced Ti-precipitates at high (10) and low (7) pH, the morphology of which differed for different pH conditions (Figure A3.5). Doped batches of silica gel were inspected under reflected light to remove all foreign particles prior to analysis or further processing. Experiments conducted under different pH conditions

indicate that pH=8 provides the highest recovery for Ti in silica gel (Figure A3.2, Table A4.1).

The accuracy and precision of the doping technique is evaluated with multiple analytical techniques for quantitative and qualitative analysis. Bulk analysis of 100 mg of silica gel with ICP-OES is the first-order approach for evaluating doping accuracy and precision. Using the optimal pH (8) and doping solvent (ethanol) determined from preliminary experiments, the synthesis procedure is capable of doping at a trace-level concentration within 10 μg g^{-1} of a targeted concentration to create a population of doped grains. Doping recovery decreases with higher target concentration (Table 3.2). Results of doping experiments at concentrations spanning 30-3000 μg g^{-1} were used to generate a linear regression for expected doping efficiency at any particular target concentration (Figure A3.6). This regression takes the form

$$X_T = \frac{X_G}{0.6764} - 168.4$$

where X_T is the target doping concentration (in μg g^{-1} Ti) and X_G is the anticipated concentration of silica gel (in μg g^{-1} Ti).

The effectiveness of nanoporous silica gel as a doping substrate was evaluated by conducting a control experiment following the same procedure except using crystalline

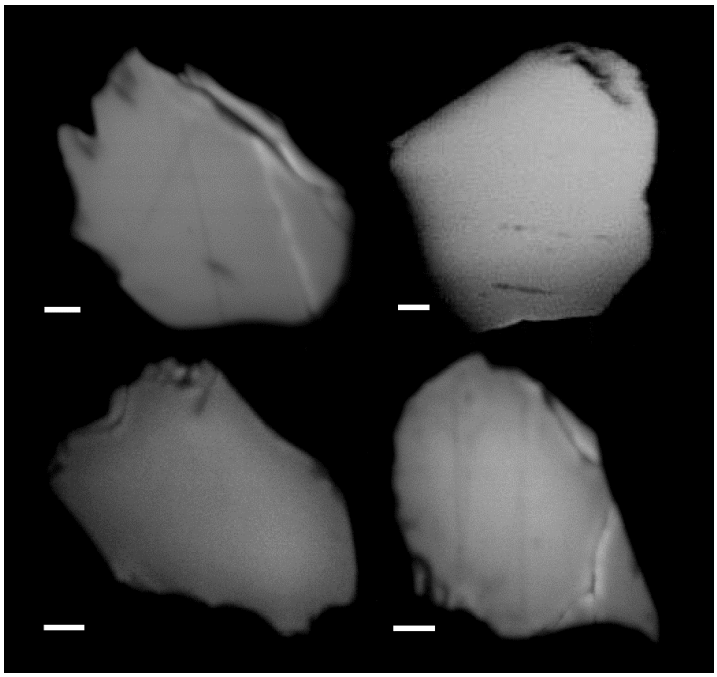

Figure 3.3. CL images of silica gel particles doped with 300 μg g^{-1} Ti. SIMS analysis of grains from this sample show Ti concentrations consistent with ICP-OES analysis of 100 mg of doped gels (see Figure A3.7, Table A4.1). Scale bar is 10 μm.

quartz as the doping substrate instead of silica gel. Pure quartz separates from Black Hills Quartzite (BHQ) are commonly used as a starting material for experimental rock mechanics (e.g., Tullis et al. (1973); Hirth & Tullis (1992); Goncalves et al. (2015)). BHQ was tested in our study as a doping substrate for comparison with silica gel. BHQ (20-50 μm grain size) was activated in HCl and doped with 300 and 3000 μg g^{-1} Ti following the same routine used for silica gel. Doping recovery using BHQ is substantially lower than silica gel (Table 3.2, Table A4.1), highlighting the importance of silica gel nanoporosity and/or surface silanization for optimizing doping recovery.

Efficiency of the doping technique was evaluated at the grain scale using qualitative CL analysis and quantitative SIMS analysis. CL analysis of mounted and polished doped silica gel grains reveals a uniform CL distribution (Figure 3.3) in 84% of grains (n=92). SIMS was used to quantify the Ti concentrations from grain mounts of silica gel doped with 300 μg g^{-1} (Figure A3.7). SIMS measurements of Ti concentration from calcined amorphous silica are similar to bulk measurements from ICP-OES (Table A4.1).

Multi-layered reference materials were fabricated with layers of doped silica gel and used to test analytical confidence at multiple, selected concentrations. Layered aggregates of silica gel doped at different concentrations were hot-pressed for short duration to compact and densify (without crystallizing) the silica aggregates. Crystallization of quartz during hot-pressing should be avoided because the Ti content of the growing quartz would be governed by the solubility at the P-T of the experiment instead of the desired dopant concentration in silica gel (Wark & Watson 2006). Secondary electron images of hot-pressed silica gel aggregates reveal numerous spherical vesicles (Figure A3.8).

A three-layered aggregate (113, 802, 2181 μg g^{-1}) of doped silica gel was sampled with 277 EPMA measurements collected along linear transects across the aggregate layering (Table A4.8). A histogram shows the distribution of EPMA measurements compared to ICP-OES bulk measurements (Figure 3.4). The mean and standard error of Ti

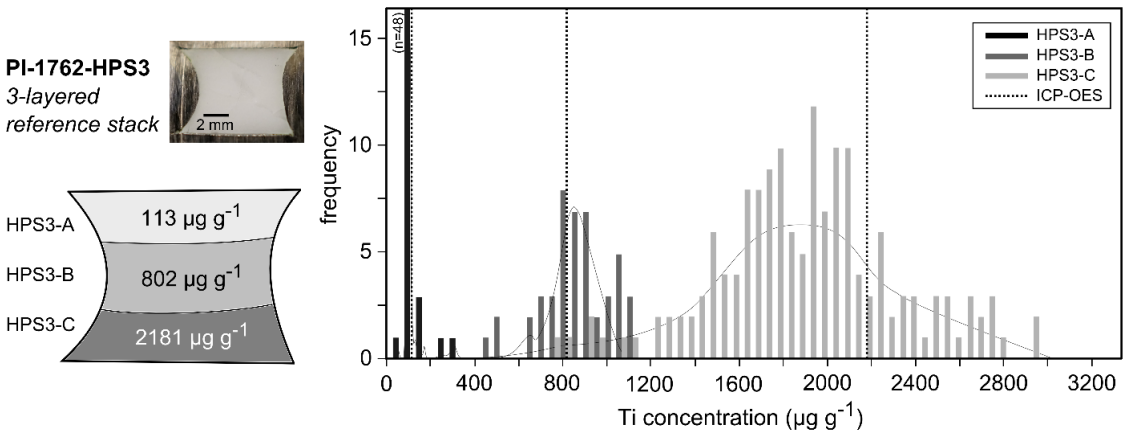

Figure 3.4. Analysis of 3-layered reference material with ICP-OES and EPMA. See Table A4.8 for complete dataset.

concentrations measured with EPMA from the 113-layer is 78 ± 5 µg g^{-1} (n=58), from the 802-layer is 828 ± 23 µg g^{-1} (n=46), and from the 2181-layer is 1914 ± 35 µg g^{-1} (n=160).

A seven-layered aggregate was prepared as a reference material containing six layers of doped silica gel (89, 113, 120, 234, 416, and 2181 µg g^{-1}; as measured with ICP-OES) and one layer of crushed Herkimer quartz (5 ng g^{-1}; as measured by Kidder et al. (2013)). This seven-layered aggregate was analysed with both EPMA and LA-ICP-MS for comparison with ICP-OES bulk measurements on the samples used to fabricate the aggregate. Measurements from these three analytical techniques show general agreement in all layers of the aggregate (Figure 3.5, Table A4.9, Table A4.10). As measured with EPMA, the mean and standard error of Ti concentrations from the 89-layer is 111 ± 9 µg g^{-1}, from the 113-

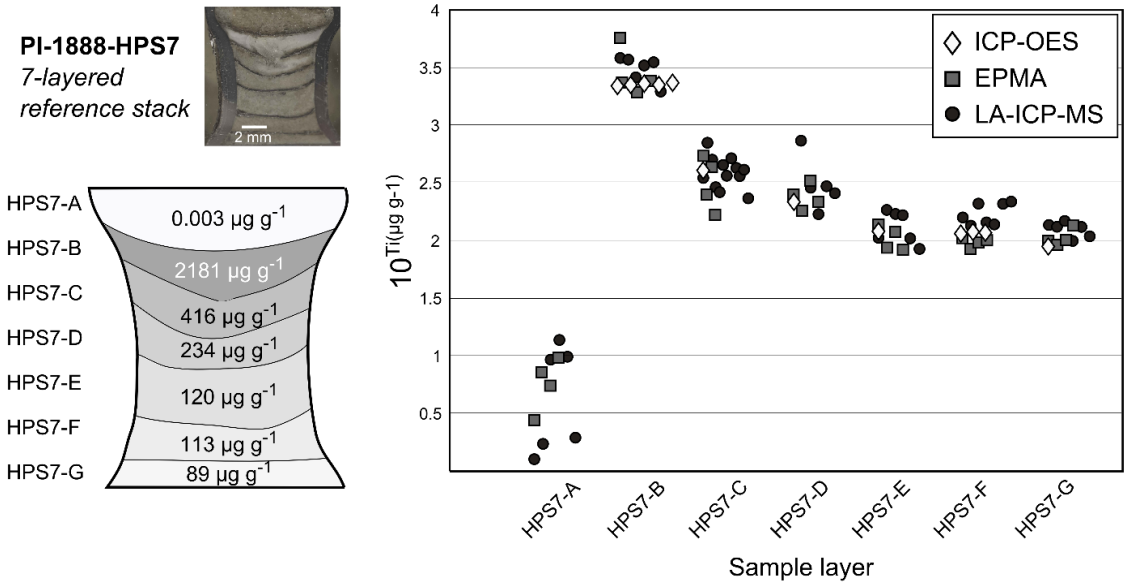

Figure 3.5. Analysis of 7-layered reference material with ICP-OES, EPMA, and LA-ICP-MS. See Tables A4.9 and A4.10 for complete datasets.

layer is 96 ± 4 µg g^{-1}, from the 120-layer is 108 ± 13 µg g^{-1}, from the 234-layer is 236 ± 27 µg g^{-1}, from the 416-layer is 365 ± 89 µg g^{-1}, from the 2181-layer is 3086 ± 891 µg g^{-1}, and from the 0.005-layer is 6 ± 1 µg g^{-1}. As measured with LA-ICP-MS, the mean of the Ti concentrations from the 89-layer is 130 ± 8 µg g^{-1}, from the 113-layer is 172 ± 14 µg g^{-1}, from the 120-layer is 138 ± 17 µg g^{-1}, from the 234-layer is 335 ± 85 µg g^{-1}, from the 416-layer is 423 ± 39 µg g^{-1}, from the 2181-layer is 3200 ± 302 µg g^{-1}, and from the 0.005-layer is 6 ± 2 µg g^{-1}. A source of error potentially-accountable for elevated Ti concentrations is cross-contamination between layers during polishing.

3.7 Conclusions

Careful preparation and doping of nanoporous silica gel is capable of fabricating trace element reference glasses containing a precise concentration of a specified element. This material is found to be homogeneous from the intragrain, intergrain, and grain population scale and can be used as a reference material for bulk analysis and microanalysis with electron, laser, and ion-beam techniques.

This study used a gas-medium apparatus to hot-press aggregates of doped silica gel to form dense glasses. An equally valid approach would be to melt and quench doped silica gel in high-temperature crucibles to form glass disks, a practice commonly-employed for synthesizing glass reference materials (e.g., Jochum et al. (2000)). However, owing to the sensitivity of silica gel geochemistry to contamination from the crucible material (Table A4.1), caution is warranted when treating silica gel at high-T.

The aim of this research is to introduce a cost-effective and relatively-straightforward approach for fabricating trace element doped glasses, and to provide a preliminary evaluation for their use as microanalytical reference materials. This approach complements existing techniques for synthesizing reference glasses (e.g., the MPI-DING glasses of Jochum et al. (2000)) by allowing selection of an individual species of interest. Because the dopant source (plasma standard solution) is available for many different elements, this

approach here may be useful for synthesizing in-house reference materials doped with a variety of elements at the trace concentration level.

Acknowledgements:

This research was supported by the National Science Foundation through grant EAR-0911497 awarded to D.L. Whitney and C. Teyssier at UMN. Discussions following presentation of an early version of this work at the Microanalysis Society topical conference on Microanalytical Reference Materials benefitted the direction of this research. The author acknowledges R. Knurr for assistance with wet chemistry procedures and analysis of samples with ICP-OES and ICP-MS; M. Zimmerman, M. Pec, and M. Tasaka in the Kohlstedt Rock and Mineral Physics Lab for assistance in running hot-press experiments; J. Singer for assistance with EPMA and LA-ICP-MS analysis at RPI; N. Seaton for assistance with SEM analysis at UMN; and T. Hiraga for advice on silica sources in the early stages of this research. Thanks to A. Handt for insightful discussions on microanalysis, and to D.L. Whitney and D.L. Kohlstedt for comments that improved the quality of this manuscript.

CHAPTER 4

Experimental constraints on the role of dynamic recrystallization on resetting the Ti-in-quartz thermobarometer

This chapter has been published in *Journal of Geophysical Research: Solid Earth* with co-author Greg Hirth and is included in this thesis with permission from the American Geophysical Union.

Synthesis

We conducted deformation experiments on Ti-doped quartz aggregates to investigate the effect of crystal-plastic deformation and dynamic recrystallization on Ti substitution in quartz. Shear experiments were conducted at 1.0 GPa and 900 °C at a constant shear strain rate (~$5x10^{-6}$ s^{-1}) for progressively longer intervals of time (24, 48, 72 h). Equivalent experiments were conducted under hydrostatic stress to compare the effect of deformation relative to static crystallization. A novel quartz doping technique is used to synthesize a quartz aggregate consisting of two layers with Ti concentrations above and below the predicted solubility level for the experimental conditions. Samples deformed to progressively higher shear strain by dislocation creep accommodated by a combination of subgrain rotation (SGR) and grain boundary migration (GBM) recrystallization show a strengthening of the crystallographic preferred orientation that correlates with a progressive evolution of Ti concentrations. Quartz grains in the highest strain, most strongly-recrystallized samples have Ti concentrations that are most similar to undeformed quartz grown in hydrostatic annealing experiments. Cathodoluminescence (CL) analysis of intragrain variations in Ti content reveals core and rim zoning present in the starting material that becomes progressively homogenized with increasing strain – recrystallized quartz in the highest strain samples exhibits a uniform CL signal. We conclude that dynamic recrystallization enhances the kinetics of trace element equilibration in quartz, illustrating that Ti-in-quartz thermobarometry is capable of recording the conditions of ductile shearing.

4.1 Introduction

Quartz incorporates trace concentrations of a wide array of elemental impurities (e.g., Dennen, [1964]. At present, only the P-T dependence of the substitution of Ti in quartz has been calibrated. The solubility of trace amounts of Ti in quartz has been determined experimentally, from analysis of quartz grown in the presence of rutile [Ostapenko et al., 1987, 2007; Wark and Watson, 2006; Thomas et al., 2010, 2015; Huang and Audétat, 2012]. These studies reveal a correlation between Ti content and temperature (T) and pressure (P) of crystallization. This relationship establishes the foundation for TitaniQ, the Ti-in-quartz solubility calibration for the T-dependence of Ti substitution proposed by Wark and Watson [2006] and later revised with a P-dependence by Thomas et al. [2010]. Thomas et al. [2015] demonstrate the reproducibility of this technique by statically recrystallizing quartz at different P-T conditions and obtaining the predicted Ti solubilities.

A Ti-in-quartz thermobarometer that is responsive to deformation would be a powerful tool to record tectonic events. Quartz is nearly ubiquitous in crustal rocks, and the occurrence of deformed quartzites in orogens worldwide attests to their importance in accommodating strain during orogenesis. However, it is unclear how, or if, dynamic recrystallization modifies Ti contents in quartz during deformation. TitaniQ was calibrated based on the results of hydrostatic experiments, yet quartz in the crust commonly crystallizes (and recrystallizes) during deformation. Moreover, the proposed importance of crystal growth rate [Huang and Audétat, 2012] introduces a parameter that is difficult to evaluate in natural

rocks, where grain boundary migration rates vary in response to local gradients in grain size, dislocation density, and temperature. The effect of dislocation creep on Ti substitution in quartz is not established and it remains unclear if the Ti content of deformed quartz preserves a meaningful record of the conditions of recrystallization.

Several investigations have analyzed Ti contents of quartz in mylonites or tectonites to test the applicability of quartz thermobarometry to reconstruct the conditions of crustal deformation. Results of these studies do not reach a consensus. For example, some investigators have challenged the applicability of the Ti-in-quartz technique because results do not agree with conventional thermobarometers (e.g., Fe-Mg garnet-biotite, Al-in-hornblende) in the same rocks or nearby rocks, or because results of Ti-in-quartz do not agree with temperatures inferred from quartz slip systems. However, quartz is known to deform at lower-grade conditions than the closure temperature estimated for relevant metamorphic exchange reactions, and if Ti substitution in quartz is sensitive to deformation, then it is conceivable that Ti-in-quartz could record later stages of a deformation event while conventional thermobarometry yields earlier, higher grade conditions. Similarly, because of the sensitivity of quartz slip systems to variables that cannot be determined by the Ti-in-quartz technique (e.g., strain rate, stress, water content), the temperatures estimated from these techniques might not always be in agreement. Indeed, while the high precision of the Ti-in-quartz thermobarometer (c. 10 °C or 100 MPa) provides a unique opportunity to interpret the P-T conditions of ductile deformation, evaluation of the accuracy of this technique from results on naturally deformed rocks needs

to be analyzed in the context of experimental constraints on the effect of deformation on the Ti-in-quartz thermobarometer.

Here we describe results from deformation experiments which indicate that dynamic recrystallization resets Ti concentrations in quartz to the equilibrium solubility for the conditions of deformation. These results differ from earlier work; Negrini et al. [2014] deformed single crystals of low-Ti quartz surrounded by rutile powder to investigate re-equilibration of Ti in quartz during dynamic recrystallization. Their measurements do not detect any increase in Ti concentrations in quartz grains that recrystallized during deformation or annealing, which led them to conclude that dynamic recrystallization does not affect Ti substitution in quartz. In contrast, we deformed layered aggregates of Ti-saturated and Ti-undersaturated quartz under isothermal and isobaric conditions at constant strain rate for increasing intervals of time. Titanium concentrations from deformed quartz are compared with measurements from hydrostatically-annealed quartz to investigate the effect of dynamic recrystallization relative to static grain growth. Characterization of experimental run products focuses on (1) analyzing deformation microstructures, (2) quantifying Ti concentration in a large population of deformed quartz grains, (3) mapping intragrain variations in Ti distribution from patterns of cathodoluminescence (CL) intensity, and (4) characterizing the extent of dynamic recrystallization from electron back-scattered diffraction (EBSD) analysis of quartz fabrics.

4.2 Experimental Methods

Experiments were designed to deform layered aggregates of Ti-doped quartz at constant pressure, temperature, and strain rate (P-T-ε̇) for three incrementally longer time/strain intervals. By holding temperature and pressure constant, a fixed Ti solubility is predicted (310 ppm for our experimental conditions using the calibration of Thomas et al. [2010]) and the influence of deformation on Ti substitution in quartz can be isolated. The sample aggregates consist of two quartz layers: a doped layer with a Ti concentration (2280 ppm) higher than the predicted solubility level for the conditions of the experiments, and an undoped layer that was leached of Ti to synthesize a Ti concentration (110 ppm) below the predicted solubility (Figure 4.1, Table 4.1). This geometry was designed to create a scenario in which crystallization of quartz is buffered with a_{TiO2} (titania activity) = 1 in the doped layer and $a_{TiO2} < 1$ in the undoped layer. In this way, we aim to investigate the role of deformation on equilibrating Ti concentrations in quartz during both prograde (increasing Ti concentration) and retrograde (decreasing Ti concentration) solubility paths.

4.2.1 Starting Material

We fabricated samples using silica gel (a form of high-purity amorphous silica) that exhibit the following qualities: (1) plastic flow strength and deformation textures similar to those observed for experiments conducted on natural quartz, (2) a concentration of trace elements similar to that found in natural quartz, and (3) an ability to be doped with sufficiently high

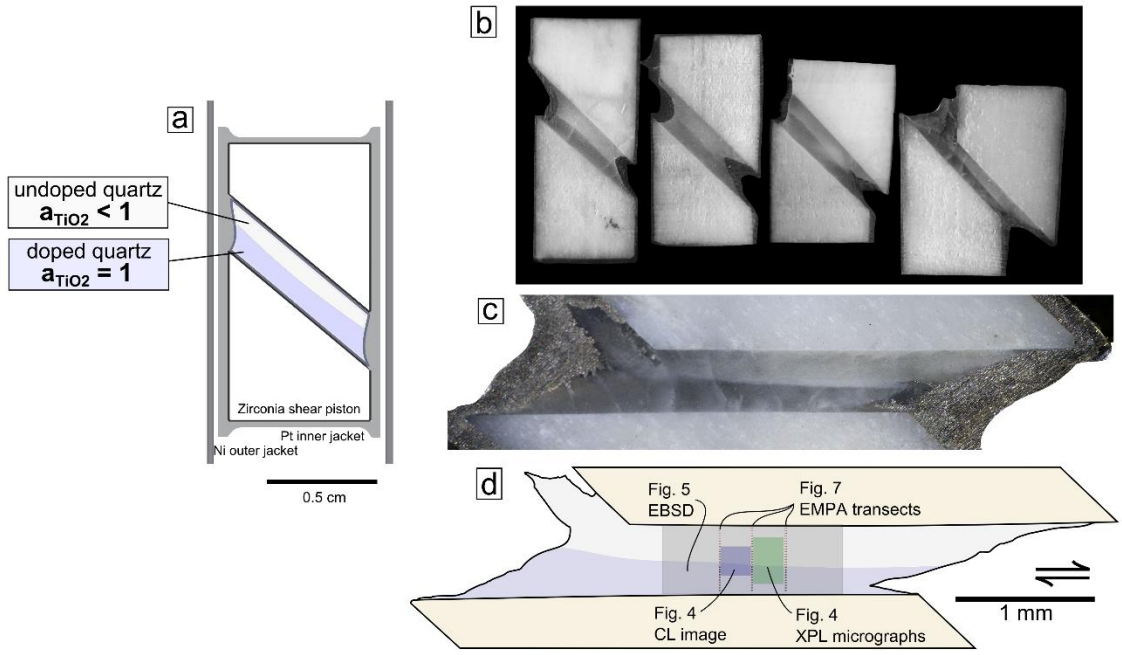

Figure 4.1. Experiments were designed to deform a layered aggregate containing quartz layers doped at different Ti concentrations. (A) A shear assembly consisting of doped (a_{TiO2} = 1) and undoped (a_{TiO2} < 1) quartz was used to deform aggregates to high shear strain. (B) Photographs of samples cut in half show the range of shear strains from a full suite of experiments. (C) A layer of undoped quartz is visible overlying a layer of doped quartz that appears blue under direct sunlight. (D) A series of analytical measurements were made on each sample to systematically investigate the effect of dynamic recrystallization on Ti substitution in quartz.

precision at a selected concentration to create a population of quartz grains that are both individually and collectively homogeneous with respect to Ti.

(1) Silica gel has previously been used as a starting material to synthesize quartz aggregates for rock deformation experiments [Paterson and Luan, 1990; Luan and Paterson, 1992]. Silica gel-derived aggregates deformed in a gas-medium apparatus exhibited flow stresses and recrystallization microstructures similar to

experiments conducted at similar conditions using natural quartz starting material (e.g., Hirth and Tullis [1992]; Heilbronner and Tullis [2006]). Deformation experiments on silica gel show that water equilibration is more readily attained than for synthetic quartz aggregates made of natural quartz powders [Luan and Paterson, 1992].

(2) Silica gel can be synthesized with a high purity trace element content. Silica gel "as-received" contains trace element abundances similar to that of a pure quartz separate derived from Black Hills Quartzite (BHQ) (Table 4.1), a commonly-used starting material for deformation studies on quartz aggregates (e.g., Tullis et al. [1973]; Hirth and Tullis [1992]; Stipp and Tullis [2003]; Heilbronner and Tullis [2006]; Gonçalves et al. [2015]). Acid-leaching is applied to clean the silica gel of the majority of its impurity content prior to doping [Nachlas, 2015]. Following acid-rinsing, silica gel possesses a considerably lower impurity content than BHQ treated the same way (Table 4.1).

(3) Silica gel is widely utilized as a desiccant owing to its dense network of nano-pores that drives capillary uptake of moisture. The high absorptive capacity of nano-pores in silica gel [Hench and Vasconcelos, 1990; Huber et al., 2007] combined with the high adsorptive capacity of dense arrays of silanol groups on the silica gel surface [Nawrocki et al., 1989; Nawrocki, 1997; Zhuravlev, 2000] make this material an ideal quartz-doping substrate. We formulated a technique for

doping silica gel with precise amounts of Ti (within 10 ppm of a target concentration that is less than 1000 ppm) that enables synthesis of a large population of grains with uniform Ti distribution [Nachlas, 2015].

Silica gel is used to create a layered aggregate (Figure 4.1): a lower layer doped at a Ti concentration higher than the predicted equilibrium solubility for the P-T conditions of the experiment and an upper layer that was cleaned in concentrated acid and contains a Ti concentration below the predicted Ti solubility (hereafter called "undoped"). A pre-experimental drying routine was followed to ensure a baseline water content in silica gel for all experiments: silica gel is first immersed in double deionized water (DIW), dried in

	Al	Ba	Ca	Fe	K	Mg	Mn	Na	P	Sr	Ti	Zr
silica gel	223	16	533	214	36	167	b.d.l.	786	12	8	142	65
(as received)												
undoped silica gel	61	3	193	201	b.d.l.	95	b.d.l.	52	10	4	110	63
(acid rinsed)												
doped silica gel	142	3	250	229	b.d.l.	87	b.d.l.	49	10	4	2282	66
(acid rinsed, Ti-doped)											±14	
											(n=13)	
BHQ	728	9	849	912	184	250	15	62	102	8	141	9
(as received)												
BHQ	457	9	620	588	38	219	13	48	15	6	47	3
(acid rinsed)												

Table 4.1. Chemical composition of starting materials. Bulk measurements reveal the composition of silica gel starting materials used to synthesize the Ti-doped and Ti-undoped layers of the quartzite aggregate and the composition of pure quartz separate from Black Hills Quartzite (BHQ) for comparison with other quartz starting materials commonly used for deformation experiments. Results of ICP-OES analysis of 100 μg samples. All values in ppm

a conventional furnace at 100 °C for 72 h, then calcined in a Y-stabilized zirconia crucible at 825 °C for 1 h [Luan and Paterson, 1992] before loading into the capsule. Mass loss-upon-calcination measurements following the drying routine indicate that silica gel at the start of the experiments contains no porosity-bound H_2O. Luan and Paterson [1992] show that hot-pressed silica gel aggregates prepared following this same drying routine contain ~8000-10000 H/10^6Si. In one suite of experiments we added 1 μL of deionized H_2O (~0.6 wt%) between the two layers immediately before sealing the capsule.

4.2.2 Experimental Procedure

Deformation experiments were conducted at Brown University using a Griggs rig solid-medium deformation apparatus [Griggs, 1967; Tullis and Tullis, 1986]. Experiments were performed using a shear assembly at 900 °C with a confining pressure of 1.0 GPa and a constant axial strain rate of 10^{-6} s^{-1} for 1-4 days, both with and without the addition of water. Hydrostatic experiments were conducted for identical durations for comparison with deformed equivalents. At the conditions of our experiments, quartz is in the β-quartz stability field; experimental studies of Thomas et al. [2010] span the α-β transition and show no inflection in Ti-in-quartz isopleths, indicating that this polymorphic phase transition does not influence Ti substitution in quartz.

The layered sample aggregate is placed between two cylindrical pistons of zirconia that are cut and polished in a 45 ° shear assembly (Figure 4.1). The shear assembly is pressed into an inner jacket of Pt that is mechanically sealed with Pt end disks and inserted into an outer

jacket of Ni. Pure NaCl is used as a confining medium to provide a uniform confining stress during long duration experiments [Holyoke and Kronenberg, 2010]. Heat is applied via a graphite resistance furnace and monitored with an S-type thermocouple (Pt_{100} – $Pt_{90}Rh_{10}$) positioned directly outside of the jacketed sample. The distance between the thermocouple tip and the surface of the sample jacket was measured to be 240 μm using X-ray tomography (XRCT) to scan through the outer salt prior to dissection of the assembly (Figure 4.2C, D, Movie 4.S1).

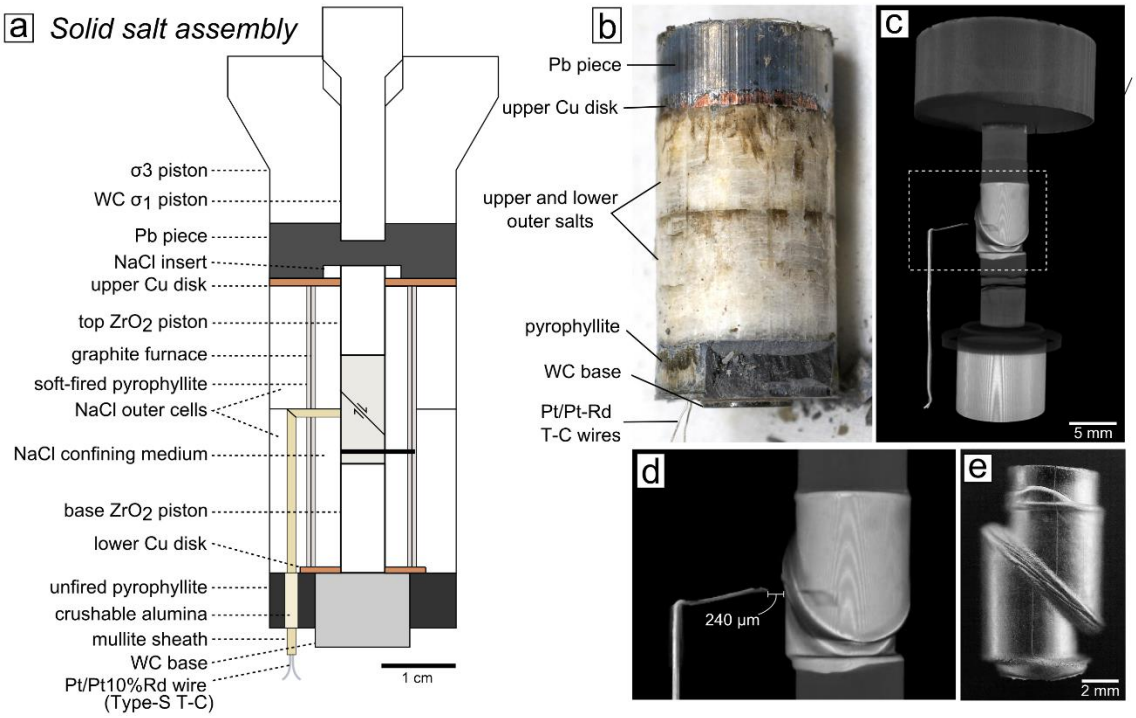

Figure 4.2. Illustration, photographs, and X-ray Computed Tomography (XRCT) images of a deformed solid-salt assembly following a high strain experiment. (A) Schematic cross-section showing components of the solid salt assembly used in all experiments. (B) Photograph of high strain sample prior to extraction from confining medium. (C) XRCT image of high strain sample prior to extraction from confining medium. (D) XRCT image showing the distance between the thermocouple and jacketed sample surface. (E) Photograph of high strain sample showing shear offset across a displaced fiducial mark.

The sample is brought to 900 °C and 1.0 GPa over a 4 h period. Heating is alternated with increases in confining pressure applied with a hydraulic pump following procedures outlined in Kronenberg and Tullis [1984], Post and Tullis [1998], and Chernak and Hirth [2011], a routine that has been documented to enable the retention of water in mechanically-sealed assemblies. Once the assembly reaches the desired P-T conditions, the apparatus is held for a 15 h annealing period to promote complete crystallization of the silica gel prior to deformation.

Following the annealing period, a rotary motor is used to apply uniaxial compression by driving a WC-σ_1 piston with an axial strain rate of 1.5×10^{-5} s^{-1} into the salt confining medium until contact with the sample assembly is made, as indicated by a hit-point inflection on the force record. After the hit-point, the motor is switched to 1.5×10^{-6} s^{-1}, producing a shear strain rate on the sample of $\sim 5 \times 10^{-6}$ s^{-1}, and is run for 24, 48, or 72 h to conduct the deformation experiment, resulting in a suite of low strain, intermediate strain, and high strain samples. Hydrostatic experiments were run following the same procedure, except that upon reaching the hit-point, the motor is turned off and the sample is held at the experimental conditions for the same duration.

At the end of the experiment, the sample is quenched rapidly to 300 °C, then held at low temperature while the pressure is slowly decreased. After extraction from the rig, the deformed assembly is cut parallel to the compression direction for the preparation of doubly-polished, ultra-thin (20 μm) thin sections for petrographic analysis. Upon initial

cutting of the sample and observation under direct sunlight, the doped quartz layer is visibly blue in color – potentially indicative of quartz with a high Ti content [Seifert et al., 2011].

4.3 Analytical Methods

We apply a systematic analysis routine to each sample using multiple techniques to investigate the behavior of Ti in quartz during our experiments (Figure 4.1D).

Quantitative analysis of Ti concentration in quartz was performed using the Cameca SX-100 electron microprobe at Rensselaer Polytechnic Institute, optimized for trace element analysis with large diffracting crystals to improve collection statistics. We followed an analysis routine similar to that outlined in Spear and Wark [2009] and Thomas et al. [2010], involving standardization on rutile and quartz and the use of the QTiP series of single crystals (synthesized by J. Thomas) as reference materials. Conditions for analysis were 15 kV accelerating voltage and 200 nA beam current with a focused beam and counting times of 400 s (on peak and high/low background). Herkimer quartz, measured using SIMS to contain 4-5 ± 2 ppb [Kidder et al., 2013], is used as a Ti-blank to evaluate background signal on each spectrometer [Kohn and Northup, 2009; Donovan et al., 2011]. Our routine yielded a calculated detection limit of 7 ppm, standard error of 8 ppm, and a reproducibility of 6-18 ppm on analysis of reference materials. Analyses made years apart reproduced measurements on reference materials and populations of measurements from unknowns (i.e., our samples).

We collected Ti in quartz measurements from three parallel transects of 50 analysis spots with equidistant spacing oriented normal to the layers of the aggregate (Figure 4.1D). Populations of measurements from doped and undoped layers form Gaussian distributions of Ti concentrations. Outliers were designated as analyses that are >2σ from the mean of the population of all doped or undoped measurements, respectively. Of the 150 total measurements collected from each sample, ~10% were discarded owing to contamination (Table 4.2, Table A7.1). Sources of analytical contamination include intersection with or within close proximity of accessory phases (e.g., rutile) or voids along grain boundaries. Analysis of the surface of a faceted single crystal of quartz (Figure A6.1) yielded Ti concentrations that are identical to the mean of the population of measurements collected from thin section analysis of the same sample.

Bulk chemical analysis of the silica gel starting materials was performed using a Thermo Scientific iCAP 6500 Inductively-Coupled Plasma Optical Emission Spectroscopy (ICP-OES) instrument in the UMN Department of Earth Sciences. An analytical uncertainty of 2% for Ti measurements with ICP-OES was determined from analysis of USGS geochemical reference materials BIR-1 and RGM-1 (Table A7.1).

Cathodoluminescence analysis (CL) was used to reveal the spatial distribution of Ti in quartz. CL measurements were collected using the JEOL-6700F scanning electron microscope with field emission source (FEG-SEM) equipped with a Gatan Mono-CL detector in the College of Science and Engineering Characterization Facility at the

University of Minnesota (UMN). A full-spectrum CL analysis collected from a Ti-doped quartz crystal shows a broad peak in the blue range (~420 nm) (Figure A6.2). We use patterns of CL intensity as a qualitative proxy for Ti content in quartz grown and recrystallized in our experiments.

Electron back-scattered diffraction (EBSD) was performed using the Oxford/HKL Technology Nordlys detector on the UMN FEG-SEM. EBSD analysis focused on large-scale mapping of recrystallized quartz fabrics. A step size was selected to intersect one point per grain (5-10 μm step size) and maps were collected from the central third of the sample layer to characterize the bulk recrystallization fabrics from each experiment (Figure 4.1D).

X-ray tomography images of a deformed sample assembly were collected using the North Star Imaging X5000 high resolution micro-CT X-ray Computed Tomography (XRCT) instrument in the UMN Department of Earth Sciences. XRCT was used to measure the distance from the thermocouple to the jacketed sample surface prior to dissection of the sample assembly.

4.4 Results

Two suites of experiments were conducted with and without the addition of water; for each suite we ran a 24-h hydrostatic experiment and 24-, 48-, and 72-h deformation experiments (Figure 4.1B). Stress versus time/shear strain curves for the deformation experiments show

strain hardening over the first day of the experiment followed by achievement of nominally steady state flow at a differential stress of ~120-150 MPa (Figure 4.3). Similar flow stresses have been documented for axial compression experiments on quartz aggregates derived from silica gel starting materials [Luan and Paterson, 1992], and general shear experiments conducted on quartzite at the same conditions [Heilbronner and Tullis, 2006].

4.4.1 Quartz in Hydrostatic Experiments

Experiments conducted under hydrostatic stress serve as a control to isolate any effects of deformation and stress state on Ti substitution in quartz. Quartz in hydrostatically-annealed samples exhibit a relatively uniform grain size (~20-40 μm) composed of equant crystals that are devoid of internal deformation features (Figures 4.4A and 4.6A). EBSD analysis of the hydrostatically-annealed samples shows a random distribution of crystallographic axes (Figure 4.5A). Porosity (ranging from <1 to 2 vol%) is evident in both the water-added and no-water-added hydrostatic experiments as void-spaces at three- and four-grain junctions (Figures 4.4A and 4.6A).

Quartz grains in hydrostatic experiments contain two concentric zones in CL intensity, with cores emitting higher intensity luminescence than rims (Figure 4.4A). This zoning may reflect crystallization and growth over two separate intervals during the experiment – the 15-h annealing period and the 24-h hydrostatic period – as the pressure increased slightly while the piston advanced to the hit-point. Since the pressure increase was <100 MPa, it is expected that the core and rim zones reflect no more than a 12 ppm change in Ti

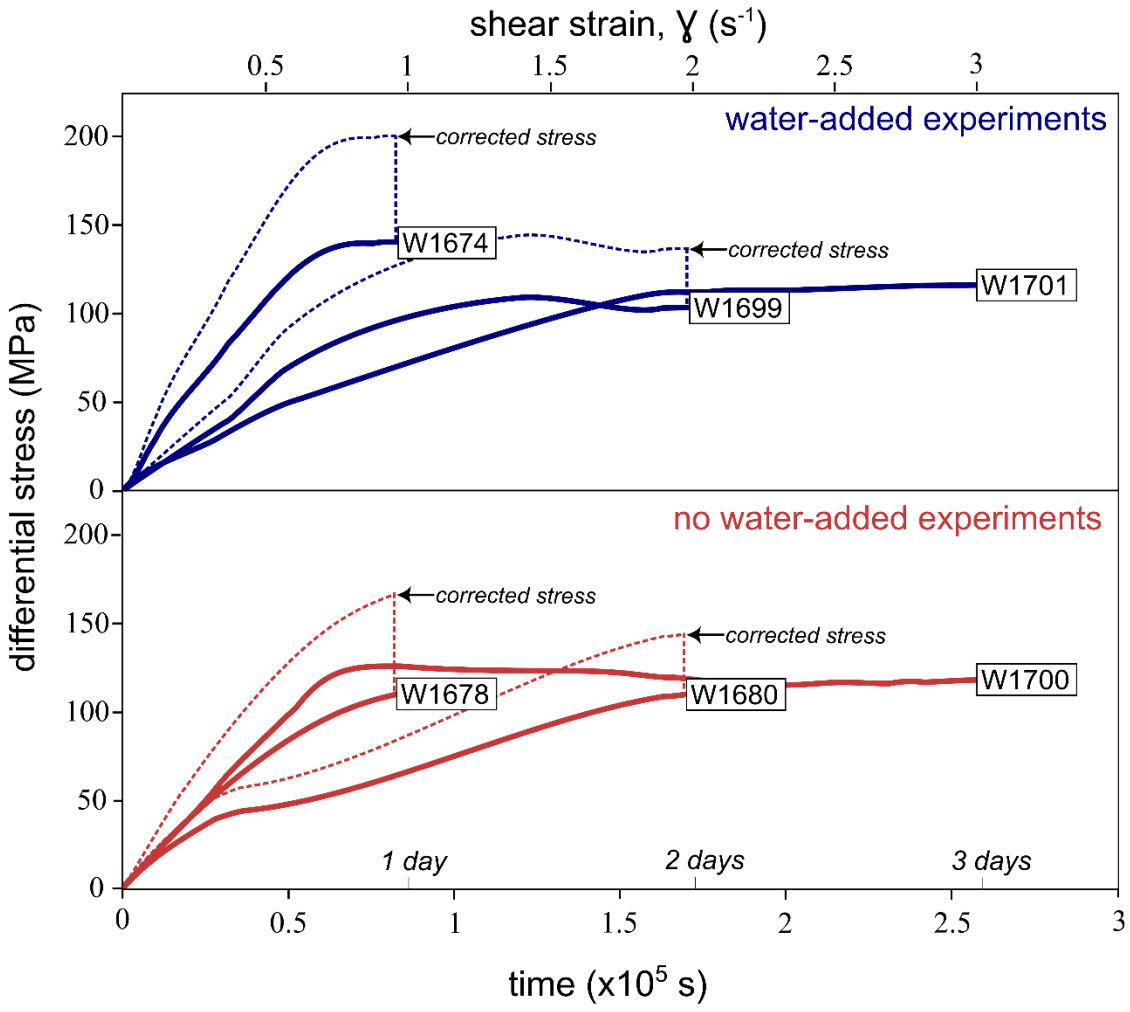

Figure 4.3. Differential stress vs. time/shear strain plot shows the strength of each experimental aggregate from the water-added and no water-added suites of experiments. Shear strains were calculated from piston offset and are treated as approximate values due to the evolution of the load-bearing areas resulting from compaction and shearing over the course of an experiment. Peak stresses on the sample aggregate are higher in low strain samples after correcting for the measured load-bearing area (see Figure 1B). Raw force data were smoothed using a moving average fit.

					EPMA	*doped quartz*			*undoped quartz*		
Exp	**time (hr)**	**shear strain rate (s^-1)**	**H2O (±1µL)**	**aggregate thickness (µm)**	**n= (total)**	**[Ti] (ppm)**	**st. err.**	**n=**	**[Ti] (ppm)**	**st. err.**	**n=**
W1674	24	10^-6	wet	1300	209	230	4	88	134	2	55
W1678	24	10^-6	dry	1850	150	117	4	61	76	2	72
W1680	48	10^-6	dry	1340	175	211	6	59	130	3	86
W1696	24	hydrostatic	dry	2120	209	123	5	62	79	2	114
W1698	24	hydrostatic	wet	2140	160	140	7	72	63	2	61
W1699	48	10^-6	wet	1770	152	191	4	65	106	4	63
W1700	72	10^-6	dry	1270	175	146	4	64	60	3	81
W1701	72	10^-6	wet	1110	150	151	4	62	83	2	74

Table 4.2. Data table of experiments. Results of EPMA measurements show aggregated results of (at minimum) three parallel transects of 50 points with equidistant spacing. Thickness of layers was measured along 4 transects spaced evenly across the layer to calculate an average thickness of each sample aggregate.

concentration (based on Thomas et al. [2010]) and are unlikely to be accurately resolved by our population of electron probe analyses. We assume that quartz grown under hydrostatic conditions incorporates the equilibrium Ti concentration based on the local a_{TiO2}. Therefore we use these experiments to compare the compositional changes that are observed after deformation experiments.

4.4.2 Quartz in Deformation Experiments

The deformed samples show a progression in quartz shape-preferred orientation (SPO) and dynamic recrystallization microstructures with greater imposed strain. The magnitude of the SPO increases with increasing strain and follows the rotation of the maximum elongation direction. Quartz grains in the low strain ($\gamma \sim 0.7$) experiments are slightly

flattened, forming a weak SPO inclined at a high angle to the shear plane. Numerous grains preserve undulatory extinction, and some evidence for limited grain boundary migration (GBM) can be observed at grain margins (Figures 4.4B and 4.6B). The SPO of quartz is stronger after intermediate strain ($\gamma \sim 1.5$) experiments, wherein grains exhibit irregular boundaries with evidence for subgrain rotation recrystallization (SGR) (Figures 4.4C and 4.6C). In the high strain ($\gamma \sim 3$) experiments, quartz grains are pervasively recrystallized via a combination of progressive SGR and GBM recrystallization, with recrystallized grains forming a strong SPO oriented at a low angle to the shear plane (Figures 4.4D and 4.6D). Microstructural criteria for combined SGR and GBM include irregular grain shapes, lobate grain boundaries, and oblique grain shape fabrics (Figures 4.4C, D and 4.6C, D). Recrystallization textures in our highest strain experiments are similar to those characterized for dislocation creep Regime III from the deformation experiments of Hirth and Tullis [1992].

EBSD analysis reveals a strengthening in crystallographic-preferred orientation (CPO) with increasing strain. The lower strain experiments show a modest fabric with a weak point maximum of quartz [0001] axes in the Y-orientation, as well as more dispersed maxima indicative of slip on the rhomb planes (Figure 4.5B, C). At high strain, the samples develop a very strong Y-axis maximum of c-axes, reflecting the dominance of prism <a> slip [Law, 1990, 2014]. Similar recrystallized quartz fabrics have been reported in previous

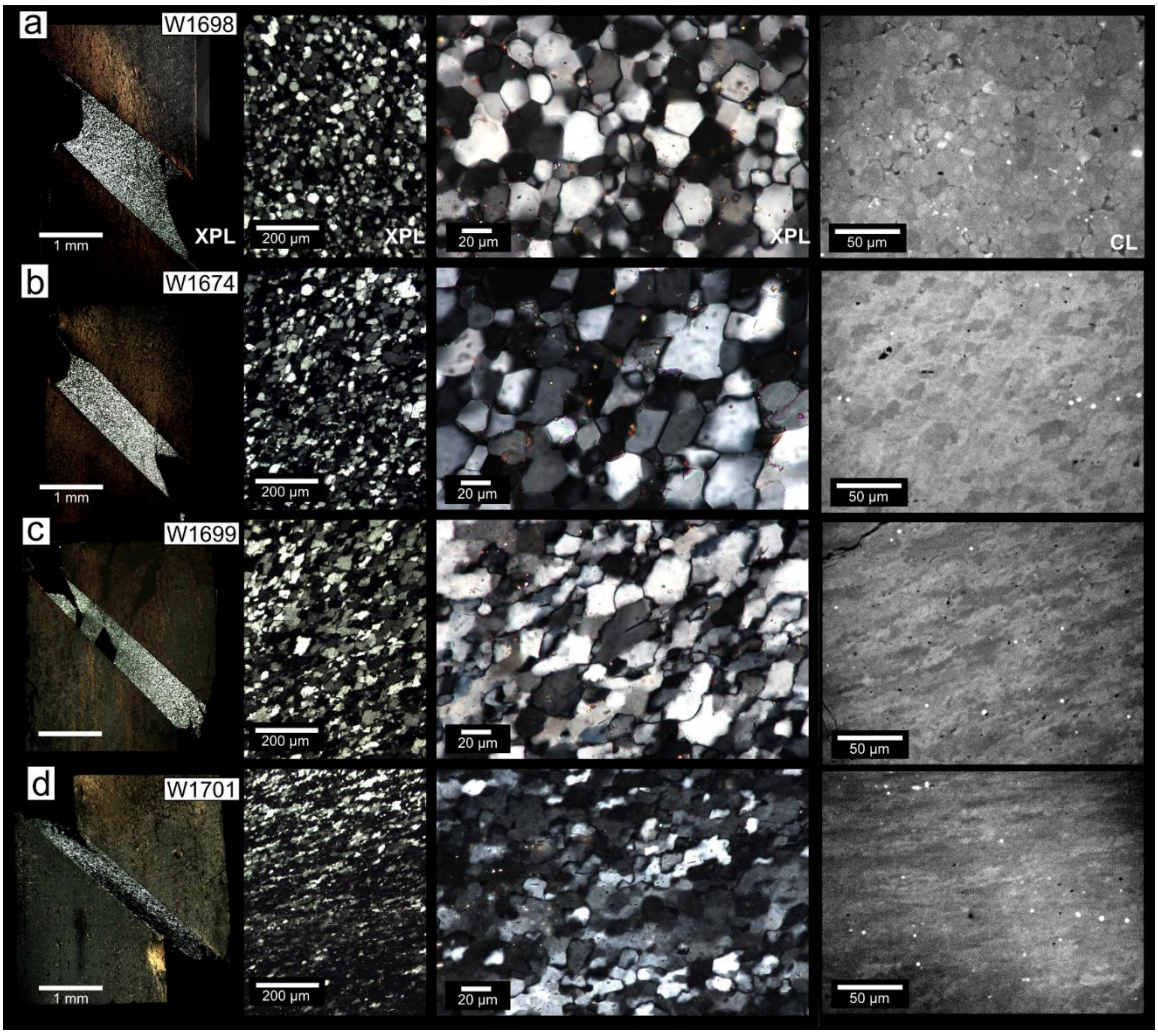

Figure 4.4. Cross-polarized light (XPL) and cathodoluminescence (CL) images of quartz microstructures in the water-added sample suite – (A) hydrostatic, (B) low strain, (C) intermediate strain, and (D) high strain. Highest magnification images show microstructures in the undoped layer of the aggregate. CL images from the undoped layer reveal core-and-rim zoning that is present in the hydrostatic annealing experiment (A) that becomes progressively homogenized in higher strain experiments (B-D). Photomicrographs and CL images are oriented parallel to the surface of the shear piston, shear sense is dextral.

experiments on quartz deformed to comparable strains, both in quartzites [Tullis et al., 1973; Stipp and Tullis, 2002; Heilbronner and Tullis, 2006] and quartz single crystals [Vernooj et al., 2006; Muto et al., 2011]. The rapid evolution with increasing strain to the strong Y-axis maximum (Figure 4.5D) has been interpreted to result from GBM recrystallization [Heilbronner and Tullis, 2006; Muto et al., 2011]. The uncontoured pole figure diagram from the highest strain experiment reveals a faint cross girdle of c-axis orientations indicative of minor slip on the rhomb and basal planes (Figure 4.5D). We measure an opening angle of ~95-105°, consistent with estimates based on the c-axis opening angle thermometer (for our experimental temperatures and strain rates) [Kruhl, 1996; Law, 2014].

CL analyses indicate homogenization of the initial core-to-rim zoning observed in hydrostatic experiments. Quartz grains in low strain experiments preserve CL zoning with a pattern that is similar to hydrostatic experiments (Figure 4.4B). In intermediate strain experiments, zoning is faintly detectable (Figure 4.4C). CL zoning is not detectable in quartz in high strain samples, in which all grains exhibit internally-uniform CL intensity (Figure 4.4D).

Ti concentrations in both the doped and undoped quartz layers initially increase with increasing strain, then decrease at the highest strains (Figure 4.7). This trend is observed for both “water-added” and “no-water-added” sample suites. The highest strain samples preserve Ti contents that are most similar to those measured in the hydrostatic samples.

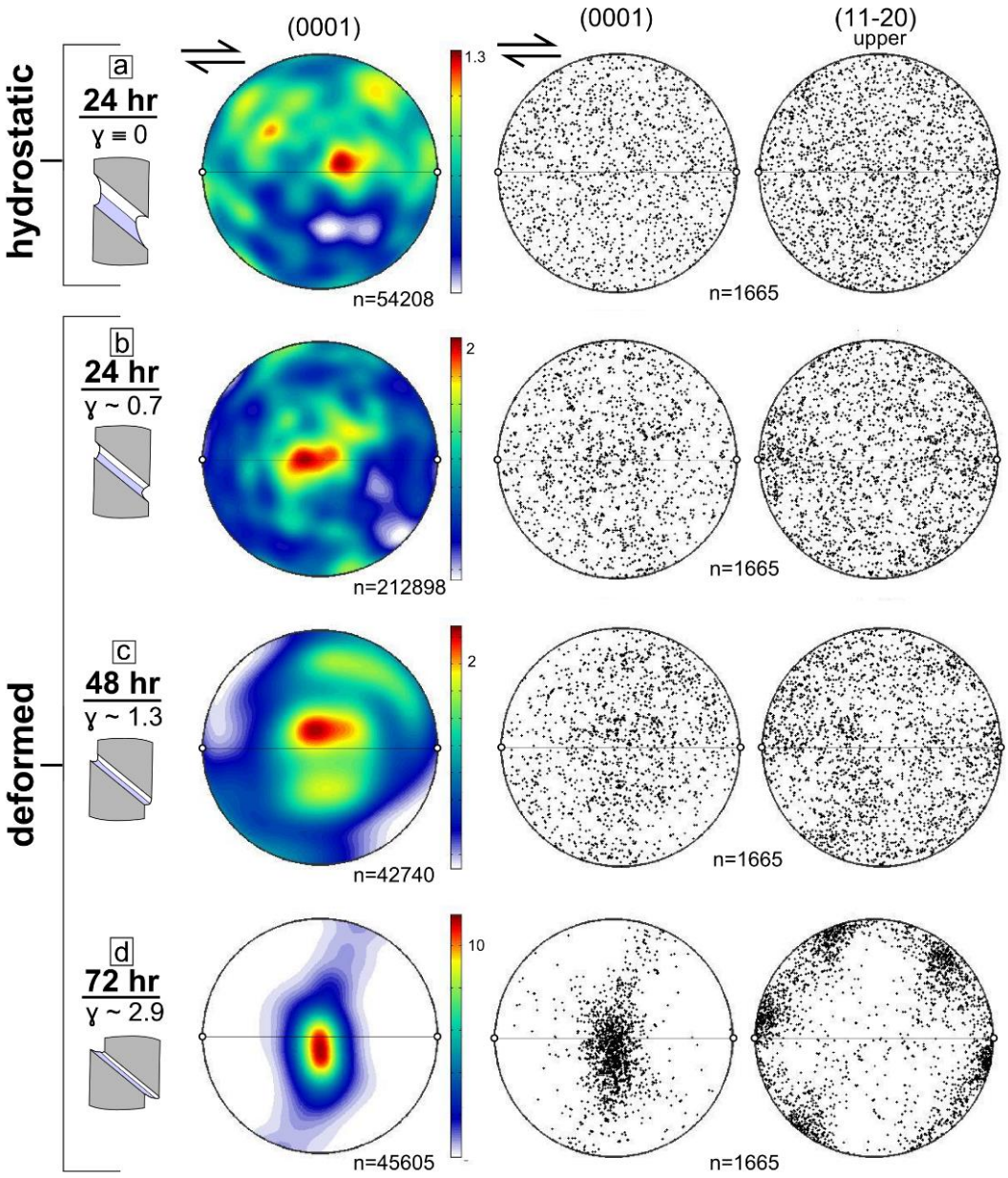

Figure 4.5. Equal area, lower hemisphere EBSD pole figure diagrams document progressive strengthening of quartz recrystallization fabrics from the water-added suite of experiments. EBSD data collected from one point per grain. Foliation and lineation are aligned with the horizontal, shear sense is dextral.

The difference in concentrations between doped and undoped layers of any sample remains constant – undoped layers of quartz are consistently 50% less than the adjacent layer of doped quartz. The decrease in the mean of Ti concentrations in doped and undoped layers follows an approximately linear trajectory with measured concentrations changing by ~30-40 ppm/day (Table 4.2, Figure 4.7).

4.4.3 Accessory Phases

Accessory phases in our experiments pin grain boundaries of quartz and thus have a first-order control on quartz grain sizes in each layer. Grain sizes are smaller in doped quartz relative to the adjacent undoped quartz in all samples.

The majority of accessory phases are rutile (TiO_2), consistent with Ti doping at a concentration higher than the predicted solubility for our experimental conditions. Phases that are identified as TiO_2 with EDS analysis are confirmed to be rutile using EBSD. However, we also observe rutile in the undoped layer, despite having synthesized this layer with a Ti content below the predicted solubility.

Rutile exhibits two distinct habits depending on whether it occurs in the doped or undoped layers. The doped layer contains euhedral, faceted nodules of rutile (Figure A6.3), similar to findings from previous studies on synthetic rutile (cf. Figure 3 of Thomas et al. [2010] and Figure 5 and Electronic Annex 2 of Huang and Audétat [2012]). Rutile nodules are

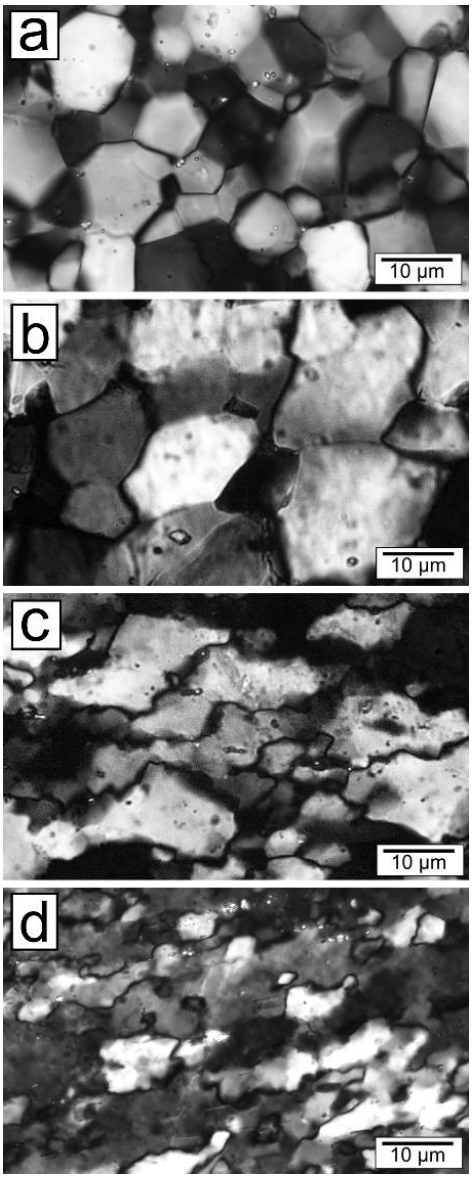

Figure 4.6. Cross-polarized light images showing quartz recrystallization microstructures from the undoped layer of the (A) hydrostatic, (B) low strain, (C) intermediate strain, and (D) high strain experiments. In low strain experiments, quartz grains are slightly flattened forming a weak SPO aligned with the elongation direction. In intermediate strain experiments, quartz microstructures are dominated by SGR recrystallization, resulting in an oblique grain shape fabric of equidimensional recrystallized subgrains. In high strain experiments, quartz deformation is dominated by GBM recrystallization, characterized by larger, irregular grain shapes with lobate grain boundaries. All photos are oriented normal to the shear plane, shear sense is dextral.

smallest and most evenly-dispersed in hydrostatically-annealed samples and become larger and localized along the shear plane in the high strain samples (Figure A6.3).

In contrast, rutile in the undoped layers occurs as acicular crystals with axial ratios >50:1 (Figure 4.8). In hydrostatic experiments, rutile needles form radiating bundles that emanate from a seed grain (Figure 4.8A, B). In deformed samples, rutile needles become progressively rotated into the shear plane (Figure 4.8C, D). Needles aligned into the stretching direction undergo extension and boudinage. Previous studies have demonstrated that rutile needles in naturally deformed quartzites behave as passive markers that can be useful as intracrystalline strain markers [Mitra, 1978; Mitra and Tullis, 1979; Mancktelow and Pennacchioni, 2004].

In the undoped layers we observe CL halos around rutile needles (Figures 4.4 and A6.4). CL halos are brightest adjacent to rutile and diminish into the surrounding quartz. CL halos become wider and smoother in longer duration experiments (Figure A6.4). Correlating CL intensity in the blue wavelength (Figure A6.2) with Ti defects in quartz (e.g., Gotze et al. [2001], Muller et al. [2003]), we interpret CL halos as reflecting Ti diffusion from rutile needles into quartz. This apparent concentration gradient is consistent with diffusive flux (from rutile to quartz) opposite of what has been previously-documented for Ti diffusion in rutilated quartz. For example, Cherniak et al. [2007] document CL depletion halos surrounding rutile needles in quartz, an observation interpreted to reflect rutile exsolution. Exsolution occurs as Ti unmixes from quartz in response to a decrease in Ti solubility in

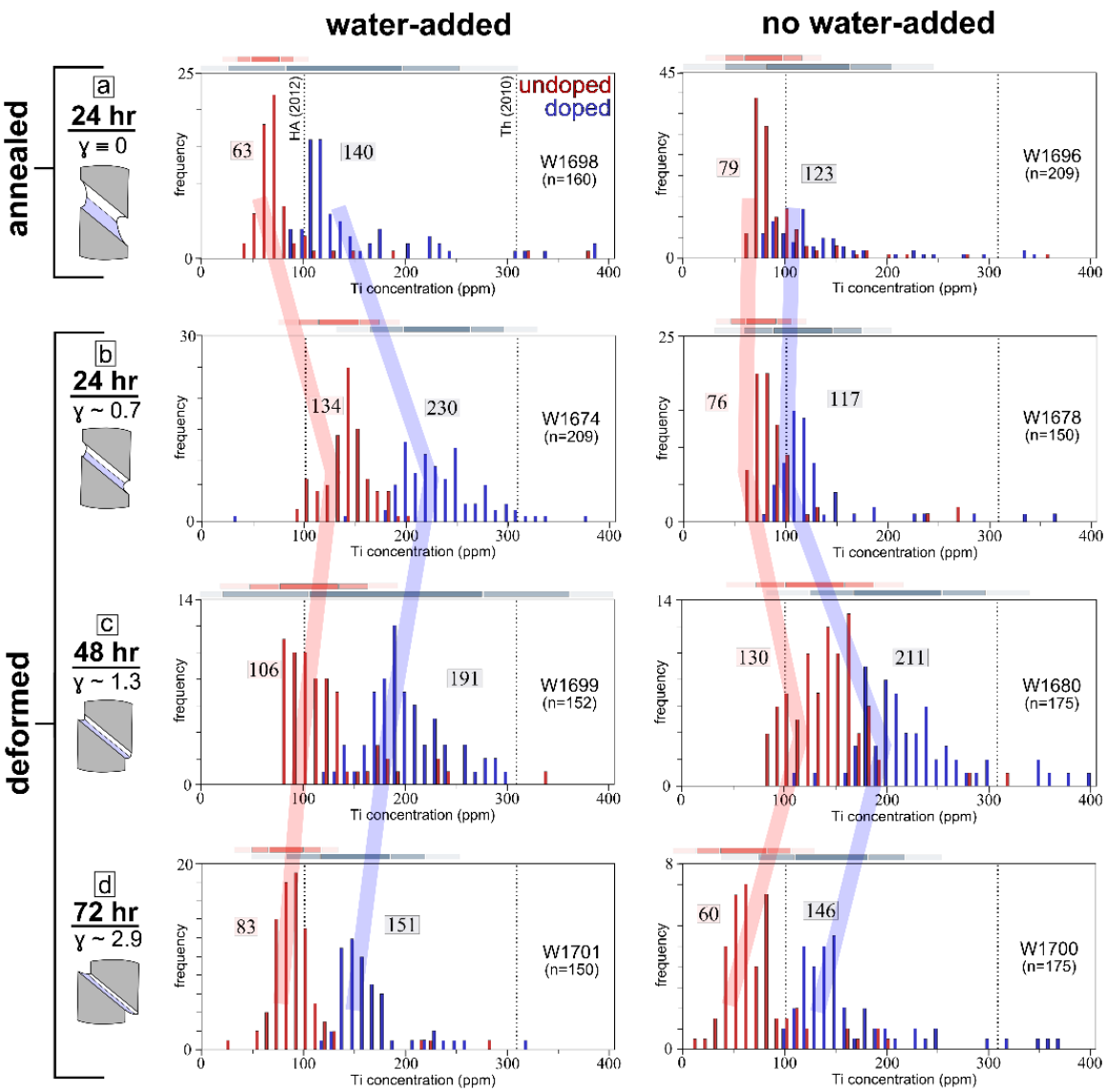

Figure 4.7. Electron probe measurements of Ti concentration in quartz from water-added and no-water-added suites of experiments. Bars above each histogram show the 78%, 95%, and 99.6% confidence intervals, and values adjacent to histograms indicate the mean of the population of measurements. Dashed lines show Ti solubilities predicted for the conditions of our experiments by the calibrations of Thomas et al. [2010] and Huang and Audétat [2012]. In both suites of experiments, Ti concentrations are lowest in the hydrostatically-annealed samples, increase initially in the low strain samples, and then decrease in high strain samples such that the highest strain samples have Ti concentrations most similar to those measured in annealed samples. Broad lines connecting histograms from each suite show the theoretical evolution of Ti contents through time.

quartz. In the case of our experiments, where Ti enrichment halos are preserved, we propose a different mechanism whereby rutile becomes included in quartz as a result of overgrowth that occurs as rutile needles (or "whiskers") precipitate from a fluid in the early stages of an experiment and are progressively overgrown by migrating quartz grain boundaries. Once included in quartz, rutile needles dissolve and Ti diffuses into the surrounding quartz that is undersaturated in Ti. Overgrowth rutilation is a previously-unrecognized mechanism to rutilate quartz and it merits further investigation in both nature and experiment to better constrain the kinetic and crystallographic relationships of different quartz rutilation mechanisms.

4.5 Discussion

Results of our experiments indicate that dynamic recrystallization resets Ti concentrations in quartz to levels measured from hydrostatically-annealed quartz. In the following section, we discuss the importance of a_{TiO2} for buffering Ti concentrations and how the distribution of Ti-bearing phases within an aggregate controls the Ti content preserved in deformed quartz. We then outline evidence from our integrated microstructural, textural, and compositional analysis of progressively-deformed quartz aggregates to explore the mechanisms by which Ti-in-quartz equilibration is achieved during dynamic recrystallization. We discuss deformation processes that can alter partitioning behavior – both solubility and diffusivity – of Ti in quartz. Finally, we place our findings in the context of previous experimental studies of Ti substitution in quartz.

4.5.1 Buffering a_{TiO2} in a deforming aggregate

Constraining a_{TiO2} remains a primary challenge for confident application of Ti-in-quartz thermobarometry to deformed rocks. The calibration experiments of Wark and Watson [2006] and Thomas et al. [2010] produced rutile that co-precipitated with quartz, which they used to assume $a_{TiO2} = 1$. For cases where rutile is absent, Thomas et al. [2010] introduced a scaling factor for the dependence of a_{TiO2} on Ti solubility. Estimating a_{TiO2} in naturally deformed rocks is difficult because it may vary through time, it may depend on the spatial distribution of Ti-buffers within the aggregate (e.g., Nachlas et al. [2014]), and the buffering capacity of other Ti-bearing phases (titanite, ilmenite) is not experimentally-constrained (but can be estimated, e.g., titanite, Ghent and Stout [1984], Behr and Platt [2011]; ilmenite, Ghent and Stout [1984]; Menegon et al. [2011]). We designed our samples with two layers of quartz doped above and below the predicted equilibrium Ti solubility to investigate resetting Ti in quartz during recrystallization in different chemical buffering environments.

We evaluate a_{TiO2} in our samples from analysis of Ti concentrations of quartz in the doped and undoped layers. The doped layer was synthesized with 2280 ppm Ti, a concentration above the predicted solubility, so that excess Ti present during quartz crystallization would precipitate as rutile throughout this layer. Indeed, there is abundant rutile along quartz grain boundaries in the doped layer of all experiments. The high spatial density of rutile grains

lends confidence to the assumption that quartz recrystallization in the doped layer was buffered with $a_{TiO2} = 1$.

The undoped layer was rinsed in concentrated acid that leached Ti contents down to a level of 110 ppm, a concentration less than the predicted solubility. Thus crystallization of quartz in this layer occurs with $a_{TiO2} < 1$. Titanium concentrations in quartz in the undoped layer are consistently 50% (70–90 ppm) lower than in the quartz in the adjacent doped layer (Figure 4.7, Table 4.2, Table A7.1). This spread is maintained throughout all hydrostatic and deformation experiments. Aside from isolated occurrences of acicular rutile (>200 μm between neighboring groups of needles), the undoped quartz layer is mostly devoid of secondary phases. These observations indicate that the a_{TiO2} in the undoped layer is set by local equilibration of titanium between the quartz and the intergranular fluid in the undoped layer. Thomas et al. [2010] predict a reduction in Ti solubility in quartz of 50% with $a_{TiO2} = 0.5$. We conclude that a_{TiO2} in the undoped layer was sustained at approximately 0.5 by the Ti content of the intergranular H_2O fluid.

The solubility of rutile in water is quite low at our experimental conditions [Audétat and Keppler, 2005; Tropper and Manning, 2005], though it can increase in the presence of complexing agents such as Si, Al, and Na [Antignano and Manning, 2008; Hayden and Manning, 2011]. Considering the abundance of Si in our experiments and the elevated concentrations of complexing ions (Na, Al) in the initial silica gel (Table 4.1), it is conceivable that the amount of Ti dissolved in solution is similar to the level contained in

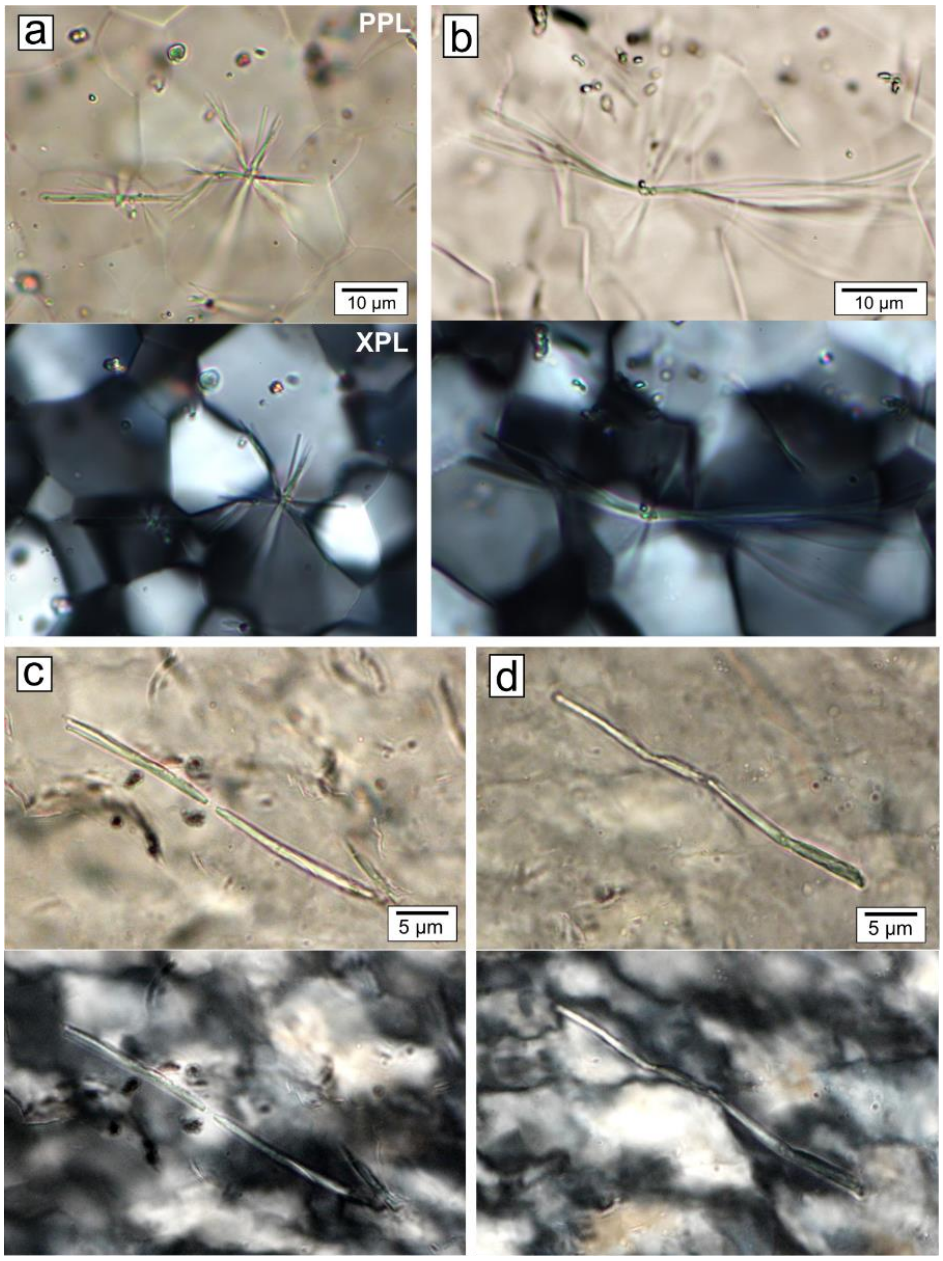

Figure 4.8. Plane-polarized (PPL) and cross-polarized light (XPL) images of acicular rutile crystals present in the undoped layer of experiments. (A, B) Radiating bundles of rutile needles are present in the hydrostatic annealing experiments. Needles in hydrostatic experiments are observed to emanate from a point defined by a small round grain of the same birefringence. (C, D) In deformation experiments, rutile needles become aligned into the shear plane and commonly show evidence for kinking and boudinage.

quartz in the undoped layer. Consequently, the intergranular fluid may be capable of buffering quartz throughout in the aggregate in the absence of nearby Ti-bearing buffers. However, we emphasize that no variations in the compositional gradients between layers were detected in our samples (at the resolution of our probe measurements); our analytical transects show a step in Ti concentration at the interface between the doped and undoped layers (Figure A6.5). This observation suggests that either the Ti concentration of the fluid was quite low (limiting the Ti flux across the layer boundary), or that the pore-fluids were not interconnected for the duration of the experiments (limiting the diffusive transport between the layers, e.g., Farver and Yund [1992]). Otherwise we would expect a significant increase in quartz Ti contents in the regions near the boundary between the layers.

4.5.2 Resetting Ti concentrations during dynamic recrystallization

Our experimental results indicate that dynamic recrystallization facilitates re-equilibration of Ti concentrations in quartz. The effect of deformation on Ti exchange is evaluated by comparing Ti contents of quartz that grew in hydrostatic annealing experiments with Ti contents of quartz that recrystallized during increasing increments of imposed shear strain. Our results show that Ti concentrations in quartz evolve with increasing strain, initially increasing relative to the hydrostatic experiments conducted for the same amount of time, then decreasing in high strain experiments to a value similar to annealed quartz (Figure 4.7). The decrease in the mean of Ti concentrations in doped and undoped layers follows an approximately linear trajectory with measured concentrations decreasing by ~30-40

ppm/day (Figure 4.7). In the highest strain experiments, where quartz grains are pervasively recrystallized and exhibit a strong CPO, Ti contents are uniform at the grain scale (i.e. grains are not zoned) (Figure 4.4) with values that are similar to those measured for hydrostatic experiments (Figure 4.7, Table 4.2).

Grain size controls the diffusion distance for the quartz Ti content to equilibrate with the grain boundary. The smallest recrystallized quartz grains (present in the high strain deformed experiments) are approximately 5 μm in diameter. With this grain size it would take c. 2 yr ($6.4*10^7$ s) to homogenize quartz grains using the Ti diffusion coefficient for 900 °C [Cherniak et al., 2007]. The predicted volume diffusion distance during the 72 h (longest) experiments is ~0.1 μm. Our measurements of homogenous Ti contents, both within deformed grains (Figure 4.4) and among large populations of quartz grains (Figure 4.7), cannot be explained by Ti volume diffusion and require other diffusive transport mechanisms to explain the observed equilibration of dynamically recrystallized quartz.

Recrystallized quartz from intermediate and high strain experiments shows that the initially-high Ti content observed in low strain experiments is gradually reduced with greater amounts of dynamic recrystallization. Dynamic recrystallization occurred dominantly by GBM recrystallization with minor SGR recrystallization. Evidence for these recrystallization mechanisms includes quartz microstructures (Figures 4.4 and 4.6) [Hirth and Tullis, 1992; Hirth et al., 2001; Stipp et al., 2002; Law, 2014] and EBSD pole figure diagrams showing the strengthening of the Y-axis maximum distribution of quartz [0001]

axes (Figure 4.5). Taken together, these results indicate that dynamic recrystallization occurred primarily by grain boundary migration (e.g., Heilbronner and Tullis [2006]).

Different mechanisms of dynamic recrystallization may influence re-equilibration of Ti contents in different ways. During SGR, dislocation climb would enable titanized dislocations to migrate, advecting Ti to both low angle subgrains and (after significant rotation occurs) high angle grain boundaries. In the case of GBM, resetting Ti concentrations may be even more efficient, as grain boundaries migrating through grain interiors enhances equilibration (cf. Yund and Tullis [1991]), assuming that quartz equilibrates with the grain boundary a_{TiO2} as the boundary migrates. We infer that our highest strain aggregates were nearly 100% recrystallized (cf. Figure 6 of Hirth and Tullis [1992]) and this allowed all quartz grains in the aggregate to return to their equilibrium defect concentration. The net result of recrystallization is to re-equilibrate Ti concentrations to the solubility level for the P-T conditions at which recrystallization occurs.

Quartz in low strain experiments incorporated higher Ti concentrations than quartz in both hydrostatic and high strain experiments (Figure 4.7, Table 4.2). This trend is observed for both the water-added and no-water-added suites of experiments, and occurs for both the doped and undoped layers of the aggregates. Three observations suggest that the Ti solubility may be influenced by the deformation history. First, the increase in Ti contents occurs in the doped layers of both suites of experiments (Figure 4.7), despite our assumption that a_{TiO2} is buffered at unity throughout these layers (and therefore should

already contain its saturated Ti content) (see section 5.1). Second, the spread of Ti concentrations between doped and undoped layers is maintained in all experiments – Ti content in undoped layers remains 50% less than Ti content in doped layers regardless of deformation history (Figure 4.7). Third, the presence of Ti diffusion halos surrounding rutile inclusions in undoped layers of quartz in all experiments (Figure A6.4) suggests that in each case, quartz was undersaturated with respect to a_{TiO2}.

Our experimental findings suggest that dislocations could act as sinks for Ti. The higher Ti contents in low strain experiments could arise because the Ti solubility increases with higher dislocation density. Low strain experiments were quenched at or near peak stress conditions (Figure 4.3). This would result in quartz with an elevated dislocation density compared to higher strain experiments. The optical micrographs of the low strain samples show pervasive undulatory extinction (Figure 4.4 and 4.6), which provides evidence for the presence of locally high dislocation densities in quartz. The final flow stress is in the range of ~120-150 MPa, which is in general agreement with piezometry [Stipp and Tullis, 2003] for the recrystallized grain sizes found in our experiments (~5 μm) (e.g., Figures 4.4 and 4.6). At these stresses, quartz would exhibit dislocation densities of c. $1.3x10^8$ cm^{-2} [Kohlstedt and Weathers, 1980; McLaren et al., 1989]. Owing to compaction during the hydrostatic annealing stage of the experiments, the load-bearing area of the low strain samples is about 40% lower than that of the high strain samples (see Figures 4.1 and 4.3); consequently, dislocation densities in quartz from low strain experiments may be considerably higher than recrystallized quartz from high strain experiments. However, at

the dislocation densities estimated for our low-strain samples, a one-to-one partitioning of Ti into dislocation cores would only account for a bulk Ti concentration of c. 2 ppm.

Elastic distortions of the lattice in the vicinity of a dislocation causes impurity segregation around the dislocation core [Weertman and Weertman, 1992; Hull and Bacon, 2011]. This process forms a solute cloud (a "Cottrell atmosphere") of impurity ions surrounding a dislocation [Cottrell and Bilby, 1949; Spencer and Haruta, 1966; Bullough and Newman, 1970; Hull and Bacon, 2011]. Direct observation of impurity clouds around line defects (e.g., Blavette et al. [1999]) and dislocation loops (e.g., Thompson et al. [2007]) reveal enrichment of impurity ions in metal alloys that are c. 2-3 orders of magnitude higher for interstitial ions than the intrinsic lattice solubility. Results of our experiments suggest that Ti may be partitioned into solute clouds surrounding dislocations in quartz, a phenomenon that could influence Ti concentrations to an appreciable extent. Increased Ti contents in the low strain samples can be explained with the following assumptions: (a) a dislocation density of $2x10^8$ cm^{-2} (for the area-corrected stresses of the low strain samples), (b) Ti concentrations elevated by 90 ppm in low strain samples relative to hydrostatic samples (see Figure 4.7, Table 4.2, Table A7.1), and (c) a titanized radius of 5 times the Burgers vector (e.g., Hull and Bacon [2011]), and (d) a Ti concentration in the core region 3500 times greater than the intrinsic lattice solubility.

While this effect of deformation on Ti content is intriguing, we remain cautious for several reasons. First, the difference in stress between the low strain and high strain samples is

relatively small, which would result in only a ~40% difference in the dislocation density. Second, the Ti atmosphere along the dislocations would likely influence the mobility of the dislocations (e.g., Jaoul, [1984]) – which is inconsistent with our result that the flow strengths and microstructures of samples are similar to those reported for natural quartz aggregates experimentally deformed at the same conditions. Third, the amount of Ti calculated to reside within the solute cloud is very high, and it is not known if quartz can accommodate the distortions associated with such large Ti concentrations. Nonetheless, further research is warranted to explore the relationship between dislocation density and Ti partitioning in quartz – both its solubility and diffusivity – to better constrain applications of quartz thermobarometry to deformed rocks.

4.5.3 Comparison with previous experimental studies

Quartz in our hydrostatic experiments crystallized at pressure-temperature-time conditions analogous to the original TitaniQ calibration experiments of Wark and Watson [2006] and Thomas et al. [2010, 2015] and experiments by Huang and Audétat [2012]. We thus provide an independent comparison between the two calibrations at the P-T condition of our experiments.

At 900 °C and 1.0 GPa, the Ti solubility (assuming $a_{TiO2} = 1$) is predicted to be 310 ppm by Thomas et al. [2010] and 101 ppm by Huang and Audétat [2012]. The Ti concentration of quartz grown in the doped layer of our hydrostatic experiments is 140 ± 7 ppm in the water-added suite and 123 ± 5 ppm in the no-water-added suite (see Figure 4.7, Table 4.2,

Table A7.1). Titanium concentrations from our hydrostatic experiments most closely agree with the lowest measurements recorded in Huang and Audétat's [2012] experiments. However, this agreement may only be fortuitous. In their experiments, they find a range of Ti measurements in quartz precipitated along the length of a polished quartz bar, and they select the lowest concentrations (lowest eight of 116 measurements) to define their solubility calibration on the basis that the lowest Ti contents reflect the slowest growth rates and thus are closest to the true equilibrium solubility [Huang and Audétat, 2012]. However, owing to the wide range of concentrations they measured, it is difficult to justify that equilibrium was achieved in their experiments. Nonetheless, we present a normally-distributed, statistically-significant dataset that coincides with their lowest Ti concentrations from which they derived their calibration.

Huang and Audétat [2012] suggest that quartz growth rate influences Ti concentration and offer this as the explanation for their modified solubility calibration. They infer that slow growth rates and lower Ti concentrations in their experiments reflect equilibrium substitution, whereas faster growth rates prevailed in the experiments of Wark and Watson [2006], Ostapenko et al. [1987; 2007], and Thomas et al. [2010] that resulted in super-saturated Ti contents and overestimated solubilities. Huang and Audétat [2012] calculate growth rates in the experiments of Thomas et al. [2010] to be 10-50x faster than their own experiments (~100-200 μm/day compared to 4-10 μm/day). However, this calculation is poorly-constrained due to variable growth rates that prevailed in both of these studies. Based on the thermal and compositional gradients that existed in the experiments of Huang

and Audétat [2012], these authors report variable growth rates along the length of their quartz bar and select one location to be representative of growth rate for each experiment. The experiments of Wark and Watson [2006] and Thomas et al. [2010, 2015] produced numerous single crystals of quartz with varying size (~20-1000 μm). Their measurements do not show any differences in Ti content between crystals of different size; these observations suggest that Ti incorporation in the experiments of Wark and Watson [2006] and Thomas et al. [2010, 2015] was not influenced by growth rate.

Distinct from previous calibration experiments, we find a uniform growth rate and normally-distributed population of Ti in quartz measurements. We estimate growth rates in our experiments by correlating the distinct core-to-rim zoning with the modest change in pressure associated with the initiation of piston advancement during loading. Rims of quartz (7.4 ± 0.3 μm) that grew during the 24-hr hydrostatic interval are 1.3-1.8 times thicker than the radius of the cores (5.1 ± 0.3 μm), that grew during the 15-hr annealing interval (n=44 grains). Approximate linear growth rates calculated from these measurements are 5-11 μm/day and 5-9 μm/day for the cores and rims, respectively. Similar rates of 10 μm/day were calculated for quartz grain growth under hydrous conditions at 1.5 GPa and 1000 °C [Tullis and Yund, 1982].

The effect of growth rate on impurity content arises from the interplay between growth entrapment of an enriched surface layer and the time required for diffusive exchange [Watson and Liang, 1995; Watson, 2004]. This relationship predicts that above a certain

threshold of growth rate, entrapment outpaces diffusive equilibration and preserves compositional zoning in growth layers. Using the diffusion rate of Cherniak et al. [2007], surface entrapment of Ti (which can result in Ti concentrations higher than the solubility [Lanzillo et al., 2014]), would require quartz growth rates in our experiments in excess of 120 μm/day ($1.4*10^{-9}$ m/s). Because estimated growth rates from our experiments are about an order of magnitude slower, we conclude that diffusion was sufficiently fast to prevent growth entrapment. It remains uncertain why our results compare more closely with Huang and Audétat [2012] than Wark and Watson [2006] and Thomas et al. [2010, 2015].

Negrini et al. [2014] concluded that dynamic recrystallization does not influence Ti substitution in experimentally deformed quartz. They deformed single crystals of quartz (with an initially-low Ti content) surrounded by rutile powder, and their Ti measurements did not detect any uptake of Ti into the recrystallized quartz. A few differences between their experiments and our study hinder direct comparison. Their experiments were conducted with a relatively low water content, whereas ours were conducted with a relatively high water content (for both the water-added and no water-added suites of experiments, because of the hydrous nature of amorphous silica gel). Higher water contents likely enhance the kinetics of grain-scale equilibration in our experiments. Additionally, their study underscores the need for well-characterized reference materials to evaluate the confidence of analytical results; measuring trace element concentrations with an electron microprobe is not trivial (cf. Donovan et al. [2011]), and therefore it is important to test the

accuracy of analytical calibrations using materials with known, trace-level Ti concentrations.

4.6 Conclusions and Implications

Our deformation experiments show that dynamic recrystallization homogenizes the grain-scale Ti contents in quartz to the equilibrium solubility for the P-T conditions at which recrystallization occurs. We conclude that dislocation creep via GBM enhances resetting of Ti in quartz as grain boundaries migrate across grain interiors. Ti partitioning into dislocations may provide a mechanism to expedite the bulk diffusivity for equilibrating quartz during deformation via both SGR and GBM mechanisms by introducing fast paths for diffusion and/or by advection during creep of titanized dislocations.

By deforming layered aggregates, our experiments imposed the same strain history onto two populations of quartz grains that were buffered with different a_{TiO2}. We find that quartz was buffered with $a_{TiO2} = 1$ in layers containing numerous nodular rutile grains, whereas quartz in layers containing rare and widely-dispersed acicular rutile has Ti concentrations indicative of buffering with $a_{TiO2} \sim 0.5$. This observation highlights the importance of a fluid phase for buffering and the need for caution when interpreting sample-scale a_{TiO2} in deformed rocks.

Findings of this study are promising for applications of the Ti-in-quartz technique to retrieve the conditions of fabric formation and deformation in metamorphic rocks and

tectonites. The sensitivity of quartz geochemistry to deformation opens the possibility of directly relating thermodynamic parameters (P, T, a_{TiO2}) with the structural kinematics of deformation events. Thus by extracting P-T conditions from shear zones, it is possible to bridge the metamorphic-rheologic gap to link metamorphic thermobarometry with tectonic deformation zones and provide a better-resolved history of past orogenic events.

Acknowledgements

This work was supported by the Earth Sciences Division of the National Science Foundation through grant EAR-0911536 and EAR-1220075 awarded to G. Hirth and grant EAR-0911497 awarded to D.L. Whitney and C. Teyssier at UMN. We would like to thank C. and L. Gonçalves for assistance with preparing experimental pieces, N. Seaton and for assistance with EBSD analysis, B. Bagley for assistance with XRCT analysis, and W. Tschudin for preparing thin sections of experimental samples. We thank C. Teyssier, D. Whitney, and D. Kohlstedt for helpful discussions and comments that improved the quality of this manuscript. We thank associate editor M. Walter for editorial handling and two anonymous reviewers for constructive comments on the manuscript.

CHAPTER 5

Geospeedometry of quartz mylonites: a technique to determine the longevity of ductile shear zones

Synthesis

Analysis of chemical diffusion profiles around rutile inclusions in ductiley-deformed quartz provides a new technique to determine the timescales of shear zone deformation. This technique was tested in a naturally-deformed quartzite mylonite from the Pioneer core complex (Idaho, USA), where it yields time estimates consistent with regional geochronology, and in experimentally-deformed quartzite mylonites, where it yields time estimates similar to the duration of experiments. Rutile needles in mylonitized quartz grains act as either a source or a sink for Ti diffusion within the host quartz. Owing to their shape, rutile needles are sensitive markers of the kinematics of ductile flow. The Pioneer core complex was exhumed in part by a ~100 m thick zone of quartzite mylonites in which quartz grains are pervasively and densely rutilated. Depletion diffusion halos around lineated and boudinaged rutile needles indicate that rutile was exsolving from quartz during dynamic recrystallization. By estimating temperature from Ti-in-quartz, Zr-in-rutile, and quartz-muscovite oxygen isotope thermometry, diffusion modeling results suggest that the quartzite shear zone deformed for a time-integrated 9 Myr. If the shear zone is interpreted to have deformed en masse, our results suggest that ductility lasted for ~1-3 Myr. With structural offset across the detachment zone, this correlates to a strain rate of $1\text{-}4 \times 10^{-13}$ s^{-1}. This deformation geospeedometer was also tested in rock deformation experiments in which the temperature-time-deformation conditions are known. Rutile needles in experimental samples become included into quartz via advancing grain boundaries and dissolve Ti into the surrounding Ti-undersaturated quartz during both annealing and high-

strain deformation experiments. Modeling of Ti enrichment diffusion halos in experiments yields the approximate number of days over which the experiment was conducted. Solving for the diffusion coefficient with the known temperature-time conditions of the experiment yields a diffusion coefficient that is 1-2 orders of magnitude faster in quartz that is deforming under high P, wet conditions than measured in previous hydrostatic calibration experiments conducted under 1-atm, dry conditions. By extending observations from laboratory experiments to natural shear zones where time conditions of ductility are difficult to determine, this deformation geospeedometer introduces a new approach to measure the longevity of crustal shear zones.

5.1 Introduction

The duration and rates of ductile deformation in shear zones have first-order controls on the geodynamics of orogenesis. Localization of ductile strain controls many lithospheric processes and accommodates tectonic activity that ultimately dictates the surface morphology of mountain belts and the distribution of rocks in orogens. Strategies to determine the duration of shear zone deformation have focused on using geochronology to date mineral crystallization in dikes that cross-cut or are transposed by ductile fabrics (e.g. Scott et al. [1993]; Phillips et al. [2004]; Sassier et al. [2009]; Searle et al. [2010]), Sherlock et al. [2003]; Vance et al. [2003]; Vogl et al. [2012]), accessory minerals that react in response to deformation (e.g. Copeland et al. [1988]; Williams and Jercinovic [2002]; Cottle et al. [2010]; Mottram et al. [2015]), metamorphic minerals that are reset during

deformation and recrystallization (e.g., Dunlap [1997], Freeman et al. [1998]; Mulch and Cosca [2004]; Mulch et al. [2005]), and crystallization in structural sites that can be correlated with deformation kinematics [e.g., Muller et al. 2000; Gordon et al. 2008]. These approaches focus on obtaining an isotopic age and relating that age to deformation processes and overprinting relationships within the shear zone. Estimating structural offsets from field observations allows determination of durations of shear zone deformation from ages of spatially-correlated samples. By applying diffusion geospeedometry to deformed quartz, we introduce a technique capable of determining ages of ductile shearing directly from the phase that accommodated the shearing event.

Geospeedometry uses the time-sensitivity of kinetics as a diffusion clock to extract rates and thermal histories of geologic processes [Lasaga 1983; Chakraborty, 2006, 2008; Watson and Baxter, 2007). Because it is not dependent on the half-life of a particular isotope system, geospeedometry is capable of resolving very short timescales, even in ancient rocks for which such short events cannot be detected at the resolution of radiogenic isotopes (e.g., Philippot et al. [2001], Olker et al. [2003]; Camacho et al. [2009]). Indeed quartz has previously been used as a geospeedometer to obtain rates of prograde [Spear et al. 2012] and contact [Morgan et al. 2011] metamorphic processes, as well as to resolve magmatic and volcanic events [Gualda et al. 2012].

The importance of quartz rheology to lithospheric strength (e.g., Kohlstedt et al. [1995]; Burgmann and Dresen 2008] provides an opportunity to use geospeedometry to inform the

timescales of continental evolution. Because of its sensitivity to deformation under a wide range of crustal conditions, quartz in a shear zone may recrystallize over the entire lifespan of a tectonic event. Therefore, by extracting timescales from deformed quartz, it is possible to determine the longevity of continental tectonic processes. In addition to being a rheologically-important mineral, quartz is also a robust single mineral thermometer, barometer, and geospeedometer. With advances in understanding the solubility of Ti in quartz [Wark and Watson, 2006; Thomas et al. 2010, 2015], and the diffusivity of Ti in quartz [Cherniak et al. 2007], both the direction and rates of Ti flux between quartz and rutile can be predicted and used to interpret geologic events. Evidence from rock deformation experiments demonstrating that deformation of quartz promotes re-equilibration of Ti-in-quartz solubilities [Nachlas and Hirth 2015] supports the application of quartz geochemistry as a record of the conditions of ductility in the crust.

We have identified a natural quartz-rutile diffusion couple that records both directions of Ti diffusive flux and is also a passive marker of ductile flow. By measuring the extent of diffusion progress in rutilated quartzite samples with different deformation histories, inverse modeling of Ti diffusion patterns was used to calculate the duration of ductile shearing and dynamic recrystallization. This approach is tested in a natural setting, where we solved for timescales and thermal conditions of ductile shearing and found them to be in general agreement with regional geochronology, and in experimental settings, where we solved for timescales that are similar to the experiment duration. By combing diffusion analysis with temperature estimates from microstructural and thermobarometric techniques

in the same and nearby rocks, we propose that deformation geospeedometry of quartz is a new technique capable of providing a high-resolution perspective into the deformation rates and thermal history of ductile shear zones.

5.2 Rutilated quartz in mylonites

Acicular inclusions of rutile ("rutile needles") are one of the most common mineral inclusions found in quartz (e.g., Seifert et al. [2011]). Quartz containing microscopic rutile needles occurs primarily in two geologic settings: high-grade metamorphic terranes and hydrothermal settings. The process of rutilation in each of these settings is different and results in rutilated quartz with diagnostic epitaxy and diffusion patterns between inclusion and host.

Studies of rutilated quartz have predominantly focused on high-grade metamorphic rocks in which the presence of rutilated quartz is typically taken to indicate retrogression from amphibolite-granulite facies conditions [Masberg et al. 1992; Kruhl and Nega 1996; Li et al. 2011; Kawasaki and Osanai 2008; Sato and Santosh 2007; Adachi et al. 2010; Korsakov et al. 2009]. Rutilated quartz in granulites and amphibolites is classically interpreted to result from exsolution during cooling as Ti unmixes from quartz [Cherniak et al. 2007; Ostapenko et al. 2007; Kawasaki and Osanai 2008; Storm and Spear 2009]. Rutile needles originating via exsolution are commonly crystallographically-oriented in coincidence with the quartz lattice [Harker 1890; Jayaraman 1939; Kruhl 1996; Adachi et al. 2010], an

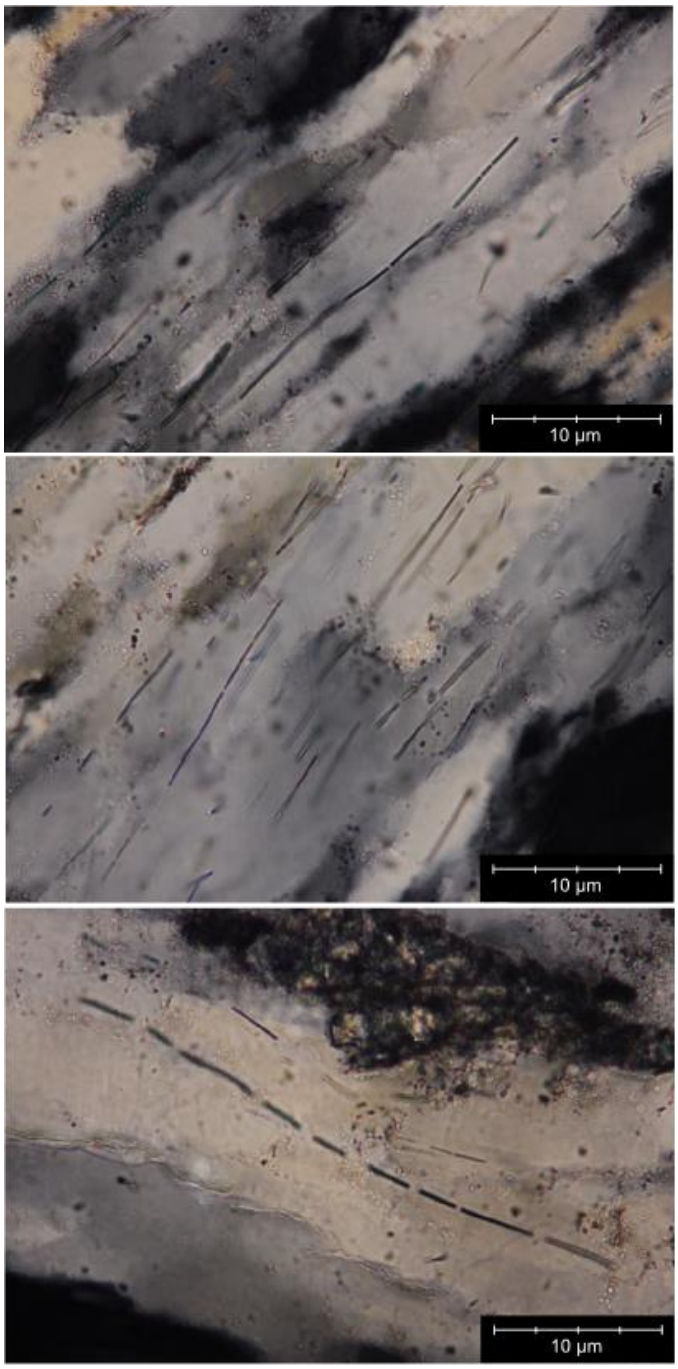

Figure 5.1. Microstructures of deformed rutile needles from the Pioneer Core Complex, Idaho.

observation that is consistent with the optical phase boundary theory of unmixing (e.g., Fleet [1982]; Feinberg et al. [2004]).

Rutilated quartz is also known to occur in hydrothermal settings (Deer et al. [1992]), which, although having received far less attention from the scientific community, is perhaps the most widely-recognized form of rutilated quartz amongst the general public. Only recently has hydrothermal rutilated quartz been studied in detail in a natural setting; Shulaker et al. [2015] performed in-situ geochronology and thermometry on rutilated quartz precipitated in hydrothermal veins. These authors argued for co-precipitation of quartz and rutile based on the random orientation of rutile needles, the presence of secondary adularia microcrystals grown onto rutile needles, the large diameter of needles relative to the sizes that would be predicted to form via diffusion, and the occurrence of acicular rutile crystals precipitated from aqueous solution in the high pressure-temperature experiments of Ayers and Watson [1993]. Nachlas and Hirth [2015] presented evidence for experimental validation of the hydrothermal overgrowth mechanism to form rutilated quartz, based on observations of rutile needles precipitated from solution that were passively overgrown by migrating quartz grain boundaries. Here, we present a diffusion geospeedometry analysis on rutilated quartz that has formed via both rutilation mechanisms – exsolution and overgrowth – that can be used to retrieve information about the rates and conditions of the geologic processes that led to their formation.

Chapter 5: Deformation geospeedometry

From a structural perspective, rutile needles are excellent indicators of ductile strain because of their geometry. Their extreme aspect ratio causes them to behave as material lines that rotate during ductile flow of the surrounding quartz. Consequently, rutile needles in quartz in tectonites are typically preferentially oriented into the lineation direction and have been shown to be useful structural indicators of the kinematics of deformation (Figure 5.1) [Mitra 1976; Mitra and Tullis 1979; Bouchez et al. 1984; Blumenfeld et al. 1986; Mancktelow and Pennacchioni 2004].

With the recently-quantified understanding of the kinetics and thermodynamics of Ti substitution in quartz, rutile needles (and their host quartz) have new geochemical importance. In theory, the presence of a rutile inclusion buffers the titania activity of quartz crystallization at unity, simplifying applications of Ti-in-quartz thermometry and barometry [Wark and Watson 2006; Thomas et al. 2010]. However in practice, the presence of concentration gradients between quartz and rutile attests to the sluggish kinetics of Ti in quartz under most crustal conditions. The advantage of slow Ti diffusion is that quartz is a robust recorder that can retain information from multiple and/or complex events. The disadvantage is that confidently resolving trace element concentration gradients at the micrometer-scale is analytically challenging.

Analysis of the Ti content of rutilated quartz using in-situ techniques (EPMA, SIMS) is hampered by the small size and close spacing of the needles as well as the trace levels of Ti in quartz. Owing to the close proximity of rutile to the concentration profile of interest,

Ti measurements are often contaminated by secondary fluorescence. Secondary fluorescence of nearby rutile is even more problematic when measuring trace concentrations because it can obscure trace element peaks even far away from the fluorescing source (e.g., Wark and Watson [2006]). Attempts to measure Ti concentration gradients around rutile needles with an electron probe suggest a Ti enrichment halo (Figure A8.1), although this is almost certainly a result of secondary fluorescence and does not reflect the actual Ti contents of quartz (indeed, it is opposite results from CL analysis – see below). The measured region of fluorescence (ca. 10 μm) is less extensive than previous estimates measured from artificial quartz-rutile mineral pairs [Wark and Watson 2006; Kronz et al. 2012]. Attempts to measure Ti concentrations from rutilated quartz with an ion probe resulted in widely variable Ti measurements from different locations within individual rutilated quartz grains (see Figure A8.2, A8.3). Many of these are interpreted as spurious measurements that reflect contamination owing to partial ionization of the rutile inclusions during ion beam sputtering. Previous attempts to measure the Ti content of rutilated quartz have utilized a broad beam or large area raster to attempt to extract the pre-exsolved Ti content [Adachi et al. 2010]. This approach could perhaps work for ionization techniques such as laser- or ion-beam instruments, but secondary fluorescence in electron-beam techniques is not linearly-proportional and therefore cannot be confidently integrated into a bulk Ti measurement (e.g., Lee [1993]). Instead, we utilize the correlation between Ti content and cathodoluminescence to semi-quantitatively map Ti distribution surrounding rutile needles.

We selected a continuous section of quartzite mylonites in the Pioneer Core Complex (PCC) (Idaho, USA) in which quartz grains are densely rutilated and the rutile needles are strongly oriented into the lineation direction (Figure 5.1). Microstructures of deformed rutile needles in natural samples are similar to those found in experimental samples (Figure 5.2). Because the preferred orientation of rutile needles originating via exsolution is obscured during subsequent ductile flow of quartz, interpreting the origin of rutile needles can be challenging. For this reason we compare analysis of samples from field settings with analysis of experimental samples to investigate the origin of rutile inclusions.

5.3 Geospeedometry of rutilated quartz – theory

We model Ti concentration gradients around rutile needles to obtain the rates and thermal histories recorded in incomplete diffusion profiles. The process of rutilation did not reach completion in our samples, as evidenced by Ti gradients surrounding rutile inclusions (Figure 5.3). Based on the geometry and extent of these gradients we interpret them as incomplete diffusion profiles. To extract kinetic information from analysis of diffusion profiles, we apply the Arrhenius relationship for Ti diffusion in quartz from Cherniak et al. [2007],

$$D_{Ti}^{Qz} = 7 \times 10^{-8} \exp(-273 \pm 12 / RT) \qquad (1)$$

where D_{Ti}^{qz} is the diffusion coefficient for Ti in quartz (m^2/s), R is the universal gas constant, and T is temperature (K).

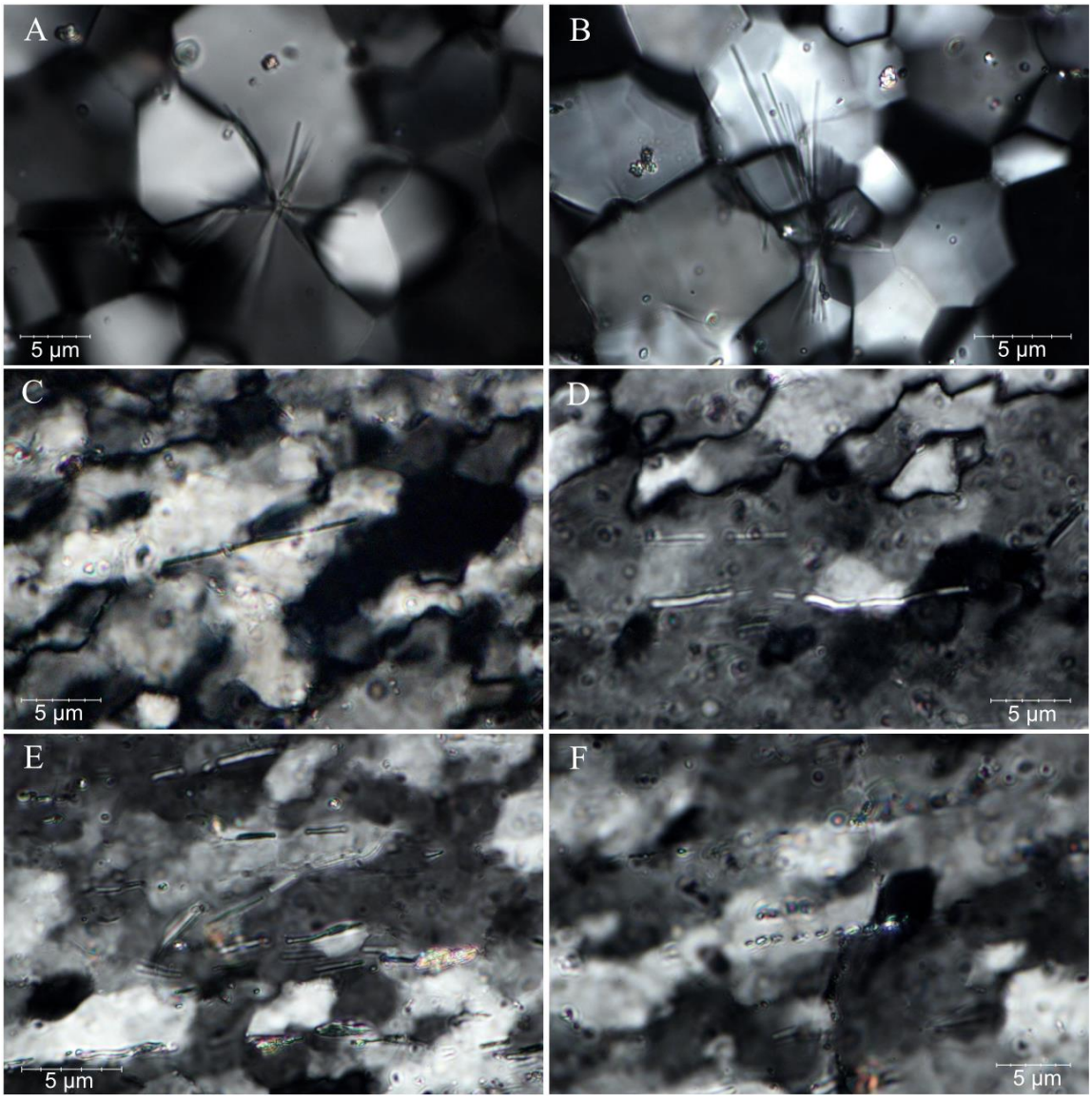

Figure 5.2. Photomicrographs of rutilated quartzite mylonite from rock deformation experiments. Rutile needles in undeformed, annealed experimental samples resemble radiation bundles of acicular crystals emanating from a seed point (A,B). In deformation experiments, needles become rotated into the shear plane and begin to undergo boudinage (C-F). In the highest strain deformation experiments, single rutile needles are found to be segmented into fine-scale boudins (F).

This empirical relationship was derived by measuring diffusion progress between quartz and rutile. Rutile needles in quartz provide a naturally-occurring quartz-rutile diffusion pair that can be used to track diffusion progress. However, in the case of our study, we tested applications of Ti in quartz diffusion parameters to quartz that is deformed in mylonites; Ti mobility in quartz deforming via dislocation creep may be influenced by diffusion pathways and mechanisms that were not occurring in the calibration experiments of Cherniak et al. [2007]. For the purposes of the following discussion, we continue to apply D_{Ti}^{qz} of Cherniak et al. [2007] to deformed quartz, with the stated caveat that volume diffusion does not fully encompass all diffusion pathways that may have operated during development of diffusion profiles in our samples. Later in this manuscript, we use diffusion profiles from experiments conducted under known T-t conditions to calculate a composite diffusive mobility term that incorporates multiple diffusion pathways to approximate diffusive behavior of Ti in deforming quartz.

Diffusion of Ti between rutile needles and the host quartz can, to first-order, be approximated as a half-space binary interdiffusion from an infinite source into a semi-infinite medium. This is represented by a 1-D solution following Crank [1975]:

$$C(x.t) = \frac{1}{2} C_0 erfc(\frac{x}{2\sqrt{Dt}}) \qquad (2)$$

This simple diffusion equation can be used to inverse-model diffusion profiles and extract conditions of formation. While this approach is effective at confidently fitting most

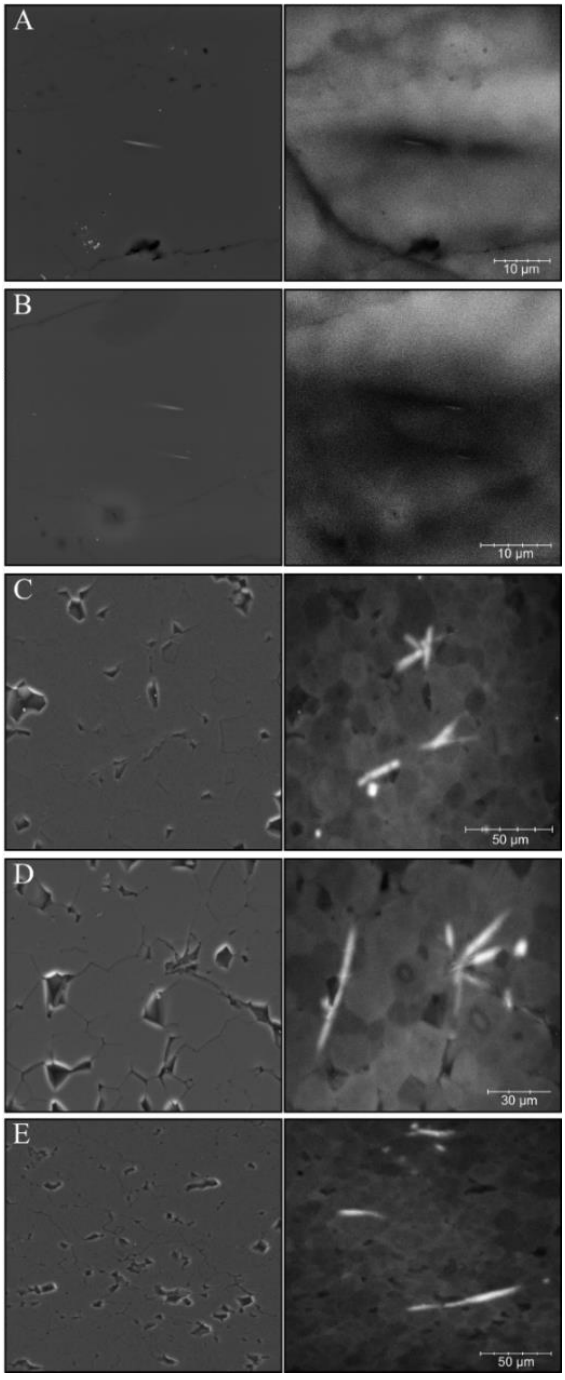

Figure 5.3. Secondary electron images (SEI) and cathodoluminescence images (CL) from natural samples (A-B) and from experimental samples (C-E).

diffusion profiles [Nachlas et al. 2015], in the case of diffusion during dynamic recrystallization, it is possible that multiple diffusion mechanisms are operative and could manifest in the geometry of the distal portions of diffusion profiles (e.g., Clay et al. [2011]; Zhang et al. [2007]). To avoid complications in fitting complex profiles, we have applied the diffusion profile slope method of Watson and Cherniak [2015] that utilizes a linear regression to fit the interior slope of a diffusion profile, S_0,

$$S_0 = \frac{C_h}{2\sqrt{\pi}\sqrt{Dt}} \qquad (3)$$

where S_0 is the slope of the diffusion profile (%/m) and C_h is the normalized height of the initial concentration plateau (equal to 100 for binary interdiffusion and 50 for diffusion at crystal margins; see Watson and Cherniak [2015]). With a measurement of the profile slope and an external constraint of temperature, equation (3) is used to directly calculate the time required for the observed diffusion progress. We use this equation to fit diffusion profiles that formed under isothermal conditions, which is appropriate for high-temperature deformation experiments and is a scenario that has been invoked for the exhumation conditions of other Cordilleran core complexes based on evidence from incomplete reaction textures in the dome rocks [Goergen and Whitney 2012] and in structurally-higher levels (Kruckenberg and Whitney [2011]) and from O isotope thermometry coupled with $^{40}Ar/^{39}Ar$ ages [Mulch et al. 2006].

For the case of Ti diffusion in quartz surrounding rutile inclusions, we can rearrange equation (3) such that the measured slope of a Ti diffusion profile and temperature can be used as input to calculate time,

$$t = 2.84\ x\ 10^{-9}\ \ S_0^{-2}\ \ exp\frac{273}{RT}. \qquad (4)$$

We have applied this technique to incomplete diffusion profiles preserved in natural samples, where it yields diffusion durations of c. 1-10 Myr, and to profiles in experimental samples, where it yields durations of ca. 10-100 days (Figures 5.4, 5.5).

We compare our approach for modeling Ti around rutile inclusions by performing this analysis on the quartz-rutile pair reported by Morgan et al. [2013]. For their Figure 8B, we solve the diffusivity-time product of Dt to be 1.70×10^{-11} m^2 which equates to a duration of 149 yr at 800 °C (compare with Dt = 3.34×10^{-11} m^2 and a duration of 300 yr at 800 °C of Morgan et al. [2013]) (Figure A8.4). The discrepancies between our results likely reflects differences in the selected diffusion geometry; we model Ti diffusion into quartz as diffusion at a crystal margin, which is effectively the half-space for the semi-infinite medium model applied by Morgan et al. [2013]. Thus, the remarkable agreement between results of our analysis and of the analysis of Morgan et al. [2013] is a testament to the robustness and reproducibility of modeling Ti diffusion around rutile inclusions.

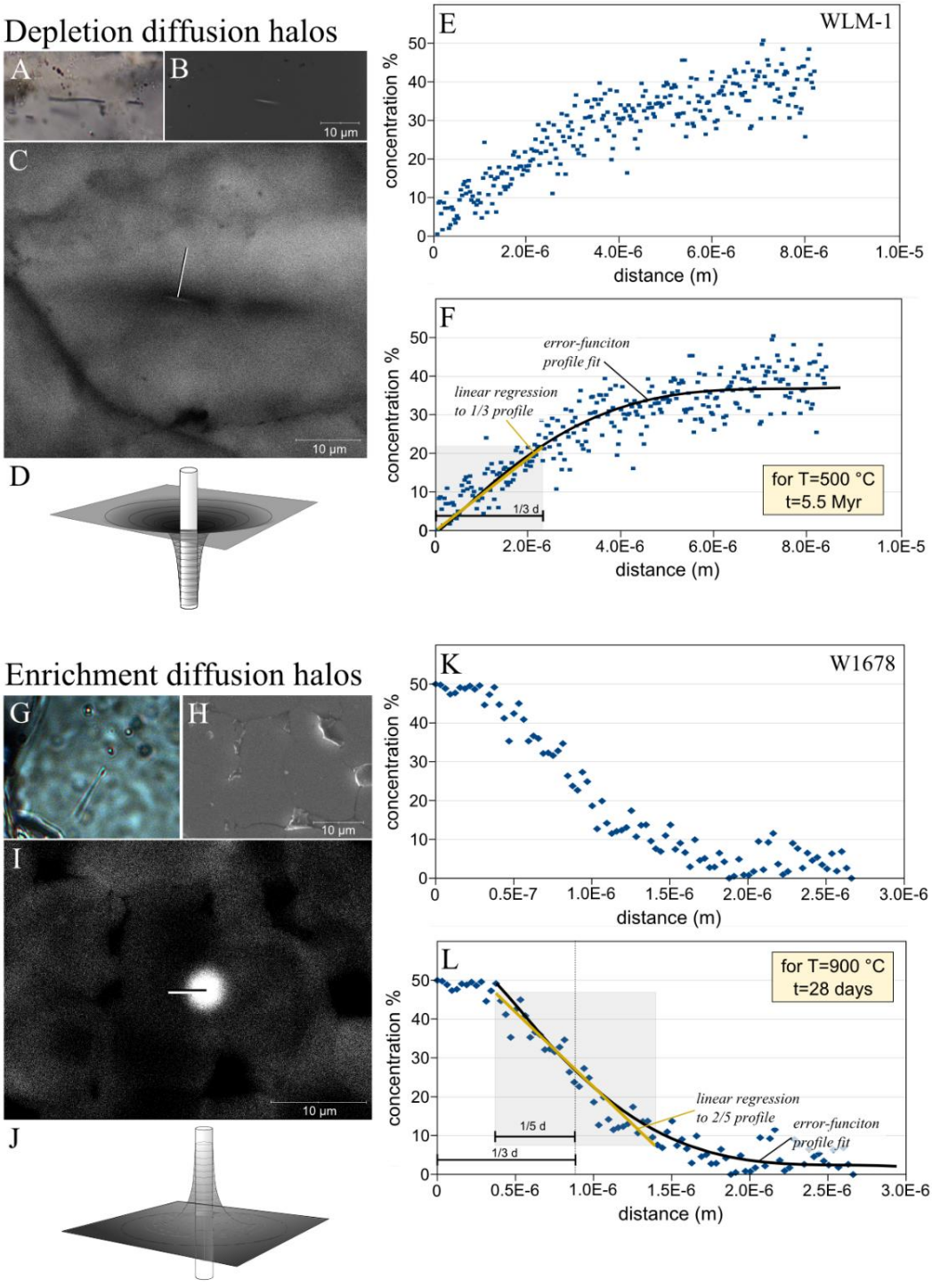
Depletion diffusion halos
A
B
10 µm
C
10 µm
D
E
WLM-1
concentration %
distance (m)
F
error-funciton profile fit
linear regression to 1/3 profile
1/3 d
for T=500 °C t=5.5 Myr
concentration %
distance (m)
Enrichment diffusion halos
G
H
10 µm
I
10 µm
J
K
W1678
concentration %
distance (m)
L
for T=900 °C t=28 days
linear regression to 2/5 profile
error-funciton profile fit
1/5 d
1/3 d
concentration %
distance (m)

Figure 5.4. Technique for modeling Ti diffusion profiles surrounding rutile needles for both depletion diffusion profiles (A-F) and enrichment diffusion profiles (G-L). The intersection of a rutile needle with the thin section surface is identified in petrographic microscope (A,G), then detected in a secondary electron image (B,H) and analyzed with cathodoluminescence (C,I) to measure the Ti concentration field surrounding rutile. Depending on the direction of Ti flux, rutile may be exsolving from quartz, indicated by a dark CL halo (C-D), or rutile may be dissolving into quartz, indicated by a bright CL halo (I-J). The CL intensity is measured along a linear transect from rutile into the surrounding quartz (C.I), revealing a gradient in inferred Ti content that resembles a diffusion profile (E,K). Profiles are normalized to a concentration percent of 0-50 for diffusion at a crystal margin, trimmed from max-min, and a regression is fit to the linear portion of the profile. For cases of depletion halos, the linear regression is measured from 1/3 the distance of the profile starting at the origin (i.e., rutile) (F). For cases of enrichment halos, where complexities in the diffusion profile may exist due to the nature of the crystal interface that results from overgrowth rutilation, the linear regression is measured from 2/5 of the distance of the profile centered about the 1/3 of the profile width (L). By assuming a fixed temperature, a diffusion coefficient can be calculated and used with the measured diffusion profile slope to calculate a duration of diffusion, which is c. 10^0-10^1 Myr for natural samples (F) and is c. 10^1-10^2 days for experimental samples (L).

In the case of our experiments, where the T-t conditions are known, we can rearrange equation 4 to solve for the diffusion coefficient for Ti in quartz:

$$D = 198.8\, S_0^{-2}\, t^{-1} \qquad (5)$$

The isothermal conditions of experiments, and the argued isothermal conditions of some ductile shear zones in the Earth, enable use of a diffusion coefficient that is spatially temporally invariant. However, in the case of diffusion during monotonic cooling, Watson and Cherniak [2015] extend the slope profile method to solve for cooling rates:

$$logS_0 = 2.504 - \frac{1}{2}logD_0 - logT_i + \frac{1}{2}logE_a + \frac{1}{2}\log(\dot{T}) + (26.11\frac{E_a}{T_i}) \qquad (6)$$

where S_0 is the profile slope (%/m), D_0 is the diffusion coefficient (m^2/s), Ti is the initial temperature (K), E_a is the activation energy (kJ/mol), and $\dot{T}$ is the cooling rate (K/s). We apply equation (6) to constrain cooling histories of a ductile shear zone based on the geometry and extent of incomplete diffusion profiles in mylonitized quartz grains.

5.4 Analytical Methods

Cathodoluminescence analysis for this study conducted with two different electron microscopes and CL detectors: a JEOL-6700F FEG SEM equipped with a Gatan Mono-CL detector (University of Minnesota, College of Science and Engineering Characterization Facility) and a JEOL 5800LV FEG-SEM equipped with a KE Developments CL detector (USGS Denver Microbeam Laboratory). A full-spectrum CL analysis collected using the UMN-SEM from a high-Ti experimental quartz crystal containing 230 ± 4 ppm Ti shows a broad peak in the blue range (~420 nm) (Figure S2 of Nachlas and Hirth [2015]). Hyperspectral CL using the USGS-SEM reveals that the CL signal is dominated by blue luminescence in grain interiors, grain boundaries, and adjacent to acicular rutile inclusions. Based on these observations, taken with past correlations between CL signal and in-situ trace element measurements (e.g., Gotze et al. [2001]; Leeman et al. [2012]; Kidder et al. [2013]), we interpret CL intensity as a qualitative proxy for Ti content in quartz. Results of diffusion analysis using CL images collected from both SEMs are statistically indistinguishable (Tables A9.1, A9.2) and are aggregated for analysis and interpretation.

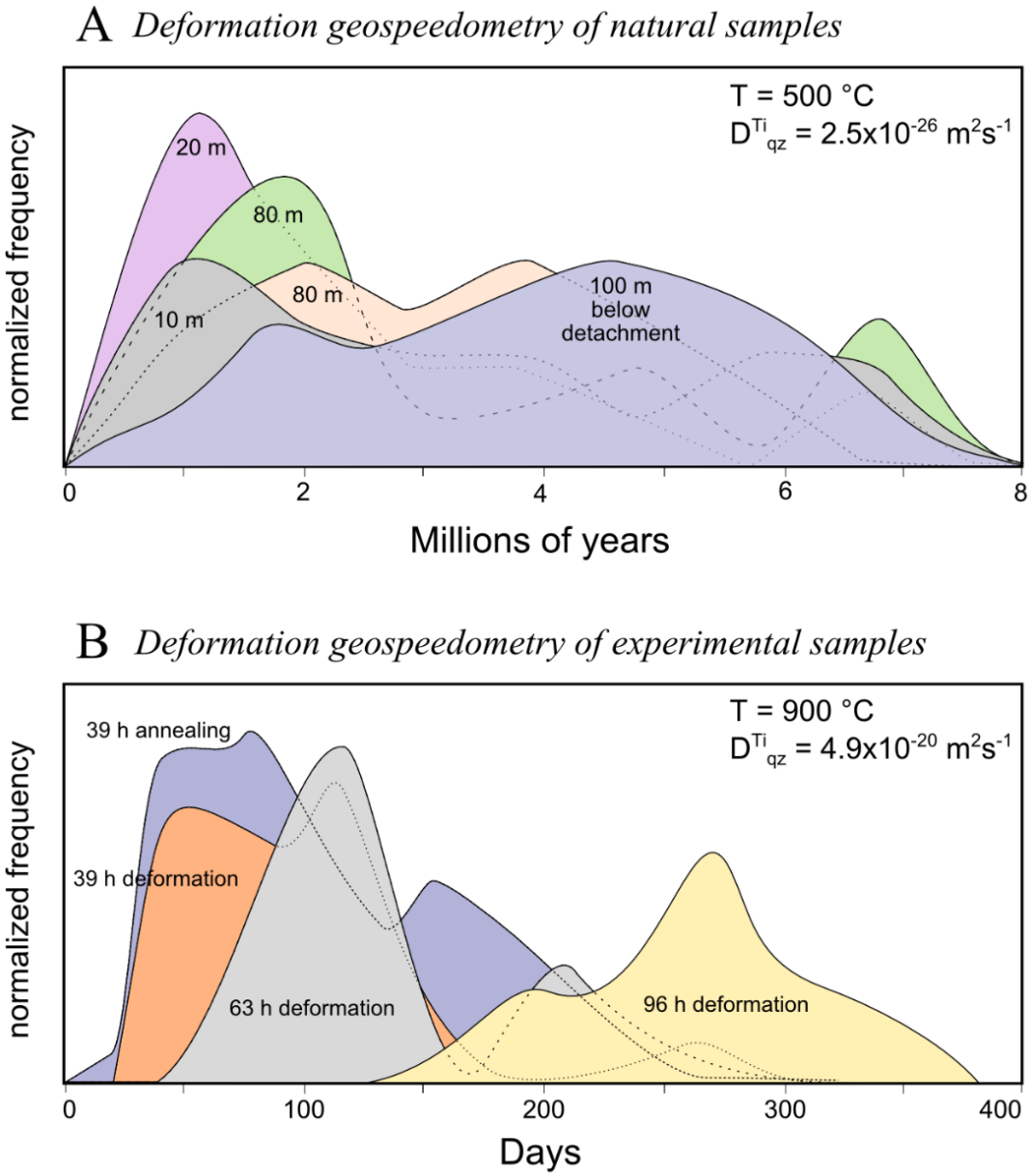

Figure 5.5. Timescales obtained from inverse-modeling of measured diffusion profiles. Results of diffusion modeling show that deformation timescales from natural samples (A) are found to be unique for different levels of the shear zone and experimental samples (B) are found to be unique for experiments conducted for different amounts of time. Diagrams calculated assuming isothermal conditions with a fixed diffusion coefficient. See Figure A8.5 and A8.6 for separate data plotted as separate histograms.

Electron probe microanalysis was conducted using the JEOL-8900 at the Microbeam Facility at the USGS Denver. An analytical routine similar to Donovan et al. [2011] was followed that yielded calculated detection limits of ~20 ppm with standard error of each measurement ranging from 5-8 ppm. Analysis of NIST SRM 610, 612, 614 trace element glasses, Ti-doped silica glasses [Chapter 2], and high-Ti quartz crystals (QTiP series of Thomas et al. [2010]) as reference materials demonstrated acceptable reproducibility (ca. 10% relative error) at concentrations <100 ppm.

Ion probe analysis was conducted using the Cameca IMS-1280 at the Northeast National Ion Microprobe Facility (NENIMF) at Woods Hole Oceanographic Institute (WHOI). In-situ measurements of Ti contents of rutilated quartz grains were made by making multiple analyses within different regions of recrystallized quartz grains. Analytical protocols including crater dimensions for SIMS analysis can be found in Nachlas et al. [2014].

5.5 Geospeedometry of quartz deformed in nature

We selected a 100 m section of quartzite mylonites exposed in the detachment of the Pioneer Core Complex (PCC) as a case study for applying deformation geospeedometry to reconstruct the rates and conditions of deformation in a crustal shear zone. The PCC is an ideal locality to test the accuracy of quartz deformation geospeedometry because: (1) the thermal and exhumation history of the complex has been studied in detail and geochronological data exist for comparison with results of our diffusion analysis, and (2)

exhumation of the PCC was localized in part within a continuous section of quartzite mylonites in which quartz grains are densely and pervasively rutilated, allowing comparison of geospeedometry results between multiple samples across the width of the shear zone. Temperature is estimated by combining thermometry estimates from past studies with new results from quartz microstructures, Ti-in-quartz thermometry, and Zr-in-rutile thermometry. By estimating both temperature and time from quartz using independent means (as opposed to obtaining temperature estimates from different petrologic systems) we seek to determine if quartz geospeedometry produces timescale estimates that are consistent with existing constraints on deformation.

5.5.1 Geologic Setting – Pioneer Core Complex

The Pioneer Core Complex of central Idaho, USA, is a domal culmination of metamorphic rocks in the hinterland of the Sevier orogenic belt. The PCC is a Cordilleran-style metamorphic core complex that formed following gravitational spreading of thickened orogenic crust during the late-stages and immediately following the Sevier orogeny [Wust 1986; Vogl et al. 2012]. The PCC is characteristic of other core complexes in the northern North America Cordillera in that it preserves abundant evidence for melt-present deformation in the footwall and detachment zone, evidenced by complex overprinting relationships and narrow age windows for cross-cutting and transposed melt injection features (e.g., Vanderhaege et al. [1999]; Teyssier et al. [2005]; Gordon et al. [2008]; Vogl. et al. [2012]; Whitney et al. [2013]). Post-magmatic stages of deformation in the PCC are

interpreted to coincide with brittle-ductile detachment faulting and infiltration of meteoric fluids [McFadden et al. 2015]. The PCC is distinct from other Cordilleran core complexes in that it records a longer time interval from syn-magmatic dome deformation (50-46 Ma) to post-magmatic detachment deformation (38-33 Ma) (Vogl et al. [2012] and references therein).

The PCC is comprised of a lower plate of variably- and complexly-deformed Archean gneisses of the Wildhorse Gneiss Complex and Eocene granitoids of the Pioneer Intrusive Suite that are overlain by an upper plate of unmetamorphosed Paleozoic sediments and Tertiary volcanic and sedimentary strata (Figure 5.6) [Wust, 1986; O'Neill and Pavlis, 1988; Silverberg, 1990; Diedesch, 2011]. Juxtaposing the upper and lower plates is the brittle-ductile Wildhorse detachment system, a ~2 km package of mylonitized, metamorphosed, and intruded metasedimentary units that accommodated much of the extensional strain in the PCC [Wust, 1986; Silverberg, 1990; Diedesch, 2011; Vogl et al. 2012]. For the purposes of our study, we refer to the entire ductiley-deformed middle plate as the Wildhorse Shear Zone (WSZ). This encompasses the Hyndman Shear Zone, defined by Silverberg [1990] as the zone of intense ductile strain observed at the Lower/Middle plate boundary. The lower bound of the WSZ grades downwards with progressively higher melt fraction and deformation intensity into the Pioneer Intrusive Suite (PIS) and complexly deformed gneisses of the Wildhorse gneiss complex (Figure 5.6). The upper bound of the WSZ is the Wildhorse detachment fault, a W-dipping brittle extensional feature that juxtaposes unmetamorphosed hangingwall against ductiley sheared footwall of

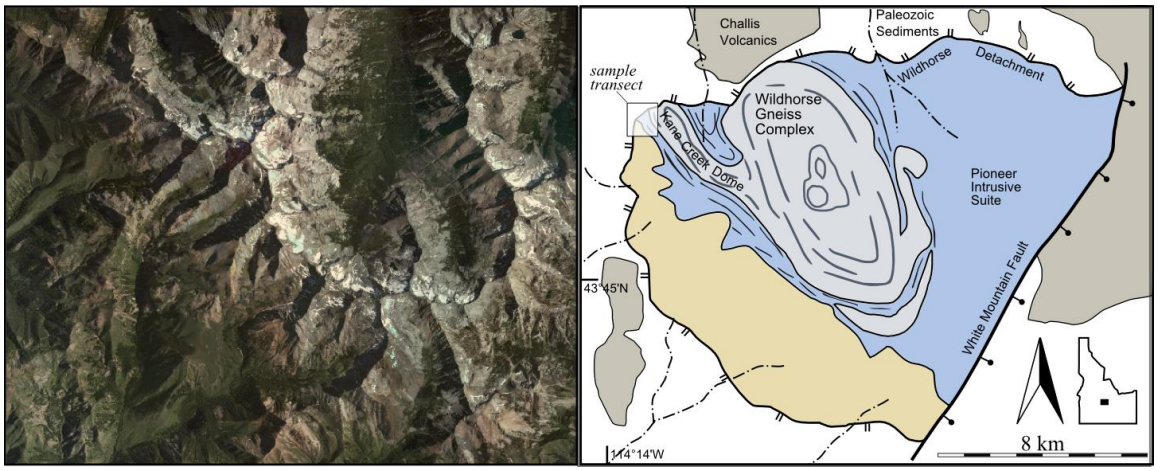

Figure 5.6. Satellite image and geologic map of the Pioneer Core Complex, Idaho. The Pioneer Mountains are cored by the Wildhorse Gneiss Complex, a domal culmination of partially-molten para- and orthogneisses overlain by the Pioneer Intrusive Suite that grades into the strongly deformed metasedimentary units that compose the Wildhorse Detachment Shear Zone. The sample transect selected for this study was collected from the NW margin of the complex on the W limb of the Kane Creek Dome. Geologic map redrawn from Wust [1986] and Vogl et al. [2012].

the middle plate [Wust 1986; Diedesch 2011]. Based on coincidence between kinematic indicators on the detachment surface and underlying mylonites of the middle plate, O'Neill and Pavlis [1988], and later corroborated by Diedesch [2011], interpreted detachment faulting to reflect a direct progression from higher-temperature ductile shearing to lower temperature brittle faulting.

The WSZ is comprised of Neoproterozoic-Ordovician quartzite, marble, calc-silicate, and metapelite estimated to be c. 1.8-2.1 km in vertical thickness [Diedesch 2011]. Near the top of the WSZ (c. 250 m below the detachment), deformation was partially localized within a continuous sequence (90-150 m) of quartzite mylonites composed of the

Kinnikinic formation. The Kinnikinic quartzite is an Ordovician quartz arenite (~99% quartz, James and Oaks [1977]) characterized by detrital zircons of Meso- and Paleoproterozoic and Archean age [Diedesch 2011]. The Kinnikinic is a target for our study because it contains quartz grains that are densely rutilated with microscopic rutile needles that are strongly oriented into the lineation direction.

5.5.2 Existing temperature-time constraints

The timing of deformation and exhumation in the core of the PCC is constrained by ages and structural relationships of melt-present deformation features. High-grade metamorphism of the lower and base of the middle plate through voluminous felsic injections and local partial melting occurred in the Eocene [Vogl et al. 2012]. U-Pb ages of monazite and zircon from layered migmatites, magmatically-foliated granodiorites, and folded and boudinaged leucogranitic intrusions range from c. 50-46 Ma, constraining the timing of intrusion of the PIS, deformation of the lower plate, and deformation at the base of the middle plate. A high-angle, cross-cutting leucocratic dike was dated at 46 Ma, interpreted to reflect the cessation of syn-magmatic deformation in the dome of the complex.

The next event resolved along the deformation history is defined by timing of brittle-ductile detachment deformation documented by $^{40}Ar/^{39}Ar$ ages of micas that indicate cooling below ~400 °C occurred from 38-35 Ma [Silverberg, 1990; McFadden et al., 2015] and

$^{40}Ar/^{39}Ar$ ages of K-feldspar that cooled below ~200 °C by 33 Ma [Silverberg, 1990]. U-Th)/He dating of apatite indicates cooling below ~75 °C by 29 Ma [Vogl. et al 2010; Carmenate et al. 2011]. There is a gap in ages between the early, syn-magmatic deformation of the footwall from 50-46 Ma and lower-temperature detachment faulting.

Compared to existing geochronology in the PCC, estimates for temperature of deformation and metamorphism are relatively sparse. Temperature estimates for deformation of the WSZ are limited to metapelitic units located near the base of the middle plate. Highest temperatures in the middle plate are recorded within contact aureoles located 25 m from intrusions of the PIS, where assemblages indicative of temperatures above the stability field of the second sillimanite isograd suggest temperatures >650 °C at moderate pressures [Holdaway 1971; Pattison and Tracy 1991]. At a distance 400 m from the contact with the PIS, assemblages are characterized by cordierite-andalusite-staurolite (garnet absent) in gneissic quartzite, suggesting temperatures of 500-700 °C and 200-600 MPa [Silverberg, 1990; Ganguly, 1979]. Calculations from garnet-biotite and garnet-plagioclase thermometry in schists near the base of the middle plate indicate temperatures in the range of 590-690 °C [Silverberg, 1990].

5.5.3 Estimating temperature of deformation

To add new temperature data for deformation of the WSZ to better apply applications of diffusion geospeedometry, we have tested multiple techniques to evaluate deformation

temperatures. These geothermometers are more or less sensitive to deformation and therefore likely record different intervals of the deformation history.

5.5.3.1 Zr-in-rutile thermometry

To estimate temperatures from nodular, detrital rutile grains in the Kinnikinic quartzites, we apply the Zr-in-rutile thermometer [Zack et al., 2004; Watson et al., 2006] following the experimental calibration of Tomkins et al. [2007] for pressures within the α-quartz field:

$$T = \frac{83.9+0.410P}{0.1428-R\ln(\phi)} - 273 \qquad (7)$$

where T is temperature (°C), P is pressure (kbar), R is the universal gas constant, and φ is Zr concentration in rutile (ppm).

Rutile grains in two samples were analyzed for Zr concentrations. Measured Zr concentrations range from 850 – 1450 ppm, equating to temperatures of 720 – 770 °C at 5 kbar. Smaller grains had lower Zr contents, and replicate measurements for each grain were in agreement. There are two possible interpretations of these high-temperature results, either 1) these concentrations preserve an earlier magmatic/volcanic history of rutile grains prior to erosion and Ordovician deposition, or 2) these temperatures reflect the conditions of burial and residence in the mid-lower crust prior to extensional deformation.

It may be possible to discriminate between these two interpretations based on the known diffusion parameters of Zr in rutile. Using experimentally-derived diffusion rates of Zr in

rutile [Cherniak et al. 2007b], it would require c. 100 Myr at 700 °C to homogenize rutile grains with 500 μm diameter. Based on the geological history of this region of the Cordillera, it is possible that Ordovician quartzites were buried during Cretaceous crustal thickening, resided in the middle crust throughout the Cretaceous, and were later exhumed with the PCC during extension. For this reason, we interpret high temperatures from Zr-in-rutile to be compatible with burial and residence history of the Kinnikinic quartzite prior to involvement in detachment exhumation.

5.5.3.2 Ti-in-quartz thermometry

We have applied the Ti-in-quartz thermobarometry calibration of Thomas et al. [2010] to calculate the temperatures of recrystallization for quartz mylonites in the WSZ,

$$RTlnX_{TiO_2}^{quartz} = -60952 + 1.520 \cdot T - 1741 \cdot P + RTlna_{TiO_2} \quad (8)$$

where R is the ideal gas constant, T is temperature (K), $X_{TiO_2}^{quartz}$quartz is the mole fraction of TiO_2 in quartz, P is pressure (kbar), and a_{TiO2} is activity of TiO_2.

To overcome difficulties with contamination owing to the abundance of microscopic rutile inclusions, we take our lowest SIMS measurements of Ti content as most representative, with the assumption that higher concentrations were affected by contamination. Ti concentrations in quartz were measured in a sample from the top of the section (WLM-12) to be 19-23 ppm and in a sample from the middle of the section (WLM-9) to be 3-6 ppm

in quartz interiors and 0.5 ppm in cross-cutting quartz veins (Figure A8.3). Abundant nodular and acicular rutile is present throughout the thin section, lending confidence to the assumption of a_{TiO2}=1 for applications of quartz thermobarometry.

Estimates of pressure for applications of quartz thermometry are derived from phase equilibria and major element barometry. Assemblages of cordierite-andalusite-staurolite (garnet absent) found in contact aureoles in schist adjacent to intrusions of the PIS [Silverberg 1990] indicate pressures in the upper part of the andalusite stability field, around 3-5 kbar [Pattison and Tracy 1991]. Al-in-hornblende barometry from metapelites near the base of the middle plate records pressures of 2-2.8 kbar [Silverberg 1990].

We assume a pressure of 3 kbar for applications of Ti-in-quartz thermometry. With the concentrations measured, this equates to a temperature of 460-475 °C at the top of the section and 370-390 °C in quartz interiors and 280 °C in cross-cutting vein quartz in the center of the section. Overall, we interpret a range in temperatures from quartz thermometry of c. 370-470 °C for ductile deformation of quartz and c. 300 °C for the onset of brittle deformation in the shear zone. This range of temperature estimates is similar to constraints from Ti-in-quartz thermometry applied to reconstruct the deformation conditions in the Shuswap core complex, were Ti contents from different recrystallization microstructures provide a reasonable estimate of deformation and exhumation of a ductile quartzite shear zone [Nachlas et al. 2014].

5.5.4 Microstructures

5.5.4.1 Quartz microstructures

Microstructures for deformed quartz and feldspar in the Kinnikinic Formation are used as additional independent constraints on deformation conditions. Quartz microstructures indicate dynamic recrystallization via combined grain-boundary bulging and progressive subgrain rotation recrystallization [Hirth and Tullis 1992; Law 1990; 2014]. At the top of the Kinnikinic section, quartz microstructures are characterized by elongate quartz ribbons, the long-axis of which is sub-parallel to the foliation plane, that are mantled by subgrains defining an oblique fabric (Figure 5.7A, 5.8A). Grain boundary bulges are occasionally observed at the margins of quartz ribbons or subgrains and exhibit long-range (>2x bulge diameter) and delicate bulging structures (Figure 5.8A). In the middle of the section, subgrains are present but less abundant, and small grain boundary bulges are found along the margins of most subgrains (Figure 5.7B, 5.8B). Quartz ribbons commonly display undulose extinction with a weak checkered pattern. At the base of the section, quartz grains are flattened and elongated into the shear plane and exhibit sweeping undulose extinction. Subgrains are poorly developed at the base of the section, but grain boundary bulges are nearly ubiquitous along the margins of nearly all quartz subgrains (Figure 5.7C, 5.8C). Grain boundary bulging at the base of the section is characterized by short-range (<1x bulge diameter) bulging structures.

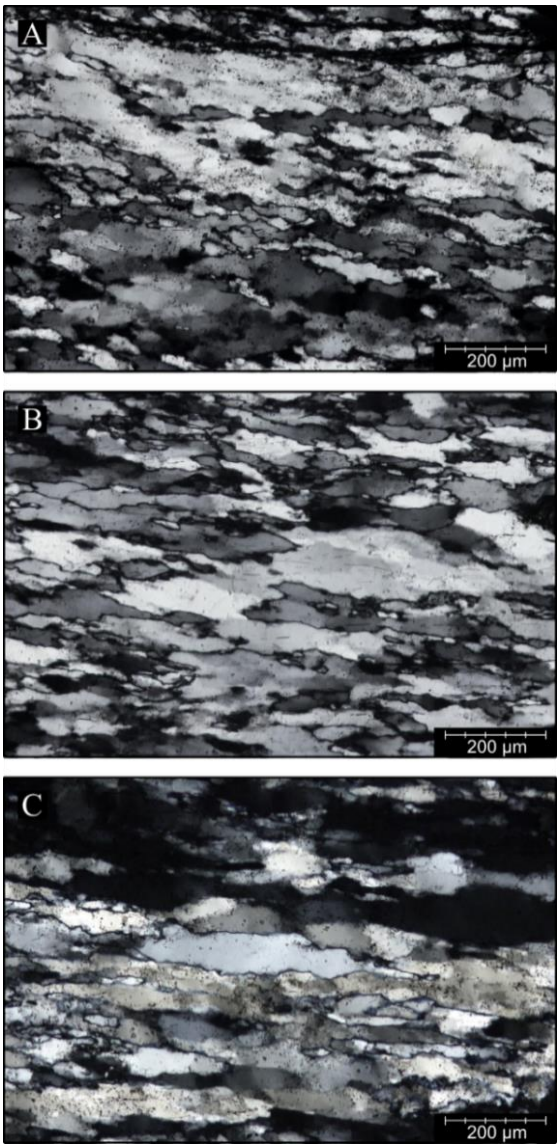

Figure 5.7. Quartz microstructures from the Kinnikinic quartzite in the WSZ. Cross-polarized images of quartz microstructures from the top (A), center (B), and base (C) show the range of quartz microstructures exhibited by samples selected for diffusion analysis. Samples in the highest levels of the detachment (closest to the hangingwall) are dominated quartz microstructures that suggest the operation of subgrain rotation recrystallization (A), which grades into combined subgrain-rotation and grain boundary bulging recrystallization in the center of the shear zone (B), with quartz in the samples from the base of the shear zone exhibiting evidence for grain boundary bulging as the dominant deformation mechanism (C). Thin sections cut parallel to XZ direction (parallel to lineation, perpendicular to foliation). Shear sense is sinistral, shear plane is subhorizontal.

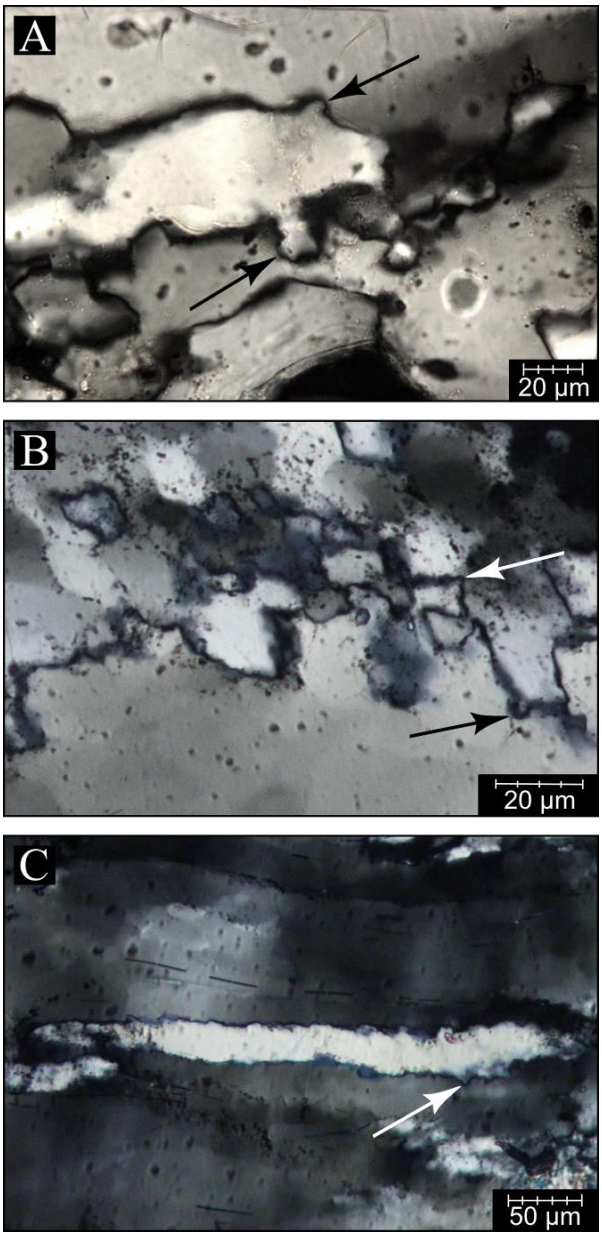

Figure 5.8. Evidence for subgrain rotation and grain boundary bulging deformation mechanisms in quartz. Samples at the top of the shear zone contain long-range grain boundary bulges (A). In the center of the shear zone, fine-scale grain boundary bulges are present over-printing subgrain boundaries within a fabric of subgrains (B). In samples from the base of the shear zone, elongated quartz ribbons commonly exhibit finely serrated grain boundaries with evidence for local grain boundary bulging into neighboring grains that exhibit sweeping undulose extinction (C).

Malekpour [2012] measured quartz recrystallization fabrics from four samples across the Kinnikinic section. This analysis showed that c-axis fabric patterns resemble asymmetrical single girdles with adjacent maxima of c-axes oriented ~60 ° from the Y direction. Asymmetry of quartz fabrics is consistent with top-to-NW deformation kinematics. Fabrics are relatively consistent from all levels of the shear zone, although a slight progression of c-axes toward the Y-axis maximum direction is observed at the base of the shear zone. Overall, these quartz fabrics suggest that quartz deformed predominantly by rhomb <a> slip, with minor contributions of prism <a> and basal <a> slip systems [Law, 1990; 2014]. Interpreting these microstructures in terms of deformation conditions, we can approximate the temperatures of quartz recrystallization to be roughly 400-550 °C, at modest strain rates and water-present conditions [Passchier and Trouw, 2005].

5.5.4.2 Feldspar microstructures

Microstructures of feldspar provide additional insight into deformation conditions in the shear zone. Feldspar occurs as isolated porphyroclasts comprising ~10% of the sample mineralogy. The majority of feldspar porphyroclasts are orthoclase with minor plagioclase. Feldspar porphyroclasts in the WSZ exhibit predominantly cataclastic microstructures indicative of brittle deformation. Feldspar porphyroclasts show a strong shape-preferred orientation, with many clasts inclined synthetically or antithetically to the shear plane. Where porphyroclasts have been divided by sliding along brittle microfractures, feldspars

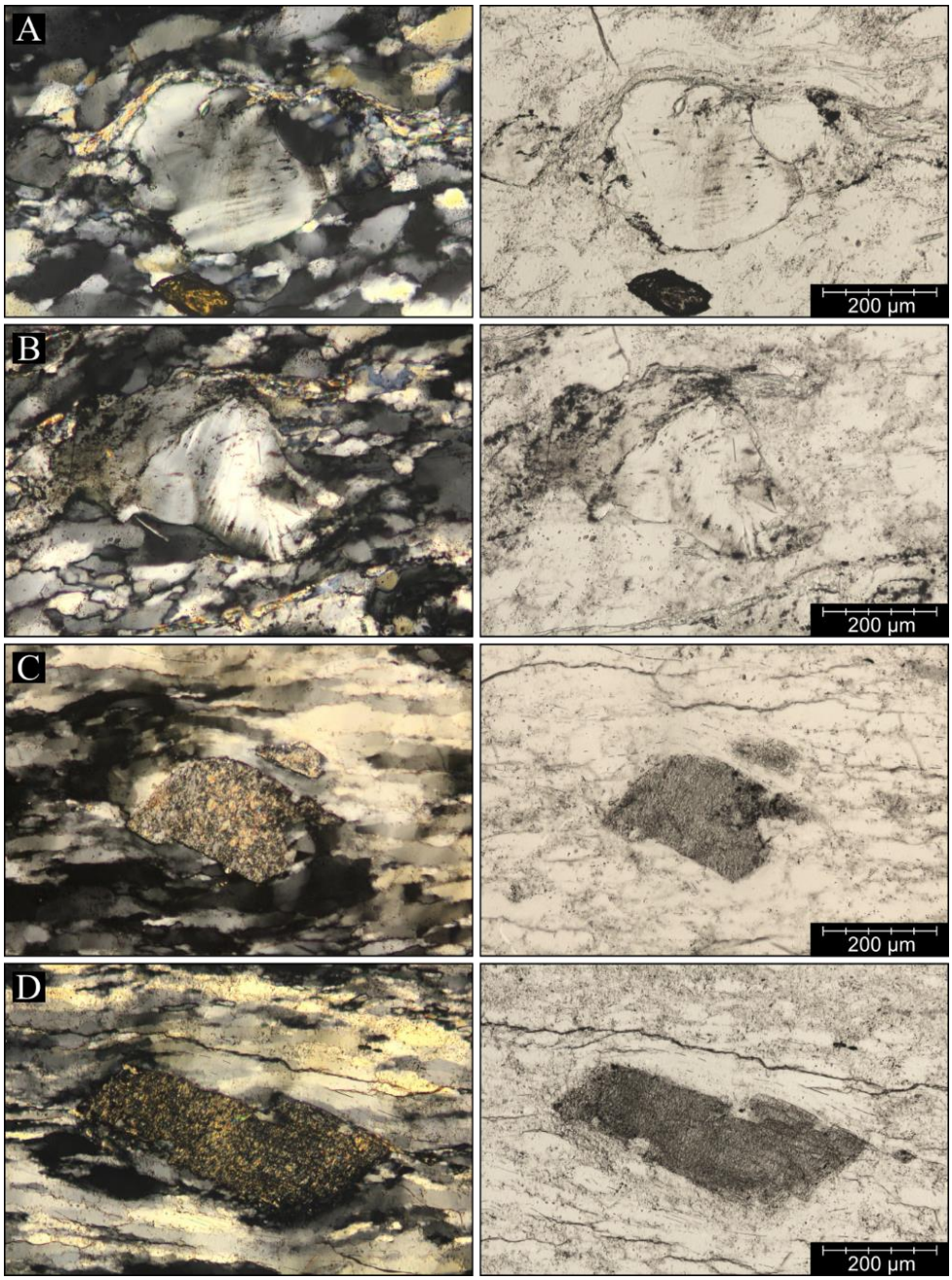

Figure 5.9. Comparison of feldspar microstructures from the top (A-B) and base (C-D) of the shear zone. Images in the left column taken under cross-polarized light, images in the right column taken under plane-polarized light. Thin sections cut parallel to XZ direction (parallel to lineation, perpendicular to foliation). Shear sense is sinistral, shear plane is subhorizontal.

are found to exhibit imbrication that, together with shape asymmetry, can be used to determine shear sense.

There is limited evidence for plastic deformation of feldspar. Some grains preserve undulose extinction (Figure 5.9), indicative of intracrystalline plastic deformation, although no clear evidence for dislocation recovery (subgrains, grain boundary migration microstructures) is observed. Deformation twins, bent twins, and undulose extinction in feldspar suggest deformation mainly by internal cataclasis assisted by minor dislocation glide [Pryer, 1993]. In the upper levels of the WSZ, feldspar porphyroclasts contain perthite lamellae that taper towards grain boundaries oriented in the shortening quadrants of strain.

Perhaps the most significant difference in feldspar microstructures across the width of the shear zone is the variable degrees of sericitization. At the top of the shear zone, neoblastic white micas are present around the margins, within grain fractures, and in wings and tails of porphyroclasts (Figure 5.9). At the base of the section, pervasive and complete sericitization of feldspar is evidenced by porphyroclast pseudomorphs composed of fine-grained white mica (Figure 5.9). It is apparent that sericitization was more pervasive towards the base of the section, but it is unclear if this is a result of the temperature of deformation, the amount of fluid-rock interaction during deformation, or the duration of deformation and thus time allowed for sericite reaction progress.

Brittle deformation of feldspars is commonly interpreted to reflect greenschist facies deformation conditions (e.g., Fitz Gerald and Stunitz [1993]; Tullis [2002]) corresponding to temperatures of c. 300-400 °C [Passchier and Trouw, 2005].

5.5.4 Results of Ti diffusion modeling during natural deformation

Deformation geospeedometry was applied to rutilated quartzites in the WSZ by measuring 138 diffusion profiles from 5 samples across the 100 m shear zone. Two samples from the same outcrop location were analyzed separately (WLM-2 and -3) to evaluate reproducibility. Measurements of profile thicknesses and geospeedometry results are shown in Figure A8.5 and Table A9.1. Diffusion profile thicknesses range from 3-14 μm, and measured profile slopes (S_0) range from ~$2x10^{-6}$ – $2x10^{-7}$ %/m (Table A9.1). Solving the diffusion equation using the measured profiles and with an assumed constant temperature (e.g., 500 °C) shows that each sample preserves a unique result (Figure 5.5). Diffusion modeling results from two replicate samples are indistinguishable.

Diffusion modeling results can be interpreted in two ways; either the base of the shear zone was deforming for ~3 Myr longer than the top (assuming T=500 °C), or the base of the shear zone was deforming at ~25 °C hotter (assuming deformation over 1 Myr). Cooling rates can also be extracted from modeled diffusion profiles to estimate the thermal history during deformation at different levels of the shear zone (Figure 5.11). If cooling started from an initial temperature of 550 °C, results suggest that cooling rate is higher in upper

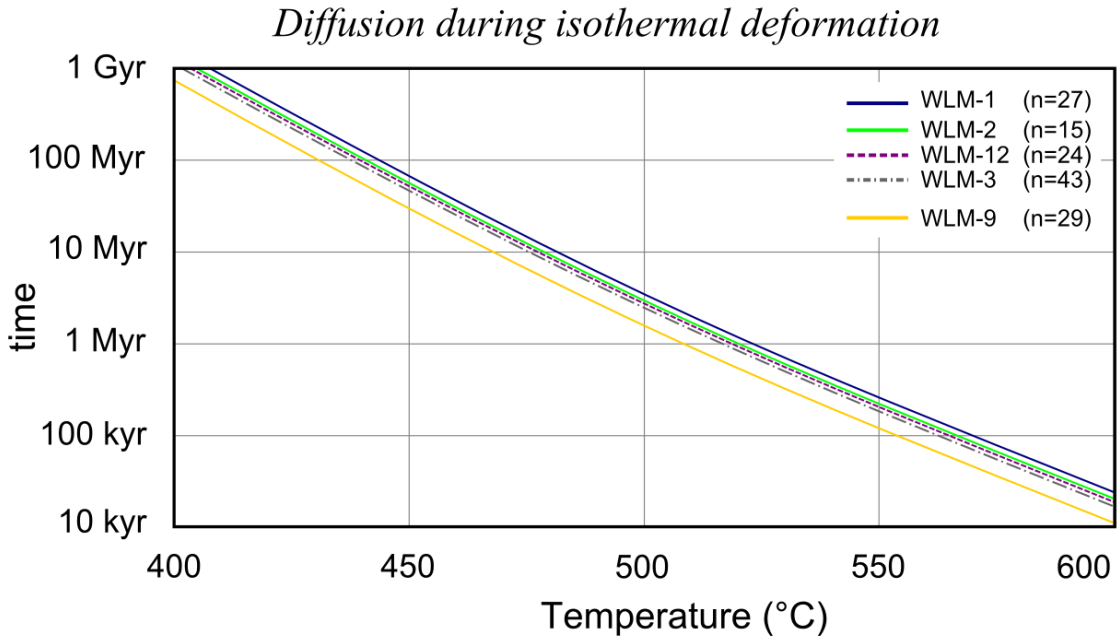

Figure 5.10. Temperature-time conditions calculated from measured diffusion profiles.

levels of the shear zone, increasing from ~20 °C/Myr at the base to 45 °C/Myr at the top. Similarly, assuming a fixed cooling rate (e.g., 10 °C/Myr), our results suggest that the base of the shear zone was initially ~25 °C hotter than the top of the shear zone.

5.6 Geospeedometry of quartz deformed in experiments

The accuracy of deformation geospeedometry is evaluated by testing this method on experimental samples where relevant variables (temperature, time, chemical environment, strain) are known. This is particularly valuable for studies of diffusion, where

extrapolations across multiple orders of magnitude enable use of the same diffusion laws for experiments that run a few days (at high temperatures) as for natural shear zones that deformed for millions of years (at moderate temperatures). We took advantage of the scale-independence of diffusion to test our deformation geospeedometer on experimental samples of quartz aggregates that were ductiley-deformed at a fixed temperature for increasing intervals of time [Nachlas and Hirth 2015]. Because laboratory experiments allow characterization of the starting materials prior to high-strain deformation, we document a more complete picture of deformation and rutilation than can be resolved in most geologic settings. Additionally, because variables in the diffusion equation (T, t) can be controlled in the laboratory, we are able to use diffusion profiles measured from our samples to solve for the diffusion coefficient at the conditions of our experiments. Our analysis suggests that diffusive mobility in our experiments differs from existing experimental calibrations [Cherniak et al. 2007], and we discuss possible explanations for this, including differences in experimental conditions (high-pressure and water-present or atmospheric-pressure and water-absent) and/or the effect of dynamic recrystallization on Ti diffusion.

5.6.1 Experiment design

Experiments were conducted at a singular, elevated P-T condition (10 kbar, 900 °C) on Ti-doped quartz aggregates that were sheared under steady-state flow conditions [Nachlas and Hirth 2015]. Samples were deformed by applying a σ_1 load at fixed axial displacement rate

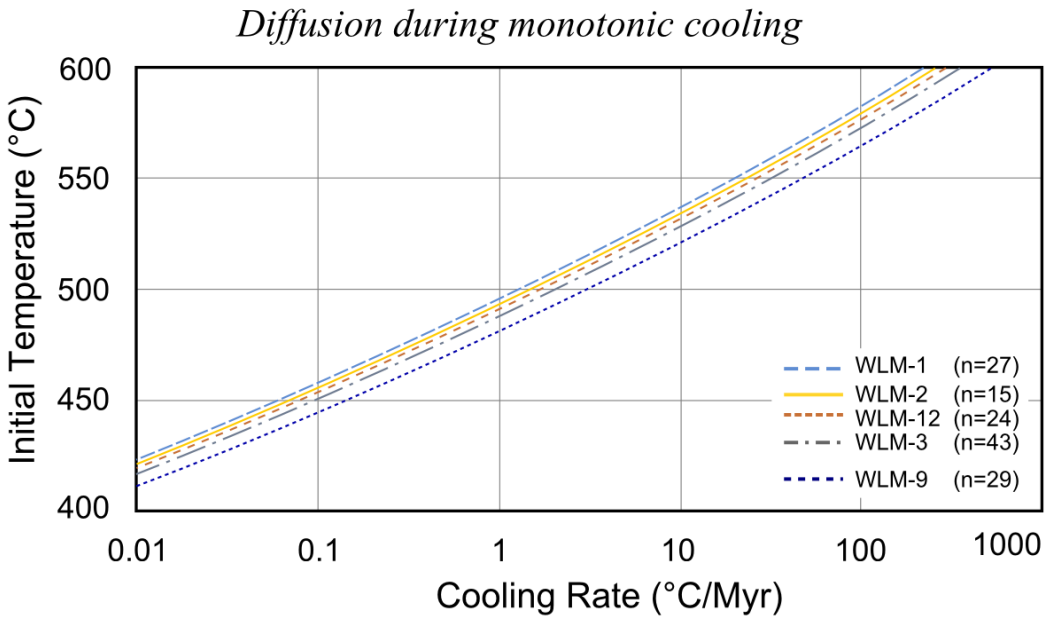

Figure 5.11. Cooling rates for different initial temperatures calculated from measured diffusion profiles.

to exert a constant strain rate on the sample for increasing intervals of time. This allows testing of the deformation geospeedometer for calculating the amount of time over which the sample was undergoing dynamic recrystallization. Experiments were designed in this way to provide a close analogue to evaluating the duration of dynamic recrystallization in ductile shear zones deforming under isothermal conditions.

5.6.2 Rutile needles in deformation experiments

Experimental quartzite aggregates contained a layer of quartz that was sub-saturated with respect to Ti for the pressure-temperature conditions of the experiment, and an adjacent layer that was saturated with Ti. In the undersaturated layer, rutile needles occur as radiating whiskers of needles emanating from a seed grain (Figure 5.2A,B) that became rotated, deformed, and boudinaged in progressively-higher strain experiments (Figure 5.2C-F). High-resolution secondary electron images of a broken sample surface reveal delicate acicular crystals radiating from a central point and piercing into surrounding quartz grains (Figure 5.12). In one case an individual rutile needle is observed emanating from a hexagonal crystal and passing laterally into a nearby quartz grain (Figure 5.12D). Rutile needles exhibit a tetragonal shape in cross-section (Figure 5.12F). These observations support our interpretation that rutile needles precipitated from aqueous solution and were passively overgrown by coarsening quartz crystals [Nachlas and Hirth 2015].

All CL analyses of rutile needles in experimental samples exhibit bright enrichment halos (Figure 5.3C-F, 5.4B). Enrichment halos are radially symmetric around rutile needles oriented sub-perpendicular to the analysis surface, and exhibit planar symmetry around needles oriented sub-parallel to the analysis surface. Halos become progressively wider and smoother in samples from longer duration experiments (Figure S4 of Nachlas and Hirth [2015]). A direct correlation between rutile needle inclusions and bright CL halos is made

by comparing secondary electron images of rutile needles emergent within pore spaces with CL patterns in the surrounding quartz (Figure 5.13).

We interpret CL halos as Ti diffusion profiles that developed as rutile needles dissolved Ti into the surrounding quartz. This direction of Ti flux is consistent with the fact that quartz in this layer of the experimental aggregate was subsaturated in Ti with respect to the equilibrium solubility for the experimental conditions. It is also consistent with observations of CL halos that have nearly disappeared in the highest-strain duration experiments that were deformed long enough to have returned to the equilibrium solubility [Nachlas and Hirth 2015], which would eliminate the driving force for further dissolution of Ti into quartz.

5.6.3 Results of Ti diffusion modeling during experimental deformation at T=900 °C for t=39-87 h

Halos in CL intensity were measured from 253 quartz-rutile pairs from four experimental samples including a 39-h annealing experiment and 39-, 63-, and 87-h deformation experiments. Deformation experiments included a 15 h annealing interval at P-T prior to deformation [Nachlas and Hirth 2015], which we include in the total experiment duration. The measured slopes of diffusion profiles are unique for samples with different experiment durations, but are indistinguishable between samples from low-strain and annealing experiments that were run for the same duration (Figure 5.5, A8.6).

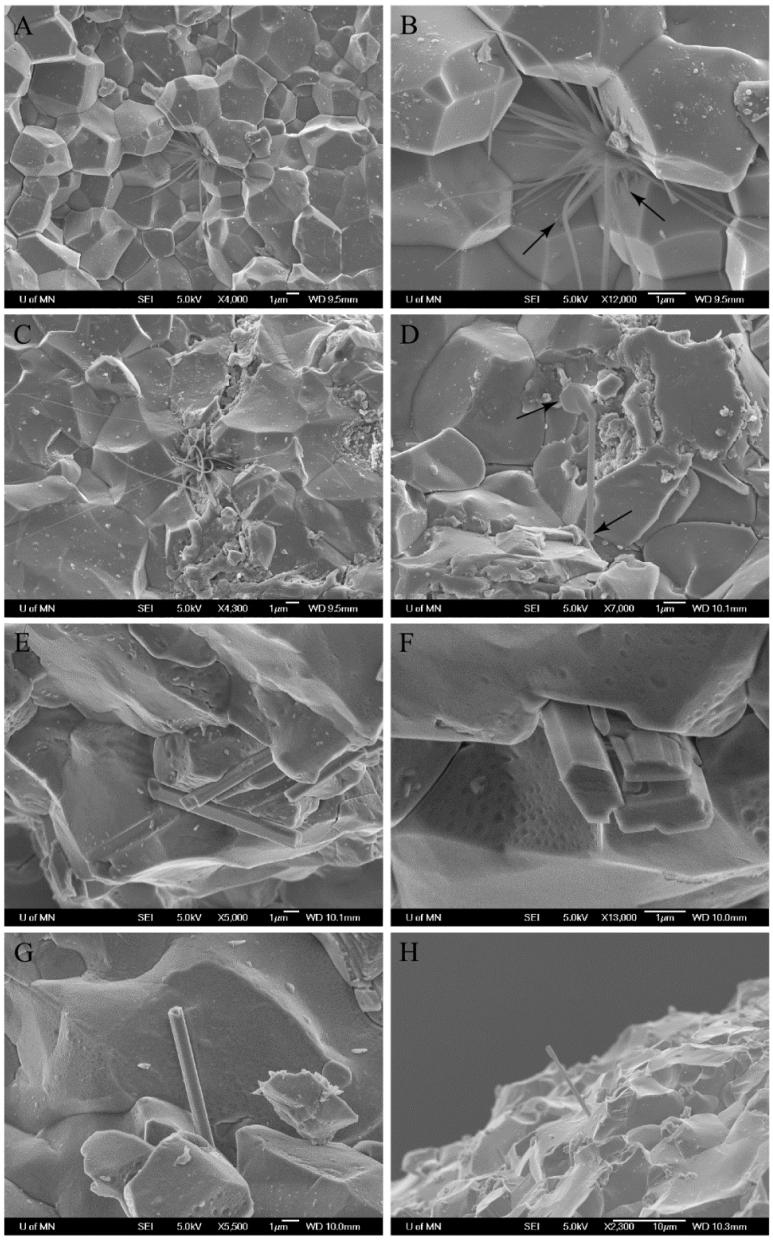

Figure 5.12. Secondary electron images of rutile needle microstructures present along grain boundaries of a broken sample surface. Bundles of acicular inclusions of rutile are found emanating from a singular point and radiating into multiple surrounding quartz grains (A-C). Individual fibers of rutile can be seen being overgrown by quartz (B, E, G, H). In some cases, rutile needles emanate from hexagonally-shaped seed crystal (D). Where observable, cross-section geometries of rutile needles resemble tetragonal prisms (F).

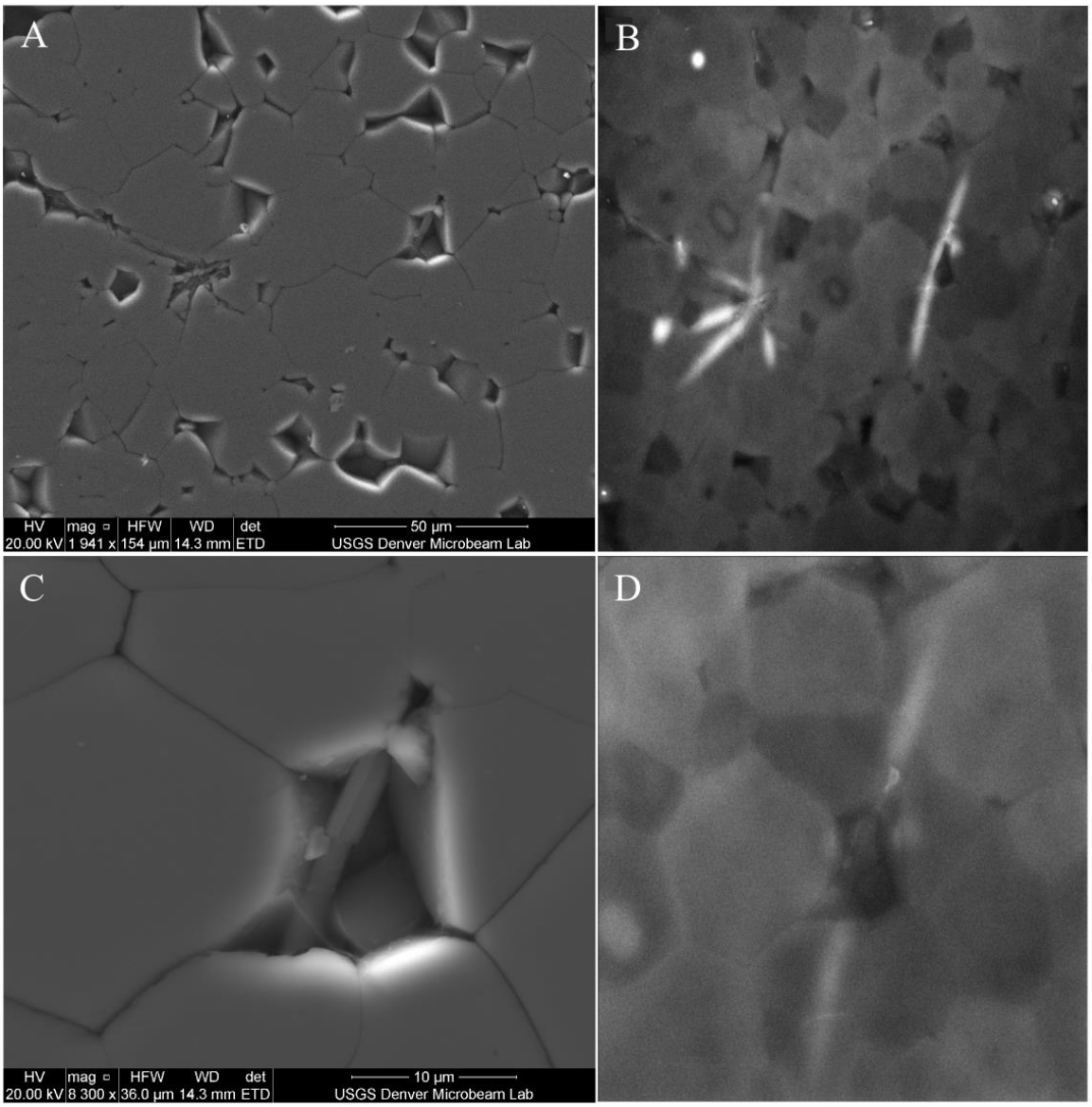

Figure 5.13. Secondary electron (left) and cathodoluminescence (right) images of polished thin sections demonstrating the correlation between rutile needle inclusions and high-intensity CL halos. Imagery reveals a rutile needle emergent within an intergranular pore space, and CL analysis displays a bright CL halo that correlates with the location of the rutile needle. The CL signal in (D) has become partially quenched due to repeated analysis.

For direct comparison with applications of the deformation geospeedometer to natural samples, we follow the same approach as outlined in Section 5.4 using the imposed temperature of the experiments to calculate the amount of time recorded in the measured diffusion profile. This analysis reveals populations of timescale values for each experimental sample, which as a first-order test, appropriately coincide with increasing experiment duration (Figure 5.5, A8.6). However, disagreement exists in the magnitude of the calculated timescales; modeling results suggest that in order to form the measured profiles at 900 °C, it would require a factor of 100 longer time than the experiments were known to have been conducted. This finding may be reflecting our use of a diffusion coefficient that is not fully representative of all diffusion pathways active in our samples.

Because the temperature and time conditions of our experiments are known, we can use the measured diffusion profiles to solve a coefficient for diffusive mobility for Ti in quartz under the conditions of our experiments (Figure 5.14). All diffusion coefficients measured from our experiments are 1 to 2 orders of magnitude faster than the coefficient predicted by Cherniak et al. [2007] for the temperature of our experiments.

5.7 Findings and Implications

Incomplete Ti diffusion profiles preserved in mylonitized quartz grains are used to constrain the rates and conditions of ductile shearing in a field setting and in rock deformation experiments. In both cases, rutile needle inclusions contained within deformed

quartz grains are strongly-oriented into the shear direction and were diffusively-mediating Ti concentrations with their host quartz. Using results from diffusion modeling combined with microstructural characterization for natural and experimental samples, we discuss interpretations of diffusion modeling results in terms of a kinematically-evolving ductile shear zone, we solve for and consider the appropriateness of different coefficients for diffusive mobility for Ti in deforming quartz, and we use our observations of diffusive flux directions and inclusion textures to describe two end-member process that can result in the formation of rutilated quartz.

5.7.1 Timescales and kinematics of shear zone deformation in the PCC

In the Pioneer Core Complex, rutile needles were exsolving from quartz during extensional ductile shearing. Existing geochronology from the PCC reveals a hiatus in the deformation history over an ~8 Myr window from the cessation of melt-present deformation (46 Ma; Vogl et al. [2012]) to the earliest closure ages of $^{40}Ar/^{39}Ar$ in muscovite (38 Ma; Silverberg [1990]; McFadden et al. [2015]). Results from our deformation geospeedometry analysis are consistent with prolonged deformation of quartz over this interval (Figure 5.15) and add independent constraints on the duration of deformation and cooling history of the WSZ.

The 46 Ma age reflects crystallization of zircon within a cross-cutting leucocratic dike. Structurally-up section from this undeformed dike is a foliated leucocratic dike that was transposed and boudinaged, which also yields an age of 46 Ma. It is possible that both of

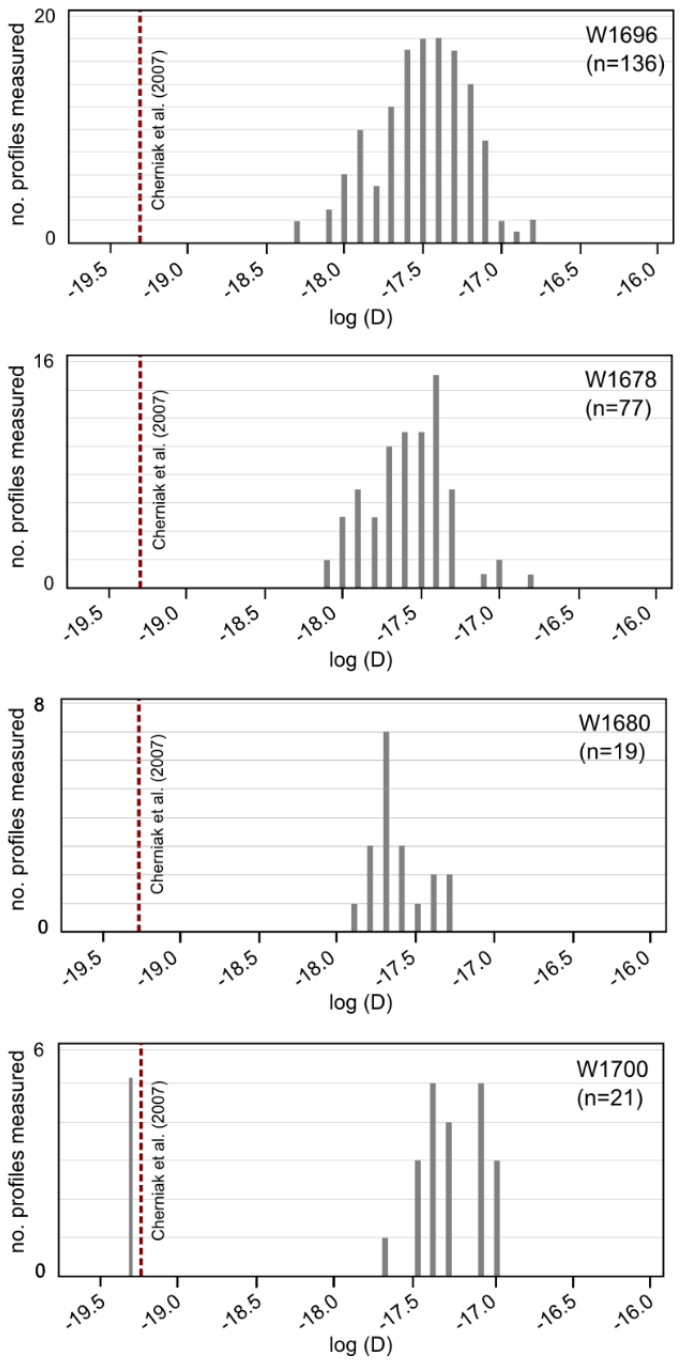

Figure 5.14. Diffusive mobility coefficients solved for Ti in deforming quartz at the conditions of our experiments.

these dikes were originally emplaced at the same time, but later deformation that localized in higher levels of the middle plate transposed the upper dike, an event that would be accommodated by ductility of quartz and feldspar but likely would not reset the age of zircon completely (e.g., Timms et al. [2011]). We interpret the U-Pb ages of Vogl et al. [2012] to reflect crystallization of zircon within leucocratic melt at ~ 700 °C, although it is clear that ductile strain continued to accumulate, at least at the base of the middle plate, following emplacement and crystallization of the youngest zircons.

The next temperature constraint along the exhumation path derives from the $^{40}Ar/^{39}Ar$ age of muscovite, the oldest of which is 38 Ma [Silverberg, 1990; McFadden et al. 2015]. Considering a closure temperature of 405 °C [Harrison et al. 2009], this would suggest that the hiatus was characterized by a linear cooling rate of c. 60 °C/Myr. The low-temperature history of the PCC outlined by Silverberg [1990] who analyzed muscovite, biotite (closure temperature of ~330 °C; McDougall and Harrison [1988]), and orthoclase (closure temperature of ~200 °C; McDougall and Harrison [1988]) from mylonites beneath the detachment and found ages of 36, 35, and 33 Ma, respectively. McFadden et al. [2015] determined the $^{40}Ar/^{39}Ar$ age for muscovite from samples collected across the 100 m section of Kinnikinic quartzite to be 38-37 Ma. Together these $^{40}Ar/^{39}Ar$ ages span an interval of 38-33 Ma that is interpreted to represent cooling from ~400 – 200 °C during extensional faulting on the Wildhorse detachment [Silverberg, 1990; Diedesch, 2011; Vogl

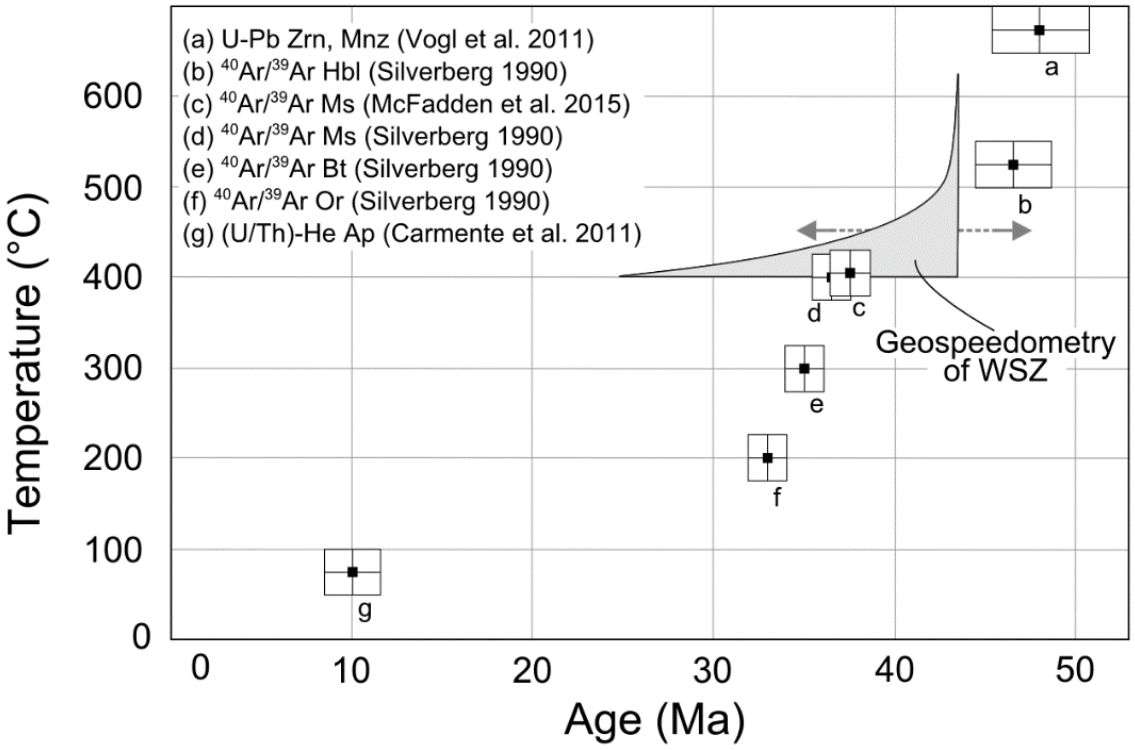

Figure 5.15. Comparison of T-t history from deformation geospeedometry with that of existing geochronological constraints.

et al. 2012]. Linear cooling rates for cooling during deformation of the detachment are c. 40 °C/Myr.

Quartz is essentially closed to Ti diffusion below 400 °C (effective diffusion distance is 1 μm in 350 Myr). Therefore we can assume that the measured diffusion profiles developed before $^{40}Ar/^{39}Ar$ closure ages of muscovite (i.e., prior to 38 Ma). For this reason we place our results in the context of the hiatus in deformation history that lasts 8 Myr from the youngest zircon ages to the oldest muscovite ages.

Results of diffusion modeling of stranded Ti profiles suggests that at temperatures estimated for deformation of the Kinnikinic quartzite (~ 500 °C), duration of deformation in individual samples ranged from 1.4-3.1 Myr (Figure 5.10, 5.16). If deformation in the shear zone was assumed to have occurred en masse, then these results suggest that the shear zone was active for as long as 3 Myr. If samples are assumed to have deformed separately, integrating the duration of all samples across the shear zone width indicates a deformation duration of 9 Myr. In contrast, a second interpretation of these results is to consider a temperature gradient across the shear zone that is 15 °C higher at the base shear zone than

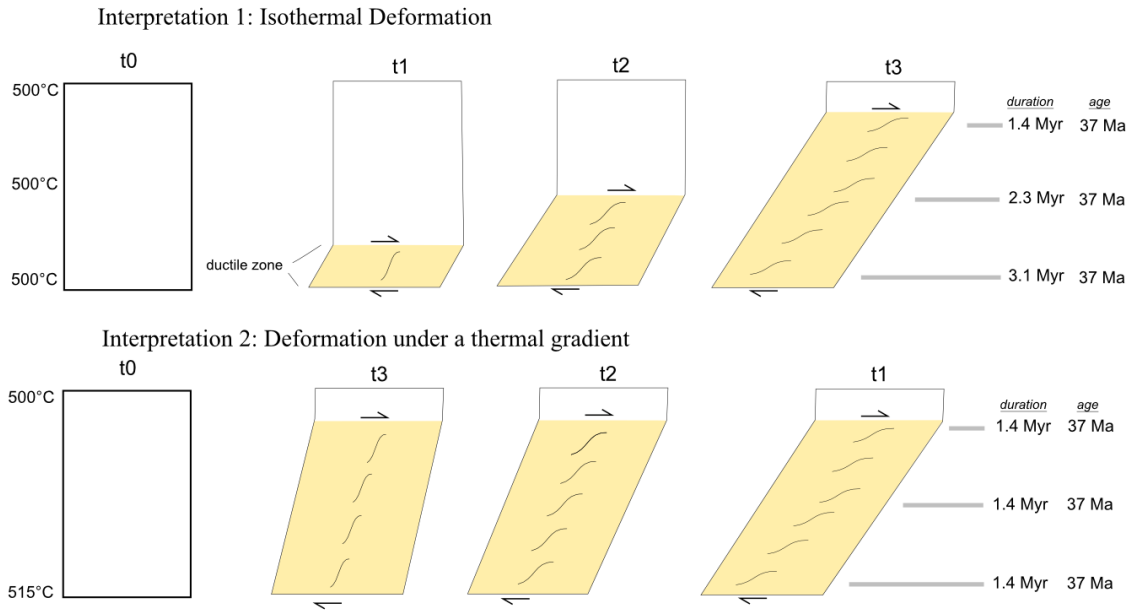

Figure 5.16. Schematic interpretation of two end-member interpretations of diffusion geospeedometry results. Ages of $^{40}Ar/^{39}Ar$ muscovite taken from McFadden et al. [2015].

at the top; if this were the case, diffusion modeling results predict that samples could have been deforming for the same duration (Figure 5.16). Discrimination between these two interpretations cannot be made from our current observations; both of these scenarios are compatible with $^{40}Ar/^{39}Ar$ ages from the same samples (Figure 5.16), and the potential temperature differences between samples are too small to be confidently resolved. However, these two interpretations would result in microstructures reflecting different intensities of finite strain, or strain rates that are variable across the shear zone width.

Cooling rates for the 8 Myr hiatus as well as during deformation of the Wildhorse detachment have been previously calculated based on progression of cooling ages for minerals with different closure temperatures. We are also able to use the slope profile diffusion modeling method of Watson and Cherniak [2015] to solve for cooling rates that would be required to form the diffusion profiles measured in our samples. With modest assumptions for initial temperature (e.g., 550 °C) results of our analysis show that cooling rates for our samples were ~25-40 °C/Myr (Figure 5.11). Measured cooling rates are faster for samples located at higher levels of the shear zone (Figure 5.11).

The amount of horizontal extension accommodated by the Wildhorse Shear Zone and Wildhorse Detachment Fault has been estimated from maximum exhumation depths and features that have been structurally-offset by the detachment. Pressure estimates from contact aureoles indicating depths of 12-15 km [Silverberg 1990] equate to horizontal displacements of 12-26 km assuming dips of 30-45 °. Structural offset of the Summit Creek

stock and the North Fork Lake quartz porphyry dike complex indicates displacements of 15-16 and 30-32 km, respectively [Wust 1986; Silverberg 1990; Vogl et al. 2012]. Using these displacement estimates with the measured durations from diffusion results (3 Myr) equates to strain rates in the quartzite shear zone of $1\text{-}4\text{x}10^{-13}$ s^{-1}. This value is on the faster end of estimates of geologically-realistic strain rates (e.g., Pfiffner and Ramsay [1982]).

5.7.2 Ti diffusion in deforming quartz

We measured Ti diffusion profiles between rutile inclusions and the surrounding quartz, and used the experimentally-derived diffusion parameters to extract information about timescales over which profiles developed. The difference between our application and the calibration experiments is that in our case, quartz was undergoing dynamic recrystallization via dislocation mechanisms simultaneous with development of the diffusion profile. It is possible (likely) that the availability of multiple diffusion pathways operative during dislocation creep of quartz influences the diffusive mobility of Ti. We emphasize that our calculations are not true diffusion coefficients but are more appropriately considered coefficients of diffusive mobility. This diffusive mobility term encompasses diffusion along multiple pathways -- lattice diffusion, pipe diffusion, grain boundary diffusion, and creep of titanized dislocations – during dynamic recrystallization of quartz.

We solve for a diffusive mobility term for Ti diffusion in deforming quartz by measuring profiles in experiments where the T-t conditions are constrained. All experiments were

conducted at 900 °C and deformation experiments sheared samples under near-steady-state conditions for 39, 63, 87 h. Overall, diffusive mobility coefficients are 1-2 orders of magnitude faster than volume diffusion measured by Cherniak et al. [2007] (Figure 5.14). Mobility coefficients solved for short and moderate duration deformation and annealing experiments, but mobility coefficients increase slightly in high-strain deformation experiments (Figure 5.14).

Faster diffusive mobility coefficients measured in our experiments compared to those of Cherniak et al. [2007] could be a consequence of a few different factors. Firstly, as aforementioned, our measurements are of diffusion profiles that were developing within quartz that is deforming via dislocation mechanisms. This would provide both a higher density of dislocations, enabling more access to fast diffusion pathways, and a greater mobility of dislocations during dislocation creep, a process that could be capable of advecting titanized dislocations (e.g., Nachlas and Hirth [2015]). Additionally, our experiments were conducted at elevated pressure and under wet conditions; the experiments of Cherniak et al. [2007] were performed at 1 atmosphere and dry conditions. It is possible that our accelerated diffusive mobility coefficient is reflecting a dependence of water fugacity on Ti diffusion in quartz. This would be consistent with previous studies that have documented faster of diffusion of O and Si in quartz under wet conditions [Farver and Yund 1991; Farver and Yund 2000]. Importantly, if water fugacity is the primary faster responsible for our measured faster diffusion rates, then our results are in fact reflecting a true diffusion coefficient (one that happens to have a water fugacity dependence), instead

of a multi-path diffusive mobility term, because our measured diffusion coefficients are indistinguishable for annealed and deformed experimental samples.

5.7.3 Two mechanisms to rutilate quartz – exsolution and overgrowth

Our diffusion analysis of rutilated quartz supports the existence of two end-member processes for quartz rutilation. In natural samples, depletion halos in Ti content surround rutile needles, indicating exsolution as Ti diffused from quartz to the growing rutile needle. In experimental samples, enrichment halos surround rutile, indicating that Ti was diffusing from rutile into the surrounding quartz. For both of these scenarios, the processes that led to rutilation were different.

Exsolution of rutile requires that quartz be decreasing its Ti solubility, and a primary way to accomplish this is through cooling [Wark *and* Watson 2006; Thomas et al. 2010]. As high-temperature (and therefore high Ti) quartz cools, compositional instabilities develop from which rutile needles nucleate and grow. The presence of high Ti contents in original quartz in the WSZ is consistent with high temperatures obtained from Zr-in-rutile thermometry, supporting a long residence time in the mid-lower crust that would have homogenized quartz with a high, uniform Ti content. This scenario is analogous to previous studies that have measured high Ti contents from undeformed, mid-crustal quartzites [Nachlas et al. 2014].

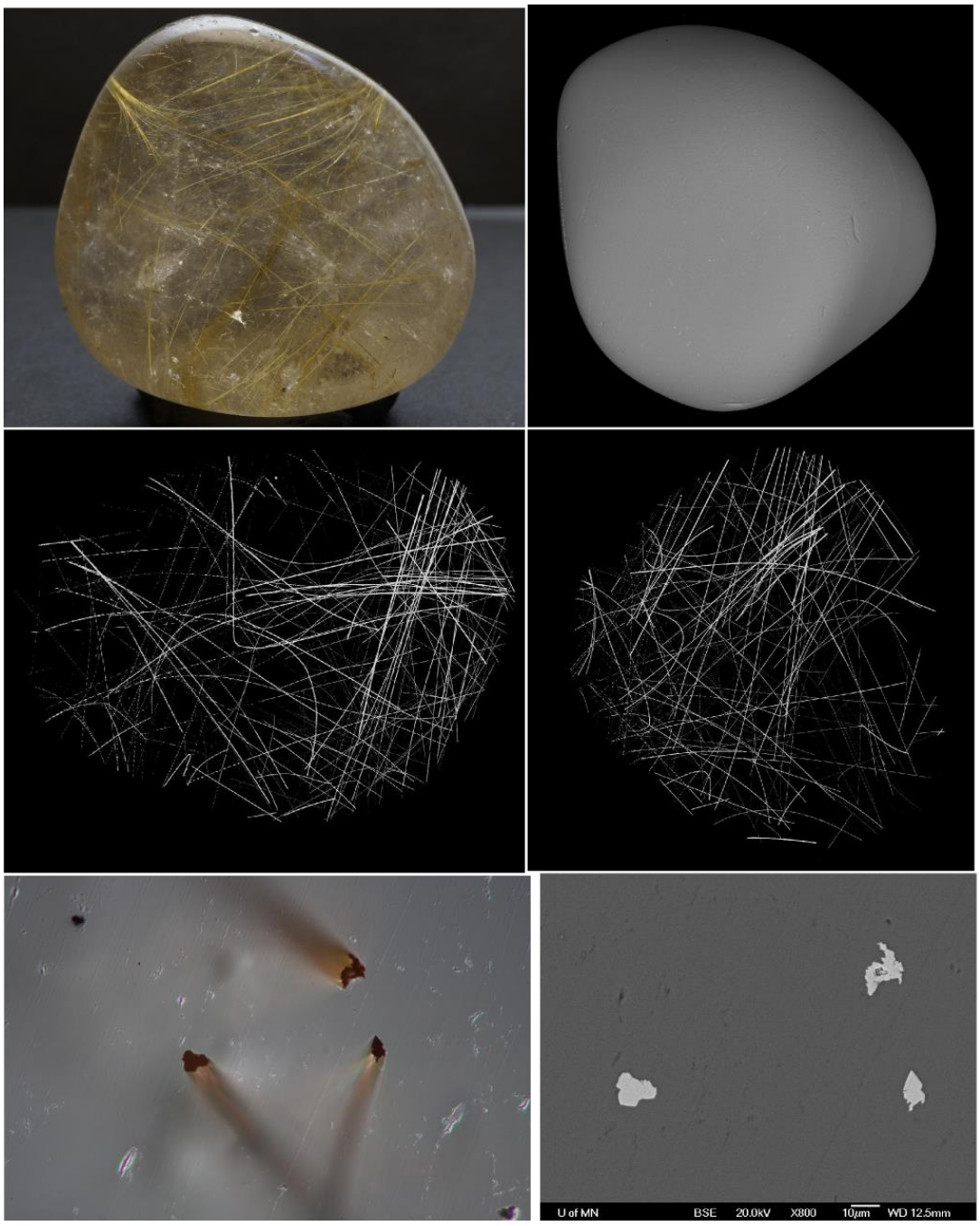

Figure 5.17. 3-D tomography analysis reveals curving, arcuate rutile needles in a rutialted quartz gemstone. Needles are confirmed to be rutile via EDS analysis (Figure A8.9).

In the case of experimental samples, diffusion proceeded in the opposite direction; rutile needles were dissolving into quartz. This diffusion direction requires a new mechanism to describe the process of incorporation of rutile into the quartz crystal interior. We show that rutile needles nucleated outside of quartz and were later passively overgrown by coarsening quartz grain boundaries. This overgrowth mechanism results in needles that are randomly-oriented and is capable of preserving fine fibers of rutile without disturbing their intricate forms (Figure 5.2, 5.12).

There is sparse evidence in the literature for the overgrowth rutilation mechanism, in part because only recently have Ti solubilities in quartz been quantified, and in part because of the difficulties in resolving concentration gradients surrounding fine mineral inclusions. To our knowledge observations supporting this mechanism have only been formally proposed recently, by Shulaker et al. [2015], based on the presence of secondary adularia crystals grown onto rutile needles that were later included by quartz. Our analysis reveals time-series observations of the overgrowth rutilation mechanism, including precipitation of rutile from solution as needle- and whisker-shaped crystallites (Figure 5.12), passive overgrowth and inclusion into quartz (Figure 5.2, 5.12), and finally ductile flow of quartz that rotates and stretches rutile needles into the lineation direction in high-strain experiments (Figure 5.2).

The diffusion direction alone does not allow discrimination between different rutilation mechanisms. In the case of experiments, the quartz that overgrew rutile was undersaturated

in Ti content, which led to dissolution of Ti into quartz. However, it can be imagined that in a case where quartz is initially saturated in Ti, rutile needles that become included via overgrowth could act as a sink to accept Ti from the migrating quartz crystal. Instead, our results suggest that the pattern of needles within quartz is a primary difference between the two mechanisms – either crystallographically-oriented, which would imply exsolution, or randomly-oriented, which would imply overgrowth.

Based on the random orientations of rutile needles in the vast majority of gem-quality rutilated quartz, we argue that the overgrowth rutilation mechanism represents the most common process for forming this type of rutilated quartz. Indeed, X-ray computed tomography analysis of rutilated quartz from Brazil reveals rutile needles that are arcuate and randomly-oriented with respect to each other and the symmetry of the host quartz (Figure 5.17). These rutile needle geometries are similar to those found in experimental samples (Figure 5.2, 5.12).

An overgrowth mechanism to rutilate quartz is also capable of explaining the occurrence of other acicular mineral inclusions in quartz. Needles of sillimanite are a common occurrence in high-temperature quartzites and metapelites (e.g., Menegon et al. [2011]). In this case, where syn-metamorphic deformation may have caused grain boundary migration of quartz to incorporate, just as if sweeping through a pinning phase. Additionally, many other acicular mineral inclusions in quartz are documented from hydrothermal and pegmatitic settings, such as needles of actinolite, tourmaline, and dumortierite (a hydrous

B-Fe-Al silicate responsible for the pink coloration of rose quartz; Goreva et al. [2001]). The overgrowth mechanism is capable of explaining the origin of these inclusions without necessitating consideration of the solubility of the inclusion components within the host phase.

5.8 Conclusions

Deformation of continental crust localizes into quartz-rich layers, and owing to the wide range of conditions under which quartz deforms plastically, it is likely that quartz actively recrystallized over a prolonged interval of an orogenic event. Deformation geospeedometry is capable of extracting timescales that we interpret as durations of ductile shearing that confirms quartz deformation was occurring for a few Myr during exhumation of the PCC. Constraining shear zone deformation directly from the strain-accommodating mineral itself is a new approach that provides independent estimates on ductility in continental shear zones.

We have tested this technique in the Pioneer Core Complex, where it reflects deformation of the quartzite shear zone over a period of ~3-9 Myr that is consistent with constraints from high- and low-temperature geochronometers. Results from samples across the width of the shear zone can be interpreted to indicate that the shear zone progressively widened upward, or that a thermal gradient persisted across the shear zone for ~1-3 Myr during deformation. Using geospeedometry results coupled with estimates of structural offset

accommodated by the ductile zone, we calculate strain rates for the Wildhorse Shear Zone to be $1\text{-}4x^{10\text{-}13}$ s^{-1}.

Testing this technique on experimental samples where the temperature-time conditions are known yields trends that are broadly consistent with known conditions, but estimated timescales are 1-2 orders of magnitude too long. Using the temperature-time conditions of the experiments, we calculate a diffusive mobility term for Ti in quartz that better represents Ti diffusion in quartz that is under high-pressure, water-present conditions during dynamic recrystallization via dislocation mechanisms. Our results can be interpreted to suggest that diffusion of trace elements in quartz is faster under conditions where quartz is deforming, or under conditions of high water fugacity. It is clear that additional experimental and theoretical research is necessary to fully determine the effect of both fugacity and dislocation processes on Ti diffusion in quartz.

Acknowledgements

This research was supported by NSF grants EAR-0911497 awarded to D. Whitney and C. Teyssier and EAR-0911536 awarded to G. Hirth. Thank you to Heather Lowers for assistance with EPMA and SEM-CL analysis at USGS-Denver, to Nobu Shimizu and Brian Monteleone for assistance with SIMS analysis at WHOI, and to Brian Bagley for assistance with XRCT analysis at UMN. WN acknowledges a GSA Graduate Student Research Grant and a UMN Thesis Research Travel Grant that supported components of this research.

CHAPTER 6

Conclusions of the thesis

6.1 Summary of results

6.1.1 Chapter 2

A study of quartzite mylonites from the Shuswap metamorphic core complex provided a first test of evaluating the applicability of the Ti-in-quartz thermobarometer to determine the conditions of shear zone deformation. Four compositional populations of Ti measurements were identified and correlated with different quartz microstructures. Quartz in the undeformed quartzite protolith contains the highest Ti contents, consistent with residence in the middle crust for an extended period of time (sufficiently long for large quartz grains to diffusively equilibrate, ca. 100 Myr). In the mylonites, cores of quartz ribbons contain the highest Ti contents, followed by recrystallized rims and subgrains, and finally neocrystallized quartz precipitated in fractures and pressure shadows that preserves the lowest Ti concentration. Applying Ti-in-quartz thermometry and barometry to these measurements indicates a retrograde progression in P-T conditions that agrees with the trend of decreasing deformation reflected in the overprinting of quartz microstructures. Variations in the 2- and 3-D spatial density of Ti-bearing buffering phases does not

demonstrably affect titania activity in the quartz aggregate. White mica porphyroclasts within quartzite mylonites become progressively-homogenized in higher-strain samples, suggesting that a substantial component of dissolution-precipitation assisted in element mobilization during deformation of the shear zone. Overall, results of Ti-in-quartz produce reasonable estimates of the conditions of shear zone deformation and provide a record of polyphase deformation that is consistent with other constraints on exhumation of the core complex.

6.1.2 Chapter 3

An experimental study was conducted to determine the best approach for synthesizing high-purity quartz aggregates with trace-level precision. Nanoporous silica gel was found to be an effective doping substrate owing to the dense network of nanoporosity within grains and the abundance of silanol groups that populate the grain surface. Controlling the pH conditions of the doping solvent enables optimization of dopant recovery. Washing silica gel in concentrated acid is effective at leaching many of its initial impurities and is a critical step in vacating silanol groups to prepare silica gel for doping. The experimental synthesis approach presented here enables doping a large population of silica gel particles with a Ti concentration that is within 10 ppm of a targeted trace-level concentration. The Ti dopant was found to be uniform at the grain and sample population scale. General agreement on Ti measurements between bulk and laser-, electron-, and ion-beam

microanalysis techniques demonstrates that this doping technique could provide a useful approach for synthesizing trace element microanalytical reference materials.

6.1.3 Chapter 4

A series of rock deformation experiments was conducted (using the doping approach outlined in Chapter 3) on layered aggregates with quartz doped at Ti concentrations above and below the equilibrium solubility predicted for the experimental conditions. Shear experiments were conducted at constant strain rate for three incrementally-longer times to deform quartz aggregates to increasing levels of finite shear strain. Deformed samples were compared with hydrostatic samples that were statically annealed at the same experimental conditions to provide a control on the effect of deformation on Ti exchange. Titanium measurements from quartz in the saturated and undersaturated layers shows an increase in Ti contents in low-strain samples, followed by a progressive decrease of Ti contents such that samples deformed to highest shear strain have re-equilibrated to the equilibrium solubility predicted by the annealing experiments. Acicular rutile crystals nucleated and grew from fluid in the undersaturated layer of the experiments and were later overgrown by migrating quartz boundaries. Once included into quartz, rutile needles dissolve Ti into the undersaturated quartz host, as evidenced by resorption halos indicating Ti diffusion away from rutile inclusions. The undersaturated layer contained sparse rutile needles, nearly all of which were isolated within quartz during the course of the experiment, yet quartz Ti contents in this layer were upheld at a fixed level relative to the adjacent saturated

layer. This finding suggests that an intergranular aqueous fluid is capable of buffering Ti contents of recrystallizing quartz in the absence of abundant Ti-bearing phases.

6.1.4 Chapter 5

Incomplete Ti diffusion profiles in deformed quartz were used to explore applications of quartz geochemistry as a geospeedometer to decipher the rates and thermal histories of quartz deformation. In samples of quartzite mylonite from the Pioneer core complex, rutile needles were in the process of exsolving from quartz during deformation, as indicated by depletion diffusion halos surrounding rutile inclusions. Modeling diffusion progress in mylonitized quartz grains indicates that deformation was sustained over ca. 1-3 Myr within individual samples or up to 9 Myr if deformation is assumed to have localized at discrete levels. Using structural offset across the detachment, geospeedometry results indicate strain rates of $1\text{-}4 \times 10^{-13}$ s^{-1} within the 100 m shear zone. These results are consistent with regional geochronology, suggesting that geospeedometry of deformed quartz can provide a reasonable estimate of the longevity of ductile shear zones. In experimental samples, the direction of Ti flux was opposite; Ti diffused away from rutile inclusions as needles dissolved into the host quartz, as indicated by resorption halos. Applying quartz geospeedometry to experimental samples enables the accuracy of this technique to be tested to reproduce the known temperature-time conditions of the experiments. Results of this analysis suggest that Ti diffusion may be faster under high-P, water-present conditions compared to the 1-atm, dry conditions at which Ti diffusion in quartz was calibrated.

6.2 Implications of this research

Findings of this dissertation indicate that quartz trace element geochemistry is sensitive to the conditions of dynamic recrystallization, and by measuring the concentration and distribution of Ti in deformed quartz and correlating it with microstructures and recrystallization fabrics, it is possible to reconstruct the temperatures, pressures, and rates at which plastic deformation of quartz occurred. This finding has important implications for understanding the styles of crustal deformation accommodated by quartz, and it contributes to developing a new approach for applying thermobarometry to reconstruct shear zone deformation using the deformation-accommodating mineral itself. Quartz that was precipitated into high-angle cross-cutting fractures is capable of preserving the P-T condition of incipient brittle-to-ductile transition, an important variable for understanding earthquake rupture. By combining barometry of Ti-in-quartz with thermometry of oxygen isotopes in quartz, it is possible to estimate the maximum depths of meteoric fluid infiltration, a critical component in developing the crustal-scale hydrothermal convection cells that accompany exhumation of core complexes. The effect of dynamic recrystallization on the thermodynamic and kinetic behavior of Ti, a slow-diffuser in quartz present at trace-level concentrations, could be representative of the behavior of other trace elements that partition into lattice structural sites and obey Henrian behavior. Geospeedometry of quartz mylonites introduces a new possibility for calculating strain rates of ductile shear zones, a parameter that has classically been difficult to quantify.

6.3 Concluding Remarks

Prior to conducting this research, it was recognized that Ti-in-quartz had great potential as a new tool for reconstructing geologic events, but its reliability for estimating the conditions of deformation remained uncertain. Differences in the mechanisms of crystallization in the experiments that calibrated this technique, in which quartz grew statically from a fluid, and in deformed rocks, in which multiple competing recrystallization processes accommodate plastic deformation, created justifiable uncertainties about the accuracy of applying a crystallization-based thermobarometer to minerals that have been dynamically recrystallized. Results of this thesis research demonstrate that deformation is capable of re-equilibrating Ti concentrations in quartz to the equilibrium solubility for the conditions of recrystallization and that this resetting occurs at rates faster than would be accomplished by static volume diffusion. If ductile deformation is more efficient at resetting Ti contents in quartz than static diffusion, then quartz thermobarometry applied to ductile shear zones could provide a more-detailed continuum history of tectonic events compared to statically-metamorphosed rocks away from deformation zones.

References Cited

Adachi, T., T. Hokada, Y. Osanai, T. Toyoshima, S. Baba, and N. Nakano. (2010), Titanium behavior in quartz during retrograde hydration: Occurrence of rutile exsolution and implications for metamorphic processes in the Sør Rondane Mountains, East Antarctica. *Polar Science*, *3*(4), 222–234. Elsevier B.V. and NIPR. doi: 10.1016/j.polar.2009.08.005

Adachi, T., and S. Sakka. (1990), Dependence of the elastic moduli of porous silica gel prepared by the sol-gel method on heat-treatment. *Journal of Materials Science*, *25*(11), 4732–4737. doi: 10.1007/BF01129933

Akl, M. A. A., I. M. M. Kenawy, and R. R. Lasheen. (2004), Organically modified silica gel and flame atomic absorption spectrometry: employment for separation and preconcentration of nine trace heavy metals for their determination in natural aqueous systems. *Microchemical Journal*, *78*(2), 143–156. doi: 10.1016/j.microc.2004.03.019

Allan, M. M., and B. W. D. Yardley. (2007), Tracking meteoric infiltration into a magmatic-hydrothermal system: A cathodoluminescence, oxygen isotope and trace element study of quartz from Mt. Leyshon, Australia. *Chemical Geology*, *240*(3-4), 343–360. doi: 10.1016/j.chemgeo.2007.03.004

References Cited

Antignano, A., and C. E. Manning. (2008), Rutile solubility in H2O, H2O–SiO2, and H2O–NaAlSi3O8 fluids at 0.7–2.0 GPa and 700–1000 °C: Implications for mobility of nominally insoluble elements. *Chemical Geology*, *255*(1-2), 283–293. doi: 10.1016/j.chemgeo.2008.07.001

Ashley, K. T., L. E. Webb, F. S. Spear, and J. B. Thomas. (2013), P-T-D histories from quartz: A case study for the application of the TitaniQ thermobarometer to progressive fabric development in metapelites. *Geochemistry Geophysics Geosystems*, (0420). doi: 10.1002/ggge.

Audétat, A., D. Garbe-Schönberg, A. Kronz, T. Pettke, B. Rusk, J. J. Donovan, and H. A. Lowers. (2014), Characterisation of a Natural Quartz Crystal as a Reference Material for Microanalytical Determination of Ti, Al, Li, Fe, Mn, Ga and Ge. *Geostandards and Geoanalytical Research*, *39*(2), 171–184. doi: 10.1111/j.1751-908X.2014.00309.x

Audétat, A., and H. Keppler. (2005), Solubility of rutile in subduction zone fluids, as determined by experiments in the hydrothermal diamond anvil cell. *Earth and Planetary Science Letters*, *232*, 393–402. doi: 10.1016/j.epsl.2005.01.028

Ayers, J. C., and E. B. Watson. (1993), Rutile solubility and mobility in supercritical aqueous fluids. *Contributions to Mineralogy and Petrology*, 321–330.

van Baalen, M. R. (1993), Titanium mobility in metamorphic systems: a review. *Chemical Geology*, *110*(1-3), 233–249. doi: 10.1016/0009-2541(93)90256-I

Baes, C., and R. Mesmer. (1976), *The hydrolosis of cations*. Wiley, New York.

Baldwin, S. L., B. D. Monteleone, L. E. Webb, P. G. Fitzgerald, M. Grove, and E. J. Hill. (2004), Pliocene eclogite exhumation at plate tectonic rates in eastern Papua New Guinea. *Nature*, *431*(7006), 263–7. doi: 10.1038/nature02846

Barrett, D. A., V. A. Brown, R. C. Watson, M. C. Davies, P. N. Shaw, H. J. Ritchie, and P. Ross. (2001), Effects of acid treatment on the trace metal content of chromatographic silica: bulk analysis, surface analysis and chromatographic performance of bonded phases. *Journal of chromatography. A*, *905*(1-2), 69–83.

Behr, W. M., and J. P. Platt. (2011), A naturally constrained stress profile through the middle crust in an extensional terrane. *Earth and Planetary Science Letters*, *303*(3-4), 181–192. Elsevier B.V. doi: 10.1016/j.epsl.2010.11.044

Behr, W. M., and J. P. Platt. (2012), Kinematic and thermal evolution during two-stage exhumation of a Mediterranean subduction complex. *Tectonics*, *31*(4), n/a–n/a. doi: 10.1029/2012TC003121

References Cited

Behr, W. M., J. B. Thomas, and R. L. Hervig. (2011), Calibrating Ti concentrations in quartz for SIMS determinations using NIST silicate glasses and application to the TitaniQ geothermobarometer. *American Mineralogist*, *96*(7), 1100–1106. doi: 10.2138/am.2011.3702

Benesi, H. A., and A. C. Jones. (1959), An infrared study of the water-silica gel system. *Journal of Physical Chemistry*, *63*(40).

Betz, E. (2015), Trace Element Holds the Key to Deformation of Continents. *Eos*, *96*, 1374–1397. doi: 10.1002/2013GC005200

Blavette, D., E. Cadel, A. Fraczkiewicz, and A. Menand. (1999), Three-Dimensional Atomic-Scale Imaging of Impurity Segregation to Line Defects. *Science*, *286*(December), 2317–2319. doi: 10.1126/science.286.5448.2317

Blumenfeld, P., J. L. Bouchez, and D. Nantes. (1986), C-slip in quartz from subsolidus deformed granite. *Tectonophysics*, *127*, 97–115.

Bouchez, J. L., D. H. Mainprice, L. Trepied, and J. C. Doukhan. (1984), Secondary lineation in a high-T quartzite (Galicia, Spain): an explanation for an abnormal fabric. *Journal of Structural Geology*, *6*(1-2), 159–165. doi: 10.1016/0191-8141(84)90093-2

References Cited

Brace, W. F., and D. L. Kohlstedt. (1980), Limits on lithospheric stress imposed by laboratory experiments. *Journal of Geophysical Research*, *85*(B11), 6248. doi: 10.1029/JB085iB11p06248

Brown, R. L., J. M. Journeay, L. S. Lane, D. C. Murphy, and C. J. Rees. (1986), Obduction, backfolding and piggyback thrusting in the metamorphic hinterland of the southeastern Canadian Cordillera. *Journal of Structural Geology*, *8*(3-4), 255–268. doi: 10.1016/0191-8141(86)90047-7

Brown, R. L., and P. B. Read. (1983), Shuswap terrane of British Columbia: A Mesozoic "core complex." *Geology*, 11, 164-168. doi: 10.1130/0091-7613(1983)11<164

Brown, R. L., and C. R. Tippett. (1978), The Selkirk fan structure of the southeastern Canadian Cordillera The Selkirk fan structure of the southeastern Canadian Cordillera. *Geological Society of America Bulletin*, *89*(4), 548–558. doi: 10.1130/0016-7606(1978)89<548

Bucholz, C. E., and J. J. Ague. (2010), Fluid flow and Al transport during quartz-kyanite vein formation, Unst, Shetland Islands, Scotland. *Journal of Metamorphic Geology*, *28*(1), 19–39. doi: 10.1111/j.1525-1314.2009.00851.x

References Cited

Bullough, R., and R. C. Newman. (1970), The kinetics of migration of point defects to dislocations. *Reports on Progress in Physics*, *33*, 101–148. doi: 10.1088/0034-4885/33/1/303

Bürgmann, R., and G. Dresen. (2008), Rheology of the Lower Crust and Upper Mantle: Evidence from Rock Mechanics, Geodesy, and Field Observations. *Annual Review of Earth and Planetary Sciences*, *36*(1), 531–567. doi: 10.1146/annurev.earth.36.031207.124326

Camacho, A., P. Yang, and A. Frederiksen. (2009), Constraints from diffusion profiles on the duration of high-strain deformation in thickened crust. *Geology*, *37*(8), 755–758. doi: 10.1130/G25753A.1

Carmenate, A., J. J. Vogl, and M. K. (2011), (U - TH)/ HE EVIDENCE FOR MIOCENE YELLOWSTONE HOTSPOT - RELATED UPLIFT IN SOUTH - CENTRAL IDAHO. GSA Abstracts with Programs

Carr, S. D. (1992), TECTONIC SETTING AND U-Pb GEOCHRONOLOGY OF THE EARLY TERTIARY LADYBIRD LEUCOGRANITE SUITE, THOR-ODIN - PINNACLES AREA, SOUTHERN OMINECA BELT, BRITISH COLUMBIA. *Tectonics*, *11*(2), 258–278.

Chacko, T., X. Hu, T. K. Mayeda, R. N. Clayton, and J. R. Goldsmith. (1996), Oxygen isotope fractionations in muscovite, phlogopite, and rutile. *Geochimica et Cosmochimica Acta*, *60*(14), 2595–2608. doi: 10.1016/0016-7037(96)00112-3

Chakraborty, S. (2006), Diffusion modeling as a tool for constraining timescales of evolution of metamorphic rocks. *Mineralogy and Petrology*, *88*(1-2), 7–27. doi: 10.1007/s00710-006-0152-6

Chakraborty, S. (2008), Diffusion in Solid Silicates: A Tool to Track Timescales of Processes Comes of Age. *Annual Review of Earth and Planetary Sciences*, *36*(1), 153–190. doi: 10.1146/annurev.earth.36.031207.124125

Chernak, L. J., and G. Hirth. (2011), Syndeformational antigorite dehydration produces stable fault slip. *Geology*, *39*(9), 847–850. doi: 10.1130/G31919.1

Cherniak, D. J., J. Manchester, and E. B. Watson. (2007), Zr and Hf diffusion in rutile. *Earth and Planetary Science Letters*, *261*(1-2), 267–279. doi: 10.1016/j.epsl.2007.06.027

Cherniak, D. J., E. B. Watson, and D. A. Wark. (2007), Ti diffusion in quartz. *Chemical Geology*, *236*(1-2), 65–74. doi: 10.1016/j.chemgeo.2006.09.001

Cherniak, D. J., E. B. Watson, and D. A. Wark. (2007), Ti diffusion in quartz. *Chemical Geology*, *236*(1-2), 65–74. doi: 10.1016/j.chemgeo.2006.09.001

References Cited

Chin, E. J., C.-T. Lee, D. L. Tollstrup, L. Xie, J. B. Wimpenny, and Q.-Z. Yin. (2013), On the origin of hot metasedimentary quartzites in the lower crust of continental arcs. *Earth and Planetary Science Letters*, *361*, 120–133. Elsevier. doi: 10.1016/j.epsl.2012.11.031

Chuang, I., and G. E. Maciel. (1997), A Detailed Model of Local Structure and Silanol Hydrogen Bonding of Silica Gel Surfaces. *Journal of Physics and Chemistry*, *5647*(96), 3052–3064.

Clay, P. L., E. F. Baxter, D. J. Cherniak, S. P. Kelley, J. B. Thomas, and E. B. Watson. (2010), Two diffusion pathways in quartz: A combined UV-laser and RBS study. *Geochimica et Cosmochimica Acta*, *74*(20), 5906–5925. Elsevier Ltd. doi: 10.1016/j.gca.2010.07.014

Copeland, P., R. R. Parrish, and T. M. Harrison. (1988), Identification of inherited radiogenic Pb in monazite and its implications for U–Pb systematics. *Nature*, *333*(6175), 760–763. doi: 10.1038/333760a0

Cottle, J., M. P. Searle, M. Horstwood, and D. J. Waters. (2010), Timing of midcrustal metamorphism, melting and deformation in the Mount Everest Region of Southern Tibet revealed by U(Th)-Pb geochronology, *117*(6), 643–664. doi: 10.1086/605994

Cottrell, A. H., and B. A. Bilby. (1949), Dislocation Theory of Yielding and Strain Ageing of Iron. *Proceedings of the Physical Society*, *62*, 49–62. doi: 10.1088/0370-1298/62/1/308

Crank, J. (1975), The Mathematics of Diffusion. Oxford University Press, 414 pp.

Cruz-Uribe, A. M., R. Mertz-Kraus, T. Zack, M. D. Feineman, and G. Woods. (2014), A new LA--ICP--MS method for Ti--in-Quartz: Implications and application to HP rutile-quartz veins from the Czech Erzgebirge. *AGU Fall Meeting*.

Decottignies, M., J. Phalippou, and J. Zarzycki. (1978), Synthesis of glasses by hot-pressing of gels. *Journal of Materials Science*, *13*(12), 2605–2618. doi: 10.1007/BF00552690

Deer, W., R. A. Howie, and J. Zussman. (1992), *Introduction to the Rock - Forming Minerals*. Longmans, London, UK.

Dennen, W. H. (1964), Impurities in quartz. *Geological Society of America Bulletin*, *75*, 241–246. doi: 10.1130/0016-7606(1964)75

Dennen, W. H. (1966), Stoichiometric substitution in natural quartz. *Geochimica et Cosmochimica Acta*, *30*(12), 1235–1241. doi: 10.1016/0016-7037(66)90122-0

Dennis, P. F. (1984), Oxygen self-diffusion in quartz under hydrothermal conditions. *Journal of Geophysical Research*, *89*, 4047–4057.

Diedesch, T. (2011), KINEMATIC ANALYSIS OF THE WILDHORSE DETACHMENT FAULT. MS Thesis, Idaho State University, 86 pp.

References Cited

Donovan, J. J., H. A. Lowers, and B. G. Rusk. (2011), Improved electron probe microanalysis of trace elements in quartz. *American Mineralogist*, *96*(2-3), 274–282. doi: 10.2138/am.2011.3631

Dunlap, W. J. (1997), Neocrystallization or cooling? 40Ar/39Ar ages of white micas from low-grade mylonites. *Chemical Geology*, *2541*(97).

Eggins, S. M., and J. M. G. Shelley. (2002), Compositional Heterogeneity in NIST SRM 610-617 Glasses. *Geostandards and Geoanalytical Research*, *26*(3), 269–286. doi: 10.1111/j.1751-908X.2002.tb00634.x

Farver, J. R., and R. A. Yund. (1991), Oxygen diffusion in quartz : Dependence on temperature and water fugacity. *Chemical Geology*, *90*(1984), 55–70.

Farver, J., and R. Yund. (1992), Oxygen diffusion in a fine-grained quartz aggregate with wetted and nonwetted microstructures. *Journal of Geophysical Research*, *97*(92), 14017. doi: 10.1029/92JB01206

Farver, J., and R. Yund. (2000), Silicon diffusion in a natural quartz aggregate: constraints on solution-transfer diffusion creep. *Tectonophysics*, *325*(3-4), 193–205. doi: 10.1016/S0040-1951(00)00121-9

Feinberg, J. M., H. Wenk, P. R. Renne, and G. R. Scott. (2004), Epitaxial relationships of clinopyroxene-hosted magnetite determined using electron backscatter diffraction (EBSD) technique. *American Mineralogist*, *89*(2), 462–466.

Fitz Gerald, J., and H. Stunitz. (1993), Deformation of granitoids at low metamorphic grade. I: Reactoins and grain size reduction. *Tectonophysics*, *30*(3-4), 269–297. doi: 10.1016/0040

Fleet, M. E. (1982), Orientation of phase and domain boundaries in crystalline solids. *American Mineralogist*, *67*, 926–936.

Freeman, S. R., R. W. H. Butler, R. A. Cliff, and D. C. Rex. (1998), Direct dating of mylonite evolution: a multi-disciplinary geochronological study from the Moine Thrust Zone, NW Scotland. *Journal of the Geological Society*, *155*(5), 745–758. doi: 10.1144/gsjgs.155.5.0745

Fricke, H. C., S. M. Wickham, and J. R. O'Neil. (1992), Oxygen and hydrogen isotope evidence for meteoric water infiltration during mylonitization and uplift in the Ruby Mountains-East Humboldt Range core complex, Nevada. *Contributions to Mineralogy and Petrology*, *111*(2), 203–221. doi: 10.1007/BF00348952

Ganguly, J. (1979), Garnet and clinopyroxene solid solutions, and geothermometry based on Fe-Mg distribution coefficient. *Geochimica et Cosmochimica Acta*, *43*(7), 1021–1029. doi: 10.1016/0016-7037(79)90091-7

Gébelin, A., A. Mulch, C. Teyssier, M. Heizler, T. Vennemann, and N. C. A. Seaton. (2011), Oligo-Miocene extensional tectonics and fluid flow across the Northern Snake Range detachment system, Nevada. *Tectonics*, *30*(5), 1–18. doi: 10.1029/2010TC002797

Ghent, E. D. (1976), Plagioclase-garnet-Al2SiO5-quartz : a potential geobarometer-geothermometer. *American Mineralogist*, *6*(1967), 2–6.

Ghent, E. D., and M. Z. Stout. (1984), TiO2 activity in metamorphosed pelitic and basic rocks: principles and applications to metamorphism in southeastern Canadian Cordillera. *Contributions to Mineralogy and Petrology*, *86*(3), 248–255. doi: 10.1007/BF00373670

Ghiorso, M. S., and G. A. R. Gualda. (2013), A method for estimating the activity of titania in magmatic liquids from the compositions of coexisting rhombohedral and cubic iron–titanium oxides. *Contributions to Mineralogy and Petrology*, *165*(1), 73–81. doi: 10.1007/s00410-012-0792-y

Gibson, H. D., R. L. Brown, and R. R. Parrish. (1999), Deformation-induced inverted metamorphic field gradients : an example from the southeastern Canadian Cordillera. *Journal of Structural Geology*, *21*, 751–767.

Giletti, B. J., and R. A. Yund. (1984), Oxygen diffusion in quartz. *Journal of Geophysical Research*, *89*(B6), 4039–4046.

Gleason, G. C., and S. DeSisto. (2008), A natural example of crystal-plastic deformation enhancing the incorporation of water into quartz. *Tectonophysics*, *446*(1-4), 16–30. doi: 10.1016/j.tecto.2007.09.006

Goergen, E. T., and D. L. Whitney. (2012a), Corona networks as three-dimensional records of transport scale and pathways during metamorphism. *Geology*, *40*(2), 183–186. doi: 10.1130/G32452.1

Goergen, E. T., and D. L. Whitney. (2012b), Long length scales of element transport during reaction texture development in orthoamphibole-cordierite gneiss: Thor-Odin dome, British Columbia, Canada. *Contributions to Mineralogy and Petrology*, *163*(2), 337–352. doi: 10.1007/s00410-011-0671-y

Gonçalves, C. C., L. Gonçalves, and G. Hirth. (2015), The effects of quartz recrystallization and reaction on weak phase interconnection, strain localization and evolution of microstructure. *Journal of Structural Geology*, *71*, 24–40. Elsevier Ltd. doi: 10.1016/j.jsg.2014.11.010

Gonzalez-Oliver, C. J. R., P. F. James, and H. Rawson. (1982), Silica and silica-titania glasses prepared by the sol-gel process. *Journal of Non-crystalline solids*, *48*, 129–152.

Gordon, S. M., D. L. Whitney, R. B. Miller, N. McLean, and N. C. A. Seaton. (2010), Metamorphism and deformation at different structural levels in a strike-slip fault zone, Ross Lake fault, North Cascades, USA. *Journal of Metamorphic Geology*, *28*(2), 117–136. doi: 10.1111/j.1525-1314.2009.00860.x

Gordon, S. M., D. L. Whitney, C. Teyssier, M. Grove, and W. J. Dunlap. (2008), Timescales of migmatization, melt crystallization, and cooling in a Cordilleran gneiss dome: Valhalla complex, southeastern British Columbia. *Tectonics*, *27*(4), n/a–n/a. doi: 10.1029/2007TC002103

Goreva, J. S., C. Ma, and G. R. Rossman. (2001), Fibrous nanoinclusions in massive rose quartz: The origin of rose coloration. *American Mineralogist*, *86*(4), 466–472.

Goswami, A., and A. K. Singh. (2002), 1,8-Dihydroxyanthraquinone anchored on silica gel: synthesis and application as solid phase extractant for lead(II), zinc(II) and cadmium(II) prior to their determination by flame atomic absorption spectrometry. *Talanta*, *58*(4), 669–78.

Gottardi, R., C. Teyssier, A. Mulch, T. W. Vennemann, and M. L. Wells. (2011), Preservation of an extreme transient geotherm in the Raft River detachment shear zone. *Geology*, *39*(8), 759–762. doi: 10.1130/G31834.1

Götze, J., M. Plötze, T. Graupner, D. K. Hallbauer, and C. J. Bray. (2004), Trace element incorporation into quartz: A combined study by ICP-MS, electron spin resonance, cathodoluminescence, capillary ion analysis, and gas chromatography. *Geochimica et Cosmochimica Acta*, *68*(18), 3741–3759. doi: 10.1016/j.gca.2004.01.003

Gotze, J., M. Plotze, and D. Habermann. (2001), Origin , spectral characteristics and practical applications of the cathodoluminescence (CL) of quartz - a review. *Mineralogy and Petrology*, *71*, 225–250.

Griggs, D. (1967), Hydrolytic Weakening of Quartz and Other Silicates. *Geophysical Journal of the Royal Astronomical Society*, *14*(1-4), 19–31. doi: 10.1111/j.1365-246X.1967.tb06218.x

ten Grotenhuis, S. M., R. A. J. Trouw, and C. W. Passchier. (2003), Evolution of mica fish in mylonitic rocks. *Tectonophysics*, *372*(1-2), 1–21. doi: 10.1016/S0040-1951(03)00231-2

Gruener, S., T. Hofmann, D. Wallacher, A. V. Kityk, and P. Huber. (2009), Capillary rise of water in hydrophilic nanopores. *Physical Review E - Statistical, Nonlinear, and Soft Matter Physics*, *79*(6), 6–9. doi: 10.1103/PhysRevE.79.067301

Gruener, S., and P. Huber. (2011), Imbibition in mesoporous silica: rheological concepts and experiments on water and a liquid crystal. *Journal of physics. Condensed matter : an Institute of Physics journal*, *23*(18), 184109. doi: 10.1088/0953-8984/23/18/184109

Grujic, D., M. Stipp, and J. L. Wooden. (2011), Thermometry of quartz mylonites: Importance of dynamic recrystallization on Ti-in-quartz reequilibration. *Geochemistry Geophysics Geosystems*, *12*(6), 1–19. doi: 10.1029/2010GC003368

Gualda, G. A R., A. S. Pamukcu, M. S. Ghiorso, A. T. Anderson, S. R. Sutton, and M. L. Rivers. (2012), Timescales of quartz crystallization and the longevity of the Bishop giant magma body. *PloS one*, *7*(5), e37492. doi: 10.1371/journal.pone.0037492

Haertel, M., M. Herwegh, and T. Pettke. (2013), Titanium-in-quartz thermometry on synkinematic quartz veins in a retrograde crustal-scale normal fault zone. *Tectonophysics*, *608*, 468–481. Elsevier B.V. doi: 10.1016/j.tecto.2013.08.042

Halfpenny, A., D. J. Prior, and J. Wheeler. (2006), Analysis of dynamic recrystallization and nucleation in a quartzite mylonite. *Tectonophysics*, *427*(1-4), 3–14. doi: 10.1016/j.tecto.2006.05.016

Harker, A. (1890), Petrological Notes on some of the Larger Boulders on the Beach, South of Flambro' Head. *Proceedings of the Yorkshire Geological Society*, *11*(3), 409–423. doi: 10.1144/pygs.11.3.409

Harrison, T. M., J. Célérier, A. B. Aikman, J. Hermann, and M. T. Heizler. (2009), Diffusion of 40Ar in muscovite. *Geochimica et Cosmochimica Acta*, *73*(4), 1039–1051. doi: 10.1016/j.gca.2008.09.038

Hay, R. S., and B. Evans. (1987), Chemically induced grain boundary migration in calcite: temperature dependence, phenomenology, and possible applications to geologic systems. *Contributions to Mineralogy and Petrology*, *97*, 127–141. doi: 10.1007/BF00375220

Hayden, L. A., and C. E. Manning. (2011), Rutile solubility in supercritical NaAlSi3O8–H2O fluids. *Chemical Geology*, *284*(1-2), 74–81. doi: 10.1016/j.chemgeo.2011.02.008

Heilbronner, R., and J. Tullis. (2006), Evolution of c axis pole figures and grain size during dynamic recrystallization: Results from experimentally sheared quartzite. *Journal of Geophysical Research*, *111*(B10), B10202. doi: 10.1029/2005JB004194

Hench, L. L., and W. Vasconcelos. (1990), Gel-silica science. *Annual Review of Material Science*, *20*, 269–298.

Hillert, M., and G. R. Purdy. (1978), Chemically induced grain boundary migration. *Acta Metallurgica*, *26*, 333–340.

Hirth, G., C. Teyssier, and J. Dunlap. (2001), An evaluation of quartzite flow laws based on comparisons between experimentally and naturally deformed rocks. *International Journal of Earth Sciences*, *90*(1), 77–87. doi: 10.1007/s005310000152

Hirth, G., and J. Tullis. (1992), Dislocation creep regimes in quartz aggregates. *Journal of Structural Geology*, *14*(2), 145–159.

Hirth, G., and J. Tullis. (1994), The brittle-plastic transition in experimentally deformed quartz aggregates. *Journal of Geophysical Research*, *99*(B6), 11731. doi: 10.1029/93JB02873

Holdaway. (1971), Stability of Andalusite and the aluminum silicate phase diagram. *American Journal of Science*. 271, 97-131.

Holk, G. J., and H. P. Taylor. (1997), 18O/16O homogenization of the middle crust during anatexis: The Thor-Odin metamorphic core complex , British Columbia. *Geology*, *25*(1), 31–34. doi: 10.1130/0091-7613(1997)025<0031

Holyoke, C. W., and A. K. Kronenberg. (2010), Accurate differential stress measurement using the molten salt cell and solid salt assemblies in the Griggs apparatus with applications to strength, piezometers and rheology. *Tectonophysics*, *494*(1-2), 17–31. Elsevier B.V. doi: 10.1016/j.tecto.2010.08.001

Horn, I., R. W. Hinton, S. E. Jackson, and H. P. Longerich. (1993), Ultra-Trace Element Analysis of NIST SRM 616 and 614 using Laser Ablation Microprobe-Inductively Coupled Plasma- Mass Spectrometry (LAM-ICP-MS): a Comparison with Secondary Ion Mass Spectrometry (SIMS). *Geostandards Newsletter*, *21*, 191–203.

Huang, R., and A. Audétat. (2012), The titanium-in-quartz (TitaniQ) thermobarometer: A critical examination and re-calibration. *Geochimica et Cosmochimica Acta*, *84*, 75–89. doi: 10.1016/j.gca.2012.01.009

Huber, P., S. Grüner, C. Schäfer, K. Knorr, and A. V. Kityk. (2007), Rheology of liquids in nanopores: A study on the capillary rise of water, n-Hexadecane and n-Tetracosane in mesoporous silica. *The European Physical Journal Special Topics*, *141*(1), 101–105. doi: 10.1140/epjst/e2007-00024-0

Hull, D., and D. J. Bacon. (2011), *Introduction to Dislocations, Fifth Edition*. Oxford: Butterworth-Heinemann, 272 pp.

Jabra, R., J. Phalippou, and J. Zarzycki. (1980), Synthesis of binary glass-forming oxide glasses by hot-pressing of gels. *Journal of Non-Crystalline Solids*, *42*, 489–498.

Jal, P. K., S. Patel, and B. K. Mishra. (2004), Chemical modification of silica surface by immobilization of functional groups for extractive concentration of metal ions. *Talanta*, *62*(5), 1005–28. doi: 10.1016/j.talanta.2003.10.028

James, W. C., and R. Q. Oaks. (1977), Petrology of the Kinnikinic Quartzite (Middle Ordovician), East-central Idaho. *Journal of Sedimentary Petrology*, *47*(4), 1491–1511.

Jayaraman, N. (1938), The cause of colour of the blue quartzes of the charnockites of south India and the Champion gneiss and other related rocks of Mysore. *Current Science*, 265-284.

Jiang, S.-Y., R.-C. Wang, X.-S. Xu, and K.-D. Zhao. (2005), Mobility of high field strength elements (HFSE) in magmatic-, metamorphic-, and submarine-hydrothermal systems. *Physics and Chemistry of the Earth, Parts A/B/C*, *30*(17-18), 1020–1029. doi: 10.1016/j.pce.2004.11.004

Jochum, K. P., and 35 Others. (2000), The preparation and preliminary characterisation of eigth geological MPI-DING reference glasses for in situ microanalysis. *Geostandards Newsletter*, *24*(1), 87–133.

Jochum, K. P., U. Weis, B. Stoll, D. Kuzmin, Q. Yang, I. Raczek, D. E. Jacob, et al. (2011), Determination of reference values for NIST SRM 610-617 glasses following ISO guidelines. *Geostandards and Geoanalytical Research*, *35*(4), 397–429. doi: 10.1111/j.1751-908X.2011.00120.x

Kane, J. S. (1998), A history of the development and certification of NIST glass SRMs 610-617. *Geostandards Newsletter*, *22*(1), 7–13. doi: 10.1111/j.1751-908X.1998.tb00541.x

Karbasi, M.-H., B. Jahanparast, M. Shamsipur, and J. Hassan. (2009), Simultaneous trace multielement determination by ICP-OES after solid phase extraction with modified

octadecyl silica gel. *Journal of hazardous materials*, *170*(1), 151–5. doi: 10.1016/j.jhazmat.2009.04.119

Kawasaki, T., and Y. Osanai. (2008), Empirical thermometer of TiO2 in quartz for ultrahigh-temperature granulites of East Antarctica. *Geological Society, London, Special Publications*, *308*(1), 419–430. doi: 10.1144/SP308.21

Kerrich, R., T. La Tour, and W. L. (1984), Fluid Participation in Deep Fault Zones ' Evidence From Geological , Geochemical , and. *Journal of Geophysical Research*, *89*(B6), 4331–4343.

Ketcham, R. A. (2005), Computational methods for quantitative analysis of three-dimensional features in geological specimens. *Geosphere*, *1*(1), 32. doi: 10.1130/GES00001.1

Kidder, S., J.-P. Avouac, and Y.-C. Chan. (2013), Application of titanium-in-quartz thermobarometry to greenschist facies veins and recrystallized quartzites in the Hsüehshan range, Taiwan. *Solid Earth*, *4*(1), 1–21. doi: 10.5194/se-4-1-2013

Kirschner, D., C. Teyssier, R. Gregory, and Z. Sharp. (1995), Effect of deformation on oxygen isotope exchange in the Heavitree Quartzite , Ruby Gap duplex , central Australia. *Journal of Structural Geology*, *17*(10), 1407–1423.

Kohlstedt, D. L., B. Evans, and S. J. Mackwell. (1995), Strength of the lithosphere: Constraints imposed by laboratory experiments. *Journal of Geophysical Research*, *100*(B9), 17587–17602.

Kohlstedt, D. L., and M. S. Weathers. (1980), Deformation-Induced Microstructures, Paleopiezometers, and Differential Stresses in Deeply Eroded Fault Zones. *Journal of Geophysical Research*, *85*(B11), 6269–6285.

Kohn, M. J., and C. J. Northrup. (2009), Taking mylonites' temperatures. *Geology*, *37*(1), 47–50. doi: 10.1130/G25081A.1

Korsakov, A. V., M. Perraki, V. P. Zhukov, K. De Gussem, P. Vandenabeele, and A. A. Tomilenko. (2009), Is quartz a potential indicator of ultrahigh-pressure metamorphism?
 Laser Raman spectroscopy of quartz inclusions in ultrahigh-pressure garnets. *European Journal of Mineralogy*, *21*(6), 1313–1323. doi: 10.1127/0935-1221/2009/0021-2006

Kronenberg, A. K., and J. Tullis. (1984), Flow strengths of quartz aggregates: Grain size and pressure effects due to hydrolytic weakening. *Journal of Geophysical Research*, *89*(B6), 4281. doi: 10.1029/JB089iB06p04281

Kronz, A., A. M. Van Den Kerkhof, and A. Müller. (2012), Analysis of low element concentrations in quartz by electron microprobe. In J. Götze and R. Möckel (Eds.), *Quartz:*

Deposits, Mineralogy and Analytics (pp. 191–217). Berlin, Heidelberg: Springer Berlin Heidelberg. doi: 10.1007/978-3-642-22161-3

Kruckenberg, S. C., and D. L. Whitney. (2011), Metamorphic evolution of sapphirine- and orthoamphibole-cordierite-bearing gneiss, Okanogan dome, Washington, USA. *Journal of Metamorphic Geology*, *29*(4), 425–449. doi: 10.1111/j.1525-1314.2010.00926.x

Kruhl, J. H. (1996), Prism- and basal-plane parallel subgrain boundaries in quartz: a microstructural geothermobaromether. *Journal of Metamorphic Geology*, *14*, 581–589. doi: 10.1046/j.1525-1314.1996.00413.x

Kruhl, J. H., and M. Nega. (1996), The fractal shape of sutured quartz grain boundaries : application as a geothermometer. *Geol Rundsch*, 38–43.

Kylander-Clark, A. R. C., B. R. Hacker, and C. G. Mattinson. (2012), Size and exhumation rate of ultrahigh-pressure terranes linked to orogenic stage. *Earth and Planetary Science Letters*, *321-322*, 115–120. Elsevier B.V. doi: 10.1016/j.epsl.2011.12.036

Lane, L. S., E. D. Ghent, M. Z. Stout, and R. L. Brown. (1989), P-T history and kinematics of the Monashee Decollement near Revelstoke, British Columbia. *Canadian Journal of Earth Sciences*, *26*(2), 231–243.

Lanzillo, N. A., E. B. Watson, J. B. Thomas, S. K. Nayak, and A. Curioni. (2014), Near-surface controls on the composition of growing crystals: Car–Parrinello molecular dynamics (CPMD) simulations of Ti energetics and diffusion in alpha quartz. *Geochimica et Cosmochimica Acta*, *131*, 33–46. doi: 10.1016/j.gca.2014.01.015

Lasaga, A. C. (1983), Geospeedometry: An Extension of Geothermometry. *Kinetics and Equilibrium in Mineral Reactions*, *3*(1980), 81–114.

Law, R. D. (1990), Crystallographic fabrics: a selective review of their applications to research in structural geology. *Geological Society, London, Special Publications*, *54*(1), 335–352. doi: 10.1144/GSL.SP.1990.054.01.30

Law, R. D. (2014), Deformation thermometry based on quartz c-axis fabrics and recrystallization microstructures: A review. *Journal of Structural Geology*, *66*, 129–161. Elsevier Ltd. doi: 10.1016/j.jsg.2014.05.023

Law, R. D., M. J. Jessup, M. P. Searle, M. K. Francsis, D. J. Waters, and J. M. Cottle. (2011), Telescoping of isotherms beneath the South Tibetan Detachment System, Mount Everest Massif. *Journal of Structural Geology*, *33*(11), 1569–1594. Elsevier Ltd. doi: 10.1016/j.jsg.2011.09.004

Lee, R. (1993), *Scanning electron microscopy and x-ray microanalysis*. Prentice Hall, 458 pp.

Leeman, W. P., C. M. Macrae, N. C. Wilson, A. Torpy, C.-T. Lee, J. J. Student, J. B. Thomas, et al. (2012), A study of cathodoluminescence and trace element compositional zoning in natural quartz from volcanic rocks: mapping titanium content in quartz. *Microscopy and microanalysis 18*(6), 1322–41. doi: 10.1017/S1431927612013426

Lehmann, K., T. Pettke, and K. Ramseyer. (2011), Significance of trace elements in syntaxial quartz cement, Haushi Group sandstones, Sultanate of Oman. *Chemical Geology*, *280*(1-2), 47–57. Elsevier B.V. doi: 10.1016/j.chemgeo.2010.10.013

Leyden, D. E., and G. H. Luttrell. (1975), Preconcentration of trace metals using chelating groups immobilized via silylation. *Analytical Chemistry*, *47*(9), 1612–1617. doi: 10.1021/ac60359a056

Li, X., B. Rusk, R. Wang, Y. Morishita, Y. Watanabe, and Z. Chen. (2011), Rutile inclusions in quartz crystals record decreasing temperature and pressure during the exhumation of the Su-Lu UHP metamorphic belt in Donghai, East China. *American Mineralogist*, *96*(7), 964–973. doi: 10.2138/am.2011.3574

Liang, P., E. Zhao, and R. Liu. (2008), Determination of Platinum and Palladium in Geological Samples by Inductively Coupled Plasma-Atomic Emission Spectrometry after Preconcentration with Immobilised Nanometric Titanium Dioxide. *Geostandards and Geoanalytical Research*, *33*, 63–69.

Lister, G., and A. Snoke. (1984), S-C Mylonites. *Journal of Structural Geology*, *6*(6), 617–638.

Lorencak, M., D. Seward, O. Vanderhaeghe, C. Teyssier, and J. P. Burg. (2001), Low-temperature cooling history of the Shuswap metamorphic core complex, British Columbia: constraints from apatite and zircon fission-track ages. *Canadian Journal of Earth Sciences*, *38*(11), 1615–1625. doi: 10.1139/cjes-38-11-1615

Lowry, A. R., and M. Pérez-Gussinyé. (2011), The role of crustal quartz in controlling Cordilleran deformation. *Nature*, *471*(7338), 353–7. doi: 10.1038/nature09912

Luan, F. C., and M. S. Paterson. (1992), Preparation and deformation of synthetic aggregates of quartz. *Journal of Geophysical Research*, *97*(B1), 301. doi: 10.1029/91JB01748

Luth, W. C., and C. O. Ingamells. (1965), Gel preparation of starting materials for hydrothermal experimentation. *American Mineralogist*, *50*(63), 255–258.

Mackwell, S. J., and M. S. Paterson. (1985), Point Defects in Minerals. *Eos, Transactions American Geophysical Union*, *66*, 459. doi: 10.1029/EO066i021p00459-03

Mahmoud, M. E., M. M. Osman, and M. E. Amer. (2000), Selective pre-concentration and solid phase extraction of mercury(II) from natural water by silica gel-loaded dithizone phases. *Analytica Chimica Acta*, *415*(10), 1536–1541. doi: 10.1002/cjoc.200790282

Mancktelow, N. S., and G. Pennacchioni. (2004), The influence of grain boundary fluids on the microstructure of quartz-feldspar mylonites. *Journal of Structural Geology*, *26*(1), 47–69. doi: 10.1016/S0191-8141(03)00081-6

Manning, C. E. (2006), Mobilizing aluminum in crustal and mantle fluids. *Journal of Geochemical Exploration*, *89*(1-3), 251–253. doi: 10.1016/j.gexplo.2005.12.019

Masberg, H. P., E. Holler, and S. Hoernes. (1992), Microfabrics indicating granulite-facies metamorphism in the low-pressure central Damara Orogen , Namibia, *55*, 243–257.

McCaig, A. M., and R. J. Knipe. (1990), Mass-transport mechanisms in deforming rocks: Recognition using microstructural and microchemical criteria. *Geology*, 18, 824-827.

McFadden, R. R., a. Mulch, C. Teyssier, and M. Heizler. (2015), Eocene extension and meteoric fluid flow in the Wildhorse detachment, Pioneer metamorphic core complex, Idaho. *Lithosphere*, (4), 355–367. doi: 10.1130/L429.1

McLaren, A. C., J. D. Fitz Gerald, and J. Gerretsen. (1989), Dislocation nucleation and multiplication in synthetic quartz: Relevance to water weakening. *Physics and Chemistry of Minerals*, *16*(5), 465–482. doi: 10.1007/BF00197016

Menegon, L., P. Nasipuri, H. Stünitz, H. Behrens, and E. Ravna. (2011), Dry and strong quartz during deformation of the lower crust in the presence of melt. *Journal of Geophysical Research*, *116*(B10), B10410. doi: 10.1029/2011JB008371

Miller, E. L., T. A. Dumitru, R. W. Brown, and P. B. Gans. (1999), Rapid Miocene slip on the Snake Range – Deep Creek Range fault system, east-central Nevada. *Geological Society of America Bulletin*, *111*(6), 886–905. doi: 10.1130/0016-7606(1999)111<0886

Mitra, S. (1976), A Quantitative Study of Deformation Mechanisms and Finite Strain in Quartzites. *Contributions to Mineralogy and Petrology*, *59*, 203–226.

Mitra, S. (1978), Microscopic Deformation Mechanisms and Flow Laws in Quartzites within the South Mountain Anticline. *Journal of Geology*, *86*(1), 129–152.

Mitra, S., and J. Tullis. (1979), A comparison of intracrystalline deformation in naturally and experimentally deformed quartzites. *Tectonophysics*, *53*, 21–27.

Morgan, D. J., M. C. Jollands, G. E. Lloyd, and D. a. Banks. (2013), Using titanium-in-quartz geothermometry and geospeedometry to recover temperatures in the aureole of the

References Cited

Ballachulish Igneous Complex, NW Scotland. *Geological Society, London, Special Publications*. doi: 10.1144/SP394.8

Mottram, C., R. Parrish, D. Regis, C. Warren, T. Argles, N. Harris, and N. Roberts. (2015), Using U-Th-Pb petrochronology to determine rates of ductile thrusting: Time windows into the Main Central Thrust, Sikkim Himalaya. *Tectonics*. doi: 10.1002/2014TC003743.Received

Mulch, A. (2004), *Integrated high-spatial resolutoin 40Ar/39Ar geochronology, stable isotope geochemistry, and structural analysis of extensional detachment systems: case studies from the Prosgrunn-Kristiansand shear zone (S-Norway) and the Shuswap metamorphic core complex*. PhD thesis, University of Lausanne.

Mulch, A., and M. A. Cosca. (2004), Recrystallization or cooling ages: in situ UV-laser 40Ar/39Ar geochronology of muscovite in mylonitic rocks. *Journal of the Geological Society*, *161*(4), 573–582. doi: 10.1144/0016-764903-110

Mulch, A., M. Cosca, A. Andresen, and J. Fiebig. (2005), Time scales of deformation and exhumation in extensional detachment systems determined by high-spatial resolution in situ UV-laser 40Ar/39Ar dating. *Earth and Planetary Science Letters*, *233*(3-4), 375–390. doi: 10.1016/j.epsl.2005.01.042

Mulch, A., C. Teyssier, M. A. Cosca, and C. P. Chamberlain. (2007), Stable isotope paleoaltimetry of Eocene core complexes in the North American Cordillera. *Tectonics*, *26*(4). doi: 10.1029/2006TC001995

Mulch, A., C. Teyssier, M. A. Cosca, O. Vanderhaeghe, and T. W. Vennemann. (2004), Reconstructing paleoelevation in eroded orogens. *Geology*, *32*(6), 525. doi: 10.1130/G20394.1

Mulch, A., C. Teyssier, M. A. Cosca, and T. W. Vennemann. (2006), Thermomechanical analysis of strain localization in a ductile detachment zone. *Journal of Geophysical Research*, *111*(B12), 1–20. doi: 10.1029/2005JB004032

Muller, A., M. Wiedenbeck, A. M. van den Kerkhof, A. Kronz, and K. Simon. (2003), Trace elements in quartz – a combined electron microprobe, secondary ion mass spectrometry, laser-ablation ICP-MS, and cathodoluminescence study. *European Journal of Mineralogy*, *15*(4), 747–763. doi: 10.1127/0935-1221/2003/0015-0747

Muller, W. (2000), Isotopic Dating of Strain Fringe Increments: Duration and Rates of Deformation in Shear Zones. *Science*, *288*(5474), 2195–2198. doi: 10.1126/science.288.5474.2195

Muto, J., G. Hirth, R. Heilbronner, and J. Tullis. (2011), Plastic anisotropy and fabric evolution in sheared and recrystallized quartz single crystals. *Journal of Geophysical Research*, *116*(B2), 1–18. doi: 10.1029/2010JB007891

Nachlas, W. O., and G. Hirth. (2015), Experimental constraints on the role of dynamic recrystallization on resetting the Ti-in-quartz thermobarometer. *Journal of Geophysical Research: Solid Earth*, *120*, 1–18. doi: 10.1002/2015JB012274

Nachlas, W. O., C. Teyssier, and D. L. Whitney. (2015), Timescales of ductility in an extensional shear zone recorded as diffusion profiles in deformed quartz. *EGU Abstracts*.

Nachlas, W. O., D. L. Whitney, C. Teyssier, B. Bagley, and A. Mulch. (2014), Titanium concentration as a record of multiple deformation mechanisms in an extensional shear zone. *Geochemistry, Geophysics, Geosystems*, 1–24. doi: 10.1002/2013GC005200

Nawrocki, J. (1991a), Silica Surface Controversies , Strong Adsorption Sites , their Blockage and Removal. Part I. *Chromatographia*, *31*(3-4), 177–192.

Nawrocki, J. (1991b), Silica Surface Controversies , Strong Adsorption Sites , their Blockage and Removal. Part II. *Chromatographia*.

Nawrocki, J. (1997), The silanol group and its role in liquid chromatography. *Journal of Chromatography A*, *779*(1-2), 29–71. doi: 10.1016/S0021-9673(97)00479-2

Nawrocki, J., D. L. Moir, and W. Szczepaniak. (1989), Trace Metal Impurities in Silica as a Cause of Strongly Interacting Silanols. *Chromatographia*, *28*(3-4), 143–147.

Negrini, M., H. Stunitz, A. Berger, and L. F. G. Morales. (2014), The effect of deformation on the TitaniQ geothermobarometer: an experimental study. *Contributions to Mineralogy and Petrology*, *167*(3), 982. doi: 10.1007/s00410-014-0982-x

Norlander, B. H., D. L. Whitney, C. Teyssier, and O. Vanderhaeghe. (2002), Partial melting and decompression of the Thor-Odin dome, Shuswap metamorphic core complex, Canadian Cordillera. *Lithos*, *61*(3-4), 103–125. doi: 10.1016/S0024-4937(02)00075-0

Nyman, M. W., D. R. M. Pattison, and E. D. Ghent. (1995), Melt Extraction during Formation of K-Feldspar + Sillimanite Migmatites, West of Revelstoke, British Columbia. *Journal of Petrology*, *36*(2), 351–372. doi: 10.1093/petrology/36.2.351

O'Neill, R. L., and T. L. Pavlis. (1988), Superposition of Cenozoic extension on Mesozoic compressional structures in the Pioneer Mountains metamorphic core complex , central Idaho. *Geological Society of America Bulletin*. doi: 10.1130/0016-7606(1988)100<1833

Olker, B., R. Altherr, and J. Paquin. (2003), Fast exhumation of the ultrahigh-pressure Alpe Arami garnet peridotite (Central Alps, Switzerland): constraints from geospeedometry and thermal modelling. *Journal of Metamorphic Geology*, *21*(4), 395–402. Retrieved from <Go to ISI>://000182577500006

Ostapenko, G. T., A. N. Tarashchan, and B. M. Mitsyuk. (2007), Rutile-quartz geothermobarometer. *Geochemistry International*, *45*(5), 506–508. doi: 10.1134/S0016702907050084

Parrish, R. R., S. D. Carr, and D. Parkinson. (1988), EOCENE EXTENSIONAL TECTONICS AND GEOCHRONOLOGY OF THE SOUTHERN OMINECA BELT, BRITISH COLUMBIA AND WASHINGTON. *Tectonics*, *7*(2), 181–212.

Passchier, C. W., and R. A. J. Trouw. (2005), *Microtectonics*. Springer-Verlag Berlin Heidelberg, 366 pp.

Paterson, M. S. (1986), The Thermodynamics of Water in Quartz. *Physics and Chemistry of Minerals*, *13*, 245–255.

Paterson, M. S., and F. C. Luan. (1990), Quartzite rheology under geological conditions. *Geological Society, London, Special Publications*, *54*(1), 299–307. doi: 10.1144/GSL.SP.1990.054.01.26

Pattison, D., and R. Tracy. (1991), Phase equilibria and thermobarometry of metapelites. *Reviews in Mineralogy and Geochemistry*.

Pearce, N. J. G., W. T. Perkins, J. A. Westgate, M. P. Gorton, S. E. Jackson, C. R. Neal, and S. P. Chenery. (1997), A Compilation of New and Published Major and Trace Element Data

for NIST SRM 610 and NIST SRM 612 Glass Reference Materials. *Geostandards and Geoanalytical Research*, *21*(1), 115–144. doi: 10.1111/j.1751-908X.1997.tb00538.x

Person, M., A. Mulch, C. Teyssier, and Y. Gao. (2007), Isotope transport and exchange within metamorphic core complexes. *American Journal of Science*, *307*(3), 555–589. doi: 10.2475/03.2007.01

Peterman, E. M., and M. Grove. (2010), Growth conditions of symplectic muscovite + quartz: Implications for quantifying retrograde metamorphism in exhumed magmatic arcs. *Geology*, *38*(12), 1071–1074. doi: 10.1130/G31449.1

Pfiffner, O., and J. Ramsay. (1982), Constraints on Geological Strain Rates: Arguments From Finite Strain States of Naturally Deformed Rocks. *Journal of Geophysical Research*, *87*(B1), 311–321.

Phalippou, J., M. Prassas, and J. Zarzycki. (1982), Crystallization of gels and glasses made from hot-pressed gels. *Journal of Non-crystalline solids*, *48*, 17–30.

Philippot, P., J. Blichert-Toft, A. Perchuk, S. Costa, and V. Gerasimov. (2001), Lu-Hf and Ar-Ar chronometry supports extreme rate of subduction zone metamorphism deduced from geospeedometry. *Tectonophysics*, *342*(1-2), 23–38. doi: 10.1016/S0040-1951(01)00155-X

Phillips, R. J., R. R. Parrish, and M. P. Searle. (2004), Age constraints on ductile deformation and long-term slip rates along the Karakoram fault zone, Ladakh. *Earth and Planetary Science Letters*, *226*(3-4), 305–319. doi: 10.1016/j.epsl.2004.07.037

Platt, J. P., and W. M. Behr. (2011), Grainsize evolution in ductile shear zones: Implications for strain localization and the strength of the lithosphere. *Journal of Structural Geology*, *33*(4), 537–550. Elsevier Ltd. doi: 10.1016/j.jsg.2011.01.018

Poirier, J.-P. (1985), *Creep of Crystals*. Cambridge University Press, 274 pp.

Post, A., and J. Tullis. (1998), The rate of water penetration in experimentally deformed quartzite : implications for hydrolytic weakening. *Tectonophysics*, *295*, 117–137.

Price, R. A. (1986), The southeastern Canadian Cordillera: thrust faulting, tectonic wedging, and delamination of the lithosphere. *Journal of Structural Geology*, *8*(3-4), 239–254.

Prior, D. J., Boyle, A. N., Brenker, F., Cheadle, M. C., Day, A., Lopez, G., Peruzzo, L., Potts, G. J., Reddy, S., Spiess, R., Timms, N. E., Trimby, P., Wheeler, J., Zetterstrom, L. (1999), The application of electron backscatter diffraction and orientation contrast imaging in the SEM to textural problems in rocks. *American Mineralogist*, *84*, 1741–1759.

Pryer, L. L. (1993), Micrstructures in feldspars from a major crustal thrust zone: the Grenville Front, Ontario, Canada. *Journal of Structural Geology*, *15*(1).

Read, P. B., and R. L. Brown. (1981), Columbia River fault zone: southeastern margin of the Shuswap and Monashee complexes, southern British Columbia. *Canadian Journal of Earth Sciences*, *18*(7), 1127–1145.

Reesor, J., and J. Moore. (1971), Petrology andstructure of Thor-Odin gneiss dome, Shuswap metamorphic complex, British Columbia. *Geological Survey of Canada, Paper 195* (p. 149).

Rusk, B. G., H. A. Lowers, and M. H. Reed. (2008), Trace elements in hydrothermal quartz: Relationships to cathodoluminescent textures and insights into vein formation. *Geology*, *36*(7), 547. doi: 10.1130/G24580A.1

Sassier, C., P. H. Leloup, D. Rubatto, O. Galland, Y. Yue, and D. Lin. (2009), Direct measurement of strain rates in ductile shear zones: A new method based on syntectonic dikes. *Journal of Geophysical Research*, *114*(B1), 1–22. doi: 10.1029/2008JB005597

Sato, K., and M. Santosh. (2007), Titanium in quartz as a record of ultrahigh-temperature metamorphism: the granulites of Karur, southern India. *Mineralogical Magazine*, *71*(2), 143–154. doi: 10.1180/minmag.2007.071.2.143

Scott, D. J., N. Machado, S. Handmer, and C. Gariepy (1993), Dating ductile deformation using U-Pb geochronology: examples from the Gilbert River Belt, Grenville Province, Labrador, Canada. *Canadian Journal of Earth Sciences*, *30*(7), 1458–1469.

Searle, M. P., M.-W. Yeh, T.-H. Lin, and S.-L. Chung. (2010), Structural constraints on the timing of left-lateral shear along the Red River shear zone in the Ailao Shan and Diancang Shan Ranges, Yunnan, SW China. *Geosphere*, *6*(4), 316–338. doi: 10.1130/GES00580.1

Seifert, W., D. Rhede, R. Thomas, H.-J. Forster, F. Lucassen, P. Dulski, and R. Wirth. (2011), Distinctive properties of rock-forming blue quartz: inferences from a multi-analytical study of submicron mineral inclusions. *Mineralogical Magazine*, *75*(4), 2519–2534. doi: 10.1180/minmag.2011.075.4.2519

Sepahi, A. A., D. L. Whitney, and A. A. Baharifar. (2004), Petrogenesis of andalusite-kyanite-sillimanite veins and host rocks, Sanandaj-Sirjan metamorphic belt, Hamadan, Iran. *Journal of Metamorphic Geology*, *22*(2), 119–134. doi: 10.1111/j.1525-1314.2004.00502.x

Sherlock, S. C., S. P. Kelley, J. A. Zalasiewicz, D. I. Schofield, J. A. Evans, R. J. Merriman, and S. J. Kemp. (2003), Precise dating of low-temperature deformation: Strain-fringe analysis by 40Ar-39Ar laser microprobe. *Geology*, *31*(3), 219–222. doi: 10.1130/0091-7613(2003)031<0219:PDOLTD>2.0.CO;2

Shulaker, D. Z., A. K. Schmitt, T. Zack, and I. Bindeman. (2015), In-situ oxygen isotope and trace element geothermometry of rutilated quartz from Alpine fissures. *American Mineralogist*, *100*, 915–925.

Siebenaller, L., M.-C. Boiron, O. Vanderhaeghe, C. Hibsch, M. W. Jessell, A.-S. Andre-Mayer, C. France-Lanord (2013), Fluid record of rock exhumation across the brittle-ductile transition during formation of a Metamorphic Core Complex (Naxos Island, Cyclades, Greece). *Journal of Metamorphic Geology*, *31*(3), 313–338. doi: 10.1111/jmg.12023

Silverberg, D. S. (1990), *The tectonic evolution of the pioneer metamoprhic core complex, south-central Idaho*.

Spalla, M. I., D. Zanoni, P. F. Williams, and G. Gosso. (2011), Deciphering cryptic P–T-d–t histories in the western Thor-Odin dome, Monashee Mountains, Canadian Cordillera: A key to unravelling pre-Cordilleran tectonic signatures. *Journal of Structural Geology*, *33*(3), 399–421. Elsevier Ltd. doi: 10.1016/j.jsg.2010.11.014

Spear, F. S., K. T. Ashley, L. E. Webb, and J. B. Thomas. (2012), Ti diffusion in quartz inclusions: Implications for metamorphic time scales. *Contributions to Mineralogy and Petrology*, *164*(6), 977–986. doi: 10.1007/s00410-012-0783-z

Stipp, M., H. Stunitz, R. Heilbronner, and S. M. Schmid. (2002), Dynamic recrystallization of quartz: correlation between natural and experimental conditions. *Geological Society, London, Special Publications*, *200*(1), 171–190. doi: 10.1144/GSL.SP.2001.200.01.11

Stipp, M., and J. Tullis. (2003), The recrystallized grain size piezometer for quartz. *Geophysical Research Letters*, *30*(21), 2088. doi: 10.1029/2003GL018444

Stipp, M., J. Tullis, and H. Behrens. (2006), Effect of water on the dislocation creep microstructure and flow stress of quartz and implications for the recrystallized grain size piezometer. *Journal of Geophysical Research*, *111*(B4), 1–19. doi: 10.1029/2005JB003852

Storm, L. C., and F. S. Spear. (2009), Application of the titanium-in-quartz thermometer to pelitic migmatites from the Adirondack Highlands, New York. *Journal of Metamorphic Geology*, *27*(7), 479–494. doi: 10.1111/j.1525-1314.2009.00829.x

Teyssier, C. (2011), Exhumation of deep orogenic crust. *Lithosphere*, *3*(6), 439–443. doi: 10.1130/RF.L002.1

Teyssier, C., E. C. Ferre, D. L. Whitney, B. Norlander, O. Vanderhaeghe, and D. Parkinson. (2005), Flow of partially molten crust and origin of detachments during collapse of the Cordilleran Orogen. *Geological Society, London, Special Publications*, *245*(1), 39–64. doi: 10.1144/GSL.SP.2005.245.01.03

Thomas, J. B., E. Bruce Watson, F. S. Spear, P. T. Shemella, S. K. Nayak, and A. Lanzirotti. (2010), TitaniQ under pressure: the effect of pressure and temperature on the solubility of Ti in quartz. *Contributions to Mineralogy and Petrology*, *160*(5), 743–759. doi: 10.1007/s00410-010-0505-3

Thomas, J. B., E. B. Watson, F. S. Spear, and D. A. Wark. (2015), TitaniQ recrystallized: experimental confirmation of the original Ti-in-quartz calibrations. *Contributions to Mineralogy and Petrology*, *169*. doi: 10.1007/s00410-015-1120-0

Thompson, K., P. L. Flaitz, P. Ronsheim, D. J. Larson, and T. F. Kelly. (2007), Imaging of Arsenic Cottrell Atmospheres. *Science*, *1370*(September), 1370–1375. doi: 10.1126/science.1145428

Timms, N. E., P. D. Kinny, S. M. Reddy, K. Evans, C. Clark, and D. Healy. (2011), Relationship among titanium, rare earth elements, U–Pb ages and deformation microstructures in zircon: Implications for Ti-in-zircon thermometry. *Chemical Geology*, *280*(1-2), 33–46. Elsevier B.V. doi: 10.1016/j.chemgeo.2010.10.005

Tomkins, H. S., R. Powell, and D. J. Ellis. (2007), The pressure dependence of the zirconium-in-rutile thermometer. *Journal of Metamorphic Geology*, *25*(6), 703–713. doi: 10.1111/j.1525-1314.2007.00724.x

Tropper, P., and C. E. Manning. (2005), Very low solubility of rutile in H2O at high pressure and temperature, and its implications for Ti mobility in subduction zones. *American Mineralogist*, *90*(2-3), 502–505. doi: 10.2138/am.2005.1806

Tullis, J. (2002), Deformation of Granitic Rocks: Experimental Studies and Natural Examples. *Reviews in Mineralogy and Geochemistry*, *51*(1), 51–95. doi: 10.2138/gsrmg.51.1.51

Tullis, J., J. M. Christie, and D. T. Griggs. (1973), Microstructures and Preferred Orientations of Experimentally Deformed Quartzites. *Geological Society of America Bulletin*, *84*(1), 297–314. doi: 10.1130/0016-7606(1973)84<297

Tullis, T. E., and J. Tullis. (1986), Experimental Rock Deformation Techniques. *Geophysical Monograph*, 1029. doi: 10.1029/GM036p0297

Unger, K. K. (1994), Surface Structure of Amorphous and Crystalline Porous Silicas. *American Chemical Society*, (6).

Urai, J. L., W. D. Means, and G. S. Lister. (1986), Dynamic recrystallization of minerals. *Mineral and Rock Deformation: The Paterson Volume (eds B.E. Hobbs and H.C. Heard) American Geophysical Union, Washington, D.C.* (pp. 1–49).

Valley, J. (2001), Stable Isotope Thermometry at High Temperatures. *Reviews in Mineralogy and Geochemistry*, *43*(1), 365–413. doi: 10.2138/gs

Vance, D., W. Muller, and I. M. Villa. (2003), Geochronology: Linking the isotopic record with petrology and textures - an introduction. *Geological Society, London, Special Publications* (Vol. 32, pp. 138–139). doi: 10.1144/GSL.SP.2003.220.01.01

Vanderhaeghe, O., C. Teyssier, I. McDougall, and W. J. Dunlap. (2003), Cooling and exhumation of the Shuswap Metamorphic Core Complex constrained by 40 Ar / 39 Ar thermochronology. *Geological Society of America Bulletin*, (2), 200–216.

Vanderhaeghe, O., C. Teyssier, and R. Wysoczanski. (1999), Structural and geochronological constraints on the role of partial melting during the formation of the Shuswap metamorphic core complex at the latitude of the Thor-Odin dome, British Columbia. *Canadian Journal of Earth Sciences*, *36*(6), 917–943.

Venkatesh, G., A. K. Singh, and B. Venkataramani. (2004), Silica Gel Loaded with o - Dihydroxybenzene: Design, Metal Sorption Equilibrium Studies and Application to Metal Enrichment Prior to Determination by Flame Atomic Absorption Spectrometry. *Microchimica Acta*, *144*(4), 233–241. doi: 10.1007/s00604-003-0132-z

Vernooij, M. G. C., B. den Brok, and K. Kunze. (2006), Development of crystallographic preferred orientations by nucleation and growth of new grains in experimentally deformed quartz single crystals. *Tectonophysics*, *427*(1-4), 35–53. doi: 10.1016/j.tecto.2006.06.008

Vogl, J. J., C. A, K. Min, D. W. Rodgers, and F. M. C. (2010), EXTENSIONAL AND COOLING HISTORY OF THE PIONEER CORE COMPLEX , SOUTH - CENTRAL IDAHO : LONG - LIVED EPISODIC EXTENSION AND IMPLICATIONS FOR REGIONAL PATTERNS OF, (250), 182065.

Vogl, J. J., D. A. Foster, C. M. Fanning, K. A. Kent, D. W. Rodgers, and T. Diedesch. (2012), Timing of extension in the Pioneer metamorphic core complex with implications for the spatial-temporal pattern of Cenozoic extension and exhumation in the northern U . S . Cordillera. *Tectonics*, *31*, 1–22. doi: 10.1029/2011TC002981

Wark, D. A., and E. B. Watson. (2006), TitaniQ: a titanium-in-quartz geothermometer. *Contributions to Mineralogy and Petrology*, *152*(6), 743–754. doi: 10.1007/s00410-006-0132-1

Watson, E. B. (2004), A conceptual model for near-surface kinetic controls on the trace-element and stable isotope composition of abiogenic calcite crystals. *Geochimica et Cosmochimica Acta*, *68*(7), 1473–1488. doi: 10.1016/j.gca.2003.10.003

Watson, E. B., and E. F. Baxter. (2007), Diffusion in solid-Earth systems. *Earth and Planetary Science Letters*, *253*(3-4), 307–327. doi: 10.1016/j.epsl.2006.11.015

Watson, E. B., and D. J. Cherniak. (2015), Quantitative cooling histories from stranded diffusion profiles. *Contributions to Mineralogy and Petrology*, *169*(6), 57. Springer Berlin Heidelberg. doi: 10.1007/s00410-015-1153-4

Watson, E. B., and Y. Liang. (1995), A simple model for sector zoning in slowly grown crystals: Implications for growth rate and lattice diffusion, with emphasis on accessory minerals in crustal rocks. *American Mineralogist*, *80*, 1179–1187.

Watson, E. B., D. A. Wark, and J. B. Thomas. (2006), Crystallization thermometers for zircon and rutile. *Contributions to Mineralogy and Petrology*, *151*(4), 413–433. doi: 10.1007/s00410-006-0068-5

Weertman, J., and J. R. Weertman. (1992), *Elementary Dislocation Theory*. Oxford: Oxford University Press.

Wells, M. L., T. D. Hoisch, M. T. Peters, D. M. Miller, E. D. Wolff, and L. M. Hanson. (1998), The Mahogany Peaks Fault , a Late Cretaceous-Paleocene (?) Normal Fault in the Hinterland of the Sevier Orogen. *The Journal of Geology*, *106*(5), 623–634.

Wheeler, J., D. Prior, Z. Jiang, R. Spiess, and P. Trimby. (2001), The petrological significance of misorientations between grains. *Contributions to Mineralogy and Petrology*, *141*(1), 109–124. doi: 10.1007/s004100000225

Whitney, D. L., C. Teyssier, and A. K. Fayon. (2004), Isothermal decompression, partial melting and exhumation of deep continental crust. *Geological Society, London, Special Publications*, *227*(1), 313–326. doi: 10.1144/GSL.SP.2004.227.01.16

Whitney, D. L., C. Teyssier, P. Rey, and W. R. Buck. (2013), Continental and oceanic core complexes. *Geological Society of America Bulletin*, *125*(3-4), 273–298. doi: 10.1130/B30754.1

Williams, M. L., and M. J. Jercinovic. (2002), Microprobe monazite geochronology : putting absolute time into microstructural analysis. *Journal of Structural Geology*, *24*, 1013–1028.

Winchester, J. A., and P. A. Floyd. (1977), GEOCHEMICAL DISCRIMINATION OF DIFFERENT MAGMA SERIES AND THEIR DIFFERENTIATION PRODUCTS USING IMMOBILE ELEMENTS. *Chemical Geology*, *20*, 325–343.

Wu, D., and A. Navrotsky. (2013), Small molecule - Silica interactions in porous silica structures. *Geochimica et Cosmochimica Acta*, *109*(August), 38–50. doi: 10.1016/j.gca.2013.01.038

Wust, S. L. (1986), Extensional deformation with northwest vergence, Pioneer core complex, central Idaho. *Geology*. doi: 10.1130/0091-7613(1986)14<712

Yund, R. A., and J. Tullis. (1991), Compositional changes of minerals associated with dynamic recrystallizatin. *Contributions to Mineralogy and Petrology*, *108*(3), 346–355. doi: 10.1007/BF00285942

Zack, T., R. Moraes, and A. Kronz. (2004), Temperature dependence of Zr in rutile: empirical calibration of a rutile thermometer. *Contributions to Mineralogy and Petrology*, *148*(4), 471–488. doi: 10.1007/s00410-004-0617-8

Zhang, X. Y., E. B. Watson, and D. J. Cherniak. (2007), Oxygen self-diffusion "fast-paths" in titanite single crystals and a general method for deconvolving self-diffusion profiles with "tails." *Geochimica et Cosmochimica Acta*, *71*(6), 1563–1573. doi: 10.1016/j.gca.2006.12.013

Zhang, Y., and D. Cherniak. (2010), Diffusion in Minerals and Melts. *Reviews in Mineralogy and Geochemistry*, *72*, 1038.

Zhuravlev, L. T. (2000), The surface chemistry of amorphous silica. Zhuravlev model. *Colloids and Surfaces A: Physicochemical and Engineering Aspects*, *173*(1-3), 1–38. doi: 10.1016/S0927-7757(00)00556-2

Zougagh, M., J. M. Cano Pavón, and A. Garcia de Torres. (2005), Chelating sorbents based on silica gel and their application in atomic spectrometry. *Analytical and bioanalytical chemistry*, *381*(6), 1103–13. doi: 10.1007/s00216-004-3022-2

Appendix 1

Supplementary Figures for Chapter 2

Figure A1.1. SEM-EBSD pole figure diagrams for quartz, showing the fabrics of quartzites from different levels of the shear zone. Diagrams (A) – (C) are quartzite mylonites, collected from 10 m, 40 m, and 757 m beneath the detachment. Diagram (D) was collected from the non-mylonitic quartzite protolith, the deepest sample beneath the detachment surface. Shear sense for each diagram is dextral.

Figure A1.2. Analytical transects of Ti concentration collected across an individual quartz ribbon, showing the high-Ti plateau in the cores of quartz

Figure A1.3. AFM analysis of the sputtered craters created by analysis with both ion microprobes; the SHRIMP-RG creates one large crater (beam current of 2.5 nA) (a), whereas the Cameca IMS-1280 creates a nested crater, (b) with a larger crater reflecting the pre-sputtering process (beam current of 9.3 nA for 540 s) followed by (c) a smaller inset crater representing the collection of the measurement (beam current of 3.8 nA for 240 s).

Figure A1.4. EMPA results of Si vs. Al p.f.u. from 5 samples (a) – (e) showing the variation in muscovite composition throughout the vertical extent of the shear zone.

Figure A1.5. 3-D measurements on accessory phase distribution from XRCT analysis. The 3-D aspect ratio is calculated from the longest and shortest axes of the accessory phase

volumes. The long axis of each accessory phase particle is plotted with respect to the foliation and lineation of the mylonites. The value *n* shows the number of individual accessory phase grains that were identified from each sample. Shear sense in each diagram is dextral.

Figure A1.1.

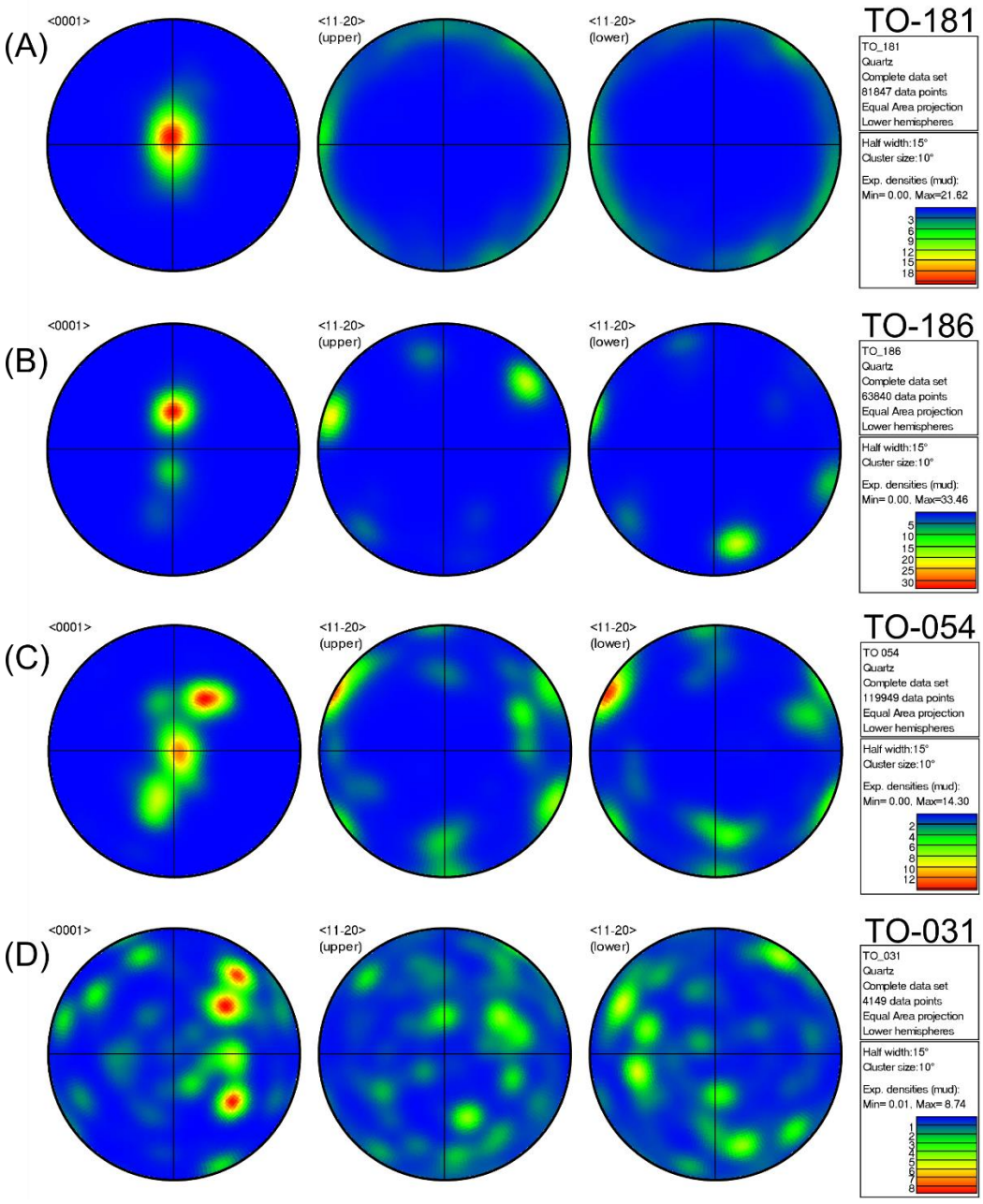
(A)
<0001>
<11-20> (upper)
<11-20> (lower)
TO-181
TO_181
Quartz
Complete data set
81847 data points
Equal Area projection
Lower hemispheres
Half width:15°
Cluster size:10°
Exp. densities (mud):
Min= 0.00, Max=21.62
3
6
9
12
15
18
(B)
<0001>
<11-20> (upper)
<11-20> (lower)
TO-186
TO_186
Quartz
Complete data set
63840 data points
Equal Area projection
Lower hemispheres
Half width:15°
Cluster size:10°
Exp. densities (mud):
Min= 0.00, Max=33.46
5
10
15
20
25
30
(C)
<0001>
<11-20> (upper)
<11-20> (lower)
TO-054
TO 054
Quartz
Complete data set
119949 data points
Equal Area projection
Lower hemispheres
Half width:15°
Cluster size:10°
Exp. densities (mud):
Min= 0.00, Max=14.30
2
4
6
8
10
12
(D)
<0001>
<11-20> (upper)
<11-20> (lower)
TO-031
TO_031
Quartz
Complete data set
4149 data points
Equal Area projection
Lower hemispheres
Half width:15°
Cluster size:10°
Exp. densities (mud):
Min= 0.01, Max= 8.74
1
2
3
4
5
6
7
8

Figure A1.2.

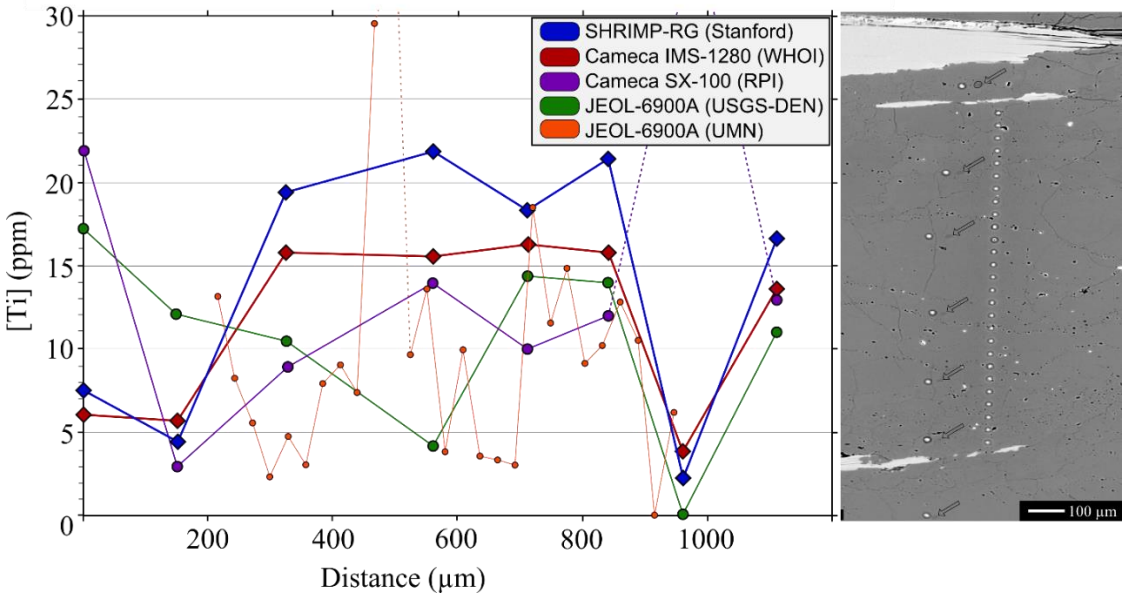
SHRIMP-RG (Stanford)
Cameca IMS-1280 (WHOI)
Cameca SX-100 (RPI)
JEOL-6900A (USGS-DEN)
JEOL-6900A (UMN)
[Ti] (ppm)
Distance (µm)
0
5
10
15
20
25
30
200
400
600
800
1000
100 µm

Figure A1.3.

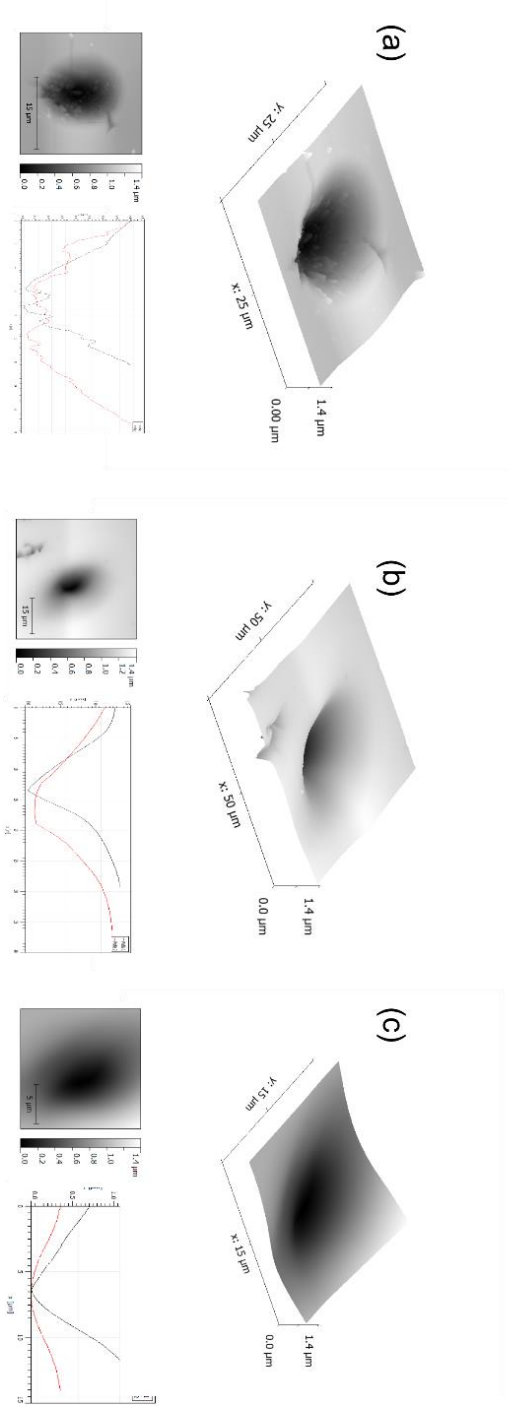
(a)
Y: 25 µm
X: 25 µm
0.00 µm
1.4 µm
(b)
Y: 50 µm
X: 50 µm
0.0 µm
1.4 µm
(c)
Y: 15 µm
X: 15 µm
0.0 µm
1.4 µm

Figure A1.4.

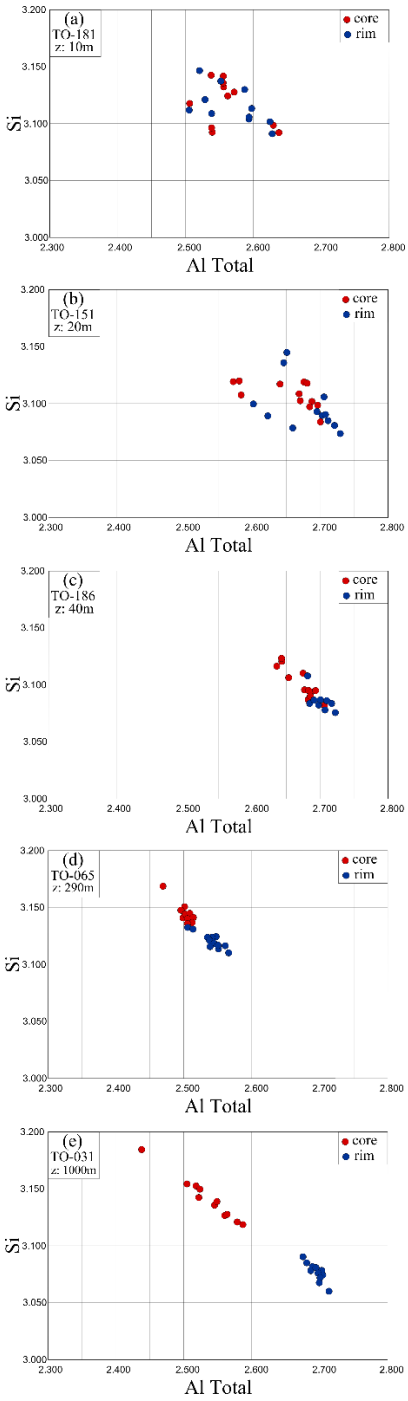
(a)
TO-181
z: 10m
core
rim
Si
Al Total
(b)
TO-151
z: 20m
core
rim
Si
Al Total
(c)
TO-186
z: 40m
core
rim
Si
Al Total
(d)
TO-065
z: 290m
core
rim
Si
Al Total
(e)
TO-031
z: 1000m
core
rim
Si
Al Total

Figure A1.5.

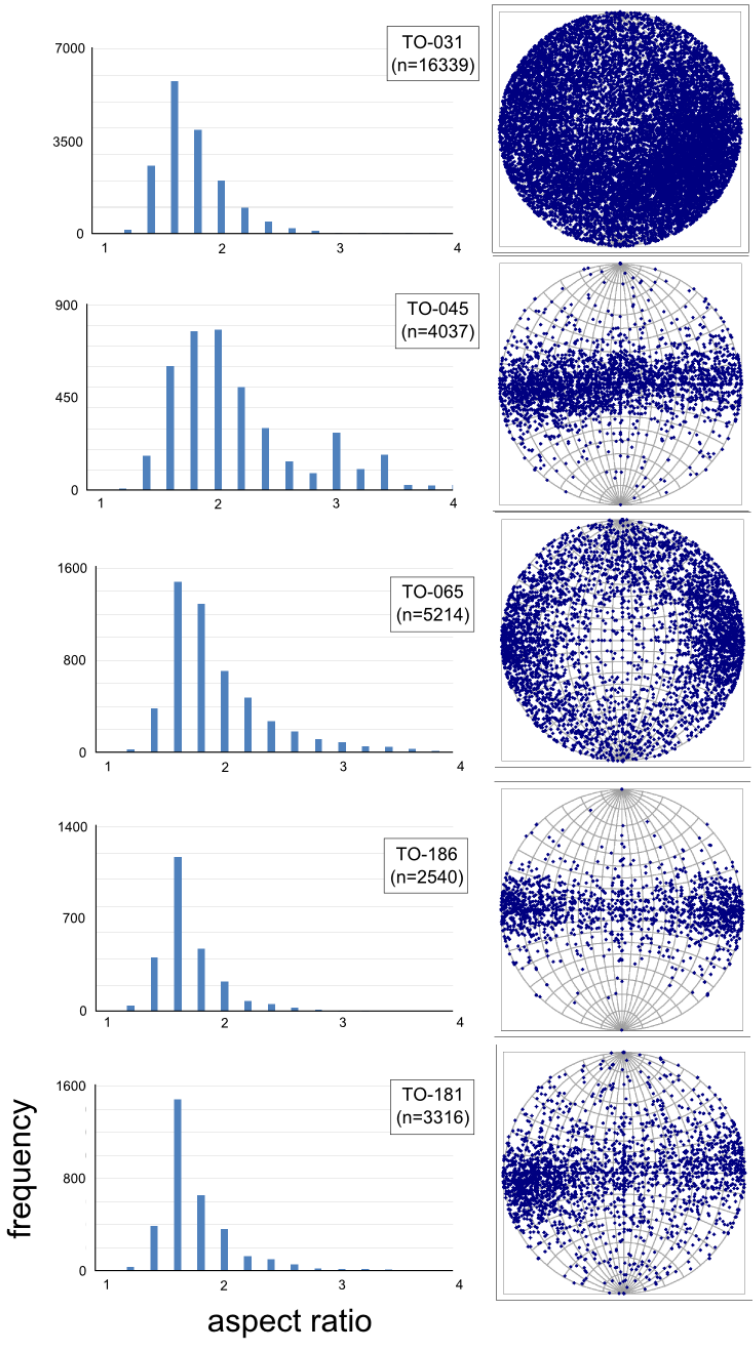
TO-031
(n=16339)
TO-045
(n=4037)
TO-065
(n=5214)
TO-186
(n=2540)
TO-181
(n=3316)
frequency
aspect ratio

Appendix 2

Supplementary Tables for Chapter 2

Table A2.1. Raw data from ion microprobe analysis using the SHRIMP-RG at Stanford/USGS used to calculate ppm Ti for each analysis spot and to monitor counts of ^{30}Si to detect possible contamination by a non-quartz phase.

Table A2.2. Raw data from ion microprobe analysis using the Cameca IMS-1280 at WHOI used to calculate ppm Ti for each analysis spot and to monitor counts of ^{30}Si to detect possible contamination by a non-quartz phase.

Appendix 2

Table A2.1

Sample	Analysis no.	SIMS session	Analysis Location	mean counts (4 cycles)	st.dev. counts	mean counts (4 cycles)	st.dev. counts	mean counts (4 cycles)
TO-054-02A-1	1	1	c	6.90E+01	4.71E+01	1.50E+04	1.70E+03	1.55E+03
TO-054-02A-2	2	1	c	2.73E+01	2.24E+01	2.52E+05	7.18E+04	5.83E+02
TO-054-02A-3	3	1	r	5.50E+00	5.20E+00	3.02E+04	2.26E+03	2.07E+03
TO-054-02A-4	4	1	r	2.50E-01	5.00E-01	7.12E+03	1.85E+03	2.49E+02
TO-054-02A-5	5	1	r	5.06E+02	1.23E+02	1.62E+06	2.32E+05	1.92E+03
TO-054-02A-6	6	1	c	5.50E+00	1.29E+00	1.74E+04	1.01E+03	2.70E+03
TO-054-02A-7	7	1	r	2.02E+02	4.27E+01	1.06E+04	1.00E+03	1.89E+03
TO-054-02A-8	8	1	c	2.25E+00	1.26E+00	6.22E+03	1.08E+03	1.48E+02
TO-054-02A-9	9	1	r	0.00E+00	0.00E+00	7.70E+03	2.07E+03	1.63E+02
TO-054-02A-10	10	1	r	4.57E+02	8.16E+01	4.01E+04	2.08E+03	1.57E+03
TO-054-02A-11	11	1	r	6.63E+01	2.15E+01	1.09E+04	1.15E+03	1.62E+03
TO-054-02A-12	12	1	r	1.15E+01	4.80E+00	1.23E+04	1.92E+03	9.29E+02
TO-054-02A-13	13	1	c	2.75E+00	2.06E+00	6.10E+03	1.32E+03	1.67E+02
TO-054-02A-14	14	1	c	3.25E+00	2.87E+00	1.41E+04	1.12E+03	9.23E+02
TO-054-02A-15	15	1	c	3.25E+01	1.13E+01	6.50E+03	7.77E+02	1.66E+02
TO-054-02A-16	16	1	c	4.36E+02	1.68E+02	8.37E+03	1.28E+03	1.93E+02
TO-054-02A-17	17	1	c	4.77E+02	1.99E+02	8.82E+03	1.71E+03	3.08E+02
TO-054-02A-18	18	1	r	7.25E+00	4.27E+00	5.73E+03	1.09E+03	1.95E+02
TO-054-02A-19	19	1	c	8.25E+02	3.47E+02	7.44E+03	1.65E+03	1.81E+02
TO-054-02A-20	20	1	c	4.60E+02	2.44E+02	8.37E+03	1.09E+03	2.25E+02
TO-054-02A-21	21	1	r	0.00E+00	0.00E+00	4.13E+03	7.09E+02	4.08E+02
TO-054-02A-22	22	1	c	2.30E+01	2.26E+01	8.30E+03	1.76E+03	1.91E+02
TO-054-02A-23	23	1	c	1.96E+02	7.56E+01	8.58E+03	1.28E+03	2.03E+02
TO-054-02A-24	24	1	r	4.00E+00	2.83E+00	4.76E+03	4.38E+02	1.71E+02
TO-054-02A-25	25	1	c	1.57E+02	4.66E+01	8.10E+03	1.81E+03	1.78E+02
TO-054-02A-26	26	1	r	1.13E+01	4.79E+00	9.82E+03	1.54E+03	1.11E+03
TO-054-02A-27	27	1	c	9.75E+00	2.06E+00	6.50E+03	1.23E+03	1.64E+02
TO-054-02A-28	28	1	c	3.50E+00	1.29E+00	7.07E+03	1.58E+03	2.40E+02
TO-054-02A-29	29	1	r	2.75E+00	9.57E-01	5.08E+03	9.57E+02	1.84E+02
TO-054-02A-30	30	1	r	2.00E+00	1.63E+00	6.30E+03	6.10E+02	8.50E+02
TO-054-02A-31	31	1	r	5.43E+01	7.04E+00	1.66E+04	4.35E+03	5.43E+03
TO-054-02A-32	32	1	r	5.74E+02	1.93E+02	8.04E+03	3.91E+02	2.46E+03
TO-054-02A-33	33	1	c	6.47E+02	3.26E+02	9.43E+03	1.71E+03	1.28E+03
TO-054-02A-34	34	1	c	3.70E+02	1.56E+02	6.05E+03	5.70E+02	1.67E+02
TO-054-02A-35	35	1	c	5.00E-01	5.77E-01	4.20E+03	1.17E+03	2.40E+02
TO-054-02A-37	37	1	c	2.50E-01	5.00E-01	5.21E+03	7.02E+02	1.23E+03
TO-054-02A-38	38	1	c	0.00E+00	0.00E+00	4.63E+03	9.18E+02	3.06E+02
TO-054-02A-39	39	1	c	2.05E+01	1.12E+01	8.95E+03	8.12E+02	3.66E+02
TO-054-02A-40		1	c	2.98E+01	1.46E+01	4.09E+04	2.09E+04	7.35E+03
TO-186-01A-1	40	1	r	7.50E-01	1.50E+00	4.37E+03	1.22E+03	2.68E+02
TO-186-01A-2	41	1	r	1.15E+02	2.28E+01	2.37E+04	7.09E+03	2.49E+03
TO-186-01A-3	42	1	c	7.68E+01	3.58E+01	1.38E+04	9.36E+03	1.02E+03
TO-186-01A-4	43	1	c	1.50E+00	1.29E+00	3.94E+03	3.95E+02	3.64E+02
TO-186-01A-5	44	1	c	2.82E+02	1.41E+02	6.89E+03	9.77E+02	4.14E+02
TO-186-01A-6	45	1	r	0.00E+00	0.00E+00	2.35E+03	3.58E+02	3.91E+02
TO-186-01A-7	46	1	r	7.73E+01	2.13E+01	1.21E+04	2.56E+03	1.58E+03
TO-186-01A-8	47	1	c	2.25E+00	1.71E+00	1.01E+04	2.11E+03	4.59E+02
TO-186-01A-9	48	1	r	2.15E+01	5.74E+00	8.39E+03	3.63E+02	1.04E+03
TO-186-01A-10	49	1	c	2.94E+02	1.28E+02	1.03E+04	1.18E+03	5.67E+02
TO-186-01A-11	50	1	c	6.79E+02	3.60E+02	4.57E+03	5.26E+02	3.45E+02
TO-186-01A-12	51	1	c	9.47E+02	5.17E+02	4.47E+03	3.54E+02	3.16E+02

Table A2.1 (cont.)

TO-186-01A-13	52	1	c	8.90E+01	5.01E+01	7.77E+03	1.73E+03	5.37E+02
TO-186-01A-14	53	1	c	1.33E+02	4.59E+01	4.22E+03	2.75E+02	2.96E+02
TO-186-01A-15	54	1	c	6.99E+02	2.99E+02	6.24E+03	6.89E+02	3.60E+02
TO-186-01A-16	55	1	r	4.00E+02	2.07E+02	6.35E+03	6.35E+02	2.52E+02
TO-186-01A-17	56	1	r	5.00E+00	1.83E+00	4.92E+03	3.56E+02	2.60E+02
TO-186-01A-18	57	1	r	3.35E+02	1.93E+02	1.32E+04	1.01E+03	8.93E+02
TO-186-01A-19	58	1	r	1.98E+03	1.05E+03	3.01E+04	8.46E+03	1.84E+03
TO-186-01A-20	59	1	c	4.01E+02	1.78E+02	4.92E+03	2.78E+02	2.90E+02
TO-186-01A-21	60	1	c	5.94E+02	3.17E+02	1.02E+04	1.71E+03	7.29E+02
TO-186-01A-22	61	1	c	2.86E+02	1.51E+02	7.86E+03	6.39E+02	3.42E+02
TO-186-01A-23	62	1	r	1.26E+02	4.77E+01	9.57E+03	1.18E+03	1.51E+03
TO-186-01A-24	63	1	c	4.88E+02	2.21E+02	3.63E+03	1.33E+02	3.11E+02
TO-186-01A-25	64	1	c	3.39E+02	1.71E+02	3.98E+03	2.48E+02	6.21E+02
TO-186-01A-26	65	1	c	3.75E+02	1.77E+02	1.48E+04	2.22E+03	1.75E+03
TO-186-01A-27	66	1	r	1.71E+02	7.04E+01	4.68E+03	5.22E+02	3.87E+02
TO-186-01A-28	67	1	r	2.02E+02	1.37E+02	2.28E+04	3.78E+03	2.28E+03
TO-186-01A-29	68	1	c	2.82E+02	1.31E+02	4.79E+03	6.77E+02	5.28E+02
TO-186-01A-30	69	1	c	7.57E+02	3.30E+02	5.00E+03	6.14E+02	4.71E+02
TO-186-01A-31	70	1	r	6.25E+00	2.87E+00	1.27E+04	5.69E+03	1.70E+03
TO-186-01A-32	71	1	r	3.80E+01	1.04E+01	8.45E+03	8.68E+02	6.58E+02
TO-186-01A-33	72	1	r	1.95E+02	4.11E+01	1.76E+04	5.70E+03	3.27E+03
TO-186-01A-34	73	1	r	2.34E+02	7.57E+01	6.17E+03	2.90E+02	5.39E+02
TO-186-01A-35	74	1	c	1.79E+03	7.17E+02	1.15E+04	2.10E+03	1.64E+03
TO-186-01A-36	75	1	c	1.59E+03	6.06E+02	4.59E+03	4.46E+02	1.16E+03
TO-186-01A-37	76	1	c	1.70E+03	7.35E+02	1.85E+04	2.50E+03	3.00E+03
TO-181-01B-1	77	1	r	3.77E+02	1.13E+02	5.08E+04	1.62E+04	2.28E+02
TO-181-01B-2	78	1	r	4.56E+02	1.83E+02	6.15E+04	5.13E+03	5.04E+02
TO-181-01B-3	79	1	X	4.39E+04	2.87E+04	7.33E+04	1.17E+04	1.34E+03
TO-181-01B-4	80	1	r	7.02E+02	3.00E+02	4.35E+04	2.34E+04	8.12E+02
TO-181-01B-5	81	1	c	6.30E+01	3.72E+01	1.76E+04	3.92E+03	8.93E+02
TO-181-01B-6	82	1	c	6.53E+02	3.18E+02	6.96E+04	3.07E+04	2.59E+03
TO-181-01B-7	83	1	c	1.73E+02	7.67E+01	4.71E+04	6.09E+03	1.56E+03
TO-181-01B-8	84	1	c	1.05E+03	5.15E+02	8.55E+04	3.98E+04	4.19E+02
TO-181-01B-9	85	1	c	1.93E+03	6.59E+02	4.01E+05	1.28E+05	7.35E+03
TO-181-01B-10	86	1	r	3.50E+02	1.58E+02	6.38E+04	3.14E+04	1.68E+03
TO-181-01B-11	87	1	r	1.88E+02	1.07E+02	2.13E+04	4.23E+03	7.73E+02
TO-181-01B-12	88	1	c	2.37E+02	1.47E+02	5.92E+04	8.34E+03	2.87E+03
TO-181-01B-13	89	1	c	1.01E+02	2.62E+01	2.93E+04	1.81E+03	1.89E+03
TO-181-01B-14	90	1	r	2.54E+02	9.40E+01	3.49E+04	4.06E+03	3.32E+03
TO-181-01B-15	91	1	c	1.15E+02	2.81E+01	7.40E+04	7.38E+03	1.78E+03
TO-181-01B-16	92	1	c	5.70E+02	3.45E+02	1.29E+04	3.50E+03	3.57E+02
TO-181-01B-17	93	1	c	2.28E+02	9.61E+01	1.96E+04	2.16E+03	3.61E+02
TO-181-01B-18	94	1	r	1.18E+02	8.63E+01	4.83E+04	5.36E+03	1.04E+03
TO-181-01B-19	95	1	r	2.06E+02	4.95E+01	3.60E+04	5.60E+03	2.30E+03
TO-181-01B-20	96	1	c	2.09E+02	8.35E+01	8.20E+03	2.06E+02	3.09E+02
TO-181-01B-21	97	1	c	5.65E+02	2.97E+02	4.67E+03	5.52E+02	2.56E+02
TO-181-01B-22	98	1	c	8.40E+02	3.93E+02	5.10E+03	1.33E+02	3.56E+02
TO-181-01B-23	99	1	c	6.90E+02	2.95E+02	6.49E+03	5.87E+02	7.80E+02
TO-181-01B-24	100	1	X	6.83E+02	3.26E+02	4.35E+04	1.29E+04	3.48E+03
TO-181-01B-25	101	1	c	1.40E+02	5.47E+01	5.75E+03	5.95E+02	2.46E+02
TO-181-01B-26	102	1	c	2.30E+02	2.43E+01	4.71E+04	1.21E+04	2.37E+03
TO-181-01B-27	103	1	r	9.27E+02	5.06E+02	9.16E+04	3.82E+04	5.29E+03
TO-181-01B-28	104	1	r	4.00E+00	2.94E+00	5.39E+03	6.27E+02	2.12E+02
TO-181-01B-29	105	1	r	5.31E+02	1.87E+02	5.74E+04	6.72E+03	3.12E+03
TO-181-01B-30	106	1	r	1.19E+03	5.72E+02	3.10E+04	4.64E+03	2.43E+03

Table A2.1 (cont.)

Sample	st.dev. counts	mean counts (4 cycles)	st.dev. counts	mean counts (4 cycles)	st.dev. counts	mean counts (4 cycles)	st.dev. counts	mean counts (4 cycles)
TO-054-02A-1	2.47E+02	1.66E+04	3.06E+03	2.36E+06	1.62E+04	8.15E+03	1.86E+03	6.03E+04
TO-054-02A-2	5.38E+01	1.53E+06	4.23E+05	2.24E+06	2.23E+04	1.42E+07	4.01E+06	5.83E+04
TO-054-02A-3	3.21E+02	1.87E+04	2.00E+03	2.30E+06	4.19E+04	2.03E+04	1.91E+03	5.12E+04
TO-054-02A-4	1.79E+02	1.04E+04	2.88E+03	2.26E+06	1.65E+04	5.88E+03	3.12E+03	1.69E+04
TO-054-02A-5	5.80E+02	8.64E+06	1.13E+06	1.92E+06	1.06E+05	5.57E+07	5.98E+06	3.81E+04
TO-054-02A-6	4.24E+02	1.43E+04	2.52E+03	2.20E+06	5.68E+04	1.33E+04	3.09E+03	2.30E+04
TO-054-02A-7	3.02E+02	1.64E+04	2.89E+03	2.31E+06	2.06E+04	1.24E+04	2.42E+03	1.82E+04
TO-054-02A-8	8.18E+01	1.21E+04	2.23E+03	2.28E+06	1.32E+04	8.03E+03	1.95E+03	1.09E+04
TO-054-02A-9	9.16E+01	1.09E+04	2.82E+03	2.24E+06	8.24E+03	5.19E+03	2.53E+03	1.29E+04
TO-054-02A-10	1.64E+02	4.19E+04	5.92E+03	2.32E+06	3.38E+04	2.56E+04	2.80E+03	4.27E+04
TO-054-02A-11	2.31E+02	1.35E+04	2.15E+03	2.26E+06	1.15E+04	8.93E+03	1.35E+03	1.59E+04
TO-054-02A-12	1.21E+02	1.51E+04	2.77E+03	2.28E+06	1.64E+04	1.37E+04	3.39E+03	1.52E+04
TO-054-02A-13	9.46E+01	1.38E+04	2.74E+03	2.30E+06	1.55E+04	5.52E+03	2.22E+03	1.22E+04
TO-054-02A-14	1.51E+02	1.38E+04	2.95E+03	2.33E+06	2.08E+04	7.87E+03	3.67E+03	5.69E+04
TO-054-02A-15	6.94E+01	1.98E+04	2.38E+03	2.35E+06	2.13E+04	6.60E+03	2.08E+03	9.77E+03
TO-054-02A-16	9.06E+01	2.72E+04	3.13E+03	2.31E+06	1.27E+04	6.05E+03	2.63E+03	1.11E+04
TO-054-02A-17	9.86E+01	2.00E+04	3.59E+03	2.26E+06	2.37E+04	6.82E+03	2.22E+03	2.08E+04
TO-054-02A-18	8.62E+01	1.40E+04	2.64E+03	2.26E+06	1.20E+04	4.82E+03	2.19E+03	9.62E+03
TO-054-02A-19	7.92E+01	1.85E+04	3.09E+03	2.28E+06	1.73E+04	5.48E+03	2.59E+03	1.10E+04
TO-054-02A-20	8.62E+01	2.52E+04	2.89E+03	2.30E+06	2.02E+04	6.29E+03	2.75E+03	1.37E+04
TO-054-02A-21	1.35E+02	1.26E+04	3.27E+03	2.29E+06	1.74E+04	4.04E+03	1.70E+03	9.25E+03
TO-054-02A-22	9.12E+01	1.39E+04	3.12E+03	2.25E+06	1.08E+04	5.46E+03	2.71E+03	1.13E+04
TO-054-02A-23	8.63E+01	1.49E+04	3.36E+03	2.22E+06	1.55E+04	5.71E+03	2.60E+03	1.24E+04
TO-054-02A-24	1.04E+02	1.32E+04	2.69E+03	2.30E+06	2.00E+04	5.97E+03	1.14E+03	7.31E+03
TO-054-02A-25	8.92E+01	1.36E+04	2.58E+03	2.25E+06	1.43E+04	6.03E+03	3.06E+03	1.10E+04
TO-054-02A-26	1.77E+02	1.42E+04	2.84E+03	2.25E+06	9.53E+03	9.76E+03	2.94E+03	1.89E+04
TO-054-02A-27	9.33E+01	1.31E+04	2.78E+03	2.28E+06	1.17E+04	8.23E+03	2.01E+03	9.69E+03
TO-054-02A-28	6.29E+01	1.27E+04	2.93E+03	2.25E+06	2.20E+04	7.22E+03	2.35E+03	1.22E+04
TO-054-02A-29	1.02E+02	1.14E+04	3.21E+03	2.25E+06	1.37E+04	7.10E+03	1.71E+03	1.07E+04
TO-054-02A-30	5.39E+01	1.92E+04	5.54E+03	2.29E+06	5.68E+04	1.12E+04	1.24E+03	1.33E+04
TO-054-02A-31	1.02E+03	2.45E+04	5.13E+03	2.26E+06	1.74E+04	1.99E+04	4.87E+03	3.43E+04
TO-054-02A-32	1.13E+02	1.46E+04	3.02E+03	2.39E+06	1.56E+04	5.79E+03	1.91E+03	3.91E+04
TO-054-02A-33	1.62E+02	2.07E+04	3.44E+03	2.40E+06	9.65E+03	7.42E+03	3.05E+03	3.15E+04
TO-054-02A-34	9.44E+01	1.29E+04	3.20E+03	2.36E+06	1.57E+04	4.54E+03	2.05E+03	1.97E+04
TO-054-02A-35	8.75E+01	1.53E+04	3.17E+03	2.25E+06	1.58E+04	4.89E+03	1.63E+03	9.82E+03
TO-054-02A-36	1.55E+02	1.59E+04	2.21E+03	2.03E+06	1.38E+04	4.18E+03	1.65E+03	1.21E+04
TO-054-02A-37	9.51E+01	1.28E+04	2.77E+03	2.09E+06	1.66E+04	4.47E+03	1.79E+03	1.17E+04
TO-054-02A-38	6.99E+01	1.24E+04	2.74E+03	2.04E+06	2.19E+04	4.60E+03	1.71E+03	1.57E+04
TO-054-02A-39	8.34E+02	1.34E+04	2.25E+03	2.03E+06	1.27E+04	1.03E+04	2.38E+03	5.20E+04
TO-186-01A-1	1.78E+02	1.57E+04	3.03E+03	2.18E+06	4.09E+04	4.46E+03	1.31E+03	1.16E+04
TO-186-01A-2	3.01E+02	3.04E+04	3.94E+03	2.23E+06	3.80E+04	2.52E+04	2.20E+03	3.27E+04
TO-186-01A-3	2.44E+02	2.18E+04	5.68E+03	2.15E+06	1.48E+04	6.52E+03	2.23E+03	1.32E+04
TO-186-01A-4	2.05E+02	2.10E+04	4.36E+03	2.24E+06	2.20E+04	5.95E+03	1.54E+03	1.40E+04
TO-186-01A-5	2.63E+02	5.03E+04	6.48E+03	2.20E+06	2.83E+04	9.41E+03	1.12E+03	1.23E+04
TO-186-01A-6	1.57E+02	1.54E+04	4.44E+03	2.26E+06	2.48E+04	3.24E+03	1.48E+03	1.12E+04
TO-186-01A-7	2.16E+02	2.79E+04	3.75E+03	2.20E+06	1.40E+04	1.30E+04	7.67E+02	2.46E+04
TO-186-01A-8	1.55E+02	1.82E+04	3.72E+03	2.22E+06	2.64E+04	8.62E+03	1.95E+03	1.27E+04
TO-186-01A-9	1.68E+02	2.21E+04	4.21E+03	2.23E+06	8.52E+03	8.75E+03	2.03E+03	3.90E+04
TO-186-01A-10	2.03E+02	3.21E+04	3.78E+03	2.21E+06	1.70E+04	8.35E+03	1.71E+03	1.94E+04
TO-186-01A-11	2.12E+02	3.61E+04	4.38E+03	2.22E+06	8.48E+03	5.23E+03	1.71E+03	2.46E+04
TO-186-01A-12	1.74E+02	3.32E+04	2.98E+03	2.23E+06	1.42E+04	5.06E+03	1.48E+03	1.37E+04

Table A2.1 (cont.)

TO-186-01A-13	1.18E+02	2.66E+04	3.66E+03	2.21E+06	1.42E+04	8.80E+03	1.27E+03	1.53E+04
TO-186-01A-14	1.77E+02	2.37E+04	3.43E+03	2.14E+06	1.53E+04	4.29E+03	1.38E+03	1.37E+04
TO-186-01A-15	2.36E+02	2.71E+04	3.76E+03	2.20E+06	1.97E+04	7.18E+03	2.87E+03	1.92E+04
TO-186-01A-16	1.59E+02	2.03E+04	3.72E+03	2.24E+06	2.82E+04	7.02E+03	1.61E+03	1.55E+04
TO-186-01A-17	1.70E+02	1.64E+04	3.33E+03	2.18E+06	2.55E+04	5.71E+03	1.55E+03	1.37E+04
TO-186-01A-18	2.43E+02	1.88E+04	4.59E+03	2.18E+06	2.13E+04	6.85E+03	1.94E+03	2.95E+04
TO-186-01A-19	2.50E+02	5.78E+04	3.66E+03	2.17E+06	2.95E+04	3.18E+04	1.98E+03	4.40E+04
TO-186-01A-20	2.01E+02	3.49E+04	3.17E+03	2.24E+06	1.39E+04	5.89E+03	1.81E+03	1.43E+04
TO-186-01A-21	2.34E+02	3.83E+04	4.08E+03	2.20E+06	2.36E+04	9.74E+03	2.35E+03	1.86E+04
TO-186-01A-22	2.30E+02	3.08E+04	4.54E+03	2.18E+06	2.52E+04	8.12E+03	3.15E+03	2.48E+04
TO-186-01A-23	3.55E+02	2.34E+04	3.93E+03	2.21E+06	3.07E+04	1.02E+04	1.84E+03	2.60E+04
TO-186-01A-24	2.20E+02	2.45E+04	4.04E+03	2.17E+06	2.28E+04	5.00E+03	1.64E+03	1.36E+04
TO-186-01A-25	3.14E+02	2.04E+04	4.28E+03	2.12E+06	2.64E+04	4.93E+03	1.56E+03	1.47E+04
TO-186-01A-26	6.48E+02	2.88E+04	4.40E+03	2.19E+06	3.18E+04	1.25E+04	2.92E+03	9.42E+04
TO-186-01A-27	2.10E+02	2.11E+04	3.83E+03	2.12E+06	1.49E+04	8.56E+03	8.31E+02	1.46E+04
TO-186-01A-28	1.16E+03	3.62E+04	3.54E+03	2.12E+06	2.33E+04	1.92E+04	3.46E+03	4.93E+04
TO-186-01A-29	2.76E+02	2.22E+04	4.52E+03	2.08E+06	2.59E+04	5.94E+03	1.75E+03	1.39E+04
TO-186-01A-30	3.33E+02	2.13E+04	4.09E+03	2.08E+06	1.52E+04	5.03E+03	1.46E+03	1.42E+04
TO-186-01A-31	6.09E+02	1.73E+04	3.96E+03	2.09E+06	2.73E+04	8.82E+03	4.01E+03	2.16E+04
TO-186-01A-32	1.32E+02	2.26E+04	4.71E+03	2.13E+06	1.65E+04	8.31E+03	1.08E+03	1.53E+04
TO-186-01A-33	6.76E+02	3.96E+04	5.91E+03	2.07E+06	2.38E+04	2.29E+04	4.30E+03	3.77E+04
TO-186-01A-34	3.41E+02	2.61E+04	3.93E+03	2.10E+06	8.65E+03	5.13E+03	1.65E+03	1.52E+04
TO-186-01A-35	4.08E+02	4.08E+04	2.51E+03	2.10E+06	4.64E+04	7.92E+03	1.65E+03	4.46E+04
TO-186-01A-36	5.62E+02	3.15E+04	3.75E+03	2.07E+06	1.84E+04	5.82E+03	1.71E+03	1.70E+04
TO-186-01A-37	7.44E+02	3.89E+04	5.37E+03	2.13E+06	2.99E+04	1.17E+04	2.19E+03	3.64E+04
TO-181-01B-1	5.36E+01	3.63E+04	1.21E+03	2.62E+06	2.27E+04	1.15E+04	2.27E+03	4.99E+03
TO-181-01B-2	3.00E+02	3.96E+04	1.62E+03	2.56E+06	1.26E+04	1.16E+04	2.12E+03	9.39E+03
TO-181-01B-3	3.98E+02	2.49E+05	9.19E+03	2.63E+06	9.97E+03	3.41E+04	8.59E+03	2.89E+04
TO-181-01B-4	1.47E+02	4.45E+04	3.50E+03	2.59E+06	1.42E+04	1.50E+04	2.57E+03	9.94E+03
TO-181-01B-5	1.79E+02	4.26E+04	1.05E+03	2.66E+06	3.10E+04	1.21E+04	1.52E+03	1.88E+04
TO-181-01B-6	7.22E+02	7.68E+04	8.60E+03	2.57E+06	8.22E+03	4.19E+04	8.12E+03	3.72E+04
TO-181-01B-7	3.79E+02	5.56E+04	7.14E+03	2.57E+06	1.78E+04	3.23E+04	4.31E+03	2.85E+04
TO-181-01B-8	3.05E+02	4.75E+04	3.42E+03	2.50E+06	5.87E+03	1.60E+04	1.12E+03	1.04E+04
TO-181-01B-9	1.96E+03	1.14E+05	1.95E+04	2.53E+06	1.34E+04	8.86E+04	2.31E+04	5.81E+04
TO-181-01B-10	1.53E+02	4.90E+04	1.93E+03	2.60E+06	1.35E+04	1.79E+04	6.77E+02	2.75E+04
TO-181-01B-11	3.35E+02	3.56E+04	2.92E+03	2.52E+06	1.83E+04	1.23E+04	1.50E+03	1.26E+04
TO-181-01B-12	3.02E+02	4.99E+04	1.46E+03	2.60E+06	3.90E+04	2.63E+04	3.87E+03	5.03E+04
TO-181-01B-13	4.73E+02	3.46E+04	3.22E+03	2.56E+06	1.48E+04	1.73E+04	1.97E+03	3.08E+04
TO-181-01B-14	4.26E+02	4.98E+04	2.02E+03	2.63E+06	4.87E+04	2.23E+04	1.81E+03	4.88E+04
TO-181-01B-15	5.63E+02	3.65E+04	3.06E+03	2.60E+06	2.20E+04	1.68E+04	3.10E+03	2.70E+04
TO-181-01B-16	2.01E+02	4.70E+04	3.87E+03	2.65E+06	2.43E+04	9.83E+03	1.24E+03	7.10E+03
TO-181-01B-17	1.74E+02	3.32E+04	3.46E+03	2.57E+06	2.43E+04	6.68E+03	9.30E+02	6.59E+03
TO-181-01B-18	5.47E+02	3.67E+04	4.44E+03	2.62E+06	3.11E+04	1.33E+04	3.14E+03	2.63E+04
TO-181-01B-19	5.85E+01	4.28E+04	9.61E+03	2.63E+06	1.80E+04	2.14E+04	4.24E+03	3.98E+04
TO-181-01B-20	2.01E+02	2.63E+04	3.67E+03	2.57E+06	1.85E+04	5.50E+03	2.16E+03	8.52E+03
TO-181-01B-21	1.53E+02	4.88E+04	2.49E+03	2.59E+06	2.08E+04	4.34E+03	1.04E+03	4.52E+03
TO-181-01B-22	1.63E+02	4.80E+04	3.00E+03	2.56E+06	1.78E+04	4.84E+03	9.08E+02	5.53E+03
TO-181-01B-23	1.29E+02	3.49E+04	3.79E+03	2.65E+06	2.75E+04	4.11E+03	7.48E+02	7.56E+03
TO-181-01B-24	3.88E+02	6.63E+04	2.68E+03	2.61E+06	9.81E+03	3.41E+04	2.18E+03	3.05E+04
TO-181-01B-25	1.42E+02	2.68E+04	3.50E+03	2.61E+06	2.15E+04	3.94E+03	1.29E+03	4.43E+03
TO-181-01B-26	1.06E+03	3.75E+04	5.24E+03	2.64E+06	1.43E+04	1.59E+04	6.32E+03	3.19E+04
TO-181-01B-27	1.45E+03	6.63E+04	7.09E+03	2.69E+06	3.93E+04	3.95E+04	1.18E+04	6.02E+04
TO-181-01B-28	1.47E+02	2.10E+04	2.57E+03	2.65E+06	6.23E+03	3.45E+03	9.73E+02	3.62E+03
TO-181-01B-29	4.25E+02	4.69E+04	1.83E+03	2.75E+06	2.09E+04	2.78E+04	2.26E+03	4.38E+04
TO-181-01B-30	3.88E+02	4.86E+04	3.51E+03	2.78E+06	4.11E+04	1.38E+04	1.95E+03	7.55E+04

Table A2.1 (cont.)

Sample	st.dev. counts	mean counts (4 cycles)	st.dev. counts	mean counts (4 cycles)	st.dev. counts	mean counts (4 cycles)	st.dev. counts	
TO-054-02A-1	1.11E+04	1.33E+03	4.00E+01	5.42E+03	7.00E+01	1.03E+03	4.36E+01	8.500
TO-054-02A-2	1.31E+04	9.84E+02	3.48E+01	3.93E+03	1.02E+02	7.21E+02	2.10E+01	6.485
TO-054-02A-3	2.21E+03	6.35E+02	2.22E+01	2.70E+03	6.14E+01	5.11E+02	1.60E+01	4.354
TO-054-02A-4	1.00E+04	5.83E+02	2.84E+01	2.38E+03	9.79E+01	4.34E+02	1.77E+01	3.885
TO-054-02A-5	7.29E+03	4.47E+02	2.85E+01	1.75E+03	1.24E+02	3.26E+02	2.25E+01	3.380
TO-054-02A-6	8.02E+03	1.20E+03	4.14E+01	4.56E+03	1.83E+02	8.76E+02	4.28E+01	7.691
TO-054-02A-7	1.26E+04	1.48E+03	1.08E+02	5.82E+03	7.98E+01	1.05E+03	3.59E+01	9.331
TO-054-02A-8	5.69E+03	1.45E+03	4.97E+01	5.90E+03	1.90E+02	1.09E+03	1.47E+01	9.570
TO-054-02A-9	6.90E+03	1.04E+03	2.66E+01	4.22E+03	1.24E+02	7.68E+02	7.19E+01	6.973
TO-054-02A-10	8.53E+03	7.77E+02	3.83E+01	3.07E+03	6.36E+01	5.90E+02	3.50E+01	4.901
TO-054-02A-11	4.28E+03	7.78E+02	5.96E+01	3.18E+03	8.72E+01	5.55E+02	2.30E+01	5.206
TO-054-02A-12	6.50E+03	1.29E+03	2.34E+01	5.16E+03	1.84E+02	9.48E+02	5.45E+01	8.370
TO-054-02A-13	5.81E+03	1.46E+03	4.46E+01	6.00E+03	1.26E+02	1.11E+03	2.00E+01	9.656
TO-054-02A-14	1.73E+03	1.61E+03	6.23E+01	6.46E+03	1.45E+02	1.26E+03	2.68E+01	10.249
TO-054-02A-15	5.26E+03	1.21E+03	5.12E+01	4.59E+03	4.08E+02	9.20E+02	4.63E+01	7.239
TO-054-02A-16	6.29E+03	1.52E+03	5.02E+01	6.03E+03	9.08E+01	1.12E+03	2.71E+01	9.676
TO-054-02A-17	1.57E+04	1.26E+03	2.64E+01	5.15E+03	1.53E+02	9.50E+02	1.88E+01	8.440
TO-054-02A-18	5.21E+03	8.50E+02	2.91E+01	3.65E+03	8.88E+01	6.75E+02	2.23E+01	5.971
TO-054-02A-19	5.98E+03	1.17E+03	4.27E+01	4.82E+03	1.93E+02	8.85E+02	1.86E+01	7.820
TO-054-02A-20	7.71E+03	1.40E+03	5.18E+01	5.64E+03	5.58E+01	1.08E+03	8.68E+00	9.068
TO-054-02A-21	4.08E+03	8.87E+02	1.28E+01	3.55E+03	5.41E+01	6.33E+02	3.66E+01	5.738
TO-054-02A-22	6.52E+03	1.13E+03	5.68E+01	4.32E+03	1.71E+02	8.33E+02	4.12E+01	7.103
TO-054-02A-23	6.88E+03	1.25E+03	3.02E+01	5.17E+03	7.85E+01	9.38E+02	2.62E+01	8.593
TO-054-02A-24	4.23E+03	9.58E+02	5.01E+01	3.87E+03	3.05E+01	7.37E+02	3.59E+01	6.231
TO-054-02A-25	6.39E+03	7.49E+02	3.58E+01	2.93E+03	1.28E+02	5.46E+02	4.15E+01	4.824
TO-054-02A-26	8.96E+03	5.33E+02	1.25E+01	2.18E+03	3.68E+01	4.00E+02	9.32E+00	3.595
TO-054-02A-27	5.37E+03	1.05E+03	2.94E+01	4.21E+03	5.59E+01	7.82E+02	3.02E+01	6.848
TO-054-02A-28	7.12E+03	1.20E+03	2.30E+01	4.73E+03	1.61E+02	8.48E+02	4.40E+01	7.785
TO-054-02A-29	5.14E+03	8.46E+02	2.82E+01	3.32E+03	1.76E+02	6.10E+02	3.38E+01	5.450
TO-054-02A-30	6.19E+03	8.68E+02	5.50E+00	3.52E+03	4.57E+01	6.67E+02	2.75E+01	5.697
TO-054-02A-31	1.27E+04	6.23E+02	1.31E+01	2.38E+03	5.84E+01	4.34E+02	4.40E+01	3.893
TO-054-02A-32	5.91E+03	9.17E+02	4.73E+01	3.74E+03	1.05E+02	6.91E+02	1.65E+01	5.787
TO-054-02A-33	6.58E+03	1.45E+03	6.50E+01	6.12E+03	9.97E+01	1.14E+03	2.24E+01	9.435
TO-054-02A-34	7.55E+03	1.34E+03	2.89E+01	5.41E+03	1.10E+02	1.03E+03	3.38E+01	8.493
TO-054-02A-35	5.24E+03	1.47E+03	5.65E+01	5.84E+03	8.92E+01	1.08E+03	9.85E+01	9.607
TO-054-02A-36	5.64E+03	9.97E+02	3.57E+01	4.07E+03	6.54E+01	7.37E+02	4.65E+01	7.399
TO-054-02A-37	5.60E+03	1.02E+03	5.36E+01	4.11E+03	6.55E+01	7.69E+02	3.29E+01	7.267
TO-054-02A-38	6.81E+03	1.18E+03	5.84E+01	4.80E+03	7.67E+01	8.99E+02	2.67E+01	8.685
TO-054-02A-39	3.70E+04	9.38E+02	1.96E+01	3.74E+03	1.32E+02	7.37E+02	3.97E+01	6.814
TO-186-01A-1	6.68E+03	9.07E+02	8.78E+01	3.74E+03	9.79E+01	6.75E+02	4.51E+01	6.182
TO-186-01A-2	4.75E+03	8.35E+02	5.62E+01	3.38E+03	1.20E+02	6.29E+02	5.43E+01	5.479
TO-186-01A-3	7.28E+03	2.12E+03	4.66E+01	8.54E+03	1.27E+02	1.60E+03	2.79E+01	14.340
TO-186-01A-4	8.18E+03	1.69E+03	1.86E+01	6.65E+03	2.12E+02	1.25E+03	4.61E+01	10.734
TO-186-01A-5	7.36E+03	2.58E+03	8.24E+01	1.02E+04	3.37E+02	1.90E+03	1.18E+02	16.728
TO-186-01A-6	6.37E+03	1.09E+03	5.11E+01	4.28E+03	1.71E+02	8.20E+02	6.93E+01	6.864
TO-186-01A-7	4.27E+03	1.85E+03	7.93E+01	7.42E+03	1.73E+02	1.41E+03	2.72E+01	12.174
TO-186-01A-8	6.48E+03	1.33E+03	1.02E+02	5.32E+03	2.89E+02	9.98E+02	5.52E+01	8.653
TO-186-01A-9	1.67E+04	1.29E+03	4.34E+01	5.19E+03	2.86E+02	9.87E+02	3.02E+01	8.406
TO-186-01A-10	1.07E+04	2.41E+03	2.06E+02	9.79E+03	7.52E+02	1.78E+03	8.59E+01	15.988
TO-186-01A-11	1.61E+04	2.29E+03	1.13E+02	9.14E+03	1.27E+02	1.70E+03	8.62E+01	14.888
TO-186-01A-12	8.66E+03	2.17E+03	7.24E+01	8.64E+03	2.74E+02	1.56E+03	3.62E+01	14.009

Table 2.1 (cont.)

TO-186-01A-13	9.03E+03	2.19E+03	8.70E+01	8.83E+03	1.89E+02	1.64E+03	8.78E+01	14.427
TO-186-01A-14	8.08E+03	1.96E+03	7.41E+01	7.88E+03	3.09E+02	1.45E+03	5.66E+01	13.300
TO-186-01A-15	1.10E+04	1.98E+03	8.54E+01	7.81E+03	4.24E+02	1.48E+03	1.01E+02	12.839
TO-186-01A-16	9.07E+03	1.62E+03	9.01E+01	6.54E+03	1.83E+02	1.18E+03	3.14E+01	10.528
TO-186-01A-17	8.60E+03	1.34E+03	1.06E+02	5.15E+03	3.30E+02	9.60E+02	8.88E+01	8.520
TO-186-01A-18	9.55E+03	1.30E+03	8.20E+01	5.28E+03	2.58E+02	9.57E+02	7.56E+01	8.745
TO-186-01A-19	6.78E+03	8.96E+02	8.06E+01	3.78E+03	2.45E+02	7.11E+02	4.72E+01	6.290
TO-186-01A-20	8.26E+03	2.09E+03	5.43E+01	8.42E+03	3.05E+02	1.60E+03	9.08E+01	13.573
TO-186-01A-21	9.85E+03	2.20E+03	8.94E+01	9.05E+03	9.77E+01	1.71E+03	1.94E+01	14.896
TO-186-01A-22	8.28E+03	1.99E+03	9.49E+01	7.87E+03	2.85E+02	1.44E+03	7.23E+01	13.054
TO-186-01A-23	1.02E+04	1.76E+03	5.81E+01	7.06E+03	2.32E+02	1.31E+03	6.32E+01	11.574
TO-186-01A-24	8.62E+03	1.99E+03	1.05E+02	8.21E+03	1.34E+02	1.48E+03	4.32E+01	13.699
TO-186-01A-25	8.90E+03	1.83E+03	7.73E+01	7.48E+03	2.82E+02	1.34E+03	9.89E+01	12.748
TO-186-01A-26	1.28E+05	1.95E+03	1.07E+02	7.42E+03	3.38E+02	1.39E+03	4.90E+01	12.273
TO-186-01A-27	8.27E+03	1.07E+03	9.02E+01	4.19E+03	3.04E+02	8.05E+02	4.86E+01	7.147
TO-186-01A-28	4.10E+04	2.11E+03	4.74E+02	8.39E+03	1.86E+03	1.54E+03	3.13E+02	14.342
TO-186-01A-29	9.03E+03	1.84E+03	3.38E+01	7.21E+03	2.74E+02	1.33E+03	7.32E+01	12.558
TO-186-01A-30	8.40E+03	1.59E+03	4.27E+01	6.29E+03	1.99E+02	1.14E+03	5.46E+01	10.931
TO-186-01A-31	1.03E+04	1.48E+03	3.48E+01	5.67E+03	3.37E+02	1.05E+03	4.25E+01	9.812
TO-186-01A-32	8.88E+03	1.57E+03	6.66E+01	6.19E+03	1.05E+02	1.16E+03	5.41E+01	10.479
TO-186-01A-33	1.17E+04	1.19E+03	9.05E+01	4.67E+03	2.10E+02	8.58E+02	3.68E+01	8.148
TO-186-01A-34	8.95E+03	1.87E+03	4.04E+01	7.27E+03	1.55E+02	1.40E+03	3.57E+01	12.526
TO-186-01A-35	5.66E+03	2.01E+03	3.33E+01	8.08E+03	7.43E+01	1.48E+03	5.99E+01	13.919
TO-186-01A-36	1.02E+04	1.61E+03	4.10E+01	6.61E+03	8.70E+01	1.24E+03	2.98E+01	11.528
TO-186-01A-37	1.24E+04	2.65E+03	2.11E+02	1.05E+04	5.79E+02	1.97E+03	1.12E+02	17.797
TO-181-01B-1	9.61E+02	2.05E+03	8.23E+01	8.38E+03	4.08E+02	1.61E+03	9.90E+01	17.043
TO-181-01B-2	3.13E+03	2.15E+03	1.97E+01	8.69E+03	5.16E+02	1.63E+03	7.18E+01	18.043
TO-181-01B-3	1.03E+04	6.45E+01	1.56E+01	2.62E+02	4.63E+01	4.75E+01	6.35E+00	0.000
TO-181-01B-4	2.18E+03	2.34E+03	7.05E+01	9.47E+03	1.58E+02	1.77E+03	4.16E+01	19.477
TO-181-01B-5	5.30E+03	2.76E+03	1.22E+02	1.09E+04	4.47E+02	2.05E+03	6.73E+01	21.912
TO-181-01B-6	1.12E+04	1.50E+03	2.25E+02	5.98E+03	7.20E+02	1.11E+03	1.62E+02	12.387
TO-181-01B-7	8.45E+03	2.34E+03	1.40E+02	9.52E+03	6.28E+02	1.78E+03	1.31E+02	19.763
TO-181-01B-8	5.18E+03	2.09E+03	8.50E+01	8.70E+03	1.13E+02	1.58E+03	4.28E+01	18.508
TO-181-01B-9	9.44E+03	1.88E+03	2.10E+02	9.33E+03	3.87E+03	1.44E+03	8.30E+01	19.636
TO-181-01B-10	2.34E+03	7.34E+02	1.38E+01	2.95E+03	1.01E+02	5.48E+02	3.50E+01	6.039
TO-181-01B-11	3.42E+03	2.18E+03	4.96E+01	8.61E+03	1.13E+02	1.66E+03	8.29E+00	18.203
TO-181-01B-12	9.94E+03	1.94E+03	1.29E+02	7.79E+03	2.13E+02	1.49E+03	8.55E+01	15.966
TO-181-01B-13	8.06E+03	2.33E+03	1.13E+02	9.14E+03	1.54E+02	1.65E+03	9.30E+01	19.006
TO-181-01B-14	8.27E+03	2.47E+03	6.30E+01	9.70E+03	2.19E+02	1.85E+03	1.17E+02	19.654
TO-181-01B-15	9.67E+03	2.54E+03	6.59E+01	1.02E+04	2.08E+02	1.90E+03	5.17E+01	20.948
TO-181-01B-16	2.50E+03	2.64E+03	1.57E+02	1.06E+04	2.95E+02	1.96E+03	8.18E+01	21.241
TO-181-01B-17	2.75E+03	3.09E+03	1.55E+02	1.21E+04	8.35E+02	2.30E+03	7.87E+01	25.153
TO-181-01B-18	4.92E+03	9.29E+02	5.17E+01	3.70E+03	5.90E+01	7.11E+02	1.29E+01	7.540
TO-181-01B-19	4.18E+03	5.44E+02	2.30E+01	2.19E+03	1.08E+02	3.96E+02	2.46E+01	4.438
TO-181-01B-20	1.54E+03	2.35E+03	8.61E+01	9.36E+03	2.31E+02	1.76E+03	3.63E+01	19.363
TO-181-01B-21	2.35E+03	2.63E+03	3.29E+01	1.06E+04	2.08E+02	1.95E+03	7.69E+01	21.771
TO-181-01B-22	2.95E+03	2.22E+03	2.11E+01	8.80E+03	1.61E+02	1.68E+03	2.54E+01	18.327
TO-181-01B-23	1.83E+03	2.69E+03	7.37E+01	1.06E+04	1.91E+02	2.00E+03	8.24E+01	21.360
TO-181-01B-24	4.56E+03	2.57E+02	1.28E+01	1.05E+03	6.17E+01	1.90E+02	3.92E+00	0.000
TO-181-01B-25	2.56E+03	1.99E+03	5.05E+01	8.12E+03	1.30E+02	1.51E+03	3.52E+01	16.552
TO-181-01B-26	8.04E+03	2.58E+03	1.26E+02	1.03E+04	3.73E+02	1.94E+03	7.24E+01	20.693
TO-181-01B-27	1.29E+04	1.45E+03	1.22E+02	5.98E+03	3.60E+02	1.07E+03	5.52E+01	11.848
TO-181-01B-28	2.18E+03	1.55E+03	4.29E+01	6.42E+03	1.62E+02	1.17E+03	1.54E+01	12.885
TO-181-01B-29	1.55E+03	1.13E+03	8.83E+01	4.59E+03	3.73E+02	8.66E+02	1.04E+02	8.898
TO-181-01B-30	5.49E+04	2.28E+03	8.33E+01	8.65E+03	2.60E+02	1.59E+03	3.21E+01	16.564

Table A2.2

				48Ti/30Si measured		40Ca/30Si measured	
Sample	Analysis no.	SIMS session	Analysis Location	mean	1σ	mean	1σ
TO-181	36	2	c	1.420E-03	3.900E-05	3.130E-03	1.400E-04
TO-181	37	2	c	1.350E-03	4.100E-05	6.010E-04	4.300E-05
TO-181	38	2	c	1.373E-03	3.700E-05	1.320E-03	6.600E-05
TO-181	39	2	c	1.389E-03	3.500E-05	7.134E-03	1.300E-05
TO-181	40	2	c	1.184E-03	4.600E-05	1.557E-03	1.500E-04
TO-181	41	2	r	4.997E-04	1.876E-05	9.389E-03	1.500E-03
TO-181	42	2	r	5.307E-04	1.700E-05	1.830E-03	7.900E-05
TO-181	43	2	r	5.010E-04	1.600E-05	4.050E-03	2.600E-04
TO-181	45	2	c	1.231E-03	3.900E-05	3.180E-03	1.800E-04
TO-181	46	2	r	3.861E-04	7.890E-05	2.640E-02	1.100E-03
TO-181	77	2	n	4.118E-05	7.040E-06	3.310E-03	2.100E-04
TO-181	78	2	n	5.919E-05	8.900E-06	7.860E-04	4.100E-04
TO-181	79	2	n	1.585E-04	1.130E-05	4.350E-03	1.100E-04
TO-181	80	2	n	1.736E-04	1.160E-05	2.870E-03	1.600E-04
TO-181	81	2	n	1.114E-04	2.150E-05	4.450E-03	2.590E-04
TO-181	82	2	n	1.075E-04	8.040E-06	4.120E-03	4.400E-04
TO-186	47	2	c	9.659E-04	2.300E-04	4.120E-02	5.700E-03
TO-186	49	2	c	1.298E-03	1.740E-04	3.260E-02	5.300E-03
TO-186	50	2	c	1.292E-03	1.970E-04	4.610E-02	3.800E-03
TO-186	51	2	c	8.941E-04	6.370E-05	2.590E-02	4.500E-03
TO-186	52	2	c	1.207E-03	1.150E-04	3.130E-02	4.400E-03
TO-186	54	2	c	1.373E-03	1.510E-04	2.990E-02	4.400E-03
TO-186	55	2	c	1.196E-03	2.110E-04	3.850E-02	5.100E-03
TO-186	56	2	c	1.178E-03	2.400E-04	1.290E-01	3.200E-02
TO-186	57	2	c	1.118E-03	1.650E-04	2.700E-02	4.500E-02
TO-186	60	2	c	1.830E-03	2.440E-04	6.060E-02	1.300E-02
TO-054	61	2	r	5.690E-04	1.240E-05	1.680E-03	3.400E-04
TO-054	62	2	r	2.372E-04	1.380E-05	1.530E-03	2.800E-04
TO-054	63	2	r	3.872E-04	9.600E-06	3.080E-03	3.500E-04
TO-054	64	2	r	3.544E-04	1.200E-05	1.420E-03	2.100E-04
TO-054	65	2	c	9.412E-04	1.930E-05	1.420E-03	2.100E-04
TO-054	66	2	c	1.030E-03	2.600E-05	3.860E-03	2.400E-04
TO-054	67	2	c	6.805E-04	2.400E-05	3.190E-03	4.400E-04
TO-054	68	2	c	7.916E-04	1.640E-05	1.500E-03	3.100E-04
TO-054	69	2	c	8.719E-04	2.300E-05	1.450E-03	2.600E-04
TO-054	70	2	c	8.507E-04	1.300E-05	6.930E-03	7.800E-04
TO-054	71	2	c	5.415E-04	1.820E-05	3.250E-03	4.600E-04
TO-054	72	2	c	8.359E-04	1.340E-05	1.430E-03	2.700E-04
TO-054	73	2	c	8.447E-04	1.070E-05	2.820E-03	2.100E-04
TO-054	74	2	r	5.696E-04	1.660E-05	2.100E-03	2.500E-04
TO-054	75	2	c	6.377E-04	1.730E-05	3.660E-03	4.200E-04
TO-054	76	2	r	4.251E-04	1.030E-05	2.690E-03	3.900E-04
TO-030	15	3	c	3.204E-03	4.502E-05	2.026E-03	1.490E-04
TO-030	16	3	c	2.921E-03	5.380E-05	3.861E-03	8.959E-04

Table A2.2 (cont.)

TO-030	17	3	c	3.048E-03	2.920E-05	2.160E-03	2.158E-04
TO-030	18	3	c	3.420E-03	1.009E-04	2.336E-03	2.413E-04
TO-030	19	3	c	2.923E-03	5.700E-05	3.526E-03	4.839E-04
TO-030	20a	3	c	3.051E-03	3.752E-05	1.549E-03	1.800E-04
TO-030	20	3	c	2.958E-03	3.839E-05	2.182E-03	3.429E-04
TO-030	21	3	c	3.390E-03	2.222E-04	4.616E-03	7.214E-04
TO-030	22	3	c	2.967E-03	3.459E-05	2.231E-03	2.147E-04
TO-030	23	3	c	3.407E-03	4.485E-05	2.547E-03	2.308E-04
TO-030	24	3	c	3.055E-03	3.791E-05	3.052E-03	3.175E-04
TO-030	25	3	c	3.254E-03	5.615E-05	3.426E-03	3.107E-04
TO-030	27	3	c	2.688E-03	6.585E-05	1.703E-03	1.561E-04
TO-030	29	3	c	2.849E-03	6.835E-05	3.646E-03	4.655E-04
TO-030	30	3	c	3.140E-03	4.613E-04	7.340E-03	1.110E-03
TO-030	31	3	c	2.669E-03	6.961E-05	3.072E-03	9.946E-05
TO-065	33	3	c	1.372E-03	2.828E-05	1.090E-03	3.876E-05
TO-065	34	3	c	1.142E-03	1.987E-05	1.133E-03	5.463E-05
TO-065	35	3	c	1.119E-03	4.353E-05	7.268E-04	8.396E-05
TO-065	36	3	n	5.247E-05	1.835E-05	1.451E-03	6.096E-05
TO-065	37	3	n	5.046E-05	6.617E-06	2.085E-03	2.428E-04
TO-065	38	3	n	5.774E-05	1.847E-05	7.153E-04	9.998E-05
TO-065	39	3	n	6.180E-05	4.462E-06	1.078E-03	6.829E-05
TO-065	40	3	c	9.614E-04	2.215E-05	2.587E-03	1.219E-04
TO-065	41	3	c	9.700E-04	2.602E-05	2.193E-03	2.440E-04
TO-065	42	3	c	8.369E-04	3.244E-05	7.429E-04	2.026E-05
TO-065	43	3	c	1.291E-03	2.034E-05	6.926E-04	9.717E-05
TO-065	44	3	c	1.073E-03	3.793E-05	6.705E-04	9.352E-05
TO-065	45	3	c	1.142E-03	2.105E-05	5.908E-04	9.778E-05
TO-065	46	3	r	9.262E-04	2.622E-05	9.657E-04	7.737E-05
TO-065	47	3	r	4.412E-04	2.101E-05	8.517E-04	4.883E-05
TO-065	48	3	r	5.741E-04	1.831E-05	2.044E-03	1.840E-04
TO-065	49	3	r	7.104E-04	2.009E-05	1.182E-03	3.671E-05
TO-151	123	3	r	2.845E-03	6.696E-05	7.180E-03	4.673E-04
TO-151	124	3	r	1.827E-03	4.570E-05	6.585E-03	1.673E-04
TO-151	125	3	r	8.584E-04	2.610E-05	2.434E-03	1.572E-04
TO-151	126	3	r	2.285E-03	1.781E-05	2.202E-03	2.162E-04
TO-151	127	3	r	2.694E-03	3.549E-05	1.701E-03	9.200E-05
TO-151	128	3	r	1.446E-03	1.911E-05	1.291E-02	3.350E-03
TO-151	129	3	r	1.350E-03	3.543E-05	5.808E-03	1.022E-03
TO-151	130	3	r	4.026E-04	3.294E-05	1.147E-02	3.918E-03
TO-151	131	3	r	1.743E-03	4.969E-05	2.040E-03	6.410E-04
TO-151	132	3	r	2.433E-03	3.542E-05	2.794E-03	8.114E-05
TO-151	133	3	r	2.061E-03	2.938E-05	1.570E-02	3.976E-03
TO-151	134	3	r	2.640E-03	3.996E-05	2.051E-03	1.480E-04
TO-151	135	3	r	1.568E-03	2.379E-05	3.873E-03	1.852E-04

Table A2.2 (cont.)

48Ti/30Si corrected

Sample	mean	1σ	Ti (ppm)	1σ (ppm)
TO-181	1.414E-03	3.874E-05	16.26	0.45
TO-181	1.349E-03	4.092E-05	15.51	0.47
TO-181	1.371E-03	3.688E-05	15.76	0.42
TO-181	1.376E-03	3.498E-05	15.82	0.40
TO-181	1.181E-03	4.572E-05	13.58	0.53
TO-181	4.822E-04	1.597E-05	5.55	0.18
TO-181	5.273E-04	1.685E-05	6.06	0.19
TO-181	4.935E-04	1.552E-05	5.67	0.18
TO-181	1.225E-03	3.867E-05	14.09	0.44
TO-181	3.370E-04	7.685E-05	3.88	0.88
TO-181	3.502E-05	6.649E-06	0.40	0.08
TO-181	5.773E-05	8.137E-06	0.66	0.09
TO-181	1.504E-04	1.110E-05	1.73	0.13
TO-181	1.683E-04	1.130E-05	1.94	0.13
TO-181	1.031E-04	2.102E-05	1.19	0.24
TO-181	9.984E-05	7.222E-06	1.15	0.08
TO-186	8.893E-04	2.194E-04	10.23	2.52
TO-186	1.237E-03	1.641E-04	14.23	1.89
TO-186	1.206E-03	1.899E-04	13.87	2.18
TO-186	8.459E-04	5.533E-05	9.73	0.64
TO-186	1.149E-03	1.068E-04	13.21	1.23
TO-186	1.317E-03	1.428E-04	15.15	1.64
TO-186	1.124E-03	2.015E-04	12.93	2.32
TO-186	9.381E-04	1.805E-04	10.79	2.08
TO-186	1.068E-03	8.130E-05	12.28	0.93
TO-186	1.717E-03	2.198E-04	19.75	2.53
TO-054	5.659E-04	1.177E-05	6.51	0.14
TO-054	2.344E-04	1.328E-05	2.70	0.15
TO-054	3.815E-04	8.949E-06	4.39	0.10
TO-054	3.518E-04	1.161E-05	4.05	0.13
TO-054	9.386E-04	1.891E-05	10.79	0.22
TO-054	1.023E-03	2.555E-05	11.76	0.29
TO-054	6.746E-04	2.318E-05	7.76	0.27
TO-054	7.888E-04	1.582E-05	9.07	0.18
TO-054	8.692E-04	2.252E-05	10.00	0.26
TO-054	8.378E-04	1.155E-05	9.63	0.13
TO-054	5.355E-04	1.734E-05	6.16	0.20
TO-054	8.332E-04	1.290E-05	9.58	0.15
TO-054	8.395E-04	1.031E-05	9.65	0.12
TO-054	5.657E-04	1.614E-05	6.51	0.19
TO-054	6.309E-04	1.652E-05	7.26	0.19
TO-054	4.201E-04	9.575E-06	4.83	0.11
TO-030	3.200E-03	4.474E-05	41.06	0.57
TO-030	2.914E-03	5.213E-05	37.39	0.67

Table A2.2 (cont.)

TO-030	3.044E-03	2.880E-05	39.06	0.37
TO-030	3.415E-03	1.005E-04	43.82	1.29
TO-030	2.916E-03	5.610E-05	37.42	0.72
TO-030	3.048E-03	3.719E-05	39.11	0.48
TO-030	2.954E-03	3.775E-05	37.91	0.48
TO-030	3.381E-03	2.208E-04	43.38	2.83
TO-030	2.963E-03	3.419E-05	38.02	0.44
TO-030	3.402E-03	4.442E-05	43.65	0.57
TO-030	3.049E-03	3.732E-05	39.12	0.48
TO-030	3.248E-03	5.557E-05	41.67	0.71
TO-030	2.685E-03	6.556E-05	34.45	0.84
TO-030	2.842E-03	6.748E-05	36.47	0.87
TO-030	3.127E-03	4.592E-04	40.12	5.89
TO-030	2.663E-03	6.942E-05	34.17	0.89
TO-065	1.370E-03	2.821E-05	17.57	0.36
TO-065	1.139E-03	1.976E-05	14.62	0.25
TO-065	1.118E-03	4.338E-05	14.35	0.56
TO-065	4.977E-05	1.824E-05	0.64	0.23
TO-065	4.658E-05	6.165E-06	0.60	0.08
TO-065	5.641E-05	1.828E-05	0.72	0.23
TO-065	5.980E-05	4.335E-06	0.77	0.06
TO-065	9.566E-04	2.192E-05	12.27	0.28
TO-065	9.660E-04	2.557E-05	12.39	0.33
TO-065	8.356E-04	3.240E-05	10.72	0.42
TO-065	1.289E-03	2.016E-05	16.54	0.26
TO-065	1.072E-03	3.776E-05	13.75	0.48
TO-065	1.141E-03	2.086E-05	14.63	0.27
TO-065	9.244E-04	2.608E-05	11.86	0.33
TO-065	4.396E-04	2.092E-05	5.64	0.27
TO-065	5.703E-04	1.797E-05	7.32	0.23
TO-065	7.082E-04	2.002E-05	9.09	0.26
TO-151	2.832E-03	6.609E-05	36.34	0.85
TO-151	1.815E-03	4.539E-05	23.29	0.58
TO-151	8.538E-04	2.580E-05	10.96	0.33
TO-151	2.281E-03	1.741E-05	29.27	0.22
TO-151	2.690E-03	3.532E-05	34.52	0.45
TO-151	1.422E-03	1.288E-05	18.25	0.17
TO-151	1.339E-03	3.353E-05	17.19	0.43
TO-151	3.812E-04	2.565E-05	4.89	0.33
TO-151	1.739E-03	4.850E-05	22.31	0.62
TO-151	2.428E-03	3.527E-05	31.15	0.45
TO-151	2.032E-03	2.199E-05	26.07	0.28
TO-151	2.636E-03	3.969E-05	33.82	0.51
TO-151	1.561E-03	2.345E-05	20.03	0.30

Appendix 3

Supplementary Figures for Chapter 3

Figure A3.1. SE images of silica gel surface topology before and after calcination.

Figure A3.2. Mass loss on ignition for water in silica gel following various heating treatments.

Figure A3.3. XRD Spectra of silica gel following various heating treatments.

Figure A3.4. Effect of molecular size of the solvent medium on doping efficiency.

Figure A3.5. SE images of TiO2 precipitates from high concentration doping experiments.

Figure A3.6. Experimentally-derived efficiency of doping technique.

Figure A3.7. SIMS analysis of polished grain mounts of doped silica gel particles.

Figure A3.8. SEI of vesicles in hot-pressed glass aggregate.

Appendix 3

Figure A3.1.

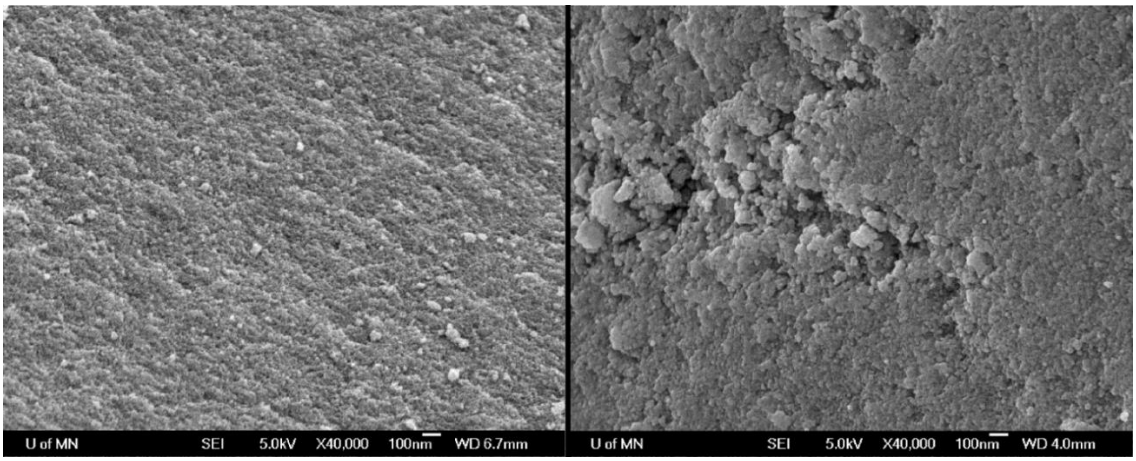

Figure A3.2.

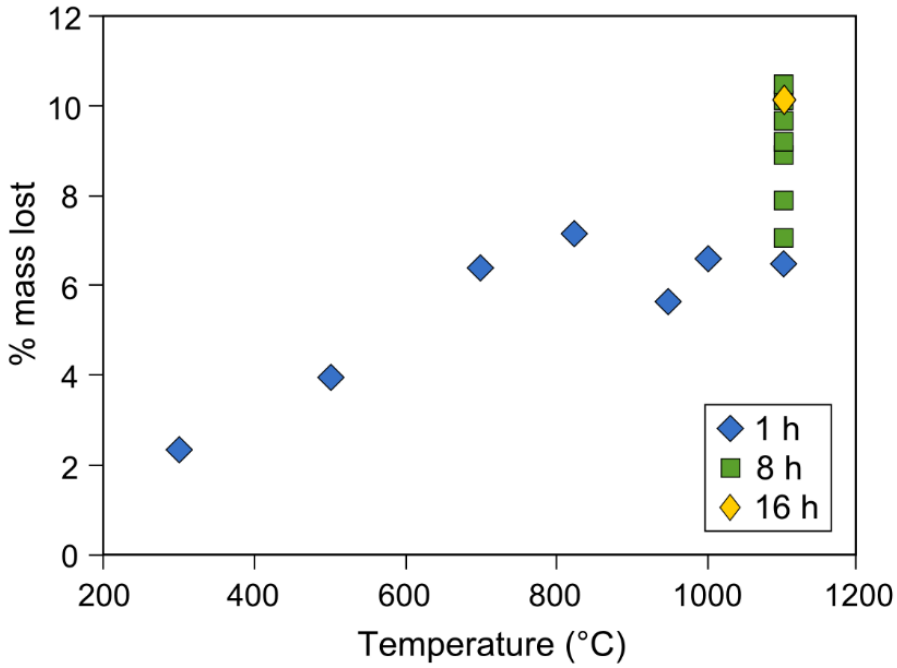
12
10
8
6
4
2
0
% mass lost
200
400
600
800
1000
1200
Temperature (°C)
1 h
8 h
16 h

Figure A3.3.

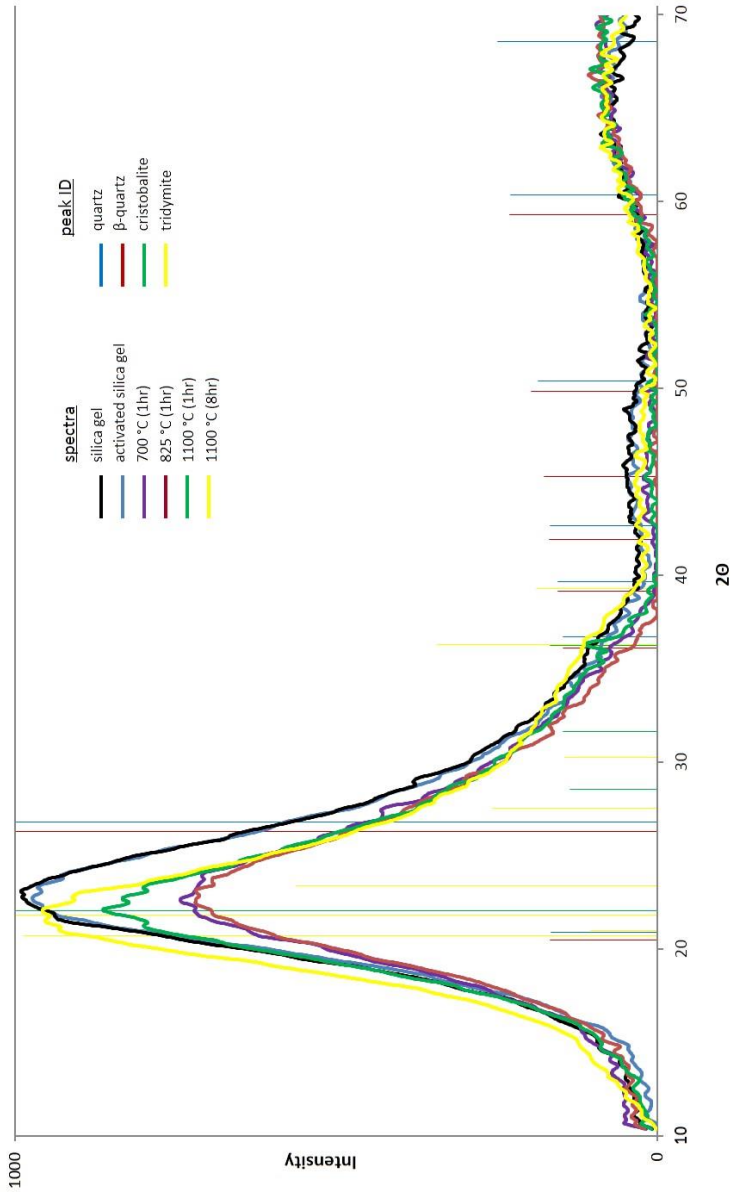
peak ID
quartz
β-quartz
cristobalite
tridymite
spectra
silica gel
activated silica gel
700 °C (1hr)
825 °C (1hr)
1100 °C (1hr)
1100 °C (8hr)
Intensity
1000
0
10
20
30
40
50
60
70
2θ

Figure A3.4.

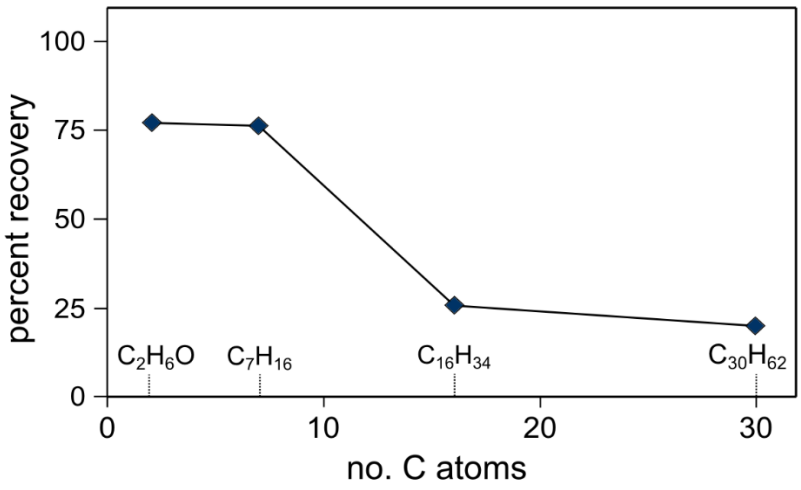
100
75
50
25
0
percent recovery
C2H6O
C7H16
C16H34
C30H62
0
10
20
30
no. C atoms

Figure A3.5.

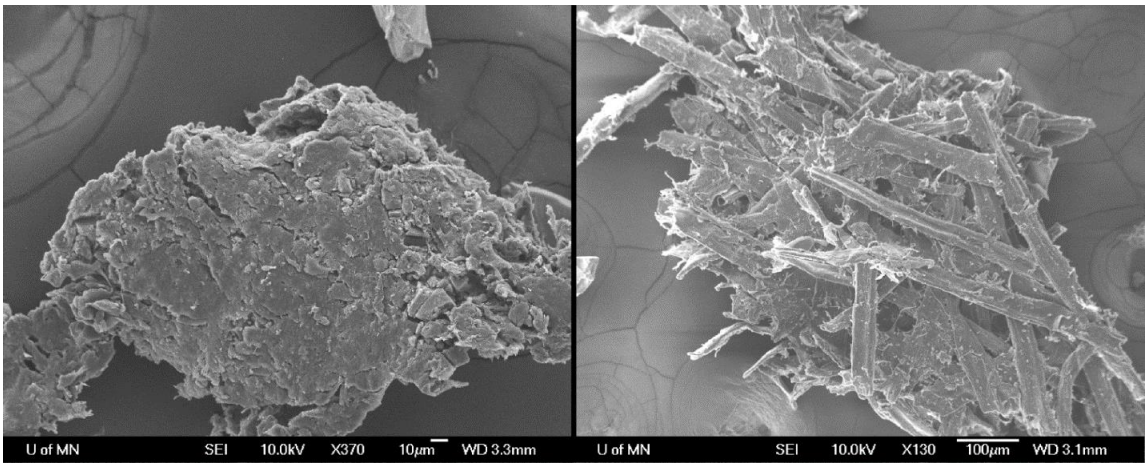
U of MN SEI 10.0kV X370 10μm WD 3.3mm
U of MN SEI 10.0kV X130 100μm WD 3.1mm

Figure A3.6.

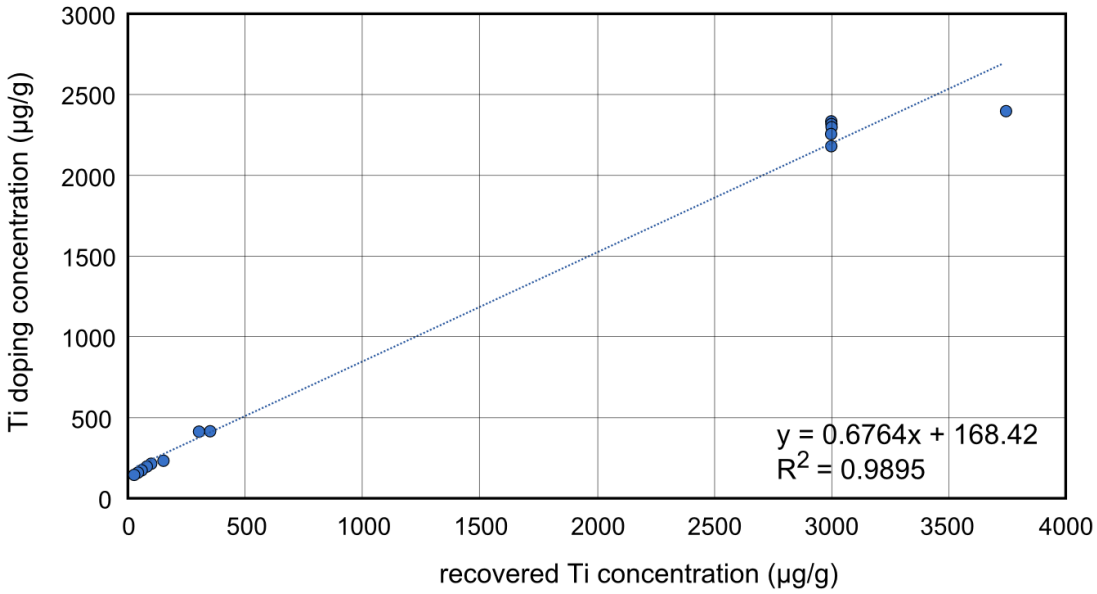
3000
2500
2000
1500
1000
500
0
Ti doping concentration (µg/g)
0
500
1000
1500
2000
2500
3000
3500
4000
recovered Ti concentration (µg/g)
y = 0.6764x + 168.42
R2 = 0.9895

Figure A3.7.

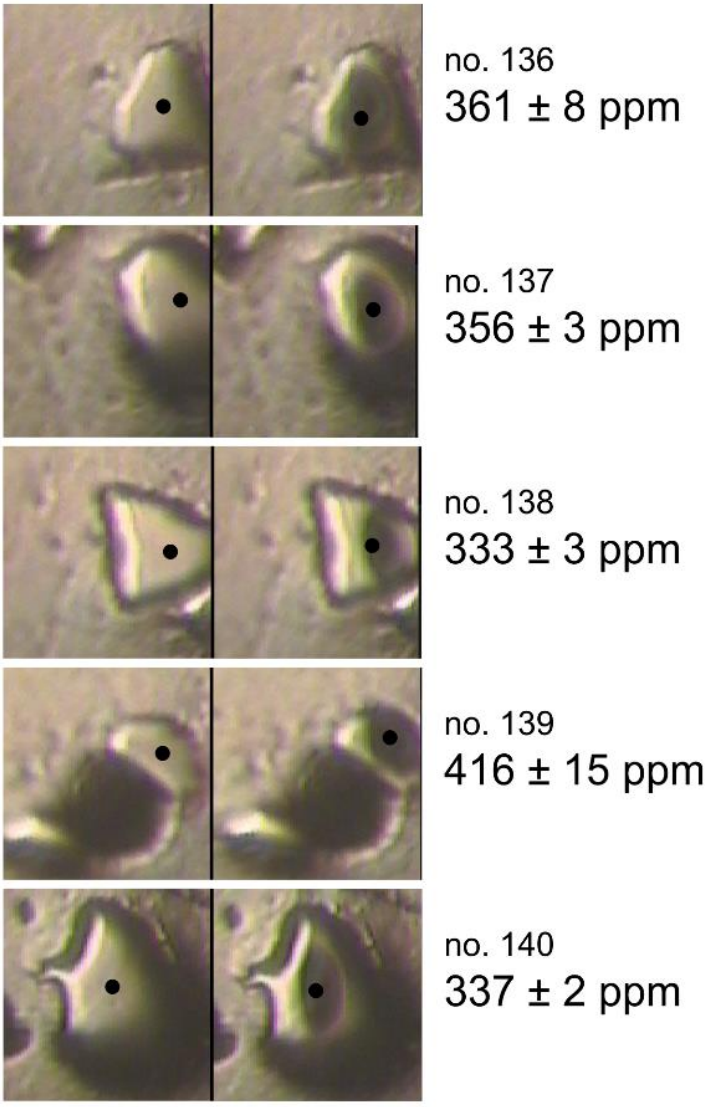
no. 136
361 ± 8 ppm
no. 137
356 ± 3 ppm
no. 138
333 ± 3 ppm
no. 139
416 ± 15 ppm
no. 140
337 ± 2 ppm

Figure A3.8.

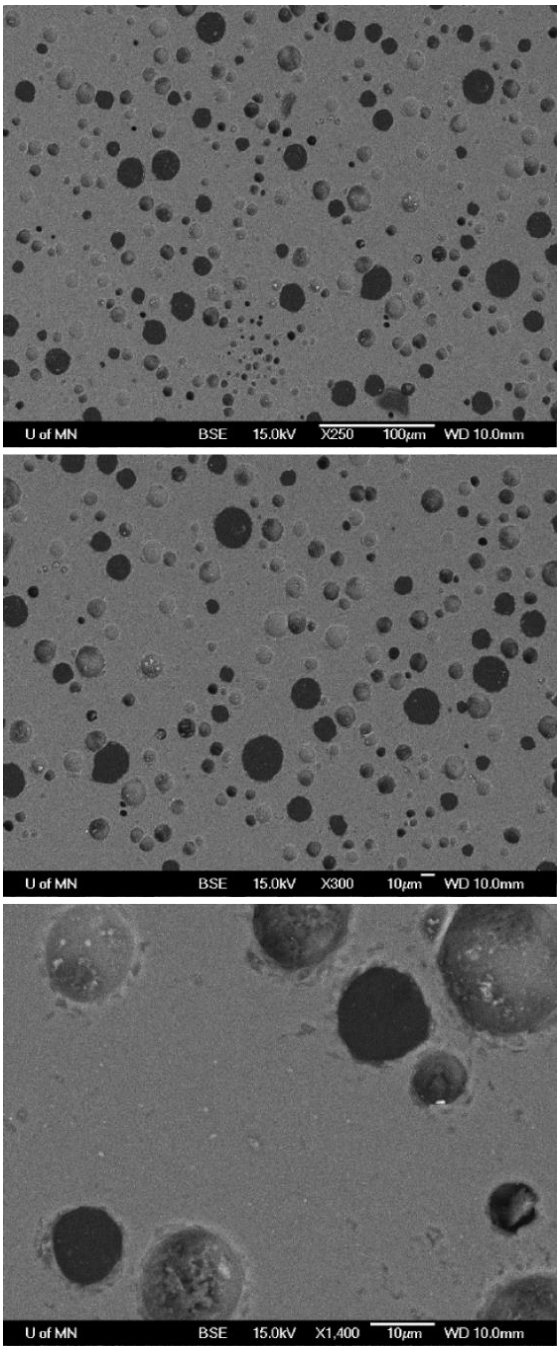
U of MN BSE 15.0kV X250 100µm WD 10.0mm
U of MN BSE 15.0kV X300 10µm WD 10.0mm
U of MN BSE 15.0kV X1,400 10µm WD 10.0mm

Appendix 4

Supplementary Tables for Chapter 3

Table A4.1. Geochemistry of silica gel following various activation and doping treatments.

Table A4.2. ICP-OES major and minor element analysis of reference materials.

Table A4.3. ICP-OES trace element analysis of silica gel.

Table A4.4. EPMA of reference materials with the JEOL-8900 at UMN.

Table A4.5. EPMA of reference materials with the Cameca SX-100 at RPI.

Table A4.6. SIMS analysis of reference materials.

Table A4.7. LA-ICP-MS analysis of reference materials.

Table A4.8. Results of EPMA of 3-layered reference material – HPS-3.

Table A4.9. Results of EPMA of 7-layered reference material – HPS-7.

Table A4.10. Results of LA-ICP-MS analysis of 7-layered reference material (HPS-7).

Appendix 4

Table A4.1. Geochemistry of silica gel following various activation and doping treatments.

ICP-OES sample ID and batch no.	sample name and description	Acid rinse (h)	pH	Doping substrate	Doping Medium	Dopant added (ppm Ti)	Al	Ba	Ca	Fe	Mg	Na	P	Sr	Ti	Zr
SG-0.01 1	**pH 7 - Target 300** uncalcined	6	7	6hr silica gel	ethanol	300	219.6	4.0	193.7	322.8	227.9	--	13.3	3.8	397.1	64.4
SG-0.02 1	**pH 7 - Target 300 - calcined** 1.00g calcined in Zr at 1100C for 8hr	6	7	6hr silica gel	ethanol	300	236.0	2.2	221.9	275.6	87.1	--	8.7	4.2	437.8	67.4
SG-0.03 1	**pH 8 - Target 300** uncalcined	6	8	6hr silica gel	ethanol	300	242.7	4.9	296.2	271.4	98.6	--	--	4.2	415.3	67.4
SG-0.04 1	**pH 8 - Target 300 - calcined** 1.00g calcined in Zr at 1100C for 8hr	6	8	6hr silica gel	ethanol	300	214.6	2.2	285.5	278.0	102.8	--	9.2	4.2	455.8	65.5
SG-0.05 1	**pH 9 - Target 300** uncalcined	6	9	6hr silica gel	ethanol	300	206.7	4.9	432.7	279.4	135.7	--	8.7	4.2	397.1	63.3
SG-0.06 1	**pH 9 - Target 300 - calcined** 1.00g calcined in Zr at 1100C for 8hr	6	9	6hr silica gel	ethanol	300	199.5	3.1	813.3	256.7	427.2	--	7.2	4.2	420.4	70.0
SG-0.07 1	**pH 10 - Target 300** uncalcined	6	10	6hr silica gel	ethanol	300	46.3	2.7	379.1	238.2	112.8	118.0	11.3	4.7	404.6	61.4
SG-0.08 1	**pH 10 - Target 300 - calcined** 1.00g calcined in Zr at 1100C for 8hr	6	10	6hr silica gel	ethanol	300	115.6	4.0	264.1	233.6	92.3	79.4	12.2	3.8	451.9	64.8
SG-0.09 1	**pH 7 - Target 3000** uncalcined	6	7	6hr silica gel	ethanol	3000	--	1.3	198.3	216.1	64.2	69.7	13.1	3.0	601.4	53.3
SG-0.10 1	**pH 7 - Target 3000 - calcined** 1.00g calcined in Zr at 1100C for 8hr	6	7	6hr silica gel	ethanol	3000	76.5	2.2	241.6	201.1	76.3	53.4	10.5	3.4	664.7	51.8
SG-0.11 1	**pH 8 - Target 3000** uncalcined	6	8	6hr silica gel	ethanol	3000	--	3.6	280.2	234.3	88.3	82.0	9.8	3.8	2181.3	66.3
SG-0.12 1	**pH 8 - Target 3000 - calcined** 1.00g calcined in Zr at 1100C for 8hr	6	8	6hr silica gel	ethanol	3000	142.1	3.1	250.5	228.7	86.8	49.3	9.6	3.8	2254.5	66.3
SG-0.13 1	**pH 9 - Target 3000** uncalcined	6	9	6hr silica gel	ethanol	3000	56.4	2.7	270.5	224.9	86.2	36.0	9.4	4.2	2428.6	61.4
SG-0.14 1	**pH 9 - Target 3000 - calcined** 1.00g calcined in Zr at 1100C for 8hr	6	9	6hr silica gel	ethanol	3000	50.0	3.1	269.1	238.2	91.4	72.7	7.0	3.8	2023.7	66.3

Table A4.1 (cont.). Geochemistry of silica gel following various activation and doping treatments.

SG-0.15 1	**pH 10 - Target 3000** uncalcined	6	10	6hr silica gel	ethanol	3000	47.9	2.7	267.6	226.6	81.1	83.5	10.3	3.4	2557.4	67.7					
SG-0.16 1	**pH 10 - Target 3000 - calcined** 1.00g calcined in Zr at 1100C for 8hr	6	10	6hr silica gel	ethanol	3000	118.8	3.1	390.2	254.2	119.7	85.3	11.8	4.2	1667.1	58.9					
SG-01 2	**initial silica gel**	--	--	--	--	0	223.2	15.5	532.7	213.8	167.0	786.4	12.1	7.6	142.0	64.7					
SG-02 2	**9hr activation silica gel**	9	--	--	--	0	61.0	3.3	193.4	200.7	94.7	52.4	10.0	3.7	110.3	62.7					
SG-03 2	**Large batch calcined in Al** 1.00g calcined in Al at 825C for 1hr	9	--	9hr silica gel	ethanol	0	46.0	2.4	193.9	165.8	91.3	42.3	9.7	3.7	113.5	61.7					
SG-04 2	**Large batch calcined in Zr** 1.00g calcined in Zr at 825C for 1hr	9	--	9hr silica gel	ethanol	0	94.2	2.7	185.1	175.1	94.5	21.5	9.9	3.7	114.5	64.2					
SG-05 2	**Small batch calcined in Al** 0.10g of SG-0.11 calicined in Al at 825C for 1hr	6	--	6hr silica gel	ethanol	3000	179.4	3.3	101.0	320.8	106.9	--	20.2	5.4	2288.1	94.8					
SG-06 2	**Small batch calcined in Zr** 0.10g of SG-0.11 calicined in Zr at 825C for 1hr	6	--	6hr silica gel	ethanol	3000	81.7	3.6	121.3	236.2	87.6	69.0	15.7	4.5	2336.9	115.5					
SG-07 3	**3hr activation silica gel**	3	--	--	--	0	126.6	6.8	744.0	365.7	232.9	154.0	--	5.2	119.7	30.1					
SG-08 3	**6hr activation silica gel**	6	--	--	--	0	137.1	6.6	797.4	421.7	245.5	254.1	1.6	5.5	121.3	32.0					
SG-10 3	**Target 3000**	9	8	9hr silica gel	reagent alcohol	3000	135.8	6.5	773.1	379.0	234.8	65.6	--	5.3	2305.3	29.2					
SG-11 3	**BHQ - as received** Black Hills Quartz (BHQ) - as received	--	--	--	--	0	728.0	9.3	849.0	912.1	250.4	61.9	102.4	7.7	140.7	8.8					
SG-12 3	**BHQ - 9hr activation** BHQ - 9hr activation	9	--	--	--	0	457.4	8.5	619.8	588.0	219.1	48.1	15.4	6.5	47.2	3.3					
SG-13 3	**Target 3746** "over-dope" to attempt Target 3000	9	8	9hr silica gel	reagent alcohol	3746	92.5	4.1	828.6	474.7	259.3	30.9	--	5.0	2397.5	20.1					
SG-14 3	**Target 2254+746** "double-dope" to attempt Target 3000	9	8	9hr silica gel	reagent alcohol	2255+746	106.1	4.5	826.4	493.7	256.9	23.2	1.5	5.1	2920.6	28.0					
SG-15 3	**Heptane Target 3000**	9	8	9hr silica gel	Heptane	3000	119.8	4.1	780.1	483.2	249.0	75.4	1.4	4.8	2280.1	20.9					
SG-16 3	**Hexadecane Target 3000**	9	8	9hr silica gel	Hexadecane	3000	100.7	3.8	797.4	484.5	253.6	37.2	8.2	4.7	770.5	12.2					

Table A4.1 (cont.). Geochemistry of silica gel following various activation and doping treatments.

SG-17 3	**Squalane Target 3000**	9	8	9hr silica gel	Squalane	3000	113.0	3.6	717.9	467.7	232.5	27.9	--	4.3	614.2	11.0
SG-18 3	**BHQ Target 3000**	9	8	9hr silica gel	reagent alcohol	3000	443.2	8.2	621.1	569.1	222.5	42.5	10.6	6.4	1846.7	13.9
SG-20 3	**Target 195**	9	8	9hr silica gel	reagent alcohol	195	102.7	4.0	768.4	475.8	246.7	35.4	6.8	4.7	208.8	22.9
SG-21 3	**DIW Target 300**	9	8	9hr silica gel	Deionized w ater	300	132.5	4.2	834.9	419.0	402.1	62.3	2.0	6.7	271.4	22.9
SG-22 3	**Hexadecane Target 300**	9	8	9hr silica gel	Hexadecane	300	113.4	4.3	798.7	417.5	389.4	61.5	15.7	4.3	379.1	24.2
SG-23 3	**Squalane Target 300**	9	8	9hr silica gel	Squalane	300	101.9	4.3	792.5	408.2	386.1	57.1	1.4	4.2	379.7	22.3
SG-24 3	**BHQ Target 300**	9	8	9hr BHQ	reagent alcohol	300	430.4	8.3	561.4	468.0	319.1	64.2	14.0	5.4	123.1	--
SG-25 3	**Target 30**	9	8	9hr silica gel	reagent alcohol	30	127.7	4.3	801.1	408.7	389.2	69.5	--	4.4	149.7	29.6
SG-26 3	**Target 60**	9	8	9hr silica gel	reagent alcohol	60	132.6	4.3	815.1	409.3	395.7	68.0	--	4.5	181.6	30.7
SG-27 3	**Target 90**	9	8	9hr silica gel	reagent alcohol	90	143.3	4.3	808.5	418.1	394.0	65.7	1.6	4.4	215.8	33.2
SG-28 4	**72hr activation silica gel**	72	--	--	--	0	--	4.1	289.3	--	--	1.8	--	0.1	77.3	37.4
SG-29 4	**Target 802_attempt1*** 802_batch1_singledope	72	8	72hr silica gel	reagent alcohol	802	--	3.0	135.8	--	--	--	--	--	192.5	22.3
SG-30 4	**Target 2916_attempt1*** 2916_batch1_singledope	72	8	72hr silica gel	reagent alcohol	2916	--	3.2	128.3	--	--	--	--	--	801.5	28.3
SG-31 5	72 hr activation_120hr dry analyzed again	72	--	--	--	0	263.2	7.0	822.5	192.5	--	273.0	--	6.3	109.0	36.0
SG-32 5	**Target 802_attempt2*** 802_batch2_singledope	72	8	72hr silica gel	reagent alcohol	802	253.7	6.5	903.7	220.5	--	294.3	--	6.6	462.8	31.4
SG-33 5	**Target 2916_attempt2*** 2916_batch2_singledope	72	8	72hr silica gel	reagent alcohol	2916	143.2	6.2	670.2	144.9	--	213.7	--	5.7	733.9	24.5

Table A4.1 (cont.). Geochemistry of silica gel following various activation and doping treatments.

SG-345	**Target 2916_attempt1_analyzed again***	72	8	72hr silica gel	reagent alcohol	2916	140.2	5.7	591.8	119.2	--	195.0	--	5.1	812.9	21.9
	2916_batch1_singledope (again)															
SG-355	**silica gel beads commercial - as received**	--	--	--	--	0	762.2	14.8	652.2	315.9	--	1471.0	--	7.5	183.9	41.3
SG-406	**7x24hr activation_stir-bar eroded**	168	8	7x24hr silica ge	--		179.6	0.5	223.3	141.3	35.9	14.1	--	1.4	92.7	16.2
	rinse for 7 days, refresh acid every 24hr															
SG-416	**7x24hr activation**	168	8	7x24hr silica ge	--		166.4	0.5	234.0	--	25.0	49.5	--	1.6	89.0	11.6
	rinse for 7 days, refresh acid every 24hr															
SG-426	**Target 147**	168	8	7x24hr silica ge	reagent alcohol	147	194.6	0.6	199.3	--	24.5	38.1	--	1.3	234.4	11.7
SG-436	**Target 347**	168	8	7x24hr silica ge	reagent alcohol	347	156.8	0.5	201.6	--	25.7	54.6	--	1.2	415.7	10.2

*Experiments conducted with Ti plasma standard solution that was 8 months past expiration data

Appendix 4

Table A4.2. Analysis of reference materials with ICP-OES.

Sample name	Al	Ba	Ca	Fe	K	Mg	Mn	Na	P	Si	Sr	Ti	Zr
USGS BIR-1	8.332	0.001	9.566	8.067	0.013	5.871	0.139	1.388	0.010	22.498	0.011	0.590	0.002
USGS BIR-1	8.289	0.001	9.460	7.978	0.016	5.759	0.138	1.381	0.009	22.569	0.011	0.589	0.002
USGS BIR-1	8.321	0.001	9.512	8.039	0.015	5.860	0.139	1.400	0.010	22.340	0.011	0.587	0.002
MEAN (atomic)	**8.314**	**0.001**	**9.513**	**8.028**	**0.015**	**5.830**	**0.139**	**1.390**	**0.009**	**22.469**	**0.011**	**0.589**	**0.002**
MEAN (wt% oxide)	**15.709**	**0.001**	**13.310**	**10.328**	**0.018**	**9.667**	**0.179**	**1.873**	**0.022**	**48.068**	**0.013**	**0.982**	**0.002**
Recommended values*	15.5	--	13.3	11.30	0.030	9.70	0.175	1.820	0.021	47.96	--	0.96	--
% error	*-1.3*	--	*-0.1*	*8.6*	*40.3*	*0.3*	*-2.2*	*-2.9*	*-3.1*	*-0.2*	--	*-2.3*	--
USGS RGM-1	7.203	0.082	0.860	1.286	3.631	0.180	0.028	3.038	0.019	34.080	0.011	0.158	0.021
USGS RGM-1	7.198	0.082	0.885	1.295	3.656	0.205	0.029	3.036	0.018	34.161	0.011	0.158	0.021
USGS RGM-1	7.212	0.083	0.896	1.291	3.686	0.182	0.029	3.086	0.018	33.712	0.010	0.159	0.021
MEAN (atomic)	**7.204**	**0.082**	**0.880**	**1.291**	**3.658**	**0.189**	**0.029**	**3.053**	**0.018**	**33.984**	**0.011**	**0.159**	**0.021**
MEAN (wt% oxide)	**13.612**	**0.092**	**1.232**	**1.661**	**4.406**	**0.313**	**0.037**	**4.116**	**0.042**	**72.703**	**0.013**	**0.264**	**0.028**
Recommended values*	13.7	--	1.15	1.86	4.30	0.28	0.036	4.07	--	73.4	--	0.27	--
% error	*0.6*	--	*-7.1*	*10.7*	*-2.5*	*-11.9*	*-3.5*	*-1.1*	--	*0.9*	--	*2.1*	--

*as reported by www.crustal.usgs.gov

Table A4.3. Trace element geochemistry of silica gel measured with ICP-OES.

Sample	45Sc	51V	52Cr	59Co	60Ni	65Cu	66Zn	71Ga	72Ge	75As	85Rb	88Sr	89Y	90Zr	93Nb	95Mo
	ppm	ppm	ppm	ppm	ppm	ppm	ppm	ppm	ppm	ppm	ppm	ppm	ppm	ppm	ppm	ppm
SG-28 1	-0.53	-0.48	-1.59	-1.09	-0.91	-0.33	--	-0.24	-1.82	-0.89	-1.06	0.38	-0.11	31.52	-0.71	-0.22
SG-28 2	-0.63	-0.44	-1.60	-1.08	-0.90	-1.05	--	-0.23	-1.79	-0.92	-1.07	0.41	-0.10	32.06	-0.64	-0.17
SG-28 3	-0.63	-0.20	-1.03	-0.57	-0.78	0.11	--	-0.14	-2.18	-0.33	-0.68	1.44	-0.05	31.93	0.32	-0.14
SG-28 4	-0.63	-0.22	-1.01	-0.56	-0.76	-0.54	--	-0.15	-2.18	-0.36	-0.70	1.43	-0.05	33.14	0.43	-0.06
SG-28 5	-0.48	-0.45	-1.06	-0.86	-1.19	-0.09	-2.70	-0.26	-3.27	-0.64	-0.87	0.95	-0.05	32.54	0.25	-0.21
SG-28 6	-0.59	-0.50	-1.00	-0.86	-1.21	-0.72	-2.87	-0.30	-3.21	-0.76	-0.88	0.97	-0.03	33.45	0.44	-0.11
MEAN	**-0.58**	**-0.38**	**-1.22**	**-0.83**	**-0.96**	**-0.44**	**-2.78**	**-0.22**	**-2.41**	**-0.65**	**-0.87**	**0.93**	**-0.07**	**32.44**	**0.02**	**-0.15**
SG-40 1	0.32	-0.01	0.35	0.02	0.30	0.89	1.14	0.02	--	-0.02	0.01	2.05	0.14	20.23	0.55	0.07
SG-40 2	0.28	-0.02	0.34	0.02	0.31	0.81	1.09	0.03	--	-0.04	0.01	1.87	0.14	19.38	0.50	0.07
MEAN	**0.30**	**-0.01**	**0.34**	**0.02**	**0.30**	**0.85**	**1.11**	**0.03**	--	**-0.03**	**0.01**	**1.96**	**0.14**	**19.81**	**0.52**	**0.07**
SG-41 1	0.01	0.06	0.21	0.01	0.16	1.24	0.93	0.04	--	-0.02	0.01	2.16	0.06	14.18	0.42	0.14
SG-41 2	-0.01	0.05	0.21	0.01	0.15	1.24	0.91	0.03	--	0.03	0.01	2.11	0.06	13.99	0.40	0.14
MEAN	**0.00**	**0.06**	**0.21**	**0.01**	**0.15**	**1.24**	**0.92**	**0.04**	--	**0.00**	**0.01**	**2.13**	**0.06**	**14.09**	**0.41**	**0.14**
SG-42 1	0.00	0.07	1.29	0.42	0.13	0.49	1.19	0.04	--	-0.06	-0.02	1.80	0.07	14.39	0.50	0.12
SG-42 2	-0.05	0.07	1.28	0.42	0.13	0.48	1.15	0.04	--	-0.04	0.00	1.92	0.08	14.14	0.46	0.13
MEAN	**-0.03**	**0.07**	**1.29**	**0.42**	**0.13**	**0.48**	**1.17**	**0.04**	--	**-0.05**	**-0.01**	**1.86**	**0.07**	**14.27**	**0.48**	**0.13**
SG-43 1	-0.04	0.10	0.21	0.18	0.17	0.90	0.79	0.04	--	-0.06	0.00	1.74	0.04	13.10	0.52	0.03
SG-43 2	-0.04	0.07	0.23	0.18	0.15	0.85	0.85	0.03	--	-0.05	0.00	1.92	0.04	13.13	0.51	0.02
MEAN	**-0.04**	**0.08**	**0.22**	**0.18**	**0.16**	**0.87**	**0.82**	**0.03**	--	**-0.05**	**0.00**	**1.83**	**0.04**	**13.12**	**0.51**	**0.02**

Table A4.3 (cont.). Trace element geochemistry of silica gel measured with ICP-OES.

Sample	111Cd ppm	118Sn ppm	121Sb ppm	133Cs ppm	138Ba ppm	139La ppm	140Ce ppm	141Pr ppm	146Nd ppm	147Sm ppm	151Eu ppm	157Gd ppm	159Tb ppm	163Dy ppm	165Ho ppm	166Er ppm
SG-28 1	-0.07	-1.60	-0.61	-0.01	1.08	-2.41	-0.13	-0.04	-0.04	-0.04	-0.02	-0.04	-0.04	-0.03	-0.04	-0.04
SG-28 2	-0.06	-1.37	-0.61	0.00	1.10	-2.37	-0.12	-0.04	-0.04	-0.05	-0.02	-0.04	-0.04	-0.03	-0.04	-0.03
SG-28 3	-0.11	-2.18	-0.17	0.00	1.97	-2.01	-0.05	0.04	0.04	0.03	0.06	0.05	0.04	0.06	0.02	0.04
SG-28 4	-0.10	-2.16	-0.17	0.01	1.95	-1.98	-0.04	0.04	0.04	0.02	0.05	0.05	0.04	0.06	0.02	0.04
SG-28 5	-0.02	-1.18	-0.25	0.00	1.11	-2.40	-0.12	-0.02	0.04	-0.03	-0.02	-0.01	-0.01	-0.02	-0.02	-0.03
SG-28 6	0.01	-0.84	-0.24	0.01	1.13	-2.36	-0.09	-0.02	0.04	-0.03	-0.03	-0.01	-0.01	-0.03	-0.02	-0.04
MEAN	**-0.06**	**-1.55**	**-0.34**	**0.00**	**1.39**	**-2.25**	**-0.09**	**-0.01**	**0.01**	**-0.01**	**0.00**	**0.00**	**0.00**	**0.00**	**-0.01**	**-0.01**
SG -40 1	0.00	0.08	0.05	0.00	0.91	0.06	0.10	0.01	0.05	0.01	0.00	0.01	0.00	0.01	0.00	0.01
SG -40 2	0.00	0.09	0.05	0.00	0.94	0.06	0.10	0.01	0.05	0.01	0.00	0.01	0.00	0.01	0.00	0.01
MEAN	**0.00**	**0.08**	**0.05**	**0.00**	**0.92**	**0.06**	**0.10**	**0.01**	**0.05**	**0.01**	**0.00**	**0.01**	**0.00**	**0.01**	**0.00**	**0.01**
SG -41 1	0.00	-0.07	0.00	0.00	1.13	0.08	0.17	0.01	0.05	0.01	0.00	0.01	0.00	0.01	0.00	0.00
SG -41 2	0.00	-0.07	0.01	0.00	1.13	0.07	0.17	0.01	0.04	0.01	0.00	0.01	0.00	0.01	0.00	0.01
MEAN	**0.00**	**-0.07**	**0.01**	**0.00**	**1.13**	**0.07**	**0.17**	**0.01**	**0.04**	**0.01**	**0.00**	**0.01**	**0.00**	**0.01**	**0.00**	**0.00**
SG -42 1	0.00	0.06	0.00	-0.02	1.15	0.09	0.11	0.02	0.05	0.01	0.00	0.01	0.00	0.01	0.00	0.01
SG -42 2	0.00	0.07	0.01	-0.02	1.14	0.08	0.11	0.01	0.05	0.01	0.00	0.01	0.00	0.01	0.00	0.01
MEAN	**0.00**	**0.06**	**0.01**	**-0.02**	**1.15**	**0.08**	**0.11**	**0.01**	**0.05**	**0.01**	**0.00**	**0.01**	**0.00**	**0.01**	**0.00**	**0.01**
SG -43 1	-0.01	0.01	-0.02	0.00	1.04	0.07	0.10	0.01	0.05	0.01	0.00	0.01	0.00	0.01	0.00	0.01
SG -43 2	-0.01	0.01	-0.02	0.00	1.06	0.06	0.10	0.01	0.04	0.01	0.00	0.01	0.00	0.01	0.00	0.01
MEAN	**-0.01**	**0.01**	**-0.02**	**0.00**	**1.05**	**0.07**	**0.10**	**0.01**	**0.05**	**0.01**	**0.00**	**0.01**	**0.00**	**0.01**	**0.00**	**0.01**

Table A4.3 (cont.). Trace element geochemistry of silica gel measured with ICP-OES.

Sample	169Tm ppm	172Yb ppm	175Lu ppm	178Hf ppm	181Ta ppm	182W ppm	208Pb ppm	232Th ppm	238U ppm
SG-28 1	-0.05	-0.08	-0.01	0.09	-1.60	-0.07	0.13	-0.38	-0.01
SG-28 2	-0.05	-0.08	-0.01	0.12	-1.38	-0.06	0.36	-0.38	-0.01
SG-28 3	0.04	0.02	0.03	0.68	-1.01	0.03	0.30	-0.04	0.00
SG-28 4	0.04	0.02	0.02	0.69	-0.72	0.05	0.56	-0.05	-0.01
SG-28 5	-0.03	-0.02	0.00	0.66	-1.16	-0.04	0.19	-0.07	0.00
SG-28 6	-0.03	-0.02	0.00	0.70	-0.59	0.00	0.53	-0.09	-0.01
MEAN	**-0.01**	**-0.03**	**0.01**	**0.49**	**-1.08**	**-0.01**	**0.35**	**-0.17**	**-0.01**
SG-40 1	0.00	0.00	0.00	0.47	-0.31	--	0.20	0.01	0.00
SG-40 2	0.00	0.00	0.00	0.51	-0.28	--	0.22	0.02	0.00
MEAN	**0.00**	**0.00**	**0.00**	**0.49**	**-0.29**	--	**0.21**	**0.01**	**0.00**
SG-41 1	0.00	0.00	0.00	0.33	-1.50	--	0.21	-0.06	-0.02
SG-41 2	0.00	0.00	0.00	0.33	-1.49	--	0.21	-0.06	-0.02
MEAN	**0.00**	**0.00**	**0.00**	**0.33**	**-1.49**	--	**0.21**	**-0.06**	**-0.02**
SG-42 1	0.00	0.00	0.00	0.42	-0.87	--	0.21	-0.05	-0.04
SG-42 2	0.00	0.00	0.00	0.45	-0.89	--	0.21	-0.05	-0.04
MEAN	**0.00**	**0.00**	**0.00**	**0.43**	**-0.88**	--	**0.21**	**-0.05**	**-0.04**
SG-43 1	0.00	0.00	0.00	0.37	-0.46	--	0.20	-0.06	-0.06
SG-43 2	0.00	0.00	0.00	0.39	-0.45	--	0.21	-0.06	-0.06
MEAN	**0.00**	**0.00**	**0.00**	**0.38**	**-0.46**	--	**0.20**	**-0.06**	**-0.06**

Table A4.4. EPMA analysis of reference materials with the JEOL-8900 at UMN.

Sample name	Expected Ti (µg/g)*	Ti-Kα (µg/g) CH1_PETJ	% error	Ti-Kα (µg/g) CH2_PETJ	% error	Ti-Kα (µg/g) CH4_PETJ	% error	Ti-Kα (µg/g) CH5_LiFH	% error	Ti (µg/g) AGGREGATED	% error	Si-Kβ (wt%) CH3_TAP	Total (wt%)
QTiP-38-1a	380	395.0	*4*	245.8	*-35*	242.6	*-36*	342.9	*-10*	277.6	*-27*	46.8	100.29
QTiP-38-1b	380	458.2	*21*	317.6	*-16*	266.0	*-30*	385.5	*1*	319.8	*-16*	46.0	98.58
QTiP-38-1c	380	316.7	*-17*	211.9	*-44*	224.2	*-41*	334.6	*-12*	253.9	*-33*	47.5	101.82
QTiP-14-1a	100	184.9	*85*	0.0	--	0.0	--	92.9	*-7*	23.7	*-76*	44.4	94.99
QTiP-14-1b	100	102.5	*2*	0.0	--	0.0	--	76.8	*-23*	9.9	*-90*	44.5	95.13
QTiP-14-1c	100	51.4	*-49*	0.0	--	0.0	--	77.7	*-22*	10.7	*-89*	44.3	94.73
QTiP-07-1a	18	19.3	*7*	0.0	--	0.0	--	15.4	*-14*	0.0	--	46.5	99.50
QTiP-07-1b	18	33.4	*86*	0.0	--	0.0	--	26.9	*49*	0.0	--	45.8	97.98
QTiP-07-1c	18	0.0	--	0.0	--	0.0	--	15.6	*-13*	0.0	--	45.6	97.50
QTiP-39-1a	764	820.1	*7*	649.3	*-15*	549.2	*-28*	680.9	*-11*	621.8	*-19*	44.6	95.83
QTiP-39-1b	764	847.2	*11*	667.3	*-13*	529.6	*-31*	679.7	*-11*	618.9	*-19*	43.9	94.35
QTiP-39-1c	764	905.9	*19*	683.2	*-11*	539.7	*-29*	690.5	*-10*	633.9	*-17*	44.3	95.29
Herk1-1	0.003	0.0	--	0.0	--	0.0	--	0.0	--	0.0	--	46.9	100.33
Herk2-1	0.003	0.0	--	0.0	--	0.0	--	0.0	--	0.0	--	47.0	100.53
Herk3-1	0.003	0.0	--	0.0	--	0.0	--	0.0	--	0.0	--	48.9	104.52
NIST614-1a	3.4	0.0		0.0		0.0		0.0		0.0		34.2	73.09
NIST614-1b	3.4	0.0		0.0		0.0		0.0		0.0		35.6	76.08
NIST612-1a	44	0.0		0.0		0.0		0.0		0.0		37.2	79.55
NIST612-1b	44	0.0		0.0		0.0		0.0		0.0		37.2	79.55
NIST610-1a	434	649.1		435.4		323.6		476.3		408.8		33.5	71.88
NIST610-1b	434	656.0		459.0		331.8		478.8		419.1		33.8	72.53
----analyze unknown samples for ~60 h----													
QTiP-38-2a	380	420.7	*11*	335.9	*-12*	382.5	*1*	374.1	*-2*	370.6	*-2*	47.4	101.66
QTiP-38-2b	380	354.7	*-7*	364.0	*-4*	396.4	*4*	379.5	*0*	380.0	*0*	47.4	101.63
QTiP-14-2a	100	115.4	*15*	75.1	*-25*	98.7	*-1*	92.5	*-8*	92.4	*-8*	47.2	101.06
QTiP-14-2b	100	119.0	*19*	50.8	*-49*	105.9	*6*	97.6	*-2*	91.4	*-9*	47.2	100.94
QTiP-07-2a	18	0.0	--	0.0	--	20.3	*13*	22.2	*23*	8.2	*-54*	47.4	101.40
QTiP-07-2b	18	0.0	--	5.6	*-69*	31.9	*77*	10.9	*-39*	15.9	*-12*	47.3	101.23
QTiP-39-2a	764	788.5	*3*	640.1	*-16*	716.3	*-6*	706.8	*-7*	698.2	*-9*	48.4	103.98
QTiP-39-2b	764	668.8	*-12*	617.0	*-19*	705.4	*-8*	693.1	*-9*	676.1	*-12*	48.4	103.98
NIST610-2a	434	580		402.5		481.8		473.2		465.9		33.6	72.21
NIST610-2b	434	528.5		441.9		502.2		478.5		482		35.19	75.61
NIST612-2a	44	24.8		24		48.5		40.1		38.8		37.77	80.83
NIST612-2b	44	0		22.5		53.3		46.5		39.5		38.3	81.97

*QTiP values reported by Thomas et al. (2010); Herkimer values reported by Kidder et al. (2013); NIST values reported by Jochum et al. (2011)

Appendix 4

Table A4.5. EPMA analysis of reference materials with the Cameca SX-100 at RPI.

comment	Sample Name	Si (atomic)	Total	Ti (atomic)	Ti (µg/g)	Expected Ti (µg/g)*	% error
session 1_start	QTiP-07a	46.1875	98.8170	0.0028	27.9	18	*-55*
	QTiP-07b	45.9831	98.3801	0.0031	31.1	18	*-73*
	QTiP-14a	46.5340	99.5672	0.0082	81.8	100	*18*
	QTiP-14b	46.6954	99.9145	0.0094	94.0	100	*6*
	QTiP-39a	45.5724	97.6207	0.0746	745.6	764	*2*
	QTiP-39b	46.2782	99.1278	0.0727	727.5	764	*5*
	Herk1a	46.7650	100.0483	0.0004	3.7	0.003	--
	Herk1b	46.9981	100.5472	0.0005	4.8	0.003	--
	Herk2a	46.4244	99.3189	-0.0005	-4.8	0.003	--
	Herk2b	47.6851	102.0156	-0.0011	-10.5	0.003	--
	Herk3a	46.7111	99.9332	0.0005	4.7	0.003	--
	Herk3b	46.4652	99.4056	-0.0012	-11.7	0.003	--
	QTiP-38a	46.3983	99.3230	0.0358	358.4	380	*6*
	QTiP-38b	46.2938	99.1014	0.0369	369.0	380	*3*

comment	Sample Name	SiO2 (wt%)	Total	TiO2 (wt%)	Ti (µg/g)	Expected Ti (µg/g)*	% error
session2_start	QTIP 38	98.5930	98.6499	0.0568	324.5	380	*15*
	QTIP 38	98.7528	98.8103	0.0575	328.6	380	*14*
	QTIP 38	98.7111	98.7707	0.0596	340.2	380	*10*
	QTIP 07	95.4322	95.4340	0.0018	10.4	18	*42*
	QTIP 14	98.6708	98.6848	0.0140	79.7	100	*20*
session2_end	QTIP 38	98.8091	98.8665	0.0574	327.8	380	*14*
	QTIP 38	98.2467	98.3045	0.0578	330.2	380	*13*
	QTIP 38	98.6080	98.6667	0.0587	335.4	380	*12*
	QTIP 07	95.0173	95.0195	0.0021	12.2	10	*-22*
	QTIP 07	95.2692	95.2714	0.0022	12.3	10	*-23*
	QTIP 07	94.7593	94.7607	0.0014	7.7	10	*23*
	QTIP 14	97.7488	97.7629	0.0141	80.5	100	*19*
	QTIP 14	97.8629	97.8779	0.0150	85.8	100	*14*
	QTIP 14	98.3794	98.3938	0.0143	81.9	100	*18*
	QTIP 38	98.1596	98.2174	0.0578	330.0	380	*13*
session3_start	QTIP 38	97.7039	97.7607	0.0568	324.4	380	*15*
	QTIP 38	97.9782	98.0355	0.0573	327.2	380	*14*
	QTIP 38	98.9954	99.0533	0.0579	330.8	380	*13*
	QTIP 07	95.2856	95.2873	0.0017	9.6	18	*47*
	QTIP 07	94.7424	94.7442	0.0018	10.4	18	*42*
	QTIP 07	93.6175	93.6190	0.0015	8.4	18	*53*
	QTIP 14	96.3435	96.3577	0.0142	81.0	100	*19*
	QTIP 14	98.5743	98.5885	0.0142	81.0	100	*19*
	QTIP 14	98.4598	98.4738	0.0140	79.8	100	*20*
session3_end	QTIP 38	98.0744	98.1353	0.0609	347.9	380	*8*
	QTIP 38	97.7607	97.8185	0.0578	330.3	380	*13*
	QTIP 38	98.1084	98.1656	0.0572	326.8	380	*14*
	QTIP 38	98.5428	98.6018	0.0590	336.9	380	*11*
	QTIP 07	93.7337	93.7354	0.0017	9.9	18	*45*
	QTIP 14	96.8543	96.8684	0.0141	80.6	100	*19*

*QTiP values reported by Thomas et al. (2010); Herkimer values reported by Kidder et al. (2013)

Appendix 4

Table A4.6. SIMS analysis of reference materials.

File Name	Standard	48Ti/30Si	1 sigma	40Ca/30Si	1 sigma	48Ti/30Si corrected	Ti (ppm)	Expected Ti (µg/g)*	% error
nst0312	QTiP_38	2.85E-02	2.22E-03	1.86E-03	1.92E-04	2.85E-02	365.7	380	*3.8*
nst0312_1	QTiP_38	3.00E-02	1.83E-04	7.34E-03	1.69E-03	3.00E-02	384.8	380	*-1.3*
nst0312_2	QTiP_38	2.96E-02	9.75E-05	6.03E-03	1.27E-03	2.96E-02	379.7	380	*0.1*
nst0312_3	QTiP_38	3.04E-02	1.81E-04	2.07E-03	2.33E-04	3.04E-02	390.1	380	*-2.7*
nst0312_4	QTiP_38	2.94E-02	1.23E-04	1.31E-03	1.65E-04	2.94E-02	376.9	380	*0.8*
nst0312_5	QTiP_14	8.96E-03	8.39E-05	3.80E-03	5.19E-04	8.95E-03	114.9	100	*-14.9*
nst0312_6	QTiP_14	8.11E-03	4.79E-05	3.00E-03	3.80E-04	8.10E-03	104.0	100	*-4.0*
nst0312_7	QTiP_14	8.27E-03	9.51E-05	2.82E-03	3.80E-04	8.26E-03	106.0	100	*-6.0*
nst0312_8	QTiP_14	8.76E-03	5.11E-05	3.76E-03	5.65E-04	8.75E-03	112.3	100	*-12.3*
nst0312_9	QTiP_7	1.17E-03	1.64E-05	2.99E-03	3.74E-04	1.16E-03	14.9	19.5	*23.7*
nst0312_10	QTiP_7	1.15E-03	2.25E-05	4.23E-03	5.92E-04	1.14E-03	14.7	19.5	*24.7*
nst0312_11	QTiP_7	1.18E-03	1.65E-05	2.79E-03	4.49E-04	1.18E-03	15.1	19.5	*22.4*
nst0312_12	QTiP_7	1.26E-03	2.63E-05	2.86E-03	3.98E-04	1.26E-03	16.1	19.5	*17.4*

*as reported by Thomas et al. (2010)

Table A4.7. LA-ICP-MS analysis of reference materials.

sample name	Duration (s)	Si29 CPS	Si29 CPS 2SE	Ti (µg/g) m49	Ti (µg/g) m49 2SE	Expected Ti (µg/g)*	%error
NIST610_1	22.179	2.255E+06	4.3E+04	429.4	4.3	452	-5.0
NIST610_2	18.583	2.097E+06	3.1E+04	440.6	4.8	452	-2.5
NIST610_3	32.434	2.655E+06	4.7E+04	431.8	3.6	452	-4.5
NIST610_4	25.947	2.425E+06	3.3E+04	431.8	3.7	452	-4.5
NIST610_5	23.978	2.488E+06	5.0E+04	428.4	4.3	452	-5.2
NIST610_6	26.376	1.833E+06	5.4E+04	438.0	4.2	452	-3.1
NIST610_7	20.981	2.045E+06	2.7E+04	441.7	4.5	452	-2.3
NIST610_8	23.378	1.792E+06	3.9E+04	445.2	4.7	452	-1.5
NIST610_9	22.179	2.152E+06	2.4E+04	436.6	4.7	452	-3.4
NIST610_10	23.978	2.177E+06	5.3E+04	425.4	4.7	452	-5.9
NIST610_11	22.779	2.126E+06	4.5E+04	439.1	4.4	452	-2.9
NIST610_12	19.782	1.695E+06	2.7E+04	443.8	4.8	452	-1.8
NIST610_13	22.779	2.002E+06	2.5E+04	432.3	4.2	452	-4.4
NIST610_14	25.177	1.207E+06	3.6E+04	433.7	5.3	452	-4.0
NIST610_15	19.782	8.480E+05	2.8E+04	418.8	6.7	452	-7.3
NIST612_1	24.577	3.019E+06	2.2E+04	36.65	0.92	44.0	-16.7
NIST612_2	23.378	3.125E+06	4.2E+04	36.95	0.93	44.0	-16.0
NIST612_3	26.376	3.185E+06	4.3E+04	37.65	0.84	44.0	-14.4
NIST612_4	26.975	3.222E+06	4.8E+04	38.09	0.87	44.0	-13.4
NIST612_5	23.378	3.543E+06	7.0E+04	36.29	0.89	44.0	-17.5
NIST612_6	25.177	2.861E+06	6.3E+04	39.00	1.1	44.0	-11.4
NIST612_7	23.378	2.958E+06	5.9E+04	37.20	1	44.0	-15.5
NIST612_8	28.773	3.128E+06	3.7E+04	37.72	0.83	44.0	-14.3
NIST612_9	26.376	2.926E+06	3.3E+04	37.98	0.87	44.0	-13.7
NIST612_10	27.574	2.699E+06	3.7E+04	37.54	0.85	44.0	-14.7
NIST612_11	24.577	2.642E+06	2.1E+04	38.36	0.95	44.0	-12.8
NIST612_12	26.376	2.390E+06	2.7E+04	37.49	0.93	44.0	-14.8
NIST612_13	21.58	2.268E+06	1.4E+04	37.10	1.1	44.0	-15.7
NIST612_14	28.773	2.570E+06	3.8E+04	38.07	0.92	44.0	-13.5
NIST612_15	25.776	2.003E+06	2.8E+04	37.20	1.1	44.0	-15.5

* as reported by Jochum et al. (2011)

Appendix 4

Table A4.8. Results of EPMA of 3-layered reference material – HPS-3.

Point#	Sample name	Layer name	Si wt% atomic	Total	Ti wt% atomic	Ti ppm	Doped Ti ppm
1	PI-1761a-1	HPS-3C	46.4334	99.8296	0.17656	1766	2273
3	PI-1761a-3	HPS-3C	46.2871	99.6715	0.23220	2322	2273
4	PI-1761a-4	HPS-3C	46.1995	99.3543	0.18554	1855	2273
5	PI-1761a-5	HPS-3C	46.0868	99.0656	0.16844	1684	2273
6	PI-1761a-6	HPS-3C	45.9624	98.7471	0.14965	1496	2273
8	PI-1761a-8	HPS-3C	46.2705	99.5218	0.19116	1912	2273
9	PI-1761a-9	HPS-3C	46.0686	99.1642	0.21787	2179	2273
10	PI-1761a-10	HPS-3C	45.9352	99.0880	0.29313	2931	2273
11	PI-1761a-11	HPS-3C	45.7801	98.5253	0.21010	2101	2273
12	PI-1761a-12	HPS-3C	46.0285	98.8795	0.14637	1464	2273
13	PI-1761a-13	HPS-3C	45.9898	98.8569	0.16808	1681	2273
14	PI-1761a-14	HPS-3C	46.1197	99.2012	0.19188	1919	2273
15	PI-1761a-15	HPS-3C	45.8474	98.5850	0.17985	1798	2273
16	PI-1761a-16	HPS-3C	45.9404	98.7784	0.17778	1778	2273
17	PI-1761a-17	HPS-3C	45.7353	98.5803	0.26434	2643	2273
18	PI-1761a-18	HPS-3C	45.6941	98.4845	0.26159	2616	2273
19	PI-1761a-19	HPS-3C	45.2878	97.5986	0.25560	2556	2273
20	PI-1761a-20	HPS-3C	45.8598	98.6518	0.19431	1943	2273
21	PI-1761a-21	HPS-3C	45.6817	98.4828	0.27045	2705	2273
22	PI-1761a-22	HPS-3C	45.3070	97.4164	0.17534	1753	2273
23	PI-1761a-23	HPS-3C	46.1867	99.2438	0.15565	1556	2273
24	PI-1761a-24	HPS-3C	45.7268	98.2364	0.14724	1472	2273
25	PI-1761a-25	HPS-3C	45.4122	97.6928	0.19377	1938	2273
26	PI-1761a-26	HPS-3C	45.5822	98.0806	0.20240	2024	2273
27	PI-1761a-27	HPS-3C	46.2236	99.4349	0.19600	1960	2273
28	PI-1761a-28	HPS-3C	45.8384	98.6317	0.20355	2036	2273
29	PI-1761a-29	HPS-3C	45.8236	98.5961	0.20207	2021	2273
30	PI-1761a-30	HPS-3C	45.2219	97.2486	0.18047	1805	2273
31	PI-1761a-31	HPS-3C	45.5928	98.1200	0.20847	2085	2273
32	PI-1761a-32	HPS-3C	45.7802	98.2927	0.12643	1264	2273
33	PI-1761a-33	HPS-3C	45.8880	98.9012	0.26225	2623	2273
34	PI-1761a-34	HPS-3C	45.6873	98.2961	0.19905	1991	2273
35	PI-1761a-35	HPS-3C	45.4622	97.6529	0.14096	1410	2273
36	PI-1761a-36	HPS-3C	45.6079	98.0462	0.17035	1704	2273
37	PI-1761a-37	HPS-3C	45.6490	98.2309	0.20507	2051	2273
38	PI-1761a-38	HPS-3C	45.1241	97.3569	0.29459	2946	2273
39	PI-1761a-39	HPS-3C	46.3770	99.7439	0.18911	1891	2273
40	PI-1761a-40	HPS-3C	45.4182	97.9313	0.27485	2749	2273
41	PI-1761a-41	HPS-3C	45.5496	97.9574	0.18324	1832	2273
42	PI-1761a-42	HPS-3C	46.1875	99.3069	0.17772	1777	2273
43	PI-1761a-43	HPS-3C	45.5882	98.0256	0.17807	1781	2273
44	PI-1761a-44	HPS-3C	45.9091	98.6775	0.16566	1657	2273
45	PI-1761a-45	HPS-3C	45.5582	98.0396	0.20613	2061	2273

Table A4.8 (cont.). Results of EPMA of 3-layered reference material – HPS-3.

46	PI-1761a-46	HPS-3C	45.6602	98.2151	0.19079	1908	2273
47	PI-1761a-47	HPS-3C	46.0418	99.0749	0.20636	2064	2273
48	PI-1761a-48	HPS-3C	45.9256	98.6905	0.15755	1576	2273
49	PI-1761a-49	HPS-3C	46.2196	99.4951	0.22069	2207	2273
50	PI-1761a-50	HPS-3C	45.9479	98.7087	0.14700	1470	2273
52	PI-1761a-52	HPS-3C	45.7078	98.2922	0.18193	1819	2273
53	PI-1761a-53	HPS-3C	45.2988	97.7498	0.30147	3015	2273
54	PI-1761a-54	HPS-3C	45.4833	97.8909	0.21027	2103	2273
55	PI-1761a-55	HPS-3C	45.5200	97.7448	0.12961	1296	2273
56	PI-1761a-56	HPS-3C	45.4421	97.8216	0.21706	2171	2273
57	PI-1761a-57	HPS-3C	45.8394	98.5172	0.16157	1616	2273
58	PI-1761a-58	HPS-3C	45.7306	98.3690	0.19196	1920	2273
59	PI-1761a-59	HPS-3C	45.4553	97.6435	0.14289	1429	2273
60	PI-1761a-60	HPS-3C	45.3361	97.5009	0.18331	1833	2273
61	PI-1761a-61	HPS-3C	45.6465	98.0937	0.15772	1577	2273
62	PI-1761a-62	HPS-3C	45.6273	97.9549	0.12263	1226	2273
63	PI-1761a-63	HPS-3C	45.7179	98.2880	0.17265	1726	2273
64	PI-1761a-64	HPS-3C	45.9946	99.0584	0.23673	2367	2273
65	PI-1761a-65	HPS-3C	45.8944	98.5776	0.14103	1410	2273
66	PI-1761a-66	HPS-3C	45.9155	98.6972	0.16778	1678	2273
67	PI-1761a-67	HPS-3C	45.4065	97.7117	0.20498	2050	2273
68	PI-1761a-68	HPS-3C	45.7610	98.6084	0.25462	2546	2273
69	PI-1761a-69	HPS-3C	45.6639	98.2604	0.20424	2042	2273
70	PI-1761a-70	HPS-3C	45.5512	98.0472	0.21425	2142	2273
71	PI-1761a-71	HPS-3C	45.6408	98.0984	0.16376	1638	2273
72	PI-1761a-72	HPS-3C	45.8047	98.3627	0.13273	1327	2273
74	PI-1761a-74	HPS-3C	45.8476	98.5405	0.16367	1637	2273
75	PI-1761a-75	HPS-3C	45.5176	98.1545	0.27871	2787	2273
76	PI-1761a-76	HPS-3C	46.0072	99.0073	0.20870	2087	2273
77	PI-1761a-77	HPS-3C	45.4725	97.9042	0.22340	2234	2273
78	PI-1761a-78	HPS-3C	45.5142	97.8352	0.16655	1665	2273
79	PI-1761a-79	HPS-3C	45.6927	98.2461	0.17698	1770	2273
80	PI-1761a-80	HPS-3C	45.8086	98.5835	0.20909	2091	2273
132	PI-1761b-2	HPS-3C	44.4309	95.6150	0.20150	2015	2273
133	PI-1761b-3	HPS-3C	45.3058	97.6084	0.24525	2452	2273
134	PI-1761b-4	HPS-3C	45.4993	97.8386	0.17925	1792	2273
135	PI-1761b-5	HPS-3C	46.7850	100.5453	0.16342	1634	2273
136	PI-1761b-6	HPS-3C	45.1283	96.9567	0.14753	1475	2273
137	PI-1761b-7	HPS-3C	45.1725	97.2134	0.20579	2058	2273
138	PI-1761b-8	HPS-3C	45.3750	97.7727	0.25108	2511	2273
139	PI-1761b-9	HPS-3C	45.6414	98.0996	0.16373	1637	2273
140	PI-1761b-10	HPS-3C	45.7076	98.3084	0.18786	1879	2273
141	PI-1761b-11	HPS-3C	45.1003	97.2280	0.26656	2666	2273
142	PI-1761b-12	HPS-3C	45.8255	98.6626	0.22454	2245	2273
143	PI-1761b-13	HPS-3C	45.3459	97.5593	0.19673	1967	2273

Table A4.8 (cont.). Results of EPMA of 3-layered reference material – HPS-3.

144	PI-1761b-14	HPS-3C	45.0622	96.9482	0.19526	1953	2273
145	PI-1761b-15	HPS-3C	45.2169	97.3932	0.23626	2363	2273
146	PI-1761b-16	HPS-3C	45.7515	98.4642	0.21016	2102	2273
147	PI-1761b-17	HPS-3C	45.3974	97.4923	0.13306	1331	2273
148	PI-1761b-18	HPS-3C	45.8544	98.7123	0.22014	2201	2273
149	PI-1761b-19	HPS-3C	45.6058	97.9822	0.14892	1489	2273
150	PI-1761b-20	HPS-3C	46.2524	99.1616	0.07568	757	2273
151	PI-1761b-21	HPS-3C	45.0749	97.0505	0.22226	2223	2273
152	PI-1761b-22	HPS-3C	44.5905	95.6573	0.09401	940	2273
153	PI-1761b-23	HPS-3C	45.6817	98.3754	0.23183	2318	2273
154	PI-1761b-24	HPS-3C	45.6443	98.2147	0.20286	2029	2273
155	PI-1761b-25	HPS-3C	45.9153	98.6922	0.16613	1661	2273
156	PI-1761b-26	HPS-3C	45.5722	98.0659	0.20481	2048	2273
157	PI-1761b-27	HPS-3C	45.5130	97.9202	0.19796	1980	2273
158	PI-1761b-28	HPS-3C	41.0465	88.3553	0.19464	1946	2273
159	PI-1761b-29	HPS-3C	45.7260	98.2911	0.16750	1675	2273
160	PI-1761b-30	HPS-3C	45.6025	98.2482	0.24707	2471	2273
161	PI-1761b-31	HPS-3C	45.7188	98.6480	0.30131	3013	2273
162	PI-1761b-32	HPS-3C	45.2976	97.5705	0.23790	2379	2273
163	PI-1761b-33	HPS-3C	46.0714	99.0105	0.16051	1605	2273
165	PI-1761b-35	HPS-3C	45.5206	97.6861	0.10803	1080	2273
166	PI-1761b-36	HPS-3C	45.8148	98.6648	0.23352	2335	2273
167	PI-1761b-37	HPS-3C	45.6604	98.5327	0.30482	3048	2273
168	PI-1761b-38	HPS-3C	45.8902	98.8749	0.25107	2511	2273
169	PI-1761b-39	HPS-3C	45.8731	98.4082	0.09652	965	2273
170	PI-1761b-40	HPS-3C	45.6535	98.2030	0.19158	1916	2273
171	PI-1761b-41	HPS-3C	45.5512	98.0509	0.21560	2156	2273
172	PI-1761b-42	HPS-3C	46.1670	99.2304	0.16603	1660	2273
173	PI-1761b-43	HPS-3C	45.8597	98.4931	0.13734	1373	2273
174	PI-1761b-44	HPS-3A	46.4442	99.4370	0.02715	272	113
176	PI-1761b-46	HPS-3A	46.5518	99.6136	0.00782	78	113
177	PI-1761b-47	HPS-3A	45.9071	98.2338	0.00767	77	113
178	PI-1761b-48	HPS-3A	46.4431	99.3804	0.00764	76	113
179	PI-1761b-49	HPS-3A	46.3030	99.0963	0.01324	132	113
180	PI-1761b-50	HPS-3A	46.2398	98.9453	0.00758	76	113
181	PI-1761b-51	HPS-3A	46.3231	99.1220	0.00702	70	113
182	PI-1761b-52	HPS-3A	45.6246	97.6271	0.00685	69	113
183	PI-1761b-53	HPS-3A	46.2603	98.9857	0.00636	64	113
184	PI-1761b-54	HPS-3A	46.2868	99.0415	0.00603	60	113
185	PI-1761b-55	HPS-3A	46.1706	98.7935	0.00620	62	113
186	PI-1761b-56	HPS-3A	46.0559	98.5518	0.00754	75	113
187	PI-1761b-57	HPS-3A	45.9278	98.2740	0.00618	62	113
188	PI-1761b-58	HPS-3A	46.0834	98.6081	0.00662	66	113
189	PI-1761b-59	HPS-3A	46.4422	99.3748	0.00630	63	113
190	PI-1761b-60	HPS-3A	46.2355	98.9318	0.00606	61	113

Table A4.8 (cont.). Results of EPMA of 3-layered reference material – HPS-3.

191	PI-1761b-61	HPS-3A	46.3444	99.1678	0.00710	71	113
192	PI-1761b-62	HPS-3A	45.9148	98.2480	0.00687	69	113
193	PI-1761b-63	HPS-3A	45.9189	98.2552	0.00634	63	113
194	PI-1761b-64	HPS-3A	46.3975	99.2793	0.00634	63	113
195	PI-1761b-65	HPS-3A	45.9134	98.2437	0.00636	64	113
196	PI-1761b-66	HPS-3A	46.0633	98.5660	0.00698	70	113
197	PI-1761b-67	HPS-3A	41.6013	89.0173	0.00595	59	113
198	PI-1761b-68	HPS-3A	44.6490	95.5532	0.01163	116	113
199	PI-1761b-69	HPS-3B	46.1842	99.0042	0.07154	715	802
200	PI-1761b-70	HPS-3B	46.2343	99.1475	0.08451	845	802
201	PI-1761b-71	HPS-3B	45.9405	98.5512	0.09604	960	802
202	PI-1761b-72	HPS-3B	46.0449	98.7535	0.08848	885	802
203	PI-1761b-73	HPS-3B	46.2361	99.1542	0.08550	855	802
204	PI-1761b-74	HPS-3B	45.8258	98.3040	0.09540	954	802
205	PI-1761b-75	HPS-3B	45.4437	97.3934	0.06196	620	802
206	PI-1761b-76	HPS-3B	45.9132	98.4466	0.07944	794	802
207	PI-1761b-77	HPS-3B	44.0594	94.5127	0.09101	910	802
208	PI-1761b-78	HPS-3B	46.0056	98.6169	0.06966	697	802
209	PI-1761b-79	HPS-3B	46.0038	98.7190	0.10769	1077	802
210	PI-1761b-80	HPS-3B	41.5187	89.0491	0.08091	809	802
211	PI-1761b-81	HPS-3B	45.8885	98.3941	0.07960	796	802
212	PI-1761b-82	HPS-3B	46.0728	98.8047	0.08548	855	802
213	PI-1761b-83	HPS-3B	46.1447	98.9353	0.07714	771	802
215	PI-1761b-85	HPS-3B	46.1246	98.9248	0.08878	888	802
216	PI-1761b-86	HPS-3B	46.3971	99.4876	0.08153	815	802
217	PI-1761b-87	HPS-3B	45.9121	98.4722	0.08948	895	802
218	PI-1761b-88	HPS-3B	46.0124	98.6829	0.08809	881	802
219	PI-1761b-89	HPS-3B	45.9637	98.5612	0.08181	818	802
220	PI-1761b-90	HPS-3B	46.2522	99.1865	0.08475	848	802
221	PI-1761b-91	HPS-3B	45.9535	98.5475	0.08476	848	802
222	PI-1761c-1	HPS-3C	44.8952	96.5274	0.17245	1724	2273
223	PI-1761c-2	HPS-3C	45.4008	97.5862	0.16425	1642	2273
225	PI-1761c-4	HPS-3C	45.6092	98.0683	0.17724	1772	2273
226	PI-1761c-5	HPS-3C	45.5121	97.8779	0.18351	1835	2273
227	PI-1761c-6	HPS-3C	45.7224	98.3533	0.19265	1926	2273
228	PI-1761c-7	HPS-3C	41.5234	89.2589	0.15273	1527	2273
229	PI-1761c-8	HPS-3C	43.6228	93.8007	0.17079	1708	2273
230	PI-1761c-9	HPS-3C	45.7183	98.3142	0.18176	1818	2273
232	PI-1761c-11	HPS-3C	46.0121	99.1132	0.24296	2430	2273
233	PI-1761c-12	HPS-3C	45.7306	98.3667	0.19116	1912	2273
234	PI-1761c-13	HPS-3C	40.0544	86.2483	0.20015	2002	2273
235	PI-1761c-14	HPS-3C	45.3436	97.5300	0.18804	1880	2273
236	PI-1761c-15	HPS-3C	44.4432	95.6613	0.20871	2087	2273
237	PI-1761c-16	HPS-3C	45.7223	98.3805	0.20247	2025	2273
238	PI-1761c-17	HPS-3C	45.2593	97.3731	0.19644	1964	2273

Table A4.8 (cont.). Results of EPMA of 3-layered reference material – HPS-3.

239	PI-1761c-18	HPS-3C	46.1709	99.0034	0.08143	814	2273
240	PI-1761c-19	HPS-3C	45.4849	97.7358	0.15333	1533	2273
241	PI-1761c-20	HPS-3C	45.3587	97.7872	0.26882	2688	2273
242	PI-1761c-21	HPS-3C	45.6694	98.1384	0.15620	1562	2273
243	PI-1761c-22	HPS-3C	46.4070	99.6181	0.12080	1208	2273
244	PI-1761c-23	HPS-3C	45.7062	98.2728	0.17617	1762	2273
245	PI-1761c-24	HPS-3C	45.5798	98.1498	0.22918	2292	2273
246	PI-1761c-25	HPS-3C	45.4553	97.8186	0.20587	2059	2273
247	PI-1761c-26	HPS-3A	45.9679	98.3738	0.01123	112	113
248	PI-1761c-27	HPS-3A	45.8001	98.0046	0.00756	76	113
249	PI-1761c-28	HPS-3A	45.3287	96.9988	0.00851	85	113
250	PI-1761c-29	HPS-3A	45.3708	97.0837	0.00666	67	113
251	PI-1761c-30	HPS-3A	45.6853	97.7571	0.00692	69	113
252	PI-1761c-31	HPS-3A	45.9471	98.3171	0.00686	69	113
253	PI-1761c-32	HPS-3A	45.9928	98.4117	0.00574	57	113
254	PI-1761c-33	HPS-3A	43.3341	92.7268	0.00684	68	113
255	PI-1761c-34	HPS-3A	46.4310	99.3528	0.00707	71	113
256	PI-1761c-35	HPS-3A	45.8200	98.0440	0.00645	64	113
257	PI-1761c-36	HPS-3A	46.3575	99.1947	0.00671	67	113
258	PI-1761c-37	HPS-3A	45.9023	98.2222	0.00721	72	113
259	PI-1761c-38	HPS-3A	46.5456	99.5964	0.00645	64	113
260	PI-1761c-39	HPS-3B	45.9994	98.5420	0.04750	475	802
261	PI-1761c-40	HPS-3B	45.8089	98.2021	0.07182	718	802
262	PI-1761c-41	HPS-3B	41.2839	88.4418	0.04318	432	802
263	PI-1761c-42	HPS-3B	45.9547	98.5200	0.07398	740	802
264	PI-1761c-43	HPS-3B	41.9952	90.0270	0.06593	659	802
265	PI-1761c-44	HPS-3B	46.2860	99.2448	0.07976	798	802
266	PI-1761c-45	HPS-3B	46.0747	98.8515	0.10079	1008	802
267	PI-1761c-46	HPS-3B	45.7036	98.0743	0.10684	1068	802
268	PI-1761c-47	HPS-3B	45.9639	98.6142	0.10072	1007	802
269	PI-1761c-48	HPS-3B	45.8131	98.2900	0.10018	1002	802
270	PI-1761c-49	HPS-3B	46.0517	98.7350	0.07662	766	802
271	PI-1761c-50	HPS-3B	45.7063	98.0295	0.08861	886	802
272	PI-1761c-51	HPS-3B	45.7978	98.1659	0.06734	673	802
273	PI-1761c-52	HPS-3B	45.8419	98.3428	0.09697	970	802
274	PI-1761c-53	HPS-3B	45.5132	97.5812	0.07601	760	802
275	PI-1761d-1	HPS-3B	44.8687	96.2165	0.08111	811	802
276	PI-1761d-2	HPS-3B	45.7644	98.2078	0.10809	1081	802
277	PI-1761d-3	HPS-3B	39.3837	84.4368	0.06486	649	802
278	PI-1761d-4	HPS-3B	45.9732	98.6422	0.10365	1037	802
279	PI-1761d-5	HPS-3B	45.1803	96.8781	0.07929	793	802
280	PI-1761d-6	HPS-3B	45.5742	97.7536	0.09102	910	802
281	PI-1761d-7	HPS-3B	46.7987	100.3359	0.07767	777	802
282	PI-1761d-8	HPS-3B	45.9960	98.6938	0.10463	1046	802
283	PI-1761d-9	HPS-3B	46.1352	98.8313	0.04702	470	802

Table A4.8 (cont.). Results of EPMA of 3-layered reference material – HPS-3.

284	PI-1761d-10	HPS-3A	46.2512	98.9658	0.00616	62	113
285	PI-1761d-11	HPS-3A	46.4347	99.3596	0.00661	66	113
286	PI-1761d-12	HPS-3A	45.8836	98.1798	0.00636	64	113
287	PI-1761d-13	HPS-3A	45.8830	98.1791	0.00653	65	113
288	PI-1761d-14	HPS-3A	46.0873	98.6190	0.00753	75	113
289	PI-1761d-15	HPS-3A	46.2655	99.0010	0.00788	79	113
290	PI-1761d-16	HPS-3A	43.7040	93.5173	0.00651	65	113
291	PI-1761d-17	HPS-3A	46.3734	99.2285	0.00659	66	113
292	PI-1761d-18	HPS-3A	45.8889	98.1936	0.00717	72	113
293	PI-1761d-19	HPS-3A	46.2893	99.0485	0.00662	66	113
294	PI-1761d-20	HPS-3A	43.0225	92.0606	0.00699	70	113
295	PI-1761d-21	HPS-3A	46.2847	99.0401	0.00709	71	113
296	PI-1761d-22	HPS-3A	46.1285	98.7047	0.00668	67	113
297	PI-1761d-23	HPS-3A	46.0715	98.5706	0.00229	23	113
298	PI-1761d-24	HPS-3A	46.4550	99.4103	0.00924	92	113
299	PI-1761d-25	HPS-3A	46.4459	99.4342	0.02480	248	113
300	PI-1761d-26	HPS-3A	46.0509	98.5476	0.00987	99	113
301	PI-1761d-27	HPS-3A	45.5205	97.4039	0.00665	66	113
302	PI-1761d-28	HPS-3A	46.1659	98.7839	0.00640	64	113
303	PI-1761d-29	HPS-3A	45.9435	98.3100	0.00706	71	113
304	PI-1761d-30	HPS-3A	45.7102	97.8108	0.00705	71	113
305	PI-1761d-31	HPS-3C	46.0441	98.9797	0.17043	1704	2273
306	PI-1761d-32	HPS-3C	46.0801	99.2035	0.22320	2232	2273
307	PI-1761d-33	HPS-3C	45.7922	98.5980	0.22697	2270	2273
308	PI-1761d-34	HPS-3C	45.7029	98.1957	0.15103	1510	2273
309	PI-1761d-35	HPS-3C	45.6229	98.0900	0.17451	1745	2273
310	PI-1761d-36	HPS-3C	45.5521	97.7598	0.11026	1103	2273
311	PI-1761d-37	HPS-3C	45.4019	97.6741	0.19494	1949	2273
312	PI-1761d-38	HPS-3C	45.1928	97.2291	0.19579	1958	2273
313	PI-1761d-39	HPS-3C	45.7110	98.3126	0.18676	1868	2273
314	PI-1761d-40	HPS-3C	45.1877	97.1562	0.17355	1736	2273
316	PI-1761d-42	HPS-3C	41.3515	88.8952	0.15413	1541	2273
317	PI-1761d-43	HPS-3C	44.8985	96.5304	0.17101	1710	2273
318	PI-1761d-44	HPS-3C	45.9718	98.7979	0.16066	1607	2273
319	PI-1761d-45	HPS-3C	45.9004	98.7688	0.20516	2052	2273
320	PI-1761d-46	HPS-3C	45.5394	97.9069	0.17295	1729	2273
321	PI-1761d-47	HPS-3C	45.6314	97.8774	0.09160	916	2273
322	PI-1761d-48	HPS-3C	45.7376	98.2269	0.13550	1355	2273
323	PI-1761d-49	HPS-3C	45.4646	97.9514	0.24639	2464	2273
324	PI-1761d-50	HPS-3C	44.3141	95.3364	0.19124	1912	2273
325	PI-1761d-51	HPS-3C	45.6192	98.3484	0.27023	2702	2273

Table A4.9. Results of EPMA of 7-layered reference material – HPS-7.

Sample name	Layer name	Si wt% atomic	Total	Ti wt% atomic	Ti ppm	Ti ppm (corrected by RMs)	Doped Ti ppm
PI1888-1b	HPS-7A	45.3508	97.0374	0.00901	90.1	104.1	89
PI1888-1a	HPS-7A	45.7856	97.9664	0.00835	83.5	97.1	89
PI1888-1c	HPS-7A	45.2050	96.7255	0.00903	90.3	104.3	89
PI1888-1d	HPS-7A	44.8300	95.9284	0.01216	121.6	137.8	89
PI1888-2a	HPS-7B	45.8357	98.0590	-0.00047	-4.7	2.7	(0.003)
PI1888-2b	HPS-7B	46.4453	99.3638	-0.00007	-0.7	7.0	(0.003)
PI1888-2c	HPS-7B	46.8440	100.2165	-0.00022	-2.2	5.3	(0.003)
PI1888-2d	HPS-7B	46.7294	99.9719	0.00017	1.7	9.5	(0.003)
PI1888-3a	HPS-7C	44.7194	96.5660	0.53622	5362.2	5746.8	2273
PI1888-3b	HPS-7C	45.4520	97.5955	0.21382	2138.2	2296.1	2273
PI1888-3c	HPS-7C	45.1691	96.9395	0.18347	1834.7	1971.3	2273
PI1888-3d	HPS-7C	45.7100	98.1529	0.21706	2170.6	2330.8	2273
PI1888-4a	HPS-7D	45.4264	97.2707	0.05201	520.1	564.3	416
PI1888-4b	HPS-7D	47.1613	100.9358	0.02412	241.2	265.8	416
PI1888-4c	HPS-7D	46.7262	100.0346	0.04193	419.3	456.4	416
PI1888-4d	HPS-7D	46.8629	100.2830	0.01547	154.7	173.3	416
PI1888-5a	HPS-7E	47.4759	101.6034	0.02089	208.9	231.2	234
PI1888-5b	HPS-7E	48.0557	102.8364	0.01636	163.6	182.7	234
PI1888-5c	HPS-7E	47.4733	101.6106	0.02842	284.2	311.9	234
PI1888-5d	HPS-7E	47.3455	101.3226	0.01972	197.2	218.7	234
PI1888-6a	HPS-7F	46.8111	100.1667	0.01221	122.1	138.4	120
PI1888-6b	HPS-7F	46.3616	99.1973	0.00743	74.3	87.2	120
PI1888-6c	HPS-7F	46.4838	99.4637	0.01046	104.6	119.6	120
PI1888-6d	HPS-7F	46.8102	100.1565	0.00721	72.1	84.8	120
PI1888-7a	HPS-7G	46.1298	98.7039	0.00900	90.0	104.0	113
PI1888-7b	HPS-7G	47.2881	101.1788	0.00720	72.0	84.7	113
PI1888-7c	HPS-7G	46.7860	100.1064	0.00813	81.3	94.7	113
PI1888-7d	HPS-7G	46.5379	99.5763	0.00862	86.2	99.9	113

Appendix 4

Table A4.10. Results of LA-ICP-MS analysis of 7-layered reference material – HPS-7.

Sample name	Layer name	Duration(s)	Si29 CPS	Si29 CPS 2SE	Ti ppm m49	Ti ppm m49 2SE	Doped Ti ppm
PI1888-1	HPS-7A	11.34	1.73E+05	1.70E+04	141	20	89
PI1888-1	HPS-7A	16.494	5.87E+05	4.10E+04	137	12	89
PI1888-1	HPS-7A	31.257	5.80E+05	4.00E+04	151	12	89
PI1888-1	HPS-7A	8.9343	4.97E+05	3.60E+04	101.6	8.5	89
PI1888-1	HPS-7A	5.8142	4.79E+05	5.30E+04	137	20	89
PI1888-1	HPS-7A	3.399	4.81E+05	4.90E+04	112	16	89
PI1888-2	HPS-7B	29.552	2.91E+06	6.80E+04	1.26	0.21	(0.003)
PI1888-2	HPS-7B	27.847	9.91E+05	6.90E+04	1.65	0.44	(0.003)
PI1888-2	HPS-7B	26.711	2.48E+06	6.20E+04	9.05	0.72	(0.003)
PI1888-2	HPS-7B	19.811	2.14E+06	4.00E+04	13.42	0.91	(0.003)
PI1888-2	HPS-7B	25.574	2.94E+06	6.90E+04	9.61	0.66	(0.003)
PI1888-2	HPS-7B	28.984	2.31E+06	4.60E+04	1.9	0.32	(0.003)
PI1888-3	HPS-7C	30.689	1.71E+06	2.60E+04	3901	72	2273
PI1888-3	HPS-7C	25.947	1.36E+06	2.10E+04	3706	46	2273
PI1888-3	HPS-7C	27.279	9.77E+05	2.70E+04	2653	52	2273
PI1888-3	HPS-7C	30.12	8.95E+05	2.00E+04	3331	58	2273
PI1888-3	HPS-7C	29.552	1.23E+06	1.70E+04	3632	44	2273
PI1888-3	HPS-7C	25.006	1.16E+06	5.10E+04	1978	46	2273
PI1888-4	HPS-7D	12.974	2.84E+06	6.90E+04	364	12	416
PI1888-4	HPS-7D	26.711	6.53E+05	2.90E+04	732	35	416
PI1888-4	HPS-7D	22.791	2.95E+06	5.90E+04	523	12	416
PI1888-4	HPS-7D	8.0647	1.83E+06	5.40E+04	299	11	416
PI1888-4	HPS-7D	17.532	2.40E+06	6.10E+04	276.3	7.6	416
PI1888-4	HPS-7D	23.142	1.95E+06	6.20E+04	471	16	416
PI1888-4	HPS-7D	26.711	1.62E+06	6.00E+04	380	19	416
PI1888-4	HPS-7D	22.732	1.34E+06	3.70E+04	544	37	416
PI1888-4	HPS-7D	25.574	1.20E+06	4.00E+04	444	25	416
PI1888-4	HPS-7D	26.142	1.24E+06	4.50E+04	378	12	416
PI1888-4	HPS-7D	25.006	7.10E+05	2.90E+04	418	22	416
PI1888-4	HPS-7D	26.711	2.38E+06	5.30E+04	243.3	9.5	416
PI1888-5	HPS-7E	26.711	2.19E+06	3.20E+04	229.8	6.6	234
PI1888-5	HPS-7E	17.006	1.46E+06	1.30E+04	747	13	234
PI1888-5	HPS-7E	24.437	1.41E+06	3.00E+04	296.4	8	234
PI1888-5	HPS-7E	19.285	1.95E+06	2.50E+04	173.5	4.6	234
PI1888-5	HPS-7E	23.869	1.84E+06	1.70E+04	302.3	5.7	234
PI1888-5	HPS-7E	21.038	8.67E+05	2.00E+04	261	12	234
PI1888-6	HPS-7F	25.574	2.87E+06	7.40E+04	107.3	4.1	120
PI1888-6	HPS-7F	25.597	2.54E+06	3.30E+04	185.9	3.6	120
PI1888-6	HPS-7F	24.437	1.96E+06	4.40E+04	172.7	5.3	120
PI1888-6	HPS-7F	22.732	2.49E+06	4.30E+04	167.8	4.2	120
PI1888-6	HPS-7F	21.564	2.10E+06	3.10E+04	105.6	3.2	120
PI1888-6	HPS-7F	22.266	1.78E+06	1.90E+04	86	2.8	120
PI1888-7	HPS-7G	22.967	1.41E+06	3.20E+04	158.9	5.5	113
PI1888-7	HPS-7G	22.616	2.66E+06	2.70E+04	134.8	2.7	113
PI1888-7	HPS-7G	23.843	1.69E+06	2.00E+04	210.4	4.5	113
PI1888-7	HPS-7G	24.545	2.60E+06	2.70E+04	140	2.9	113
PI1888-7	HPS-7G	21.74	2.16E+06	2.60E+04	136.8	3.4	113
PI1888-7	HPS-7G	23.301	1.93E+06	2.40E+04	205	4.7	113
PI1888-7	HPS-7G	21.038	1.27E+06	4.40E+04	215.4	8.1	113

Appendix 5

Supplementary Experimental Materials for Chapter 3

Appendix A5.1. Silica gel activation procedure.

Appendix A5.2. Silica gel doping procedure.

Appendix A5.3. Recipes followed for doping silica gel batches #1-9.

Appendix A5.4. Analytical procedure for electron probe analysis at UMN.

Appendix A5.1. Silica Gel Activation Procedure

Materials:

- commercial silica gel, 60-200 μm grain size, 60 Å pore size
- de-ionized water (DIW)
- 6 M HCl
- 0.100 M $AgNO_3$
- 275 mL Erlenmeyer flask
- plastic disposable spatula(s)
- Teflon magnetic stir bar

Procedure:

1. Measure 30.00 g silica gel into pristine 275 mL Erlenmeyer flask using plastic disposable spatula.

2. Add 100 mL of 6 M HCl to flask using graduated cylinder.

3. Add 1.25" Teflon magnetic stir bar to flask. Place flask onto stirring plate, stir on low power under fume hood. Place piece of parafilm adhesive paper over flask to reduce evaporation.

4. After 9 h (or other desired time), remove flask from stirring plate.

5. Add 50 mL DIW, replace on stirring plate and stir on low power for 1 min.

6. Remove from stirring plate, extract Teflon stir bar. Place flask into sonicator for 5 min to allow settling, then decant. Add 100 mL of DIW, swirl flask vigorously for 30 sec, then return to sonicator for 5 min. Decant, and test for chloride in rinsings using 0.100 M $AgNO_3$. Repeat rinsing until no chloride remains (>25x).

7. After decanting as much liquid as possible, place flask into conventional oven at 100 °C for 24 h.

8. Transfer powder from flask into glass petri dish, place into conventional oven at 120 °C for 120 h.

9. Extract and weigh activated silica gel before storage in an air-tight container.

Appendix A5.2. Silica Gel Doping Procedure

Materials:

- activated silica gel
- 160 mL reagent grade ethanol
- 3 M NH_4OH
- 0.3 M NH_4OH
- 0.2 M HNO_3
- 1000 µg/mL Ti plasma standard solution
- 10 µg/mL Ti plasma standard solution
- Finnpipette 100-1000 µL micropipette
- Finnpipette 10-100 µL micropipette
- Sigma Aldrich vacuum filtration apparatus
- 0.45 µm pore size nylon filter paper
- eight (8) 60 mL Nalgene jars with screw lid
- 250 mL Erlenmeyer flask
- pH meter
- oscillating apparatus

Procedure:

1. Combine 1.500 g of activated silica gel with 40 mL ethanol into 60 mL Nalgene plastic jar with screw lid to create a gel-ethanol slurry. Prepare all eight jars in series for 12 g of doped silica gel per batch.

2. To dope 1.500 g silica at a level of 802 ppm, add 1200 µL of the 1000 µg/mL Ti plasma standard solution and 372 µL of the 10 µg/mL Ti plasma standard solution. To dope 1.500 g silica at a level of 2916 ppm, add 4370 µL of the 1000 µg/mL

plasma standard solution and 681 μL of the 10 μg/mL plasma standard solution. Screw cap onto jar and shake vigorously for several seconds.

3. Test pH of the solution.

4. Titrate solution to the desired pH with ammonium hydroxide (3 M and 0.3 M NH_4OH) and nitric acid (0.2 M HNO_3). As an example, to reach a pH of 8 at the 802 ppm doping concentration level, buffer the pH with ~355 μL of 0.3 M NH_4OH; at the 2916 ppm doping concentration level, buffer the pH with ~920 μL of 0.3 M NH_4OH.

5. After pH = 8 has stabilized, screw cap onto jar and place into oscillating apparatus for 3 h.

6. Repeat steps #2-5 in series for each 60 mL Nalgene jar.

7. Remove from oscillating apparatus and perform filtration on each sample in series. Filter contents of plastic jar using a vacuum filtration assembly equipped with 0.45 μm nylon filter paper. Rinse jar and powder with DIW and include rinse into filtering apparatus. Use ~1 L of DIW to rinse each 1.5 g sample.

8. Extract nylon filter from filtration apparatus, place filter and powder into glass petri dish and place into conventional oven at 100 °C for 24 h.

9. Discard filter paper, place into conventional oven at 120 °C for 120 h.

10. Extract doped silica gel and obtain final mass before storage in air-tight container.

Appendix A5.3. Recipes for doping silica gel batches #1-9

Batch #1 25 May 2011

Jar	Name	Silica Source (1.50g)	Solvent (30mL)	Dopant Concentration	µL of 1000µL/mL	µL of 10µL/mL	µL of 3M NH4OH	µL of 3M NH4OH
1	7-300	6hr active	ethanol	300	1,110	970	0	600
2	8-300	6hr active	ethanol	300	5,620	270	0	1000
3	9-300	6hr active	ethanol	300	4,500	290	100	1500
4	10-300	6hr active	ethanol	300	4,500	290	1350	0
5	7-3000	6hr active	ethanol	3000	4,500	290	600	700
6	8-3000	6hr active	ethanol	3000	4,500	290	900	100
7	9-3000	6hr active	ethanol	3000	450	30	1300	400
8	10-3000	6hr active	ethanol	3000	450	30	5350	0

ICP-OES analysis of samples from this batch

Sample ID	Name
SG-0.01	7-300
SG-0.02	7-300 calcined
SG-0.03	8-300
SG-0.04	8-300 calcined
SG-0.05	9-300
SG-0.06	9-300 calcined
SG-0.07	10-300
SG-0.08	10-300 calcined
SG-0.09	7-3000
SG-0.10	7-3000 calcined
SG-0.11	8-3000
SG-0.12	8-3000 calcined
SG-0.13	9-3000
SG-0.14	9-3000 calcined
SG-0.15	10-3000
SG-0.16	10-3000 calcined

Appendix A5.3 (cont.). Recipes followed for doping silica gel batches #1-9.

Batch #2 4 Aug 2011

Jar	Name	Silica Source (1.50g)	Solvent (30mL)	Dopant Concentration	µL of 1000µL/mL	µL of 10µL/mL	µL of 3M NH4OH
1	8-3000	9hr activated	ethanol	3000	4,500	290	950
2	8-3000	9hr activated	ethanol	3000	4,500	290	950
3	8-3000	9hr activated	ethanol	3000	4,500	290	950
4	8-3000	9hr activated	ethanol	3000	4,500	290	950
5	8-3000	9hr activated	ethanol	3000	4,500	290	950
6	8-3000	9hr activated	ethanol	3000	4,500	290	950
7	8-3000	9hr activated	ethanol	3000	4,500	290	950
8	8-3000	9hr activated	ethanol	3000	4,500	290	950

ICP-OES analysis of samples from this batch

Sample ID	Name
SG-05	0.10g of SG-0.11 calcined in Al at 825C for 1hr
SG-06	0.10g of SG-0.11 calcined in Zr at 825C for 1hr

Appendix A5.3 (cont.). Recipes followed for doping silica gel batches #1-9.

Batch #3 8 Sep 2011

Jar	Name	Silica Source (1.50g)	Solvent (30mL)	Dopant Concentration	µL of 1000µL/mL	µL of 10µL/mL	µL of 3M NH4OH
1	8-3000	9hr activated	reagent alcohol	3000	4,500	290	950
2	8-3000	9hr activated	reagent alcohol	3000	4,500	290	950
3	8-3000	9hr activated	reagent alcohol	3000	4,500	290	950
4	8-3000	9hr activated	reagent alcohol	3000	4,500	290	950
5	8-3000	9hr activated	reagent alcohol	3000	4,500	290	950
6	8-3000	9hr activated	reagent alcohol	3000	4,500	290	950
7	8-3000	9hr activated	reagent alcohol	3000	4,500	290	950
8	8-3000	9hr activated	reagent alcohol	3000	4,500	290	950

ICP-OES analysis of samples from this batch

Sample ID	Name
SG-10	Target 3000 reagent alcohol

Appendix A5.3 (cont.). Recipes followed for doping silica gel batches #1-9.

Batch #4 15 Oct 2011

Jar	Name	Silica Source (1.50g)	Solvent (30mL)	Dopant Concentration	µL of 1000µL/mL	µL of 10µL/mL	µL of 3M NH4OH
1	double-dope	8-3000 (from B2)	ethanol	746	1,110	970	1000
2	over-dope	9hr active	ethanol	3746	5,620	270	350
3	heptane	9hr active	heptane	3000	4,500	290	600*
4	hexadecane	9hr active	hexadecane	3000	4,500	290	600*
5	squalane	9hr active	squalane	3000	4,500	290	600*
6	BHQ	BHQ-9hr rinse	ethanol	3000	4,500	290	900
7	8-300eth	9hr active	ethanol	300	450	30	190
8	8-300eth	9hr active	ethanol	300	450	30	190

*pH did not stabilize

ICP-OES analysis of samples from this batch

Sample ID	Name
SG-13	over-dope
SG-14	double-dope (2255+746)
SG-15	8-3000 heptane
SG-16	8-3000 hexadecane
SG-17	8-3000 squalane
SG-18	BHQ-8-3000 ethanol

Appendix A5.3 (cont.). Recipes followed for doping silica gel batches #1-9.

Batch #5 16 Oct 2011

Jar	Name	Silica Source (1.50g)	Solvent (30mL)	Dopant Concentration	µL of 1000µL/mL	µL of 10µL/mL	µL of 3M NH4OH
2	Target 195	9hr active	reagent alcohol	195	140	634	100
5	Target 195	9hr active	reagent alcohol	195	140	634	100
7	Target 431	9hr active	reagent alcohol	316	230	714	110
8	Target 216	9hr active	reagent alcohol	101	70	579	60

ICP-OES analysis of samples from this batch

Sample ID	Name
SG-20	Target 195

Appendix A5.3 (cont.). Recipes followed for doping silica gel batches #1-9.

Batch #6 29 Apr 2012

Jar	Name	Silica Source	Solvent (30mL)	Dopant Concentration	µL of 1000µL/mL	µL of 10µL/mL	µL of 3M NH4OH
1	8-300-DIW	6hr active	DIW	300	450	27	140
7	8-300-hex	6hr active	hexadecane	300	450	27	150*
8	8-300-squa	6hr active	squalane	300	450	27	150*
6	BHQ 8-300	BHQ 9hr active	ethanol	300	375	22	110
2	Target 30	9hr active	ethanol	30	22	51	15
5	Target 60	9hr active	ethanol	60	44	103	30
3	Target 90	9hr active	ethanol	90	67	54	50

ICP-OES analysis of samples from this batch

*pH did not stabilize

Sample ID	Name
SG-21	8-300-DIW
SG-22	8-300-hexadecane
SG-23	8-300-squalane
SG-24	BHQ 8-300
SG-25	Target 30
SG-26	Target 60
SG-27	Target 90

Appendix A5.3 (cont.). Recipes followed for doping silica gel batches #1-9.

Batch #7 19 Nov 2012

Jar	Name	Silica Source (1.50g)	Solvent (30mL)	Dopant Concentration	µL of 1000µL/mL	µL of 10µL/mL	µL of 3M NH4OH
1	8-802	9hr active	ethanol	802	1,200	372	290
2	8-802	9hr active	ethanol	802	1,200	372	290
3	8-2916	9hr active	ethanol	2916	4,372	681	830
4	8-2916	9hr active	ethanol	2916	4,372	681	830

ICP-OES analysis of samples from this batch

Sample ID	Name
SG-29	802_batch7
SG-30	2916_batch7
SG-34	2916_batch7 (again)

Appendix A5.3 (cont.). Recipes followed for doping silica gel batches #1-9.

Batch #8 11 Feb 2013

Jar	Name	Silica Source (1.50g)	Solvent (30mL)	Dopant Concentration	µL of 1000µL/mL	µL of 10µL/mL	µL of 3M NH4OH
1	802_batch8	9hr active	ethanol	802	1,200	372	355
2	802_batch8	9hr active	ethanol	802	1,200	372	355
3	2916_batch8	9hr active	ethanol	2916	4,372	681	920
4	2916_batch8	9hr active	ethanol	2916	4,372	681	920

ICP-OES analysis of samples from this batch

Sample ID	Name
SG-32	802_batch8
SG-33	2916_batch8

Appendix A5.3 (cont.). Recipes followed for doping silica gel batches #1-9.

Batch #9 19 Aug 2014

Jar	Name	Silica Source (1.50g)	Solvent (30mL)	Dopant Concentration	µL of 1000µL/mL	µL of 10µL/mL	µL of 3M NH4OH
1	8-347	7x24hr active	ethanol	347	520	81	170
2	8-347	7x24hr active	ethanol	347	520	81	170
3	8-347	7x24hr active	ethanol	347	520	81	170
4	8-347	7x24hr active	ethanol	347	520	81	170
5	8-147	7x24hr active	ethanol	147	220	63	60
6	8-147	7x24hr active	ethanol	147	220	63	60
7	8-147	7x24hr active	ethanol	147	220	63	60
8	8-147	7x24hr active	ethanol	147	220	63	60

ICP-OES analysis of samples from this batch

Sample ID	Name
SG-42	8-347
SG-43	8-147

Appendix A5.4. Analytical procedure for electron probe analysis at UMN.

Electron probe microanalysis was performed with a JEOL-8900 Electron Probe Microanalyser in the Department of Earth Sciences at the University of Minnesota. Probe for EPMA© software was used to improve statistics of trace element analysis [Donovan et al. 2011]. The instrumental conditions of analysis were 100 nA beam current, 20 kV accelerating voltage, and 20 μm beam size. Four spectrometers (3 PETJ, 1 LIFH) were used to simultaneously collect and aggregate Ti K-α counts to improve peak-to-background ratio. The remaining spectrometer (TAP) was used to monitor counts of Si-Kβ. Counting times were 220 s on peak, 220 s on low background, and 220 s on high background, using an alternating peak-background function to repeat this sequence 6 times (following the routine outlined by Donovan et al. [2011]). This results in a 46 min collection time for each analysis. Prior to analysis, a 12 h wavescan was performed on each spectrometer in the near vicinity of the Ti peak to monitor instrumental background values; each background was modeled with an exponential fit to most closely model the shape of the continuum beneath the Ti peak. During analysis, gain and bias of PHAs on each spectrometer was monitored in 4 h intervals. A blank correction was applied by measuring Ti concentration of three Herkimer quartz crystals (~3 ppb Ti; Kidder et al. [2013]). Accuracy of the calibration was evaluated by analyzing the QTiP series of experimental quartz [Thomas et al. 2010] and Herkimer quartz. Following this routine, calculated detection limits were 20 $\mu g\ g^{-1}$ and gave an overall reproducibility of ~50-100% on low concentration reference materials (<100 $\mu g\ g^{-1}$) and ~30% reproducibility on high concentration reference materials

(>100 μg g^{-1}) (Table A5.4). Concentrations vary by >100 μg g^{-1} between spectrometers during the same analysis and did not reproduce measurements from adjacent analysis locations. Measurements of the NIST series of reference glasses yields spuriously low totals and large errors. Despite attempting an advanced routine for trace element analysis using a conventional microprobe, the reproducibility afforded by this approach was determined to be inadequate for the purposes of this study (see Table A5.4).

Appendix 6

Supplementary Figures for Chapter 4

Figure A6.1. Analysis of Ti concentration (ppm Ti) from the grain boundary of a single crystal of quartz from the undoped layer of a low strain experiment (W1674), revealing the same concentrations as the population of measurements collected from thin section analysis (see Table 2, Table S1). This observation supports our interpretation that secondary fluorescence is not a major source of contamination for the majority of our analytical measurements.

Figure A6.2. Full CL spectrum collected from doped quartz showing luminosity in the blue region, suggesting that the CL signal is dominated by Ti substitution in quartz.

Figure A6.3. Plane-polarized light micrographs of nodular rutile inclusions present in the doped layer of experimental aggregates from hydrostatic (A-B) and high strain deformed samples (C).

Figure A6.4. Cathodoluminescence intensity halos surrounding rutile needles from hydrostatic (A), low strain (B), intermediate strain (C), and high strain (D) samples. Rutile needles emit high-intensity CL enrichment halos, which are interpreted to reflect Ti diffusion from rutile needles into quartz. CL halos are observed to be smoother and wider in high-strain (longer-duration) experiments.

Figure A6.5. Plots showing one representative transect (out of three) of EMP measurements collected across the aggregate layering (points were set with equidistant spacing in all samples except hydrostatic samples, where points were set manually to avoid porosity). Results reveal two compositionally-distinct populations of Ti-in-quartz concentrations in the doped (blue symbols) and undoped (red symbols) layers. Despite changes in the value of concentrations between hydrostatic (A), low strain (B), intermediate strain (C), and high strain (D) samples, the relative difference between quartz in the doped and undoped layer remains consistent: Ti-in-quartz concentrations in the undoped layer are ~50% of the concentrations in the undoped layer, leading us to infer $a_{TiO2} \sim 0.5$ for quartz growth in the undoped layer (see Figure 8 and Section 5.1 for further discussion).

Appendix 6

Figure A6.1.

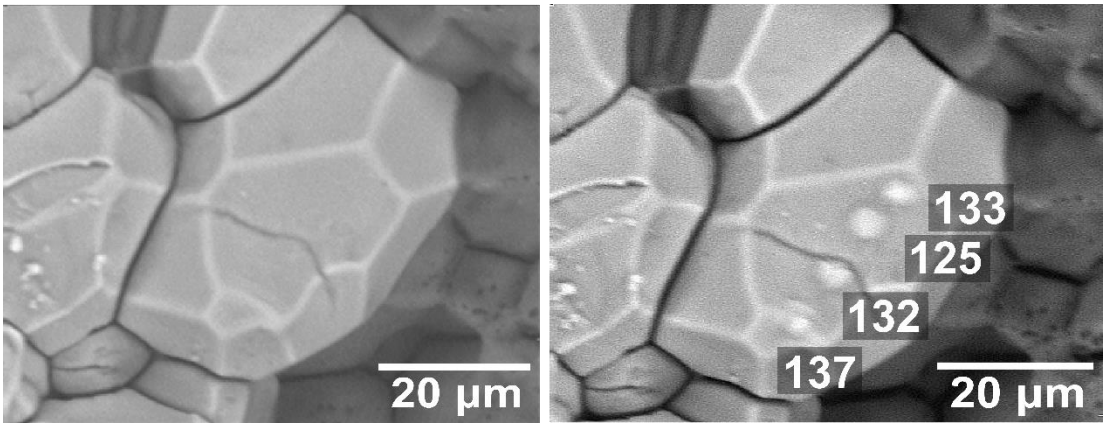

Figure A6.2.

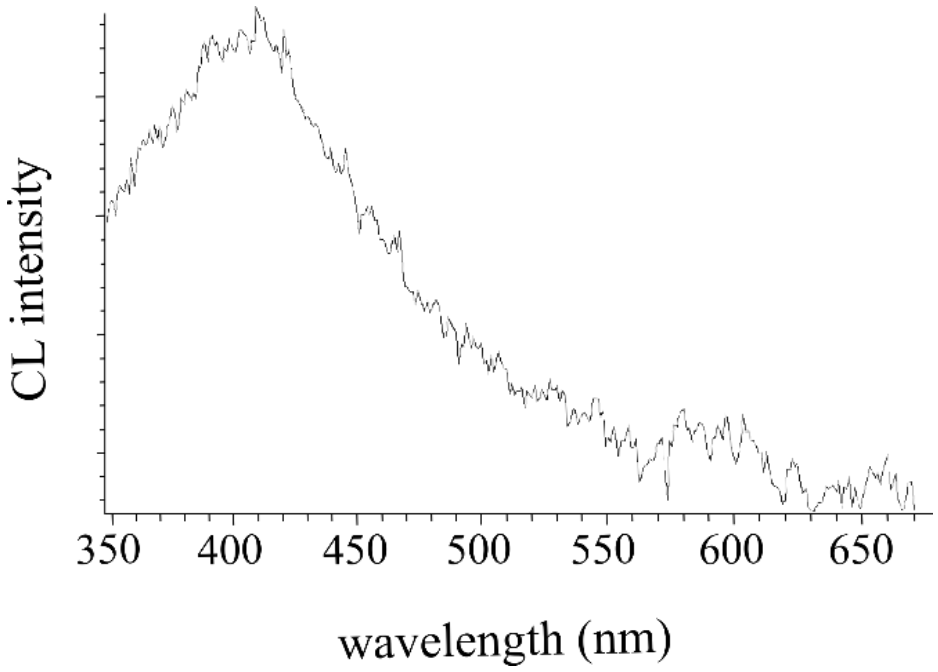

Figure A6.3.

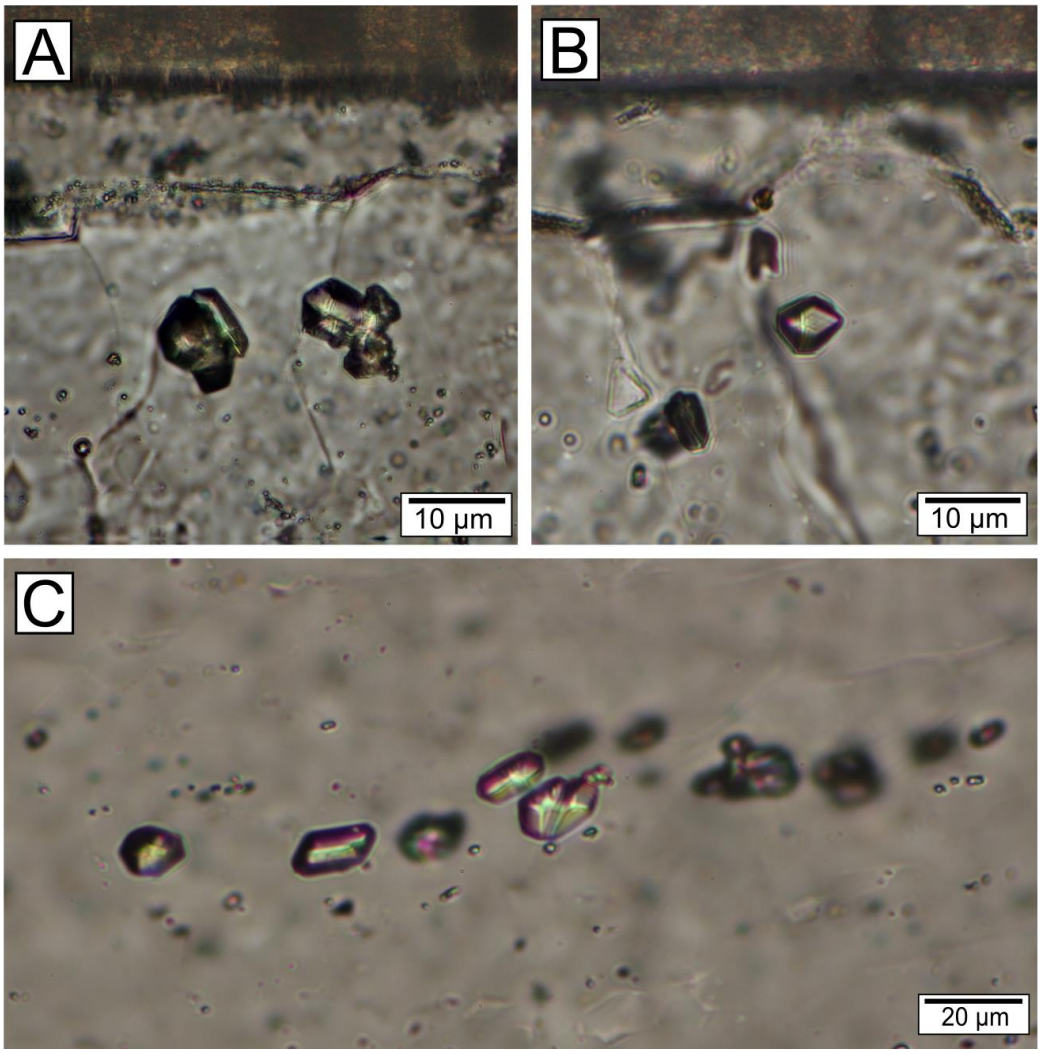

Figure A6.4.

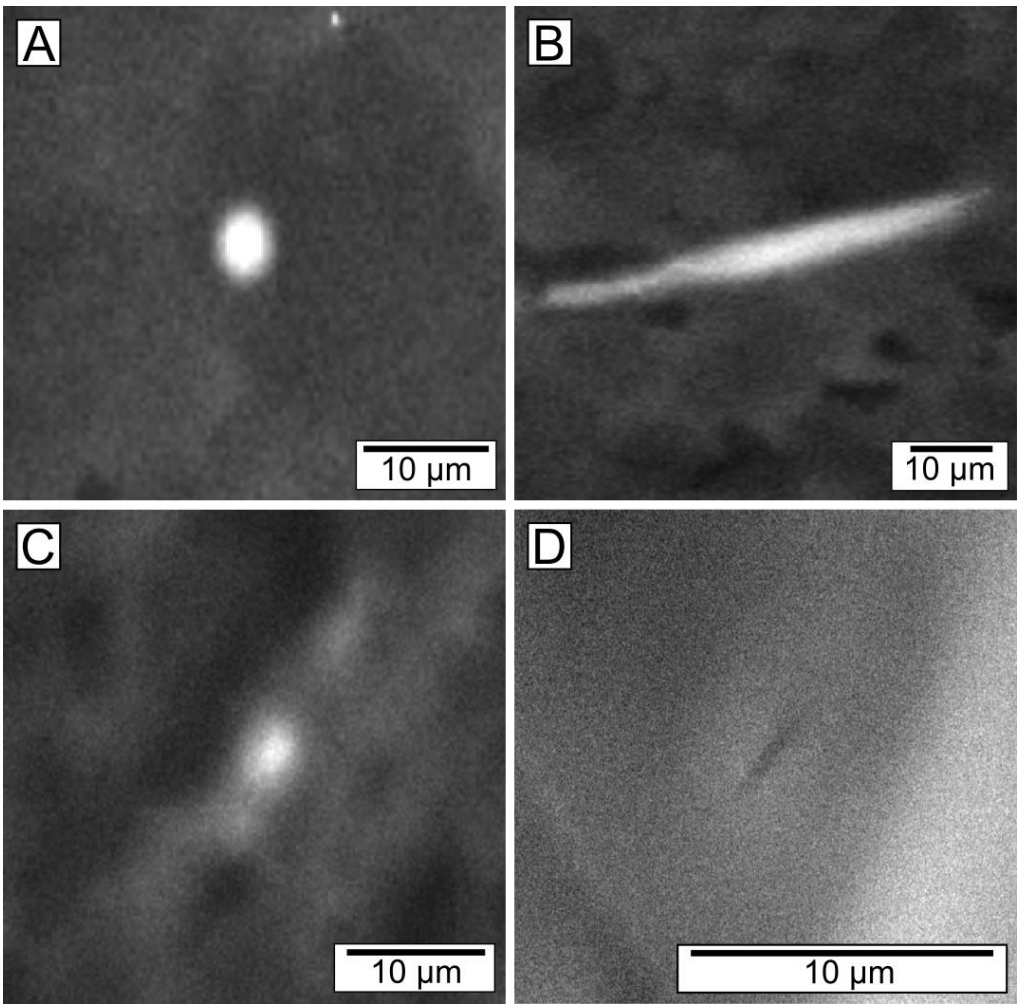

Figure A6.5.

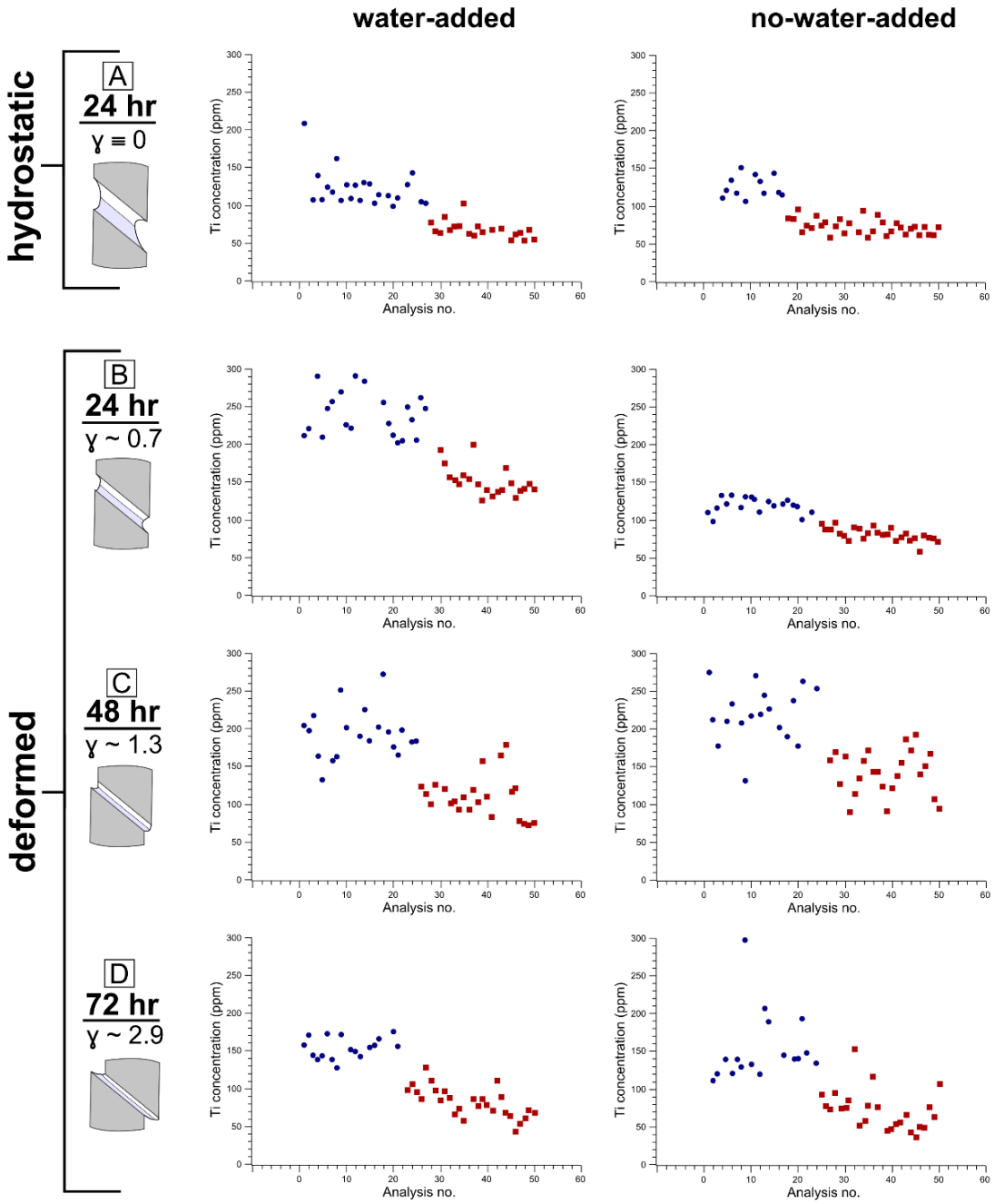
water-added
no-water-added
hydrostatic
deformed
A
24 hr
γ ≡ 0
B
24 hr
γ ~ 0.7
C
48 hr
γ ~ 1.3
D
72 hr
γ ~ 2.9
Ti concentration (ppm)
Analysis no.

Appendix 7

Supplementary Tables for Chapter 4

Table A7.1. Compiled EMP measurements from the doped and undoped layers of the aggregate showing the data processing steps of removing contaminated measurements and outliers. Final values for each sample listed in Table 4.2.

Table A7.1.

		doped layer			*undoped layer*		
		all data unfiltered	**filtered** (less than 400 ppm)	**outliers removed**	**all data unfiltered**	**filtered** (less than 300 ppm)	**outliers removed**
W1674	mean	523	230	230	135	135	134
total n=	st.dev	1356	45	34	22	22	19
209	n=	116	93	88	93	93	88
	st.err	126	5	4	2	2	2
W1678	mean	3987	127	117	349	84	76
total n=	st.dev	20381	54	29	2312	38	14
150	n=	74	64	61	76	75	72
	st.err	2369	7	4	265	4	2
W1680	mean	3807	224	211	171	132	130
total n=	st.dev	21560	61	42	314	32	29
175	n=	85	64	59	90	87	86
	st.err	2338	8	6	33	3	3
W1696	mean	1541	138	123	116	85	79
total n=	st.dev	5316	65	41	223	34	19
209	n=	84	67	62	125	120	114
	st.err	580	8	5	20	3	2
W1698	mean	5869	161	140	434	67	63
total n=	st.dev	34973	97	56	1768	24	14
160	n=	91	77	72	69	64	61
	st.err	3666	11	7	213	3	2
W1699	mean	4208	196	191	236	112	106
total n=	st.dev	24546	39	33	779	38	29
152	n=	81	69	65	71	66	63
	st.err	2727	5	4	92	5	4
W1700	mean	559	160	146	145	68	60
total n=	st.dev	1576	61	36	420	36	23
175	n=	84	69	64	91	87	81
	st.err	172	7	4	44	4	3
W1701	mean	766	163	157	108	87	83
total n=	st.dev	3391	36	25	197	36	18
150	n=	65	58	55	85	84	74
	st.err	421	5	3	21	4	2

Appendix 8

Supplementary Figures for Chapter 5

Figure A8.1. Photomicrographs of SIMS analysis locations of rutilated quartz.

Figure A8.2. Grid of EPMA analysis over rutile needle inclusion.

Figure A8.3. Histogram of Ti concentrations measured from Pioneer rutilated quartzite mylonite samples.

Figure A8.4. Comparison of diffusion modeling approach with the results of Morgan et al. [2013].

Figure A8.5 Histograms of diffusion modeling results for natural samples.

Figure A8.6 Histograms of diffusion modeling results for experimental samples.

Figure A8.7. Representative diffusion profiles and modeling results for natural samples.

Figure A8.8. Representative diffusion profiles and modeling results for experimental samples.

Figure A8.9. EDS analysis of acicular phases in rutilated quartz gemstone from Brazil.

Appendix 8

Figure A8.1.

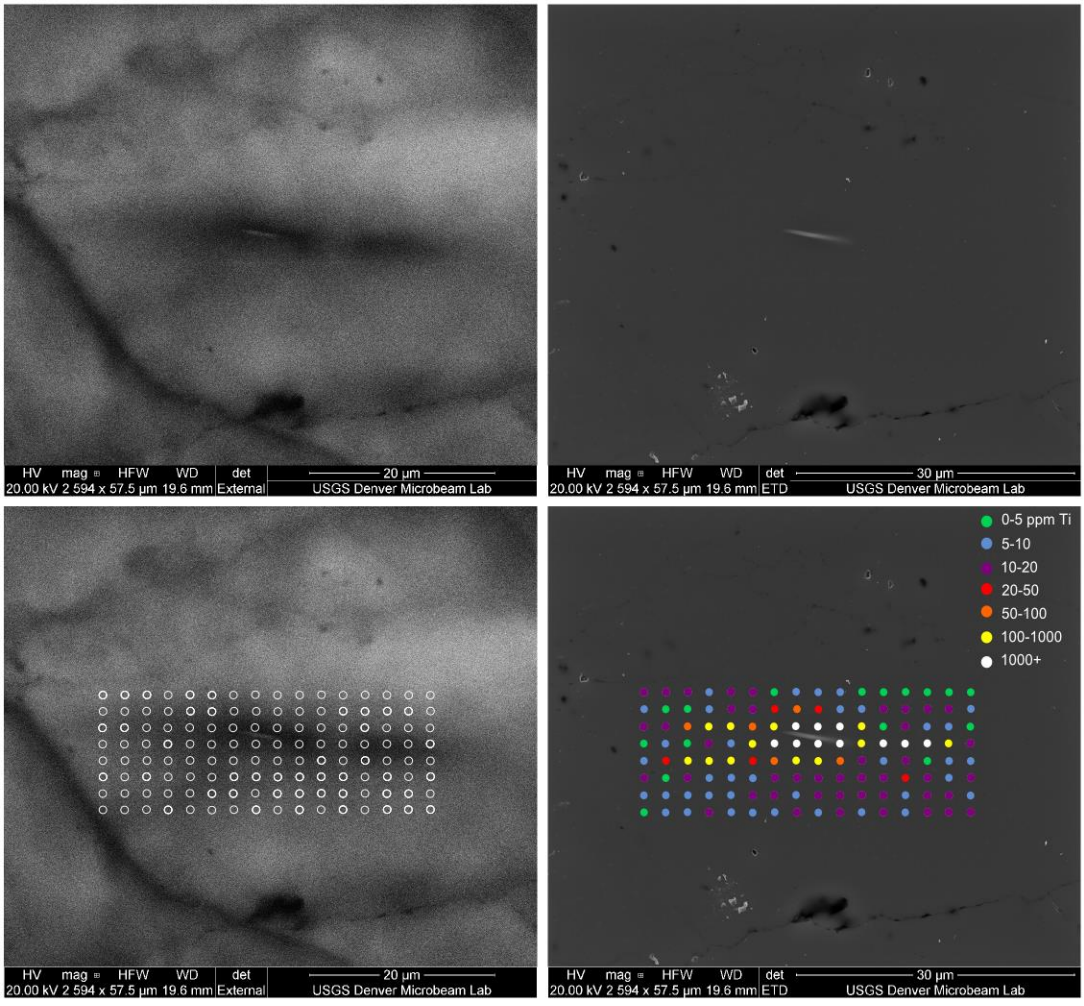

Figure A8.2.

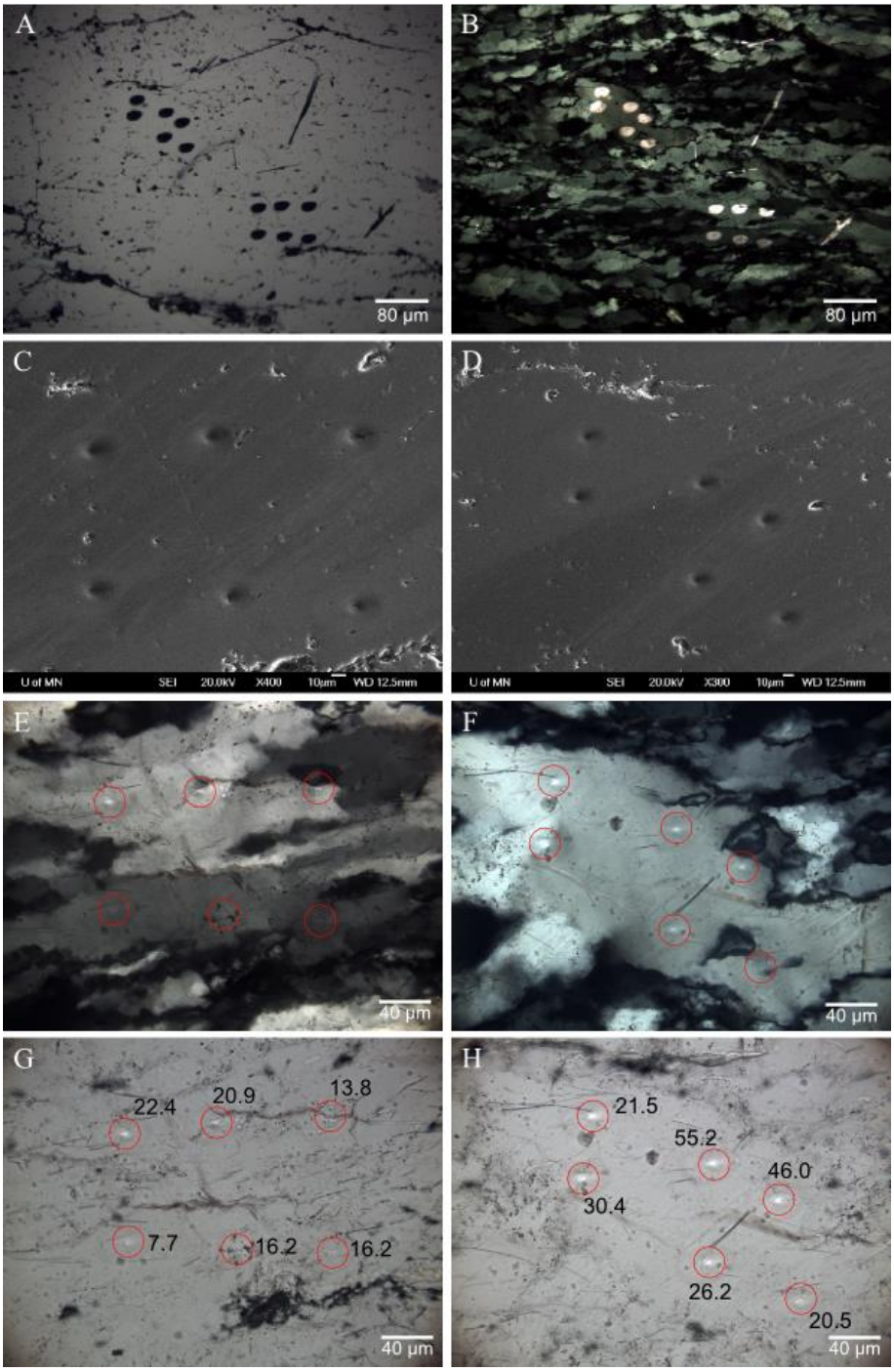
A
80 µm
B
80 µm
C
U of MN SEI 20.0kV X400 10µm WD 12.5mm
D
U of MN SEI 20.0kV X300 10µm WD 12.5mm
E
40 µm
F
40 µm
G
22.4
20.9
13.8
7.7
16.2
16.2
40 µm
H
21.5
55.2
46.0
30.4
26.2
20.5
40 µm

Figure A8.3.

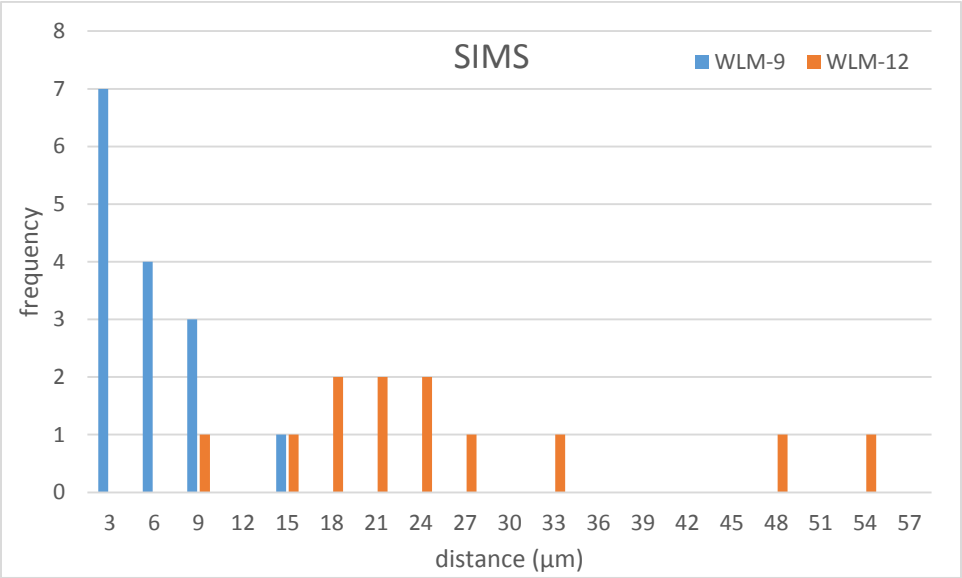
SIMS
WLM-9
WLM-12
frequency
distance (µm)
0
1
2
3
4
5
6
7
8
3
6
9
12
15
18
21
24
27
30
33
36
39
42
45
48
51
54
57

Figure A8.4.

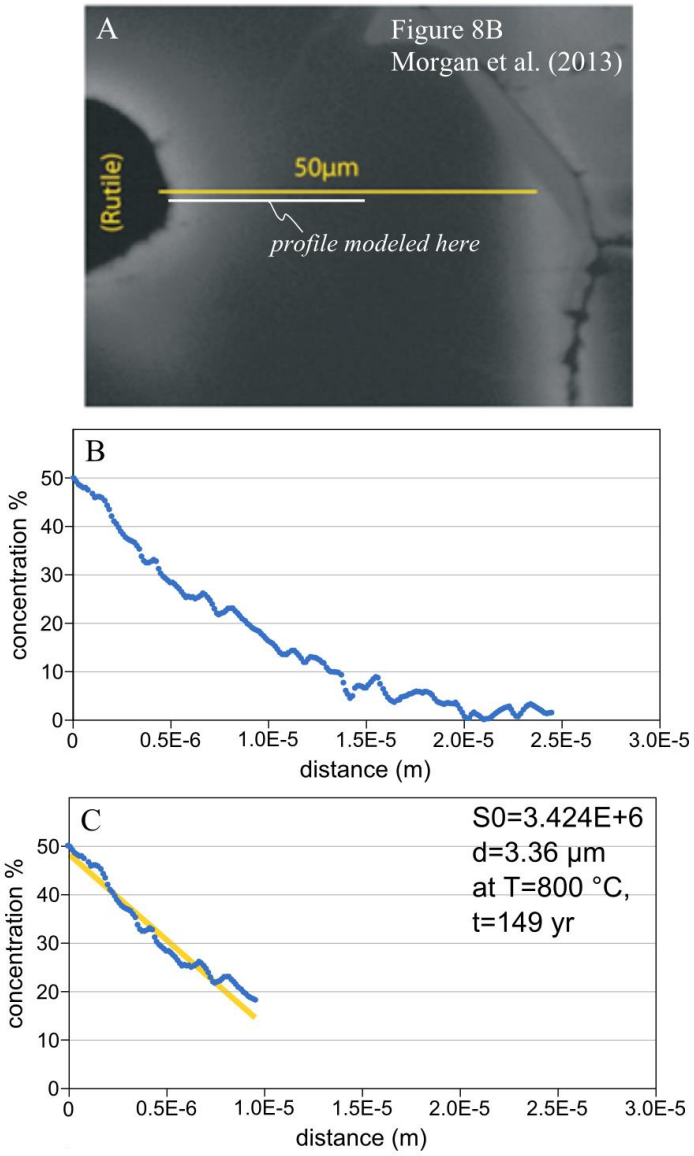
A
Figure 8B
Morgan et al. (2013)
(Rutile)
50µm
profile modeled here
B
concentration %
distance (m)
C
S0=3.424E+6
d=3.36 µm
at T=800 °C,
t=149 yr
concentration %
distance (m)

Figure A8.5.

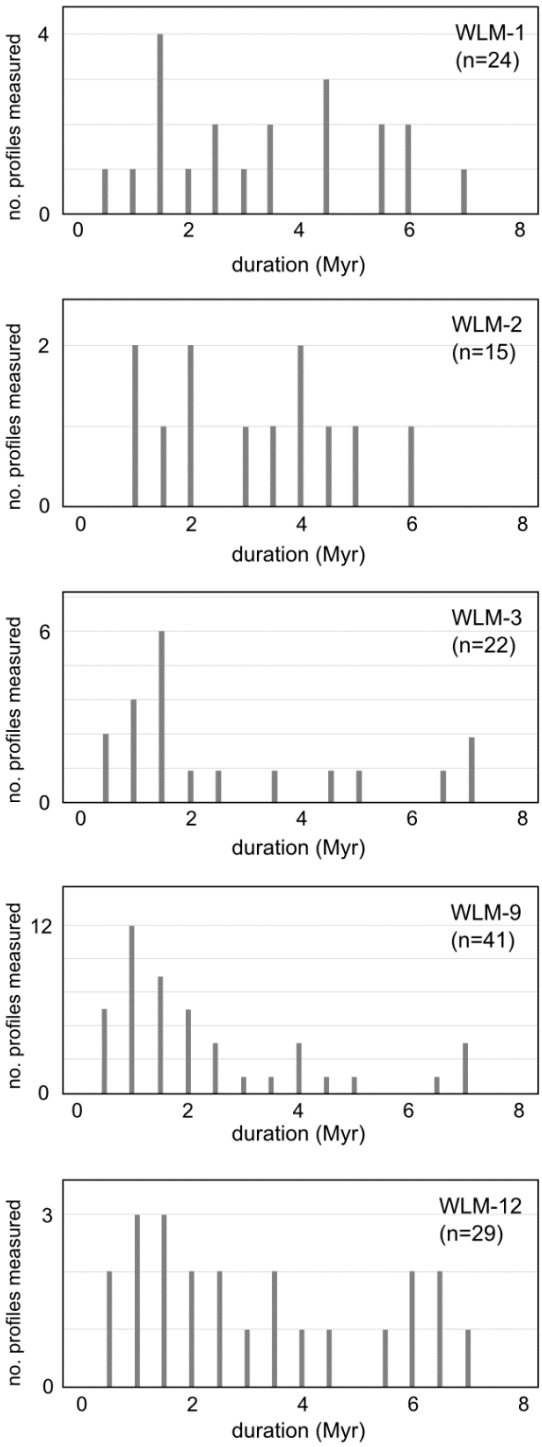
WLM-1
(n=24)
WLM-2
(n=15)
WLM-3
(n=22)
WLM-9
(n=41)
WLM-12
(n=29)
no. profiles measured
duration (Myr)
0
2
4
6
8
12
3

Figure A8.6.

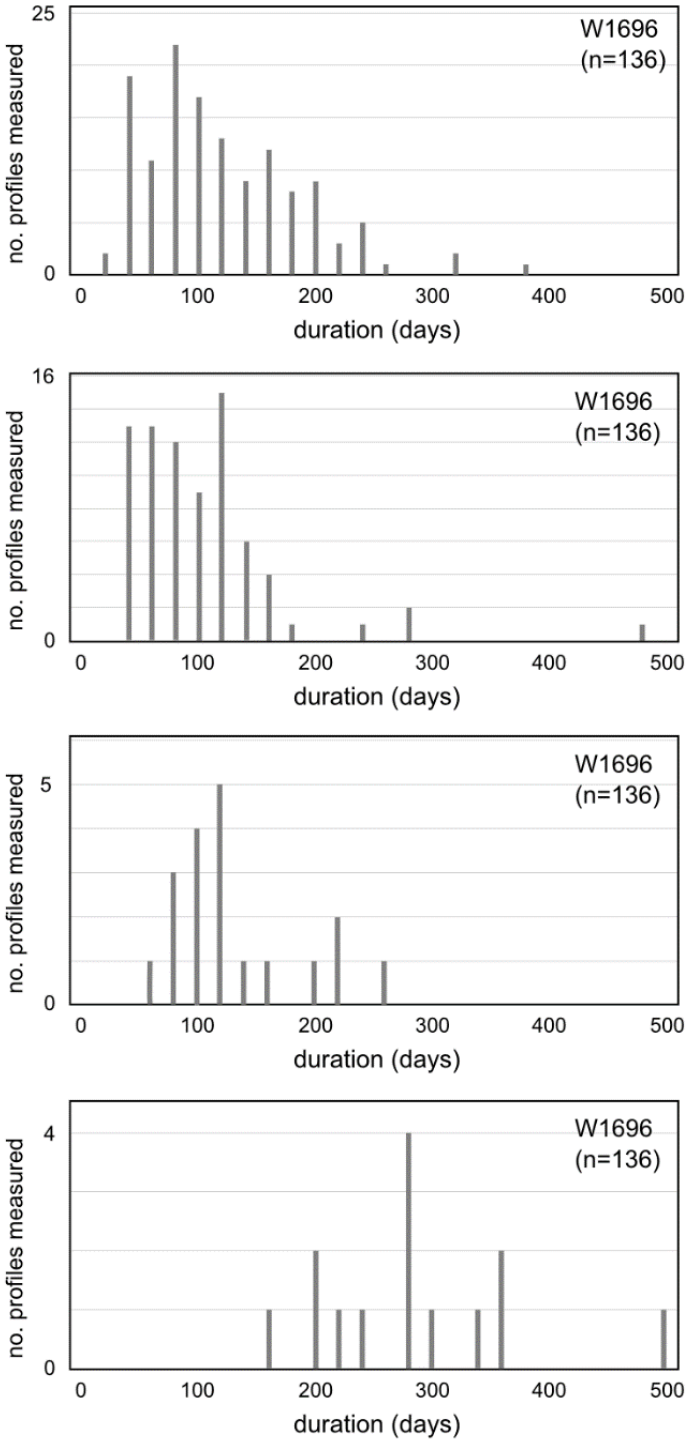
W1696
(n=136)
no. profiles measured
duration (days)
0
100
200
300
400
500
25
16
5
4

Figure A8.7.

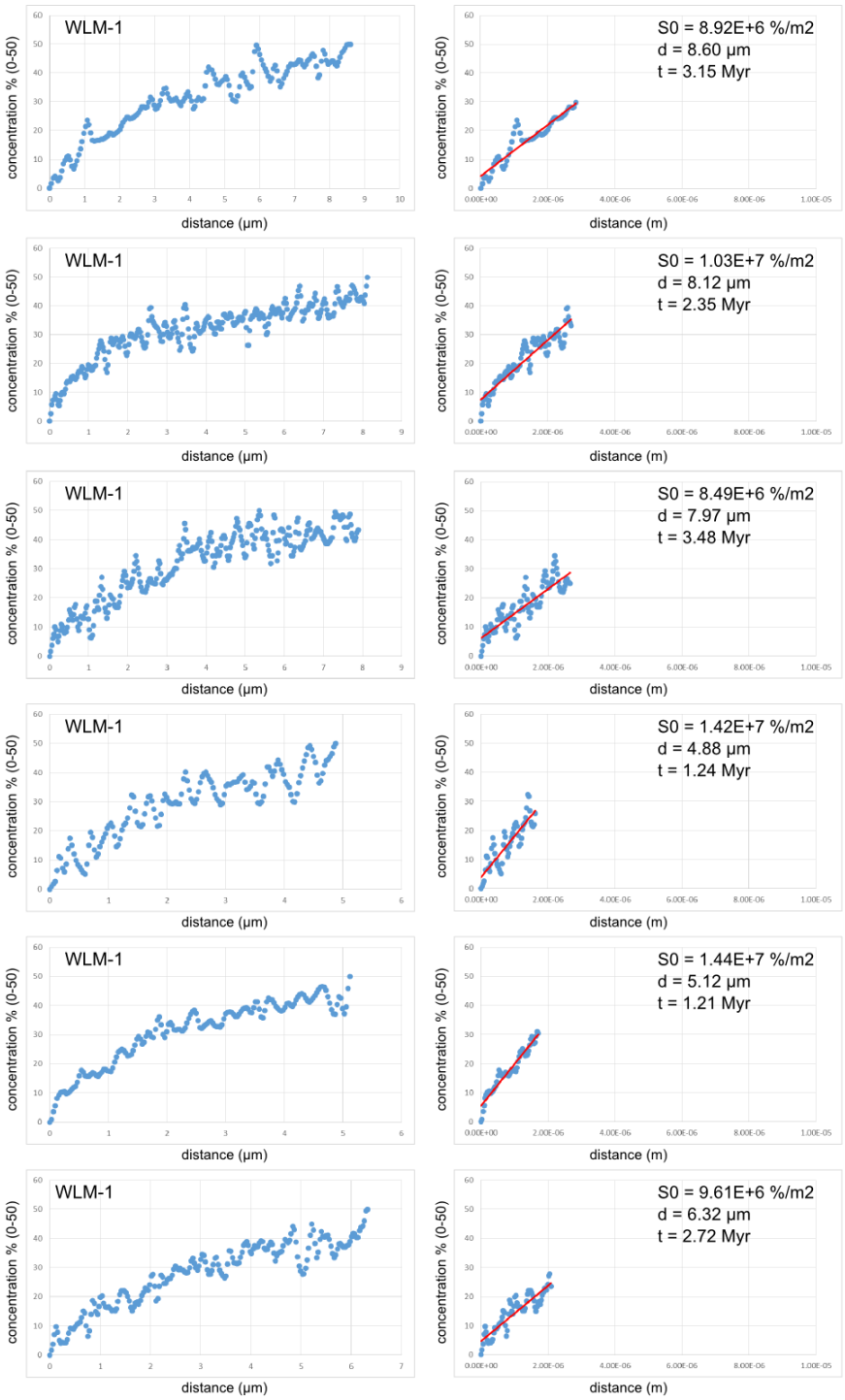
WLM-1
concentration % (0-50)
distance (μm)
S0 = 8.92E+6 %/m2
d = 8.60 μm
t = 3.15 Myr
distance (m)
WLM-1
concentration % (0-50)
distance (μm)
S0 = 1.03E+7 %/m2
d = 8.12 μm
t = 2.35 Myr
distance (m)
WLM-1
concentration % (0-50)
distance (μm)
S0 = 8.49E+6 %/m2
d = 7.97 μm
t = 3.48 Myr
distance (m)
WLM-1
concentration % (0-50)
distance (μm)
S0 = 1.42E+7 %/m2
d = 4.88 μm
t = 1.24 Myr
distance (m)
WLM-1
concentration % (0-50)
distance (μm)
S0 = 1.44E+7 %/m2
d = 5.12 μm
t = 1.21 Myr
distance (m)
WLM-1
concentration % (0-50)
distance (μm)
S0 = 9.61E+6 %/m2
d = 6.32 μm
t = 2.72 Myr
distance (m)

Figure A8.7 (cont.).

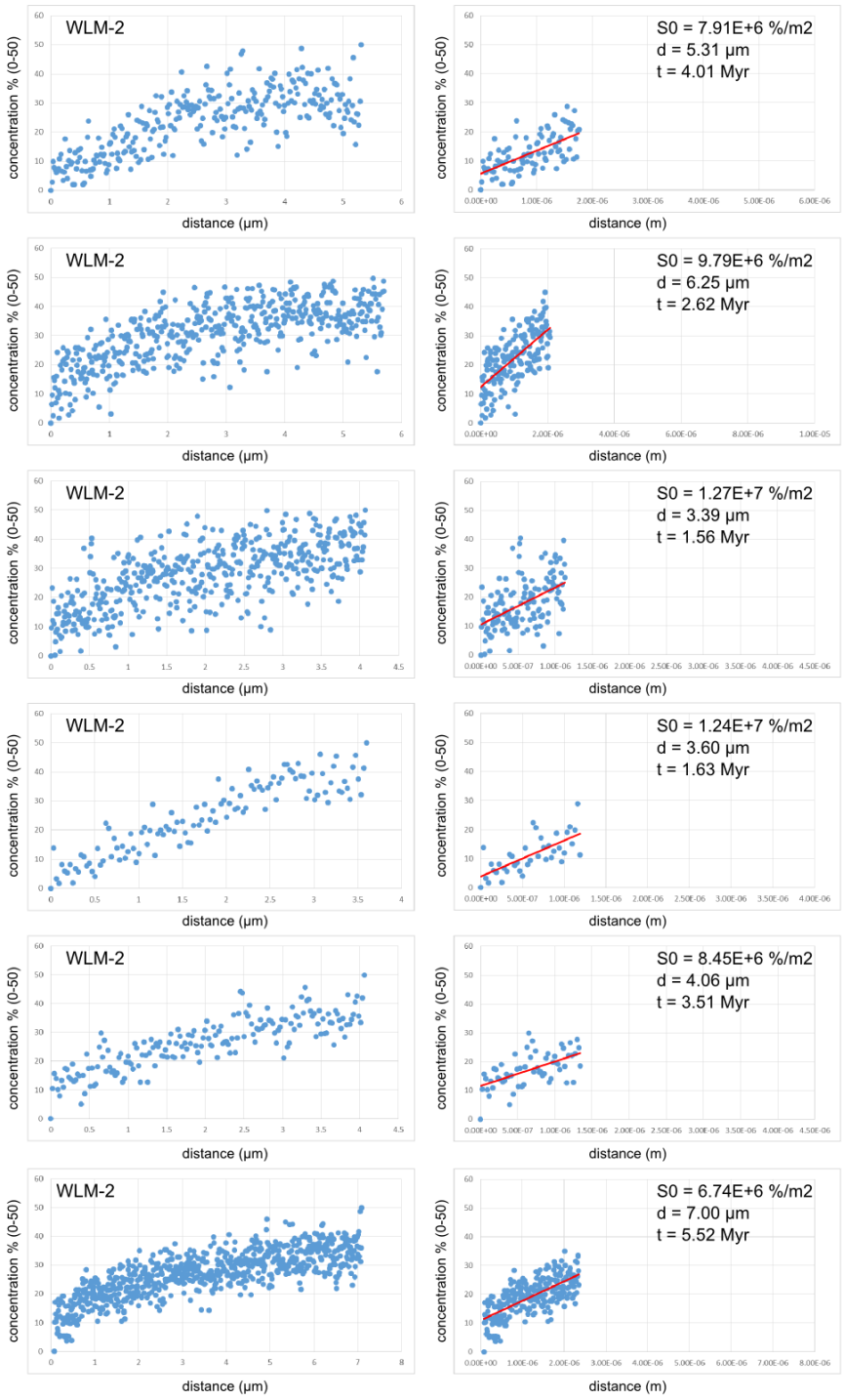

Figure A8.7 (cont.).

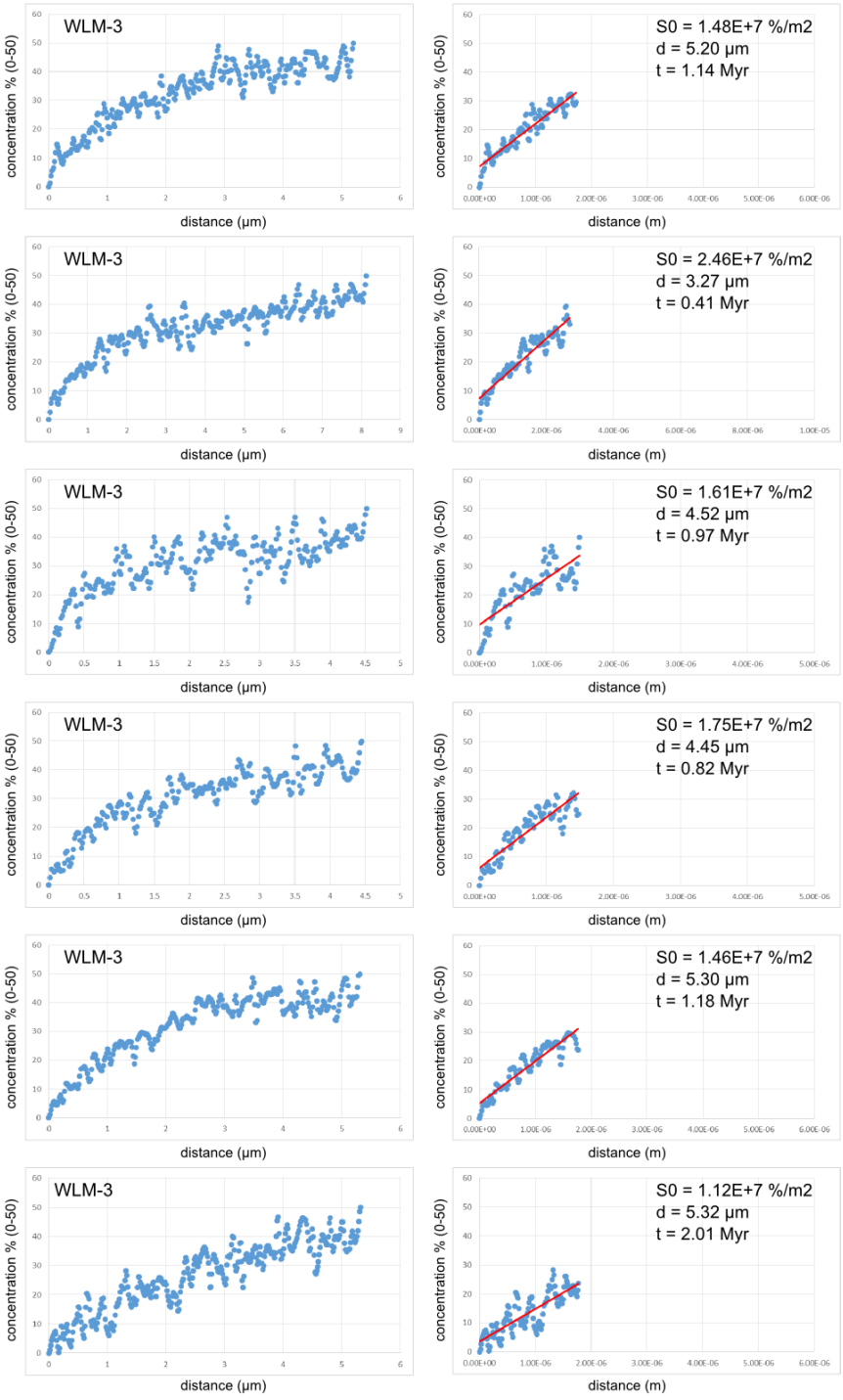

Figure A8.7 (cont.).

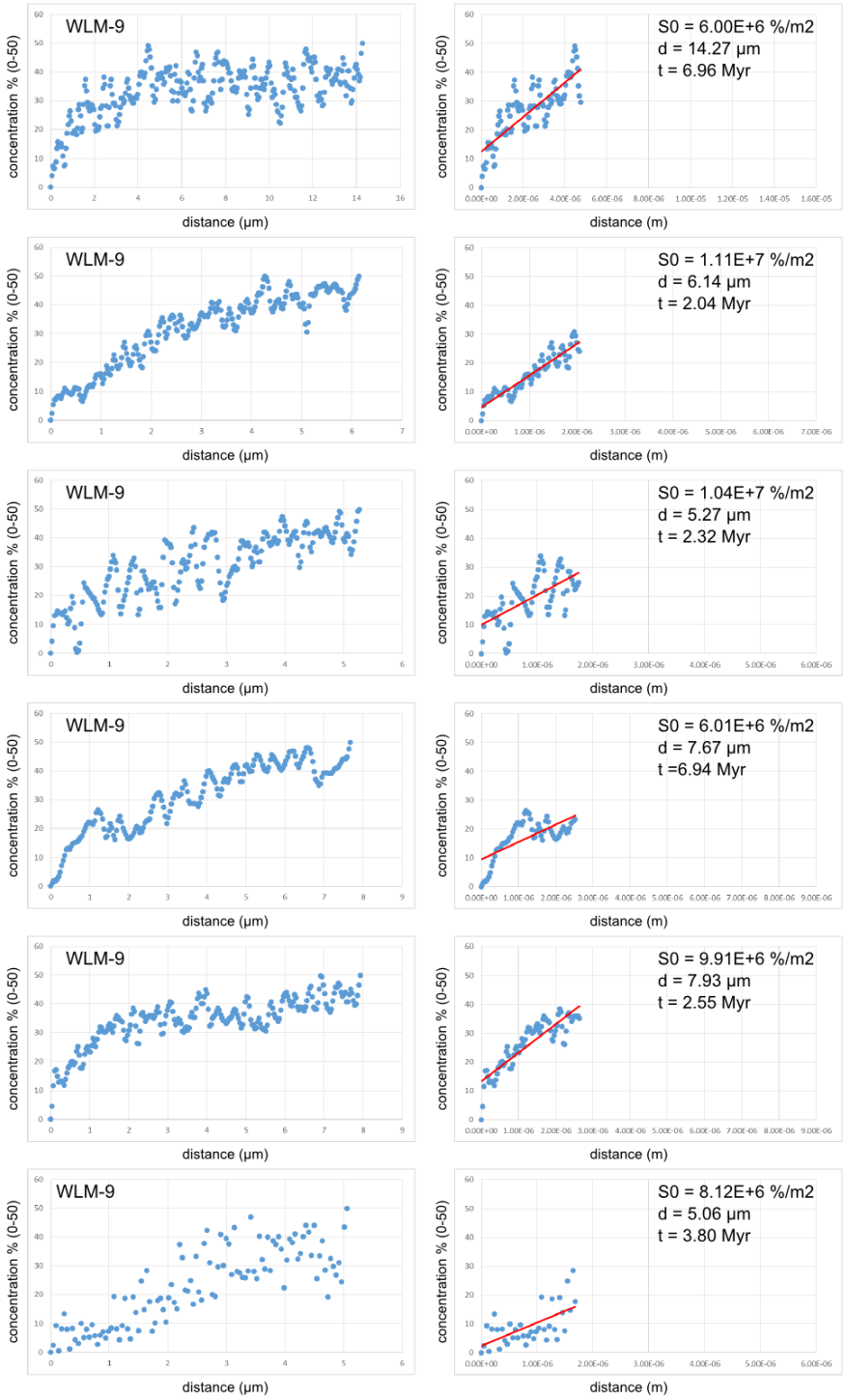

Figure A8.7 (cont.).

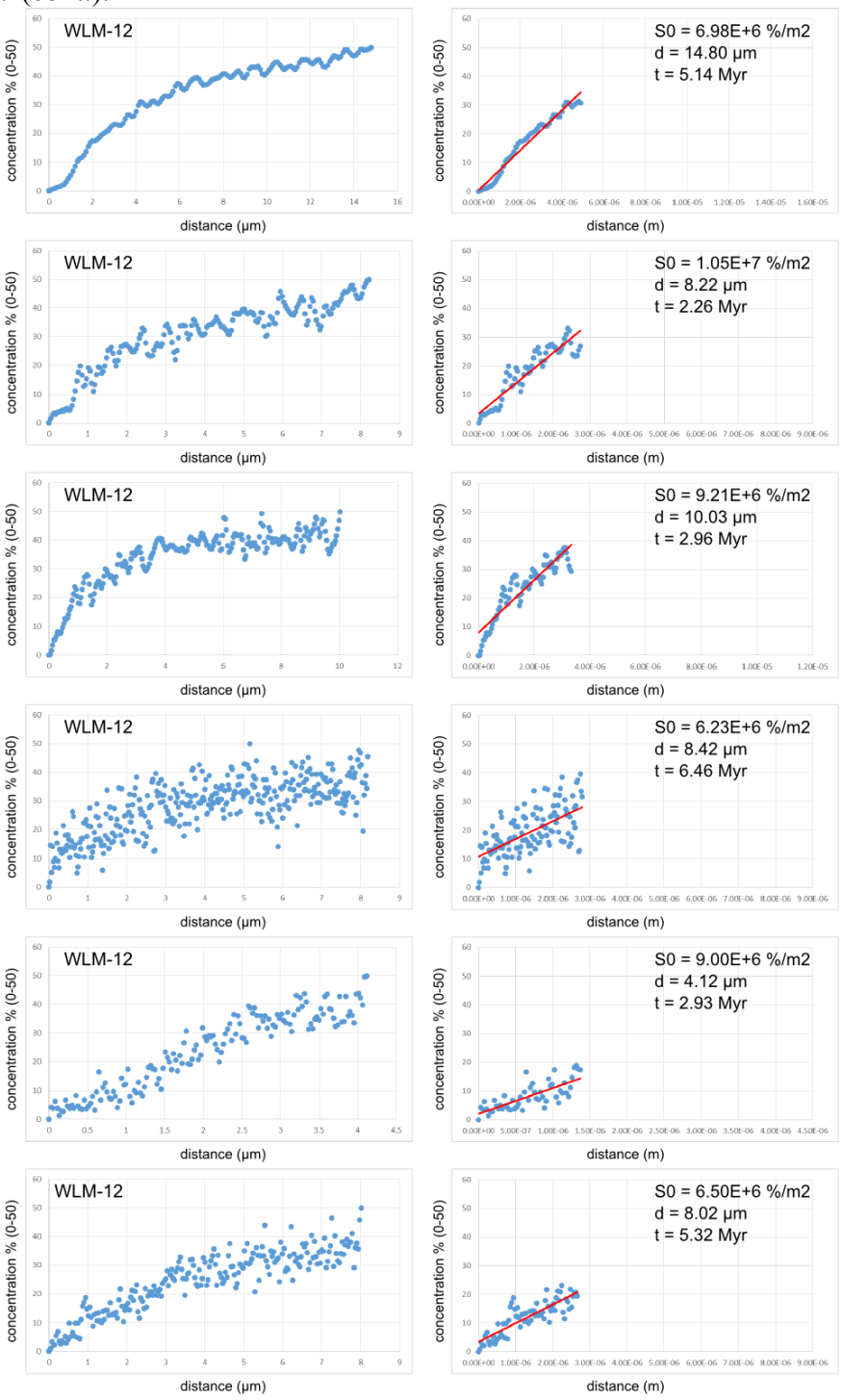

Figure A8.8.

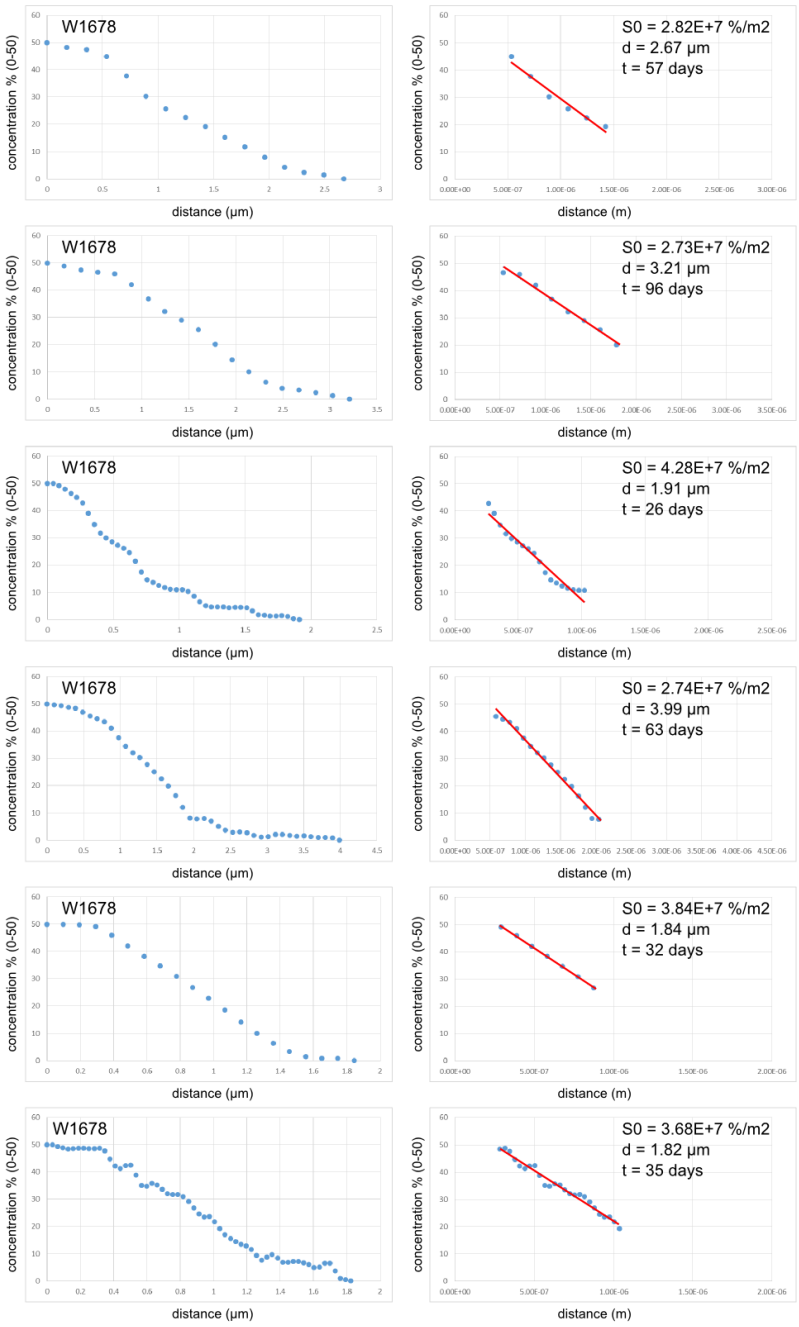
W1678
concentration % (0-50)
distance (µm)
S0 = 2.82E+7 %/m2
d = 2.67 µm
t = 57 days
distance (m)
W1678
concentration % (0-50)
distance (µm)
S0 = 2.73E+7 %/m2
d = 3.21 µm
t = 96 days
distance (m)
W1678
concentration % (0-50)
distance (µm)
S0 = 4.28E+7 %/m2
d = 1.91 µm
t = 26 days
distance (m)
W1678
concentration % (0-50)
distance (µm)
S0 = 2.74E+7 %/m2
d = 3.99 µm
t = 63 days
distance (m)
W1678
concentration % (0-50)
distance (µm)
S0 = 3.84E+7 %/m2
d = 1.84 µm
t = 32 days
distance (m)
W1678
concentration % (0-50)
distance (µm)
S0 = 3.68E+7 %/m2
d = 1.82 µm
t = 35 days
distance (m)

Figure A8.8 (cont.).

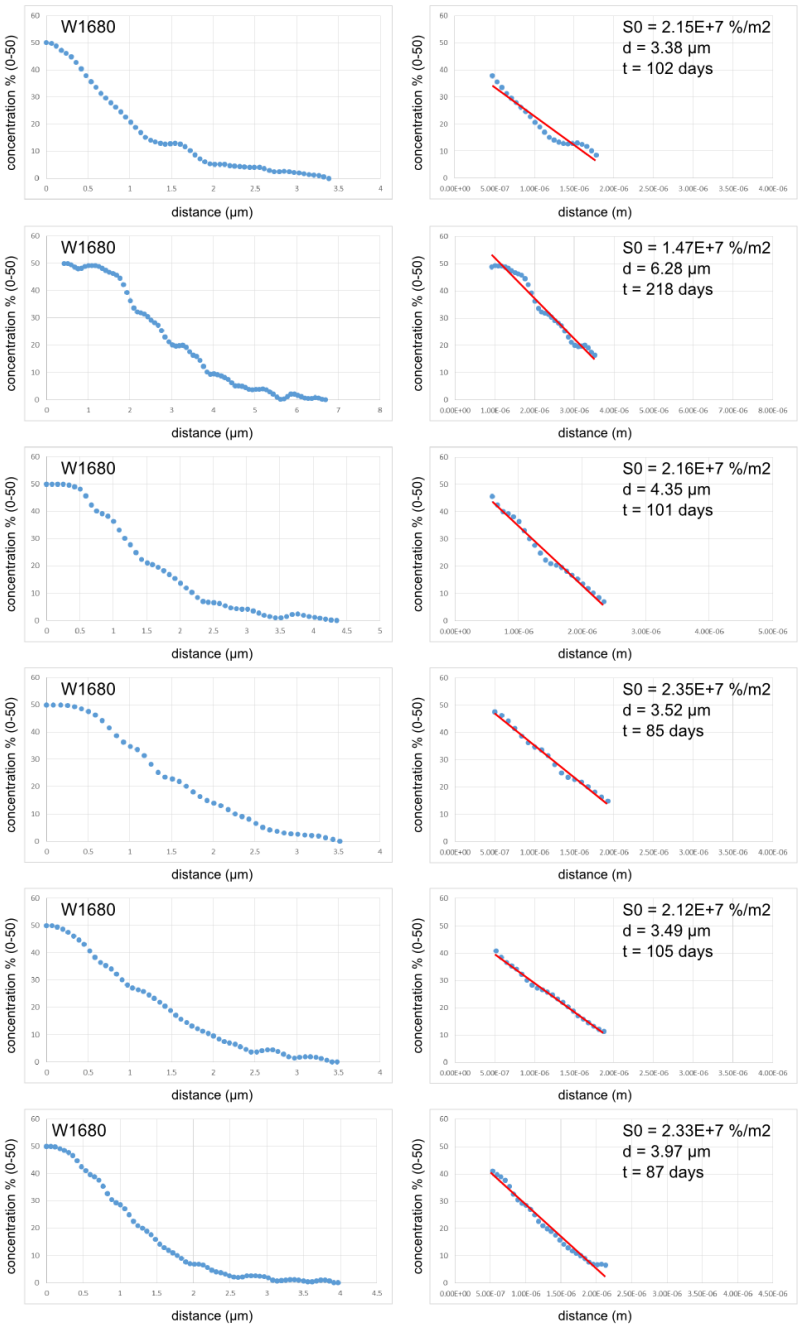

Figure A8.8 (cont.).

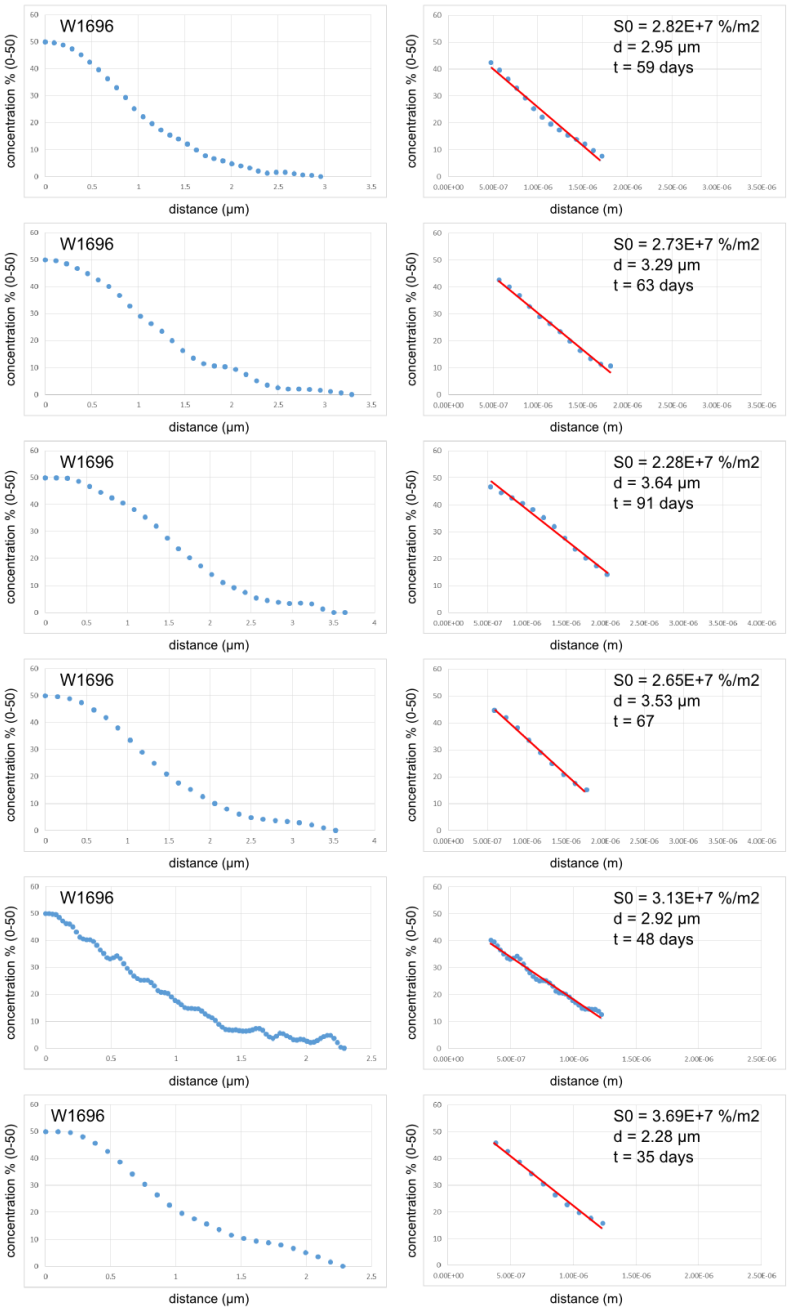

Figure A8.8 (cont.).

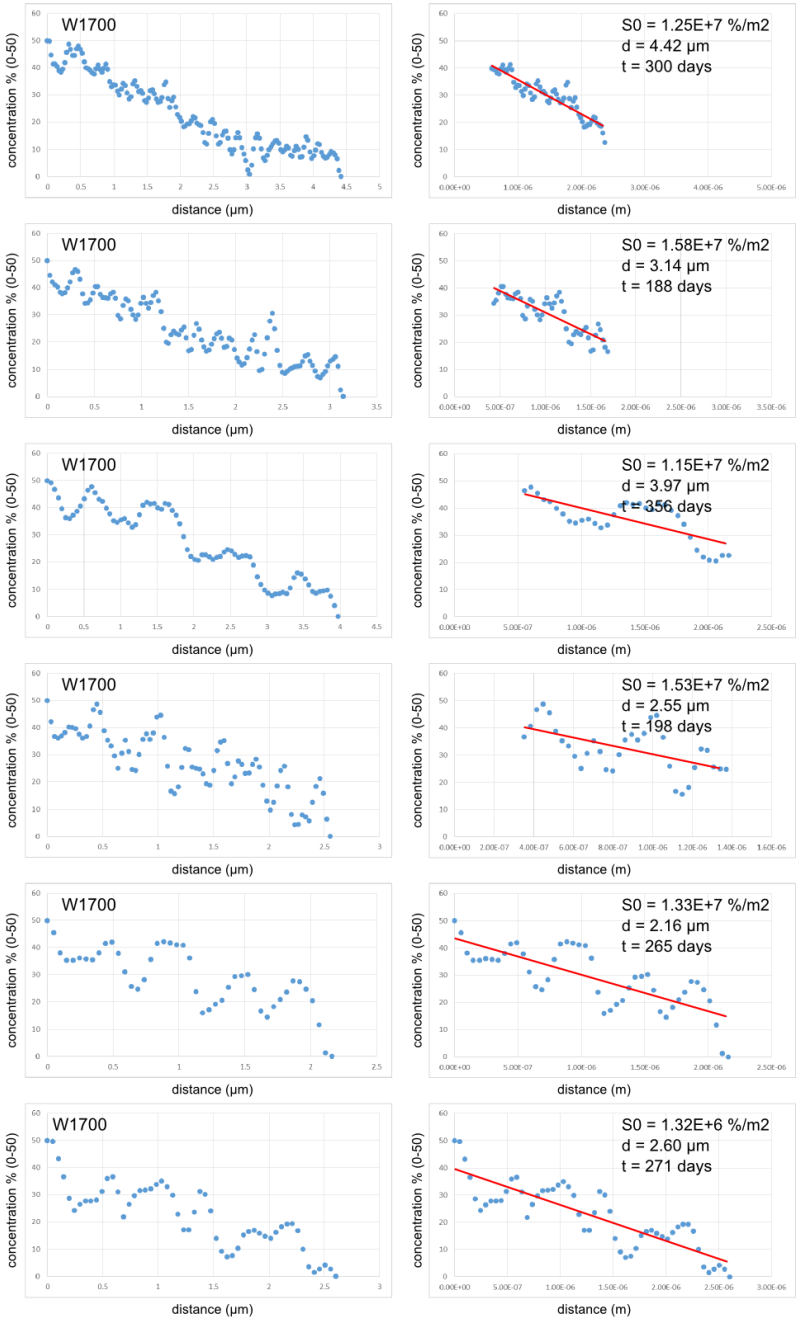

Figure A8.9.

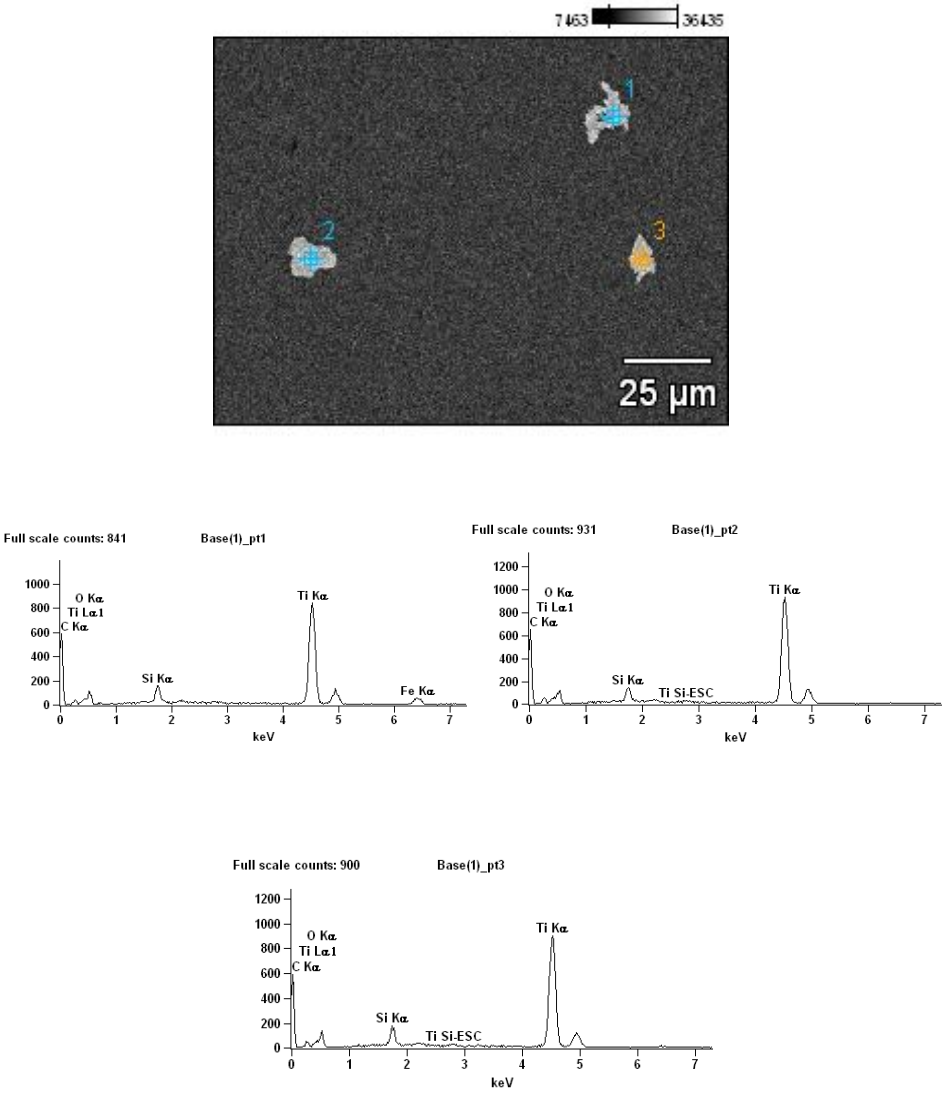
7463
36435
1
2
3
25 µm
Full scale counts: 841
Base(1)_pt1
O Kα
Ti Lα1
C Kα
Si Kα
Ti Kα
Fe Kα
keV
Full scale counts: 931
Base(1)_pt2
O Kα
Ti Lα1
C Kα
Si Kα
Ti Si-ESC
Ti Kα
keV
Full scale counts: 900
Base(1)_pt3
O Kα
Ti Lα1
C Kα
Si Kα
Ti Si-ESC
Ti Kα
keV

Figure A8.9 (cont.).

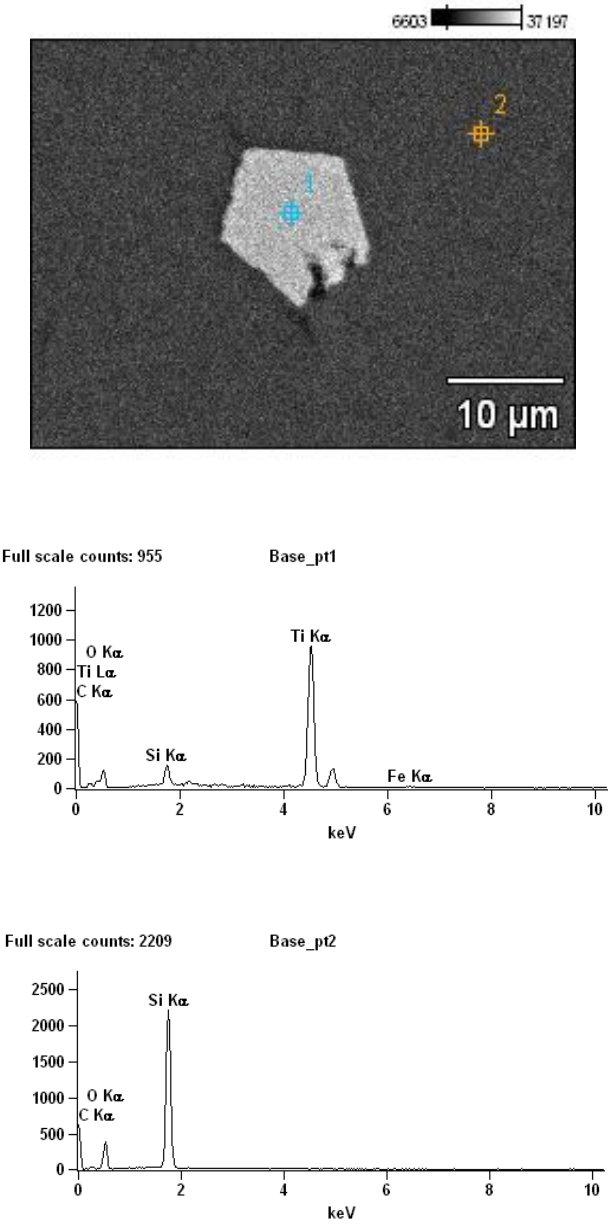

Appendix 9

Supplementary Tables for Chapter 5

Table A9.1. Results of diffusion modeling analysis of natural samples.

Table A9.2. Results of diffusion modeling analysis of experimental samples.

Appendix 9

Table A9.1. Results of diffusion modeling analysis of natural samples.

Sample	ID	thickness (um)	S0 (%/m)	Dt (m^2) at 500 C	t (sec)	t (Myr)	Tdot (deg./s)	Tdot deg/Myr
WLM-1	1	7.8404	1.79E+06	6.17E-11	2.46E+15	77.86	1.75E-15	5.52E-02
WLM-1	2	10.6889	2.15E+06	4.30E-11	1.71E+15	54.19	2.51E-15	7.93E-02
WLM-1	3	7.1333	2.03E+06	4.81E-11	1.91E+15	60.71	2.24E-15	7.07E-02
WLM-1	4	2.809	7.77E+06	3.29E-12	1.31E+14	4.15	3.28E-14	1.03E+00
WLM-1	5	6.6573	7.04E+06	4.01E-12	1.60E+14	5.06	2.69E-14	8.49E-01
WLM-1	6	8.427	6.75E+06	4.36E-12	1.74E+14	5.50	2.47E-14	7.80E-01
WLM-1	7	8.5958	8.92E+06	2.50E-12	9.94E+13	3.15	4.32E-14	1.36E+00
WLM-1	8	5.3762	1.01E+07	1.94E-12	7.72E+13	2.45	5.56E-14	1.75E+00
WLM-1	9	7.8551	5.17E+06	7.45E-12	2.96E+14	9.39	1.45E-14	4.57E-01
WLM-1	10	4.0088	1.49E+07	8.92E-13	3.55E+13	1.12	1.21E-13	3.82E+00
WLM-1	11	8.1225	1.03E+07	1.86E-12	7.41E+13	2.35	5.80E-14	1.83E+00
WLM-1	12	7.5795	7.58E+06	3.46E-12	1.38E+14	4.36	3.12E-14	9.84E-01
WLM-1	13	5.7123	6.97E+06	4.09E-12	1.63E+14	5.16	2.64E-14	8.32E-01
WLM-1	14	6.3611	4.92E+06	8.22E-12	3.27E+14	10.36	1.31E-14	4.14E-01
WLM-1	15	10.4225	5.12E+06	7.58E-12	3.01E+14	9.56	1.43E-14	4.49E-01
WLM-1	16	3.8828	2.24E+07	3.96E-13	1.58E+13	0.50	2.73E-13	8.60E+00
WLM-1	17	4.3617	6.69E+06	4.44E-12	1.77E+14	5.60	2.43E-14	7.66E-01
WLM-1	18	12.1542	4.80E+06	8.65E-12	3.44E+14	10.91	1.25E-14	3.94E-01
WLM-1	19	2.4	1.90E+07	5.48E-13	2.18E+13	0.69	1.97E-13	6.21E+00
WLM-1	20	5.2855	1.16E+07	1.47E-12	5.84E+13	1.85	7.35E-14	2.32E+00
WLM-1	21	7.9681	8.49E+06	2.76E-12	1.10E+14	3.48	3.92E-14	1.24E+00
WLM-1	22	5.4714	7.77E+06	3.29E-12	1.31E+14	4.15	3.28E-14	1.03E+00
WLM-1	23	4.8786	1.42E+07	9.85E-13	3.92E+13	1.24	1.10E-13	3.46E+00
WLM-1	24	6.7793	6.13E+06	5.29E-12	2.10E+14	6.67	2.04E-14	6.44E-01
WLM-1	25	5.1212	1.44E+07	9.60E-13	3.82E+13	1.21	1.12E-13	3.55E+00
WLM-1	26	6.3224	9.61E+06	2.15E-12	8.57E+13	2.72	5.01E-14	1.58E+00
WLM-1	27	3.5897	1.57E+07	8.04E-13	3.20E+13	1.01	1.34E-13	4.24E+00
				0.00E+00				
WLM-2	1	2.7488	2.10E+07	4.51E-13	1.79E+13	0.57	2.39E-13	7.55E+00
WLM-2	2	5.3081	7.91E+06	3.18E-12	1.26E+14	4.01	3.40E-14	1.07E+00
WLM-2	3	3.2607	1.76E+07	6.41E-13	2.55E+13	0.81	1.68E-13	5.31E+00
WLM-2	4	3.498	1.46E+07	9.31E-13	3.70E+13	1.17	1.16E-13	3.66E+00
WLM-2	5	4.8	8.09E+06	3.04E-12	1.21E+14	3.83	3.56E-14	1.12E+00
WLM-2	6	4	9.10E+06	2.40E-12	9.55E+13	3.03	4.50E-14	1.42E+00
WLM-2	7	6.248	9.79E+06	2.08E-12	8.25E+13	2.62	5.20E-14	1.64E+00
WLM-2	8	3.3906	1.27E+07	1.24E-12	4.93E+13	1.56	8.70E-14	2.75E+00
WLM-2	9	2.3738	7.34E+06	3.69E-12	1.47E+14	4.66	2.92E-14	9.22E-01

WLM-2	10	10.1458	3.72E+06	1.44E-11	5.71E+14	18.10	7.52E-15	2.37E-01
WLM-2	11	6.6188	3.81E+06	1.37E-11	5.46E+14	17.32	7.86E-15	2.48E-01
WLM-2	12	3.6031	1.24E+07	1.30E-12	5.15E+13	1.63	8.33E-14	2.63E+00
WLM-2	13	4.058	8.45E+06	2.79E-12	1.11E+14	3.51	3.88E-14	1.22E+00
WLM-2	14	10.6658	5.08E+06	7.72E-12	3.07E+14	9.73	1.40E-14	4.41E-01
WLM-2	15	7	6.74E+06	4.37E-12	1.74E+14	5.52	2.47E-14	7.78E-01
WLM-3	1	21.9799	2.23E+06	3.99E-11	1.59E+15	50.34	2.71E-15	8.53E-02
WLM-3	2	21.8078	2.85E+06	2.44E-11	9.72E+14	30.84	4.42E-15	1.39E-01
WLM-3	3	5.1962	1.48E+07	9.04E-13	3.60E+13	1.14	1.19E-13	3.76E+00
WLM-3	4	8.4585	6.27E+06	5.05E-12	2.01E+14	6.37	2.14E-14	6.74E-01
WLM-3	5	2.8228	2.39E+07	3.49E-13	1.39E+13	0.44	3.09E-13	9.76E+00
WLM-3	6	6.1137	5.11E+06	7.62E-12	3.03E+14	9.61	1.42E-14	4.47E-01
WLM-3	7	3.5649	6.19E+06	5.19E-12	2.06E+14	6.54	2.08E-14	6.57E-01
WLM-3	8	7.5945	3.89E+06	1.31E-11	5.23E+14	16.58	8.21E-15	2.59E-01
WLM-3	9	2.6125	2.00E+07	4.97E-13	1.98E+13	0.63	2.17E-13	6.85E+00
WLM-3	10	3.269	2.46E+07	3.29E-13	1.31E+13	0.41	3.29E-13	1.04E+01
WLM-3	11	4.4842	1.45E+07	9.41E-13	3.74E+13	1.19	1.15E-13	3.62E+00
WLM-3	12	4.5193	1.61E+07	7.69E-13	3.06E+13	0.97	1.40E-13	4.43E+00
WLM-3	13	6.5025	8.99E+06	2.46E-12	9.80E+13	3.11	4.38E-14	1.38E+00
WLM-3	14	4.452	1.75E+07	6.48E-13	2.58E+13	0.82	1.67E-13	5.26E+00
WLM-3	15	5.4987	1.13E+07	1.57E-12	6.24E+13	1.98	6.88E-14	2.17E+00
WLM-3	16	4.9105	1.43E+07	9.74E-13	3.88E+13	1.23	1.11E-13	3.49E+00
WLM-3	17	4.6282	1.38E+07	1.05E-12	4.17E+13	1.32	1.03E-13	3.24E+00
WLM-3	18	4.7388	6.02E+06	5.49E-12	2.18E+14	6.93	1.97E-14	6.20E-01
WLM-3	19	5.3038	1.46E+07	9.36E-13	3.73E+13	1.18	1.15E-13	3.64E+00
WLM-3	20	9.1271	4.65E+06	9.20E-12	3.66E+14	11.61	1.17E-14	3.70E-01
WLM-3	21	5.3211	1.12E+07	1.59E-12	6.33E+13	2.01	6.78E-14	2.14E+00
WLM-3	22	6.054	7.15E+06	3.89E-12	1.55E+14	4.91	2.77E-14	8.74E-01
WLM-3	23	6.3973	7.79E+06	3.28E-12	1.30E+14	4.13	3.30E-14	1.04E+00
WLM-3	24	10.9959	3.47E+06	1.65E-11	6.56E+14	20.81	6.54E-15	2.06E-01
WLM-9	1	14.2723	6.00E+06	5.51E-12	2.19E+14	6.96	1.96E-14	6.17E-01
WLM-9	2	3.1278	1.90E+07	5.49E-13	2.18E+13	0.69	1.97E-13	6.20E+00
WLM-9	3	6.1364	1.11E+07	1.62E-12	6.45E+13	2.04	6.66E-14	2.10E+00
WLM-9	4	4.1742	1.31E+07	1.16E-12	4.62E+13	1.46	9.30E-14	2.93E+00
WLM-9	5	3.8138	1.96E+07	5.18E-13	2.06E+13	0.65	2.08E-13	6.57E+00
WLM-9	6	5.9435	8.43E+06	2.80E-12	1.11E+14	3.53	3.86E-14	1.22E+00
WLM-9	7	5.2655	1.04E+07	1.84E-12	7.30E+13	2.32	5.88E-14	1.85E+00
WLM-9	8	2.4831	2.38E+07	3.51E-13	1.40E+13	0.44	3.08E-13	9.71E+00
WLM-9	9	2.4561	2.39E+07	3.48E-13	1.38E+13	0.44	3.10E-13	9.78E+00
WLM-9	10	3.4818	1.17E+07	1.46E-12	5.81E+13	1.84	7.39E-14	2.33E+00
WLM-9	11	4.6154	1.46E+07	9.31E-13	3.70E+13	1.17	1.16E-13	3.66E+00
WLM-9	12	2.5375	1.40E+07	1.01E-12	4.03E+13	1.28	1.07E-13	3.36E+00
WLM-9	13	5.9743	8.24E+06	2.93E-12	1.17E+14	3.69	3.69E-14	1.16E+00
WLM-9	14	6.3276	2.57E+06	3.00E-11	1.19E+15	37.87	3.60E-15	1.13E-01
WLM-9	15	4.5289	1.18E+07	1.43E-12	5.68E+13	1.80	7.57E-14	2.39E+00

WLM-9	16	2.6981	2.29E+07	3.80E-13	1.51E+13	0.48	2.84E-13	8.95E+00
WLM-9	17	3.6145	1.66E+07	7.21E-13	2.87E+13	0.91	1.50E-13	4.72E+00
WLM-9	18	7.6707	6.01E+06	5.50E-12	2.19E+14	6.94	1.96E-14	6.19E-01
WLM-9	19	3.7751	1.92E+07	5.41E-13	2.15E+13	0.68	1.99E-13	6.29E+00
WLM-9	20	5.0616	1.84E+07	5.89E-13	2.34E+13	0.74	1.83E-13	5.78E+00
WLM-9	21	3.1404	1.37E+07	1.06E-12	4.21E+13	1.34	1.02E-13	3.21E+00
WLM-9	22	6.3732	1.60E+07	7.78E-13	3.09E+13	0.98	1.39E-13	4.38E+00
WLM-9	23	4.0845	1.73E+07	6.66E-13	2.65E+13	0.84	1.62E-13	5.11E+00
WLM-9	24	7.9298	9.91E+06	2.02E-12	8.05E+13	2.55	5.33E-14	1.68E+00
WLM-9	25	4.4211	1.14E+07	1.53E-12	6.07E+13	1.92	7.08E-14	2.23E+00
WLM-9	26	5.06	1.75E+07	6.53E-13	2.60E+13	0.82	1.65E-13	5.22E+00
WLM-9	27	1.9159	1.76E+07	6.44E-13	2.56E+13	0.81	1.68E-13	5.28E+00
WLM-9	28	3.7422	8.98E+06	2.46E-12	9.80E+13	3.11	4.38E-14	1.38E+00
WLM-9	29	3.6175	1.15E+07	1.50E-12	5.98E+13	1.90	7.18E-14	2.26E+00
WLM-9	30	3.8046	2.63E+07	2.88E-13	1.15E+13	0.36	3.74E-13	1.18E+01
WLM-9	31	2.875	2.51E+07	3.15E-13	1.25E+13	0.40	3.43E-13	1.08E+01
WLM-9	32	4.4283	1.31E+07	1.16E-12	4.60E+13	1.46	9.33E-14	2.94E+00
WLM-9	33	6.0499	1.06E+07	1.76E-12	7.00E+13	2.22	6.14E-14	1.94E+00
WLM-9	34	7.8683	4.02E+06	1.23E-11	4.89E+14	15.49	8.79E-15	2.77E-01
WLM-9	35	3.8475	1.71E+07	6.76E-13	2.69E+13	0.85	1.60E-13	5.03E+00
WLM-9	36	4.4496	7.29E+06	3.75E-12	1.49E+14	4.72	2.88E-14	9.09E-01
WLM-9	37	5.0585	8.12E+06	3.02E-12	1.20E+14	3.80	3.58E-14	1.13E+00
WLM-9	38	2.5882	1.54E+07	8.36E-13	3.32E+13	1.05	1.29E-13	4.07E+00
WLM-9	39	4.0858	6.31E+06	4.99E-12	1.98E+14	6.29	2.16E-14	6.82E-01
WLM-9	40	4.7887	1.16E+07	1.49E-12	5.92E+13	1.88	7.26E-14	2.29E+00
WLM-9	41	5.8685	1.98E+06	5.08E-11	2.02E+15	64.07	2.13E-15	6.70E-02
WLM-9	42	4.507	1.31E+07	1.15E-12	4.58E+13	1.45	9.37E-14	2.96E+00
WLM-9	43	6.1502	7.60E+06	3.44E-12	1.37E+14	4.34	3.14E-14	9.90E-01
WLM-12	1	3.5783	2.27E+07	3.85E-13	1.53E+13	0.49	2.81E-13	8.85E+00
WLM-12	2	5.4092	1.60E+07	7.72E-13	3.07E+13	0.97	1.40E-13	4.41E+00
WLM-12	3	3.798	1.72E+07	6.74E-13	2.68E+13	0.85	1.60E-13	5.05E+00
WLM-12	4	5.5364	8.25E+06	2.92E-12	1.16E+14	3.68	3.70E-14	1.17E+00
WLM-12	5	4.3767	1.04E+07	1.84E-12	7.32E+13	2.32	5.87E-14	1.85E+00
WLM-12	6	2.5199	1.45E+07	9.51E-13	3.78E+13	1.20	1.13E-13	3.58E+00
WLM-12	7	14.8	6.98E+06	4.08E-12	1.62E+14	5.14	2.65E-14	8.35E-01
WLM-12	8	23.1	4.01E+06	1.23E-11	4.91E+14	15.56	8.75E-15	2.76E-01
WLM-12	9	5.4705	1.76E+07	6.45E-13	2.57E+13	0.81	1.67E-13	5.28E+00
WLM-12	10	17.8476	3.57E+06	1.56E-11	6.21E+14	19.69	6.92E-15	2.18E-01
WLM-12	11	15.2449	3.54E+06	1.59E-11	6.33E+14	20.07	6.79E-15	2.14E-01
WLM-12	12	10.2694	6.11E+06	5.33E-12	2.12E+14	6.72	2.03E-14	6.39E-01
WLM-12	13	10.7744	7.60E+06	3.45E-12	1.37E+14	4.35	3.13E-14	9.88E-01
WLM-12	14	13.1313	5.50E+06	6.58E-12	2.62E+14	8.30	1.64E-14	5.18E-01
WLM-12	15	8.5859	9.11E+06	2.39E-12	9.52E+13	3.02	4.51E-14	1.42E+00
WLM-12	16	7.9966	1.26E+07	1.24E-12	4.94E+13	1.57	8.69E-14	2.74E+00
WLM-12	17	8.2163	1.05E+07	1.79E-12	7.14E+13	2.26	6.02E-14	1.90E+00
WLM-12	18	10.0281	9.21E+06	2.34E-12	9.33E+13	2.96	4.60E-14	1.45E+00

WLM-12	19	6.1423	6.54E+06	4.64E-12	1.85E+14	5.86	2.33E-14	7.33E-01
WLM-12	20	8.015	6.50E+06	4.70E-12	1.87E+14	5.93	2.30E-14	7.24E-01
WLM-12	21	10.6562	3.63E+06	1.51E-11	6.01E+14	19.07	7.14E-15	2.25E-01
WLM-12	22	8.4884	6.39E+06	4.87E-12	1.94E+14	6.15	2.22E-14	6.99E-01
WLM-12	23	8.4186	6.23E+06	5.12E-12	2.04E+14	6.46	2.11E-14	6.65E-01
WLM-12	24	12.8598	3.31E+06	1.82E-11	7.23E+14	22.94	5.94E-15	1.87E-01
WLM-12	25	1.4609	1.46E+07	9.28E-13	3.69E+13	1.17	1.16E-13	3.67E+00
WLM-12	26	2.4116	1.28E+07	1.21E-12	4.80E+13	1.52	8.95E-14	2.82E+00
WLM-12	27	3.2	1.45E+07	9.46E-13	3.76E+13	1.19	1.14E-13	3.60E+00
WLM-12	28	4.1166	9.00E+06	2.45E-12	9.75E+13	3.09	4.40E-14	1.39E+00
WLM-12	29	3.3632	2.63E+07	2.88E-13	1.15E+13	0.36	3.74E-13	1.18E+01

Appendix 9

Table A9.2. Results of diffusion modeling analysis of experimental samples.

Sample_SEM	Profile no.	thickness (um)	S0 (%/m)	Dt (m^2)	t (sec)	t (days)	D (m^2/s)	log D (m^2/s)
W1696_USGS	1	2.954	2.824E+07	2.494E-13	5.099E+06	59.0	1.78E-18	-17.7505
W1696_USGS	2	2.954	2.442E+07	3.335E-13	6.820E+06	78.9	2.38E-18	-17.6243
W1696_USGS	3	2.954	2.567E+07	3.016E-13	6.168E+06	71.4	2.15E-18	-17.6679
W1696_USGS	4	3.526	2.072E+07	4.631E-13	9.471E+06	109.6	3.3E-18	-17.4817
W1696_USGS	5	2.668	2.709E+07	2.710E-13	5.542E+06	64.1	1.93E-18	-17.7144
W1696_USGS	6	3.413	2.029E+07	4.831E-13	9.879E+06	114.3	3.44E-18	-17.4633
W1696_USGS	7	3.851	1.833E+07	5.920E-13	1.211E+07	140.1	4.22E-18	-17.3751
W1696_USGS	8	3.288	2.728E+07	2.672E-13	5.464E+06	63.2	1.9E-18	-17.7206
W1696_USGS	9	2.948	2.236E+07	3.976E-13	8.130E+06	94.1	2.83E-18	-17.548
W1696_USGS	10	3.742	2.184E+07	4.167E-13	8.521E+06	98.6	2.97E-18	-17.5276
W1696_USGS	11	3.515	1.829E+07	5.945E-13	1.216E+07	140.7	4.23E-18	-17.3732
W1696_USGS	12	4.535	1.487E+07	8.989E-13	1.838E+07	212.8	6.4E-18	-17.1937
W1696_USGS	13	2.721	1.835E+07	5.904E-13	1.207E+07	139.7	4.21E-18	-17.3762
W1696_USGS	14	3.644	2.275E+07	3.840E-13	7.853E+06	90.9	2.73E-18	-17.5631
W1696_USGS	15	4.453	1.684E+07	7.010E-13	1.434E+07	165.9	4.99E-18	-17.3017
W1696_USGS	16	3.644	9.537E+06	2.186E-12	4.470E+07	517.4	1.56E-17	-16.8077
W1696_USGS	17	3.104	2.584E+07	2.977E-13	6.088E+06	70.5	2.12E-18	-17.6736
W1696_USGS	18	3.374	2.249E+07	3.930E-13	8.036E+06	93.0	2.8E-18	-17.553
W1696_USGS	19	3.235	2.918E+07	2.336E-13	4.776E+06	55.3	1.66E-18	-17.779
W1696_USGS	20	4.706	1.456E+07	9.374E-13	1.917E+07	221.9	6.68E-18	-17.1754
W1696_USGS	21	4.559	1.599E+07	7.777E-13	1.590E+07	184.1	5.54E-18	-17.2566
W1696_USGS	22	4.559	1.250E+07	1.272E-12	2.601E+07	301.0	9.06E-18	-17.043
W1696_USGS	23	4.559	1.416E+07	9.911E-13	2.027E+07	234.6	7.06E-18	-17.1513
W1696_USGS	24	4.118	1.660E+07	7.213E-13	1.475E+07	170.7	5.14E-18	-17.2893
W1696_USGS	25	3.529	2.652E+07	2.826E-13	5.779E+06	66.9	2.01E-18	-17.6962
W1696_USGS	26	4.118	1.805E+07	6.104E-13	1.248E+07	144.5	4.35E-18	-17.3618
W1696_USGS	27	4.853	1.547E+07	8.308E-13	1.699E+07	196.6	5.92E-18	-17.2279
W1696_USGS	28	2.494	3.554E+07	1.574E-13	3.219E+06	37.3	1.12E-18	-17.9503
W1696_USGS	29	4.265	2.824E+07	2.494E-13	5.099E+06	59.0	1.78E-18	-17.7505
W1696_USGS	30	3.824	2.442E+07	3.335E-13	6.820E+06	78.9	2.38E-18	-17.6243
W1696_USGS	31	3.382	2.567E+07	3.016E-13	6.168E+06	71.4	2.15E-18	-17.6679
W1696_USGS	32	3.382	2.746E+07	2.637E-13	5.393E+06	62.4	1.88E-18	-17.7262
W1696_USGS	33	3.677	1.404E+07	1.009E-12	2.063E+07	238.8	7.19E-18	-17.1436
W1696_USGS	34	3.824	1.691E+07	6.956E-13	1.422E+07	164.6	4.95E-18	-17.305
W1696_USGS	35	3.971	1.833E+07	5.920E-13	1.211E+07	140.1	4.22E-18	-17.3751
W1696_USGS	36	3.382	1.567E+07	8.095E-13	1.655E+07	191.6	5.77E-18	-17.2392
W1696_USGS	37	3.971	2.236E+07	3.976E-13	8.130E+06	94.1	2.83E-18	-17.548
W1696_USGS	38	3.529	2.184E+07	4.167E-13	8.521E+06	98.6	2.97E-18	-17.5276

W1696_USGS	39	2.087	1.829E+07	5.945E-13	1.216E+07	140.7	4.23E-18	-17.3732
W1696_USGS	40	2.087	1.487E+07	8.989E-13	1.838E+07	212.8	6.4E-18	-17.1937
W1696_USGS	41	2.167	1.970E+07	5.121E-13	1.047E+07	121.2	3.65E-18	-17.438
W1696_USGS	42	1.605	3.626E+07	1.512E-13	3.092E+06	35.8	1.08E-18	-17.9678
W1696_USGS	43	1.445	5.387E+07	6.851E-14	1.401E+06	16.2	4.88E-19	-18.3116
W1696_USGS	44	1.445	9.537E+06	2.186E-12	4.470E+07	517.4	1.56E-17	-16.8077
W1696_USGS	45	2.167	2.584E+07	2.977E-13	6.088E+06	70.5	2.12E-18	-17.6736
W1696_USGS	46	1.445	2.249E+07	3.930E-13	8.036E+06	93.0	2.8E-18	-17.553
W1696_USGS	47	1.605	5.823E+07	5.864E-14	1.199E+06	13.9	4.18E-19	-18.3792
W1696_USGS	48	2.006	1.456E+07	9.374E-13	1.917E+07	221.9	6.68E-18	-17.1754
W1696_USGS	49	1.846	4.221E+07	1.116E-13	2.282E+06	26.4	7.95E-19	-18.0998
W1696_USGS	50	1.766	1.250E+07	1.272E-12	2.601E+07	301.0	9.06E-18	-17.043
W1696_USGS	51	3.314	2.504E+07	3.171E-13	6.485E+06	75.1	2.26E-18	-17.6461
W1696_USGS	52	2.965	1.892E+07	5.556E-13	1.136E+07	131.5	3.96E-18	-17.4026
W1696_USGS	53	3.140	2.652E+07	2.826E-13	5.779E+06	66.9	2.01E-18	-17.6962
W1696_USGS	54	4.361	1.756E+07	6.447E-13	1.318E+07	152.6	4.59E-18	-17.338
W1696_USGS	55	4.361	1.756E+07	6.447E-13	1.318E+07	152.6	4.59E-18	-17.338
W1696_USGS	56	3.382	1.609E+07	7.676E-13	1.570E+07	181.7	5.47E-18	-17.2622
W1696_USGS	57	2.965	2.129E+07	4.388E-13	8.974E+06	103.9	3.13E-18	-17.5051
W1696_USGS	58	3.663	1.665E+07	7.174E-13	1.467E+07	169.8	5.11E-18	-17.2916
W1696_USGS	59	2.616	2.455E+07	3.299E-13	6.747E+06	78.1	2.35E-18	-17.629
W1696_USGS	60	2.442	1.405E+07	1.007E-12	2.060E+07	238.5	7.18E-18	-17.1442
W1696_USGS	61	2.965	2.935E+07	2.307E-13	4.718E+06	54.6	1.64E-18	-17.7843
W1696_USGS	62	2.442	3.307E+07	1.818E-13	3.718E+06	43.0	1.3E-18	-17.8877
W1696_USGS	63	1.919	3.721E+07	1.436E-13	2.936E+06	34.0	1.02E-18	-17.9903
W1696_USGS	64	2.791	2.240E+07	3.962E-13	8.102E+06	93.8	2.82E-18	-17.5495
W1696_USGS	65	2.093	3.446E+07	1.675E-13	3.425E+06	39.6	1.19E-18	-17.9234
W1696_USGS	66	3.314	3.554E+07	1.574E-13	3.219E+06	37.3	1.12E-18	-17.9503
W1696_USGS	67	3.090	2.582E+07	2.983E-13	6.101E+06	70.6	2.12E-18	-17.6727
W1696_USGS	68	4.079	1.773E+07	6.326E-13	1.294E+07	149.7	4.51E-18	-17.3463
W1696_USGS	69	3.214	2.331E+07	3.659E-13	7.483E+06	86.6	2.61E-18	-17.584
W1696_USGS	70	4.079	1.546E+07	8.320E-13	1.702E+07	196.9	5.93E-18	-17.2272
W1696_USGS	71	3.585	1.787E+07	6.225E-13	1.273E+07	147.3	4.43E-18	-17.3532
W1696_USGS	72	3.708	1.899E+07	5.514E-13	1.128E+07	130.5	3.93E-18	-17.4059
W1696_USGS	73	3.852	2.344E+07	3.619E-13	7.402E+06	85.7	2.58E-18	-17.5887
W1696_USGS	74	3.692	2.158E+07	4.270E-13	8.733E+06	101.1	3.04E-18	-17.5169
W1696_USGS	75	1.981	4.241E+07	1.106E-13	2.261E+06	26.2	7.87E-19	-18.1038
W1696_USGS	76	2.292	3.125E+07	2.036E-13	4.164E+06	48.2	1.45E-18	-17.8385
W1696_USGS	77	2.281	3.686E+07	1.463E-13	2.993E+06	34.6	1.04E-18	-17.982
W1696_USGS	78	3.232	1.921E+07	5.389E-13	1.102E+07	127.6	3.84E-18	-17.4159
W1696_USGS	79	3.042	1.989E+07	5.025E-13	1.028E+07	118.9	3.58E-18	-17.4462
W1696_USGS	80	2.662	2.509E+07	3.159E-13	6.459E+06	74.8	2.25E-18	-17.6479
W1696_USGS	81	4.658	1.673E+07	7.102E-13	1.452E+07	168.1	5.06E-18	-17.296
W1696_USGS	82	3.802	1.541E+07	8.371E-13	1.712E+07	198.1	5.96E-18	-17.2246
W1696_USGS	83	3.802	1.544E+07	8.336E-13	1.705E+07	197.3	5.94E-18	-17.2264
W1696_USGS	84	3.636	2.296E+07	3.772E-13	7.715E+06	89.3	2.69E-18	-17.5707
W1696_USGS	85	3.636	2.350E+07	3.600E-13	7.363E+06	85.2	2.56E-18	-17.591

W1696_USGS	86	3.977	1.118E+07	1.592E-12	3.255E+07	376.8	1.13E-17	-16.9455
W1696_USGS	87	4.205	2.098E+07	4.516E-13	9.236E+06	106.9	3.22E-18	-17.4926
W1696_USGS	88	3.523	2.453E+07	3.304E-13	6.756E+06	78.2	2.35E-18	-17.6284
W1696_USGS	89	4.659	1.685E+07	7.005E-13	1.433E+07	165.8	4.99E-18	-17.302
W1696_USGS	90	3.864	2.422E+07	3.389E-13	6.931E+06	80.2	2.41E-18	-17.6173
W1696_USGS	91	3.750	1.997E+07	4.985E-13	1.020E+07	118.0	3.55E-18	-17.4497
W1696_USGS	92	3.523	2.730E+07	2.667E-13	5.454E+06	63.1	1.9E-18	-17.7213
W1696_USGS	93	3.151	2.039E+07	4.781E-13	9.778E+06	113.2	3.41E-18	-17.4678
W1696_USGS	94	4.201	1.672E+07	7.110E-13	1.454E+07	168.3	5.06E-18	-17.2955
W1696_USGS	95	4.726	1.869E+07	5.692E-13	1.164E+07	134.7	4.05E-18	-17.3921
W1696_USGS	96	4.201	1.828E+07	5.951E-13	1.217E+07	140.9	4.24E-18	-17.3727
W1696_USGS	97	4.901	1.831E+07	5.927E-13	1.212E+07	140.3	4.22E-18	-17.3745
W1696_USGS	98	3.501	2.222E+07	4.025E-13	8.232E+06	95.3	2.87E-18	-17.5426
W1696_USGS	99	4.376	1.614E+07	7.631E-13	1.561E+07	180.6	5.44E-18	-17.2648
W1696_USGS	100	3.211	2.886E+07	2.387E-13	4.882E+06	56.5	1.7E-18	-17.7695
W1696_USGS	101	4.765	1.371E+07	1.058E-12	2.163E+07	250.4	7.53E-18	-17.123
W1696_USGS	102	3.315	1.555E+07	8.223E-13	1.682E+07	194.6	5.86E-18	-17.2323
W1696_USGS	103	4.351	2.025E+07	4.848E-13	9.914E+06	114.7	3.45E-18	-17.4618
W1696_USGS	104	3.729	2.017E+07	4.888E-13	9.996E+06	115.7	3.48E-18	-17.4582
W1696_USGS	105	3.419	2.294E+07	3.777E-13	7.725E+06	89.4	2.69E-18	-17.5702
W1696_USGS	106	3.833	2.037E+07	4.792E-13	9.799E+06	113.4	3.41E-18	-17.4669
W1696_USGS	107	3.937	2.268E+07	3.865E-13	7.904E+06	91.5	2.75E-18	-17.5602
W1696_USGS	108	3.729	1.889E+07	5.569E-13	1.139E+07	131.8	3.97E-18	-17.4016
W1696_USGS	109	4.662	1.676E+07	7.078E-13	1.447E+07	167.5	5.04E-18	-17.2975
W1696_USGS	110	3.648	1.941E+07	5.276E-13	1.079E+07	124.9	3.76E-18	-17.425
W1696_USGS	111	3.462	1.942E+07	5.273E-13	1.078E+07	124.8	3.76E-18	-17.4253
W1696_USGS	112	3.771	1.985E+07	5.046E-13	1.032E+07	119.4	3.59E-18	-17.4444
W1696_USGS	113	2.597	2.069E+07	4.644E-13	9.496E+06	109.9	3.31E-18	-17.4805
W1696_USGS	114	2.844	2.268E+07	3.865E-13	7.904E+06	91.5	2.75E-18	-17.5602
W1696_USGS	115	2.377	2.704E+07	2.720E-13	5.563E+06	64.4	1.94E-18	-17.7128
W1696_UMN	116	1.800	2.681E+07	2.767E-13	5.658E+06	65.5	1.97E-18	-17.7054
W1696_UMN	117	1.566	3.555E+07	1.573E-13	3.217E+06	37.2	1.12E-18	-17.9506
W1696_UMN	118	1.722	3.557E+07	1.572E-13	3.214E+06	37.2	1.12E-18	-17.951
W1696_UMN	119	1.879	1.484E+07	9.029E-13	1.847E+07	213.7	6.43E-18	-17.1917
W1696_UMN	120	2.020	3.064E+07	2.118E-13	4.331E+06	50.1	1.51E-18	-17.8215
W1696_UMN	121	2.020	1.833E+07	5.920E-13	1.211E+07	140.1	4.22E-18	-17.3751
W1696_UMN	122	2.264	3.112E+07	2.053E-13	4.199E+06	48.6	1.46E-18	-17.8349
W1696_UMN	123	2.067	3.465E+07	1.656E-13	3.386E+06	39.2	1.18E-18	-17.9283
W1696_UMN	124	2.505	3.185E+07	1.960E-13	4.008E+06	46.4	1.4E-18	-17.8551
W1696_UMN	125	3.432	2.533E+07	3.098E-13	6.335E+06	73.3	2.21E-18	-17.6563
W1696_UMN	126	2.756	2.630E+07	2.875E-13	5.880E+06	68.1	2.05E-18	-17.6887
W1696_UMN	127	2.047	4.100E+07	1.183E-13	2.419E+06	28.0	8.42E-19	-18.0744
W1696_UMN	128	2.605	2.814E+07	2.511E-13	5.136E+06	59.4	1.79E-18	-17.7475
W1696_UMN	129	1.813	4.073E+07	1.198E-13	2.450E+06	28.4	8.53E-19	-18.0688
W1696_UMN	130	1.963	3.936E+07	1.283E-13	2.624E+06	30.4	9.14E-19	-18.0391
W1696_UMN	131	3.832	2.427E+07	3.374E-13	6.901E+06	79.9	2.4E-18	-17.6192
W1696_UMN	132	1.682	4.204E+07	1.125E-13	2.300E+06	26.6	8.01E-19	-18.0962

W1696_UMN	133	1.682	4.611E+07	9.349E-14	1.912E+06	22.1	6.66E-19	-18.1766
W1696_UMN	134	1.745	4.028E+07	1.226E-13	2.506E+06	29.0	8.73E-19	-18.059
W1696_UMN	135	1.702	4.235E+07	1.108E-13	2.267E+06	26.2	7.9E-19	-18.1026
W1696_UMN	136	1.645	3.482E+07	1.640E-13	3.353E+06	38.8	1.17E-18	-17.9326
W1678_USGS	1	2.494	2.657E+07	2.817E-13	5.761E+06	66.7	2.01E-18	-17.6976
W1678_USGS	2	2.672	2.861E+07	2.428E-13	4.966E+06	57.5	1.73E-18	-17.7621
W1678_USGS	3	2.850	2.422E+07	3.388E-13	6.929E+06	80.2	2.41E-18	-17.6174
W1678_USGS	4	3.741	2.113E+07	4.455E-13	9.110E+06	105.4	3.17E-18	-17.4986
W1678_USGS	5	3.207	2.210E+07	4.069E-13	8.322E+06	96.3	2.9E-18	-17.5378
W1678_USGS	6	3.207	2.210E+07	4.069E-13	8.322E+06	96.3	2.9E-18	-17.5378
W1678_USGS	7	3.029	2.816E+07	2.507E-13	5.126E+06	59.3	1.79E-18	-17.7483
W1678_USGS	8	3.741	2.132E+07	4.373E-13	8.942E+06	103.5	3.11E-18	-17.5066
W1678_USGS	9	3.029	2.447E+07	3.319E-13	6.787E+06	78.6	2.36E-18	-17.6264
W1678_USGS	10	3.764	1.335E+07	1.115E-12	2.281E+07	264.0	7.94E-18	-17.0999
W1678_USGS	11	4.092	1.417E+07	9.897E-13	2.024E+07	234.3	7.05E-18	-17.1519
W1678_USGS	12	3.028	2.067E+07	4.653E-13	9.515E+06	110.1	3.31E-18	-17.4797
W1678_USGS	13	2.697	2.632E+07	2.870E-13	5.869E+06	67.9	2.04E-18	-17.6895
W1678_USGS	14	1.911	4.283E+07	1.084E-13	2.216E+06	25.6	7.72E-19	-18.1125
W1678_USGS	15	2.622	2.803E+07	2.530E-13	5.174E+06	59.9	1.8E-18	-17.7442
W1678_USGS	16	2.530	2.118E+07	4.434E-13	9.067E+06	104.9	3.16E-18	-17.5006
W1678_USGS	17	2.856	1.694E+07	6.925E-13	1.416E+07	163.9	4.93E-18	-17.307
W1678_USGS	18	3.307	2.373E+07	3.531E-13	7.221E+06	83.6	2.52E-18	-17.5995
W1678_USGS	19	3.988	2.740E+07	2.648E-13	5.416E+06	62.7	1.89E-18	-17.7244
W1678_USGS	20	3.988	1.790E+07	6.207E-13	1.269E+07	146.9	4.42E-18	-17.3545
W1678_USGS	21	4.070	1.952E+07	5.218E-13	1.067E+07	123.5	3.72E-18	-17.4298
W1678_USGS	22	4.070	2.024E+07	4.855E-13	9.928E+06	114.9	3.46E-18	-17.4612
W1678_USGS	23	3.973	1.851E+07	5.800E-13	1.186E+07	137.3	4.13E-18	-17.3839
W1678_USGS	24	2.164	2.236E+07	3.978E-13	8.135E+06	94.2	2.83E-18	-17.5477
W1678_USGS	25	3.097	1.011E+07	1.946E-12	3.980E+07	460.7	1.39E-17	-16.8582
W1678_USGS	26	1.844	3.842E+07	1.347E-13	2.755E+06	31.9	9.59E-19	-18.018
W1678_USGS	27	2.038	3.506E+07	1.617E-13	3.307E+06	38.3	1.15E-18	-17.9386
W1678_USGS	28	2.232	2.819E+07	2.501E-13	5.115E+06	59.2	1.78E-18	-17.7492
W1678_USGS	29	2.038	3.032E+07	2.163E-13	4.423E+06	51.2	1.54E-18	-17.8123
W1678_USGS	30	1.824	3.678E+07	1.470E-13	3.005E+06	34.8	1.05E-18	-17.9802
W1678_USGS	31	1.592	2.694E+07	2.739E-13	5.601E+06	64.8	1.95E-18	-17.7098
W1678_USGS	32	2.431	2.171E+07	4.218E-13	8.626E+06	99.8	3E-18	-17.5223
W1678_USGS	33	2.993	1.298E+07	1.180E-12	2.412E+07	279.2	8.4E-18	-17.0756
W1678_UMN	34	1.994	2.813E+07	2.513E-13	5.140E+06	59.5	1.79E-18	-17.7471
W1678_UMN	35	2.617	2.420E+07	3.394E-13	6.941E+06	80.3	2.42E-18	-17.6166
W1678_UMN	36	2.804	1.726E+07	6.671E-13	1.364E+07	157.9	4.75E-18	-17.3232
W1678_UMN	37	2.902	3.364E+07	1.757E-13	3.592E+06	41.6	1.25E-18	-17.9027
W1678_UMN	38	3.026	3.345E+07	1.777E-13	3.634E+06	42.1	1.27E-18	-17.8977
W1678_UMN	39	3.731	3.506E+07	1.618E-13	3.308E+06	38.3	1.15E-18	-17.9385
W1678_UMN	40	3.120	2.018E+07	4.884E-13	9.989E+06	115.6	3.48E-18	-17.4586
W1678_UMN	41	2.487	2.740E+07	2.648E-13	5.416E+06	62.7	1.89E-18	-17.7244

W1678_UMN	42	3.938	2.467E+07	3.268E-13	6.682E+06	77.3	2.33E-18	-17.6331
W1678_UMN	43	3.212	2.571E+07	3.007E-13	6.149E+06	71.2	2.14E-18	-17.6693
W1678_UMN	44	2.902	3.165E+07	1.985E-13	4.059E+06	47.0	1.41E-18	-17.8497
W1678_UMN	45	1.877	3.469E+07	1.652E-13	3.379E+06	39.1	1.18E-18	-17.9293
W1678_UMN	46	2.086	4.078E+07	1.195E-13	2.444E+06	28.3	8.51E-19	-18.0699
W1678_UMN	47	2.086	3.556E+07	1.572E-13	3.215E+06	37.2	1.12E-18	-17.9509
W1678_UMN	48	3.627	2.296E+07	3.773E-13	7.715E+06	89.3	2.69E-18	-17.5707
W1678_UMN	49	2.383	3.030E+07	2.166E-13	4.430E+06	51.3	1.54E-18	-17.8117
W1678_UMN	50	3.834	2.166E+07	4.237E-13	8.666E+06	100.3	3.02E-18	-17.5203
W1678_UMN	51	2.190	3.919E+07	1.295E-13	2.648E+06	30.6	9.22E-19	-18.0352
W1678_UMN	52	3.316	2.361E+07	3.566E-13	7.292E+06	84.4	2.54E-18	-17.5952
W1678_UMN	53	3.761	2.461E+07	3.282E-13	6.711E+06	77.7	2.34E-18	-17.6313
W1678_UMN	54	3.038	2.618E+07	2.900E-13	5.930E+06	68.6	2.07E-18	-17.685
W1678_UMN	55	4.340	2.040E+07	4.776E-13	9.768E+06	113.1	3.4E-18	-17.4683
W1678_UMN	56	4.340	2.047E+07	4.746E-13	9.706E+06	112.3	3.38E-18	-17.471
W1678_UMN	57	4.195	1.922E+07	5.384E-13	1.101E+07	127.4	3.83E-18	-17.4163
W1678_UMN	58	2.174	2.926E+07	2.322E-13	4.749E+06	55.0	1.65E-18	-17.7815
W1678_UMN	59	2.893	2.099E+07	4.511E-13	9.225E+06	106.8	3.21E-18	-17.4931
W1678_UMN	60	3.906	2.109E+07	4.469E-13	9.140E+06	105.8	3.18E-18	-17.4971
W1678_UMN	61	1.884	2.801E+07	2.533E-13	5.181E+06	60.0	1.8E-18	-17.7437
W1678_UMN	62	2.749	3.110E+07	2.056E-13	4.204E+06	48.7	1.46E-18	-17.8344
W1678_UMN	63	1.858	3.848E+07	1.342E-13	2.745E+06	31.8	9.56E-19	-18.0195
W1678_UMN	64	1.480	4.309E+07	1.071E-13	2.189E+06	25.3	7.62E-19	-18.1178
W1678_UMN	65	2.394	2.545E+07	3.069E-13	6.276E+06	72.6	2.19E-18	-17.6604
W1678_UMN	66	2.693	3.763E+07	1.404E-13	2.871E+06	33.2	1E-18	-18.0001
W1678_UMN	67	4.386	2.110E+07	4.466E-13	9.132E+06	105.7	3.18E-18	-17.4975
W1678_UMN	68	2.296	3.500E+07	1.623E-13	3.319E+06	38.4	1.16E-18	-17.9371
W1678_UMN	69	3.548	2.451E+07	3.309E-13	6.768E+06	78.3	2.36E-18	-17.6276
W1678_UMN	70	4.591	1.912E+07	5.439E-13	1.112E+07	128.7	3.87E-18	-17.4118
W1678_UMN	71	5.000	1.852E+07	5.799E-13	1.186E+07	137.3	4.13E-18	-17.384
W1678_UMN	72	5.417	2.059E+07	4.688E-13	9.587E+06	111.0	3.34E-18	-17.4764
W1678_UMN	73	4.583	1.786E+07	6.235E-13	1.275E+07	147.6	4.44E-18	-17.3526
W1678_UMN	74	3.750	2.155E+07	4.281E-13	8.755E+06	101.3	3.05E-18	-17.5158
W1678_UMN	75	5.417	1.892E+07	5.556E-13	1.136E+07	131.5	3.96E-18	-17.4026
W1678_UMN	76	4.167	2.063E+07	4.669E-13	9.549E+06	110.5	3.33E-18	-17.4781
W1678_UMN	77	3.133	1.768E+07	6.358E-13	1.300E+07	150.5	4.53E-18	-17.3441
W1680-USGS	1	3.383	2.145E+07	4.319E-13	8.833E+06	102.2	1.9E-18	-17.7202
W1680-USGS	2	7.199	2.124E+07	4.408E-13	9.014E+06	104.3	1.94E-18	-17.7114
W1680-USGS	3	4.353	2.258E+07	3.901E-13	7.977E+06	92.3	1.72E-18	-17.7645
W1680-USGS	4	4.353	2.258E+07	3.901E-13	7.977E+06	92.3	1.72E-18	-17.7645
W1680-USGS	5	3.516	2.349E+07	3.604E-13	7.370E+06	85.3	1.59E-18	-17.7989
W1680-USGS	6	4.688	1.390E+07	1.029E-12	2.105E+07	243.6	4.54E-18	-17.3431
W1680-USGS	7	4.018	1.617E+07	7.605E-13	1.555E+07	180.0	3.35E-18	-17.4745
W1680-USGS	8	3.687	2.016E+07	4.892E-13	1.000E+07	115.8	2.16E-18	-17.6661
W1680-USGS	9	3.488	2.120E+07	4.424E-13	9.047E+06	104.7	1.95E-18	-17.7098

W1680-USGS	10	4.866	1.795E+07	6.173E-13	1.262E+07	146.1	2.72E-18	-17.5652
W1680-USGS	11	3.970	2.328E+07	3.669E-13	7.503E+06	86.8	1.62E-18	-17.7911
W1680-USGS	12	3.793	1.464E+07	9.275E-13	1.897E+07	219.5	4.09E-18	-17.3883
W1680-USGS	13	3.378	1.990E+07	5.020E-13	1.027E+07	118.8	2.21E-18	-17.655
W1680-USGS	14	3.165	2.821E+07	2.497E-13	5.107E+06	59.1	1.1E-18	-17.9582
W1680-USGS	15	3.455	1.529E+07	8.503E-13	1.739E+07	201.3	3.75E-18	-17.4261
W1680-USGS	16	2.810	2.505E+07	3.167E-13	6.477E+06	75.0	1.4E-18	-17.855
W1680-USGS	17	2.616	2.566E+07	3.020E-13	6.176E+06	71.5	1.33E-18	-17.8756
W1680-USGS	18	2.616	2.566E+07	3.020E-13	6.176E+06	71.5	1.33E-18	-17.8756
W1680-USGS	19	3.557	1.966E+07	5.144E-13	1.052E+07	121.8	2.27E-18	-17.6443
W1700-USGS	1	3.023	9.467E+06	2.218E-12	4.537E+07	525.1	7.08E-18	-17.1498
W1700-USGS	2	2.901	1.318E+07	1.145E-12	2.342E+07	271.1	3.66E-18	-17.437
W1700-USGS	3	3.694	1.417E+07	9.907E-13	2.026E+07	234.5	3.16E-18	-17.4999
W1700-USGS	4	5.593	8.535E+06	2.729E-12	5.581E+07	646.0	8.71E-18	-17.0598
W1700-USGS	5	4.415	1.253E+07	1.267E-12	2.590E+07	299.8	4.04E-18	-17.3932
W1700-USGS	6	4.564	1.465E+07	9.259E-13	1.893E+07	219.2	2.96E-18	-17.5293
W1700-USGS	7	3.141	1.583E+07	7.933E-13	1.622E+07	187.8	2.53E-18	-17.5964
W1700-USGS	8	4.392	1.299E+07	1.178E-12	2.408E+07	278.7	3.76E-18	-17.4248
W1700-USGS	9	3.827	9.128E+06	2.386E-12	4.879E+07	564.7	7.62E-18	-17.1182
W1700-USGS	10	2.679	1.163E+07	1.471E-12	3.008E+07	348.1	4.7E-18	-17.3283
W1700-USGS	11	3.189	9.555E+06	2.178E-12	4.453E+07	515.4	6.95E-18	-17.1579
W1700-USGS	12	4.464	1.212E+07	1.354E-12	2.770E+07	320.6	4.32E-18	-17.3641
W1700-USGS	13	3.972	1.150E+07	1.502E-12	3.072E+07	355.6	4.8E-18	-17.3191
W1700-USGS	14	1.669	8.642E+06	2.662E-12	5.444E+07	630.1	8.5E-18	-17.0706
W1700-USGS	15	3.469	9.753E+06	2.090E-12	4.274E+07	494.7	6.67E-18	-17.1757
W1700-USGS	16	2.553	1.543E+07	8.351E-13	1.708E+07	197.7	2.67E-18	-17.5741
W1700-USGS	17	1.787	1.832E+07	5.926E-13	1.212E+07	140.3	1.89E-18	-17.7231
W1700-USGS	18	2.904	9.385E+06	2.257E-12	4.616E+07	534.3	7.21E-18	-17.1422
W1700-USGS	19	2.162	1.334E+07	1.118E-12	2.286E+07	264.6	3.57E-18	-17.4475
W1700-USGS	20	2.604	1.317E+07	1.147E-12	2.346E+07	271.5	3.66E-18	-17.4362
W1700-USGS	21	3.832	8.134E+06	3.005E-12	6.146E+07	711.3	9.6E-18	-17.018